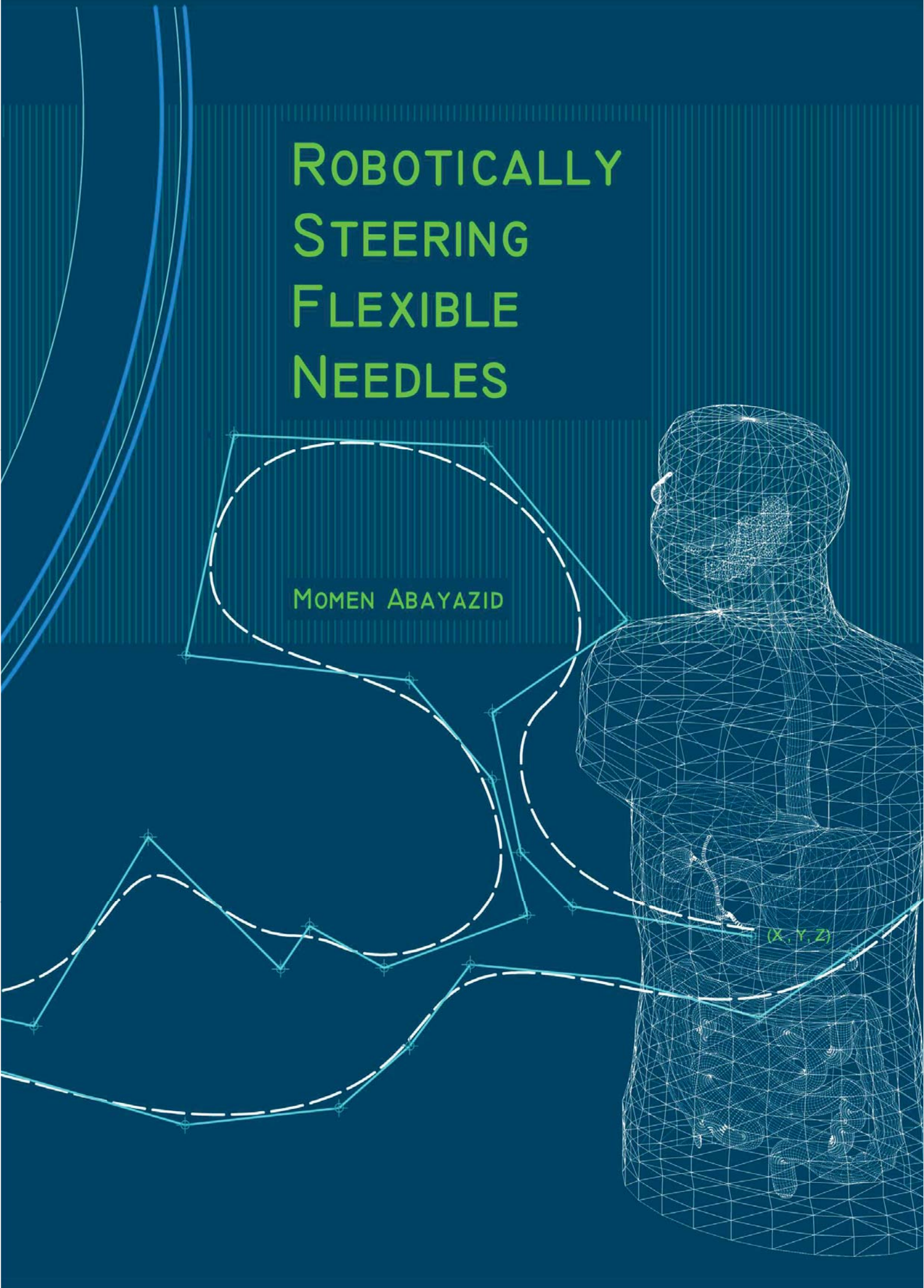


# ROBOTICALLY STEERING FLEXIBLE NEEDLES

MOMEN ABAYAZID

(X, Y, Z)



# ROBOTICALLY STEERING FLEXIBLE NEEDLES

Momen Abayazid

## **Doctoral Thesis Graduation Committee**

### **Chairman and secretary**

Prof. dr. G.P.M.R. Dewulf  
University of Twente, The Netherlands

### **Promotor**

Prof. dr. S. Misra  
University of Twente, The Netherlands

### **Members**

Prof. dr. ir. H.F.J.M. Koopman  
University of Twente, The Netherlands

Prof. dr. ir. W. Steenbergen  
University of Twente, The Netherlands

Prof. dr. J. Dankelman  
Delft University of Technology, The Netherlands

Prof. dr. ir. M. Steinbuch  
Eindhoven University of Technology, The Netherlands

Prof. dr. M. Oudkerk  
University of Groningen and University Medical Center Groningen, The Netherlands

Robotically Steering Flexible Needles  
by Momen Abayazid – University of Twente, 2015 – PhD thesis.

A catalogue record is available from the University of Twente Library.  
ISBN: 978-90-365-3941-8  
DOI: 10.3990/1.9789036539418

Cover Design: Hazem Ahmed Fouad.  
Reproduction: Ipskamp Drukkers B.V., Enschede, The Netherlands.

Copyright ©2015 by Momen Abayazid. All rights reserved.

# ROBOTICALLY STEERING FLEXIBLE NEEDLES

DISSERTATION

to obtain

the degree of doctor at the University of Twente,

on the authority of the rector magnificus,

prof. dr. H. Brinksma,

on account of the decision of the graduation committee,

to be publicly defended

on Wednesday August 26<sup>th</sup> 2015 at 16.45

by

**Momen Abayazid**

born on 30 August 1985

in Gouda, The Netherlands

---

This dissertation has been approved by:

**Prof. dr. Sarthak Misra**

*To my parents:  
Mohamed Nasr El-Din Abayazid,  
and Hoda Omar*

*To the memory of my father:  
Mohamed Nasr El-Din Abayazid*

## Acknowledgements

First and foremost, I would like to thank God (Almighty) for providing me with the strength and patience to complete this work. I would not be able to complete my thesis except by Allah's will.

I would like to thank my father for his support and for being there for me in good times and difficult times during the first two years of my PhD and during the second two years of my PhD his memories were motivating me. I got extra support during the second half of my PhD from my brother Karim who was always providing me with all kinds of help and support. I would like to thank my mother and my sisters (Marwa and Jalila) back home for their continuous support. Though, miles away, their wishes and prayers have always surrounded me.

I would like to thank my supervisor Prof. Sarthak Misra who made me grow in my thesis from scratch and also for his thoughtful guidance and critical comments. From the beginning of my research, he gave me many responsibilities that helped me to gain great experience in a short period. His trust and confidence in me encouraged me to do my best to be worthy of his trust. I believe that he is one of the main reasons that made me aim to continue working in academia after finishing my PhD. Prof. Bart Koopman and Prof. Stefano Stramigioli, although I did not have the chance to directly work with you in research, I could feel the support and the nice atmosphere that you create in both the Department of Biomechanical Engineering (BW) and the Robotics and Mechatronics group (RAM). Thank you for giving me the opportunity to work in your groups, and for being supportive during my difficult times. In addition, I am extremely grateful to Gerben, Lianne, Henny, Nikolai and Alfred for their help throughout my work in the university of Twente. I would like to thank Dr. Ron Alterovitz, Prof. Domenico Prattichizzo, Dr. Claudio Pacchierotti, Dr. Sachin Patil and Dr. Chris de Korte for the fruitful collaborations that we had that helped me in my research.

My warm and sincere thank goes to my colleagues Wissam, Alex, Guus and Navid. I was lucky to do research with each one of you. I really enjoyed our scientific as well as our general discussions. Special thanks to my paranymphs Pedro and Roy for being very helpful and friendly during the period we worked together. I am also very thankful to all RAM and BW colleagues, especially the M.Sc. and B.Sc. students that I worked with during my PhD (Anastasios, Peter-Jan, Frank, Marius, Kaj, Teresa,

Marco, Mitchel and Thomas). Many thanks goes to Taha and Nabeel, who are defending their PhD theses in the same period, for spending time to discuss how to finalize our research and produce our theses in the best way. I would like to express my gratitude to the committee members for agreeing to evaluate my PhD thesis.

Outside the scientific environment, the life in Enschede was very enjoyable with UT-Muslims and IVEO communities, in which I can recharge myself. My sincere thanks to: Ahmad Al-Hanbali and his family, Ahmed Zayed and his family, Bayu, Omar, Islam Fadel and his family, Andry, Sarwar, Ahmed Ragab, Salem, Mohamed Morsi, Ahmed Abo Nada and his family, Alaa, Ahmed Youssef and his family, Muzaffar, Yusuf Wibisono, Suleyman, Ibrahim Imam and Abdul-Rahman Alburaidi, and all. The list will be very long as I indebted many people during those four years. I also would like to offer my great appreciation to my friends in Egypt for their continuous support, especially my close friend Mostafa Abel-Nasser who I depended on (after Allah) in many things. He always gives me the feeling that I need to focus on my work in the Netherlands, and I should not worry about things that need to be done in Egypt if he is there. I am very grateful to Hazem for helping me in every design-related thing, starting from the design of the cover of this thesis to the interior design of my apartment. I am also grateful to Ahmed Hamdy and Saleem Al-Ahdab for being caring and supportive during the last years. Despite the distances, we could keep our strong friendship.

Last but not least, I would like to thank my dear wife Eman for standing by my side and for her understanding and patience. My life would never been so enjoyable and meaningful without Eman and Mosa. Thank you for your love, patience and prayers.

*Momen Abayazid*  
*Enschede, The Netherlands*  
*August 26, 2015.*

---

# Summary

Needle insertion into soft tissue is one of the common minimally invasive surgical procedures. Many diagnostic and therapeutic clinical procedures require insertion of a needle to a specific location in soft-tissue, including biopsy, drug injection, or radioactive seed implantation for cancer treatment (brachytherapy). Imaging modalities such as ultrasound and magnetic resonance (MR), fluoroscopy and computed tomography (CT) scans are used during needle insertion procedures to localize the needle and target for accurate tip placement. The accuracy of needle placement affects the precision of diagnosis during biopsy, and the success of treatment during brachytherapy. Rigid needles are used in such procedures, but they provide the clinician with limited steering capabilities to avoid obstacles and reach the target. Moreover, the needles that are currently used in surgical procedures are often thick. Such thick needles cause deformation of tissue that leads to target motion, which affects the targeting accuracy. Another practical issue concerning the use of thick needles is patient trauma. Currently, rigid needle insertions are performed manually, where the clinician relies on imaging systems e.g., two-dimensional (2D) ultrasound imaging to estimate the needle path and target location in three-dimensional (3D) space. Flexible needles were introduced to improve the steering capabilities that allow reaching target locations inaccessible by traditional rigid needles. They can be used to avoid sensitive tissue that might be located along the path to the target. Flexible needles with an asymmetric tip (e.g., bevel tip) naturally bend during insertion into soft tissue. Manually steering of flexible needles towards a desired location is unintuitive and challenging. Robotic needle insertion systems can assist in achieving improved targeting accuracy for various clinical applications. Such a system requires online needle tracking, target localization, path planning and control algorithms to steer the needle to reach a certain location while avoiding obstacles.

In this thesis, we start with modeling the effect of skin thickness on target motion during insertion. A closed-loop control algorithm is then developed for needle steering using camera images and 2D ultrasound for feedback (Part I). An ultrasound-based 3D needle tracking algorithm is then combined with real-time path planning for needle steering. The needle is steered during insertion in gelatin-based soft-tissue phantoms and also biological tissue. A non-imaging approach (fiber Bragg grating (FBG) sensors) is also used for real-time needle shape reconstruction and tip tracking (Part II). FBG sensors are used as feedback to the control algorithm to steer the needle towards a virtual target in 3D space. We then focus on physical target localization and 3D shape reconstruction for needle steering in phantoms with curved surfaces. A clinical application (needle insertion in the prostate) is also investigated where the needle is

---

steered in a multi-layer phantom with different tissue elasticities (Part III). In order to bring the proposed algorithms to clinical environments, we consider practical issues such as including the clinician in the control loop to merge robot accuracy with clinical expertise. The proposed system is adapted to enable clinicians to directly control the insertion procedure while receiving navigation cues from the control algorithm (Part IV). Navigation cues are provided through a combination of haptic (vibratory) and visual feedback to the operator who controls the needle for steering. The proposed system is further adapted by using a clinically-approved Automated Breast Volume Scanner (ABVS) which is experimentally evaluated to be used for needle insertion procedures. The ultrasound-based ABVS system is used for pre-operative scanning of soft-tissue for target localization, shape reconstruction, and also intra-operatively for needle tip tracking during the steering process. The achieved targeting errors suggest that our approach is convenient for targeting lesions that can be detected using clinical ultrasound imaging systems. These promising results allow us to proceed further in bringing our system towards clinical practice.

# Samenvatting

Het inbrengen van naalden in zachte weefsels is een van de meest toegepaste, minimaal invasieve procedures. Veel diagnostieke en therapeutische procedures vereisen het inbrengen van een naald naar een specifieke locatie in het zachte weefsel van de mens. Voorbeelden van dergelijke procedures zijn biopsies, het toedienen van medicijnen of het inbrengen van radioactieve zaadjes ter behandeling van kanker (brachytherapie). Beeldvormende modaliteiten zoals echografie, magnetische resonantie (MR), fluoroscopie en computertomografie (CT) worden gebruikt ter ondersteuning tijdens deze procedures. De beeldvorming wordt gebruikt om de naald en het beoogde doelwit te localiseren zodat de naaldpunt nauwkeurig geplaatst kan worden. De nauwkeurigheid van de naaldplaatsing bepaald de effectiviteit van de diagnose bij een biopsie en het succes van de behandeling in het geval van brachytherapie. In deze procedures worden stijve naalden gebruikt met beperkte stuurmogelijkheden om obstakels te ontwijken en het doelwit te bereiken. Bovendien hebben de naalden die gebruikt worden voor deze chirurgische procedures een grote diameter. Dit zorgt ervoor dat het weefsel vervormd en het doelwit zich verplaatst, hetgeen de nauwkeurigheid van de naald plaatsing beïnvloedt. Een ander probleem dat het gebruik van naalden met een grote diameter met zich meebrengt is het letsel dat bij de patient wordt veroorzaakt. Het inbrengen van naalden wordt momenteel handmatig uitgevoerd, waarbij de clinicus beeldvormende systemen zoals tweedimensionale (2D) echografie gebruikt om het naaldpad en de locatie van het doelwit te bepalen in de driedimensionale (3D) ruimte. Flexibele naalden zijn geïntroduceerd om de stuurmogelijkheden te verbeteren, waarbij het mogelijk wordt om doelen te bereiken die met traditionele, stijve naalden niet te bereiken zijn. Deze naalden kunnen gebruikt worden om gevoelig weefsel te vermijden dat mogelijk op het traject richting het doelwit ligt. Flexibele naalden met een asymmetrische punt (bijv. een afgeschuinde punt) buigen af wanneer ze in zacht weefsel worden ingebracht. Het handmatig sturen van flexibele naalden naar een gewenste locatie is lastig en niet intuïtief. Robotisch aangestuurde systemen die de naald inbrengen kunnen hulp bieden bij het verkrijgen van een verhoogde nauwkeurigheid van naaldplaatsing voor verschillende klinische procedures. Een dergelijk systeem moet voldoen aan een aantal eisen: De naald moet online gevolgd worden, het doelwit moet worden gelokaliseerd, het traject richting het doelwit moet gepland worden en het systeem moet beschikken over regelalgoritmen die de naald aansturen richting een beoogd doelwit terwijl obstakels worden vermeden.

In dit proefschrift beginnen we met het modeleren van de invloed van huiddikte op de verplaatsing van het doelwit tijdens het inbrengen van de naald. Vervolgens is

---

er een regelalgoritme ontwikkeld waarbij de naald gestuurd wordt met camerabeelden en 2D echografie als terugkoppeling (Deel I). Daarna wordt een 3D naald-lokalisatie algoritme, dat gebruikt maakt van echografie beelden, gecombineerd met real-time trajectplanning om de naald te sturen. De naald wordt tijdens het inbrengen gestuurd in zowel gelatine fantomen als biologisch weefsel. Naast de beeldvormende technieken worden er ook gebruik gemaakt van optische rekstrookjes (fiber bragg grating (FBG) sensoren) om de naaldvorm in real-time te reconstrueren en de naalpunt te volgen (Deel II). FBG sensoren worden gebruikt voor terugkoppeling naar het regelalgoritme om de naald in de 3D ruimte richting een virtueel doelwit te sturen. Vervolgens richten we ons op het lokaliseren en 3D reconstructie van fysieke doelwitten voor het sturen van naalden in fantomen met een gebogen oppervlak. Klinische toepassingsgebieden, zoals het inbrengen van de naald in de prostaat, worden onderzocht door de naald te sturen in een fantoom dat bestaat uit meerdere lagen van verschillende stijftheden (Deel III). Om de voorgestelde algoritmen naar een klinische omgevingen te brengen worden praktische zaken zoals acceptatie door de klinische gemeenschap overwogen waarbij de clinicus in de regellus wordt geïntroduceerd. De nauwkeurigheid van een robotisch systeem wordt hierdoor gecombineerd met klinische expertise. Het voorgestelde systeem geeft een clinicus de directe controle over het inbrengen van de naald, terwijl er stuur-aanwijzingen worden gegeven door het regelalgoritme (Deel IV). Stuuraanwijzingen worden gegeven door een combinatie van haptische (trillingen) en visuele terugkoppeling. Het voorgestelde systeem wordt verder aangepast door gebruik te maken van een klinisch goedgekeurde automatische borst-volume scanner (ABVS) die experimenteel wordt geëvalueerd voor het inbrengen van naalden. De op echografie gebaseerde ABVS wordt gebruikt bij een preoperatieve scan van het zachte weefsel om het doelwit te lokaliseren en de vorm te reconstrueren, maar ook voor het intraoperatief volgen van de naaldpunt tijdens het stuurproces. De behaalde nauwkeurigheden van naaldplaatsing geven aan dat onze aanpak geschikt is om laesies te bereiken die gedetecteerd kunnen worden door klinische echografie systemen. Deze veelbelovende resultaten stellen ons in staat verder te gaan om ons systeem richting de kliniek te brengen.

# Contents

<b>1</b>	<b>Introduction</b>	<b>1</b>
1.1	Clinical procedures and imaging . . . . .	2
1.1.1	Needle-based interventions in the breast . . . . .	2
1.1.1.1	Fine needle aspiration (FNA) . . . . .	3
1.1.1.2	Core needle biopsy . . . . .	3
1.1.1.3	Vacuum-assisted biopsy (VAB) . . . . .	4
1.1.1.4	Surgical biopsy . . . . .	4
1.1.2	Needle-based interventions in the prostate . . . . .	4
1.1.2.1	Prostate biopsy . . . . .	4
1.1.2.2	Prostate cancer therapy . . . . .	5
1.2	Flexible needle steering . . . . .	6
1.3	Challenges and proposed solutions . . . . .	7
1.3.1	Environment modeling . . . . .	7
1.3.2	Needle tracking . . . . .	8
1.3.3	Needle steering . . . . .	8
1.3.4	Obstacle avoidance . . . . .	9
1.3.5	Practical issues . . . . .	10
1.4	Outline of the thesis . . . . .	10
1.5	Contributions . . . . .	11
<b>I</b>	<b>Two-Dimensional Needle Steering</b>	<b>15</b>
<b>2</b>	<b>Effect of Skin Thickness on Target Motion during Needle Insertion into Soft-Tissue Phantoms</b>	<b>19</b>
2.1	Introduction . . . . .	20
2.2	Elasticity of soft-tissue phantom . . . . .	22
2.3	Experimental setup . . . . .	22
2.3.1	Soft-tissue phantom preparation . . . . .	22
2.3.2	Needle insertion experiments . . . . .	23
2.3.3	Target motion tracking . . . . .	24
2.4	Results . . . . .	24
2.4.1	Elastic modulus . . . . .	24

## CONTENTS

---

2.4.2	Insertion force and target displacement . . . . .	25
2.4.3	Discussion . . . . .	27
2.5	Conclusions and future work . . . . .	28
<b>3</b>	<b>Integrating Deflection Models and Image Feedback for Real-Time Flexible Needle Steering</b>	<b>29</b>
3.1	Introduction . . . . .	30
3.2	Related work . . . . .	31
3.2.1	Needle deflection models . . . . .	32
3.2.2	Needle and target tracking . . . . .	32
3.2.3	Proposed algorithm for steering . . . . .	33
3.3	Needle deflection models . . . . .	33
3.3.1	Kinematics-based model . . . . .	34
3.3.2	Mechanics-based model . . . . .	36
3.3.3	Experimental setup . . . . .	40
3.3.4	Model fitting . . . . .	41
3.3.5	Open-loop needle steering . . . . .	43
3.4	Control of flexible needles . . . . .	44
3.4.1	Closed-loop needle steering . . . . .	44
3.4.2	Needle and target tracking algorithms . . . . .	45
3.4.2.1	Needle-tip tracking algorithm . . . . .	45
3.4.2.2	Target motion tracking . . . . .	47
3.5	Experimental results . . . . .	47
3.5.1	Experimental plan . . . . .	48
3.5.1.1	Camera image-guided needle steering . . . . .	48
3.5.1.2	Ultrasound image-guided needle steering . . . . .	49
3.5.2	Results . . . . .	50
3.6	Discussion . . . . .	51
3.6.1	Conclusions . . . . .	51
3.6.2	Future work . . . . .	52
<b>II</b>	<b>Three-Dimensional Needle Steering</b>	<b>53</b>
<b>4</b>	<b>3D Flexible Needle Steering in Soft-Tissue Phantoms using Fiber Bragg Grating Sensors</b>	<b>57</b>
4.1	Introduction . . . . .	57
4.2	Three-dimensional needle shape reconstruction . . . . .	59
4.2.1	Fiber Bragg Grating sensors . . . . .	59
4.2.2	Needle curvature calculation . . . . .	60
4.2.3	Needle shape reconstruction . . . . .	61
4.3	Three-dimensional needle steering algorithm . . . . .	62
4.4	Experiments . . . . .	64
4.4.1	Experimental setup . . . . .	64
4.4.2	Hysteresis calibration of the Fiber Bragg Grating sensors . . . . .	65

4.4.3	Validation of the needle shape reconstruction method . . . . .	66
4.5	Results . . . . .	66
4.5.1	Needle shape reconstruction . . . . .	66
4.5.2	Needle steering . . . . .	67
4.6	Discussion . . . . .	68
<b>5</b>	<b>Experimental Evaluation of Ultrasound-Guided 3D Needle Steering in Biological Tissue</b>	<b>71</b>
5.1	Introduction . . . . .	71
5.2	Three-dimensional needle tracking . . . . .	74
5.3	Three-dimensional needle path planning and control . . . . .	75
5.3.1	Path planning . . . . .	76
5.3.2	Control algorithm . . . . .	76
5.4	Experiments . . . . .	78
5.4.1	Setup . . . . .	78
5.4.2	Results . . . . .	78
5.5	Discussion . . . . .	80
<b>III</b>	<b>Steering in Phantoms with Non-Uniform Surfaces</b>	<b>83</b>
<b>6</b>	<b>Ultrasound-Guided Three-Dimensional Needle Steering in Biological Tissue with Curved Surfaces</b>	<b>87</b>
6.1	Introduction . . . . .	88
6.1.1	Related work . . . . .	88
6.1.2	Contributions . . . . .	89
6.2	Ultrasound scanning over curved surfaces . . . . .	90
6.2.1	Mechanical design . . . . .	91
6.2.2	Alignment control algorithm . . . . .	91
6.2.3	Target localization and shape reconstruction . . . . .	91
6.3	Ultrasound-guided needle steering . . . . .	92
6.4	Experimental results . . . . .	93
6.4.1	Experimental setup . . . . .	95
6.4.2	Effect of needle parameters on target motion . . . . .	95
6.4.3	Needle steering results . . . . .	96
6.4.3.1	Experimental plan . . . . .	96
6.4.3.2	Results . . . . .	97
6.5	Conclusions and recommendations . . . . .	97

## CONTENTS

---

<b>7</b>	<b>Needle Steering Towards a Localized Target in a Prostate Phantom</b>	<b>99</b>
7.1	Introduction . . . . .	100
7.2	Methods . . . . .	102
7.2.1	Experimental setup . . . . .	102
7.2.2	Needle steering . . . . .	104
7.2.3	Alignment control algorithm . . . . .	106
7.2.4	Target localization . . . . .	107
7.3	Experiments . . . . .	107
7.3.1	Experimental plan . . . . .	108
7.3.2	Results . . . . .	108
7.4	Conclusions and future work . . . . .	110
<b>IV</b>	<b>Towards Clinical Practice</b>	<b>111</b>
<b>8</b>	<b>Experimental Evaluation of Co-Manipulated Ultrasound-Guided Flexible Needle Steering</b>	<b>115</b>
8.1	Introduction . . . . .	115
8.1.1	Haptic feedback for shared control . . . . .	116
8.1.2	Contributions . . . . .	118
8.2	Materials and methods . . . . .	119
8.2.1	Slave system . . . . .	119
8.2.1.1	Needle tip tracking . . . . .	120
8.2.1.2	Path planning and control algorithms . . . . .	121
8.2.2	Master system . . . . .	121
8.2.2.1	Setup . . . . .	122
8.2.2.2	Visual feedback . . . . .	122
8.2.2.3	Vibratory feedback . . . . .	123
8.2.3	Experiments . . . . .	123
8.2.3.1	Experimental protocol . . . . .	123
8.2.3.2	Subjects . . . . .	124
8.3	Results . . . . .	124
8.4	Discussion . . . . .	128
8.4.1	Conclusions . . . . .	129
8.4.2	Future work . . . . .	130
<b>9</b>	<b>Reconstruction of 3D Shapes and Needle Steering Using Automated Breast Volume Scanner (ABVS)</b>	<b>131</b>
9.1	Introduction . . . . .	132
9.1.1	Robotic control of ultrasound transducers . . . . .	132
9.1.2	Flexible needle steering . . . . .	133
9.1.3	Contributions . . . . .	134
9.2	Target localization and shape reconstruction . . . . .	134
9.2.1	Registration and synchronization . . . . .	135
9.2.2	Localization . . . . .	135

9.2.3	Target reconstruction algorithm . . . . .	135
9.3	Three-dimensional needle steering . . . . .	136
9.3.1	Needle tip tracking . . . . .	136
9.3.1.1	Image processing . . . . .	137
9.3.1.2	Velocity control . . . . .	137
9.3.2	Three-dimensional needle path planning and control . . . . .	138
9.4	Experiments . . . . .	139
9.4.1	Setup . . . . .	139
9.4.2	Experimental plan . . . . .	139
9.4.2.1	Shape reconstruction . . . . .	140
9.4.2.2	Steering . . . . .	140
9.4.3	Results . . . . .	141
9.5	Conclusions and future work . . . . .	142
9.5.1	Conclusions . . . . .	142
9.5.2	Future work . . . . .	142
<b>V Outlook</b>		<b>145</b>
<b>10 Conclusions and Future Work</b>		<b>147</b>
10.1	Conclusions . . . . .	148
10.2	Future work . . . . .	150
<b>References</b>		<b>153</b>

## CONTENTS

---

# 1

## Introduction

During the last decade, there has been a significant increase in Minimally Invasive Surgery (MIS). In MIS, the surgical instrument is inserted into the body via a small incision allowing the clinician to perform the procedure [1]. The potential benefits of MIS include minimizing patient trauma, less blood loss, reduced risk of infection and faster recovery from surgery with respect to conventional open surgery. As research in the direction of MIS advances, more technologies become available for such procedures. These technologies include robotic systems such as the da Vinci (Intuitive Surgical, Sunnyvale, CA, USA), NeuroArm (IMRIS Inc., Minnetonka, MN, USA), MiroSurge (DLR, Oberpfaffenhofen-Wessling, Germany), Raven (University of Washington, Washington, DC, USA), MicroSure (Eindhoven University of Technology, Eindhoven, The Netherlands), Rosa (MedTech, Montpellier, France) and Sofie (Eindhoven University of Technology, Eindhoven, The Netherlands), and also imaging modalities such as transrectal ultrasound and endoscopic camera [2, 3, 4, 5]. These robotic systems and imaging modalities can assist in achieving precise control of the surgical tools during MIS.

There are various applications of MIS such as endoscopy, spine surgery, neurosurgery and percutaneous needle insertion. In this thesis, we focus on percutaneous needle insertion procedures that are used for diagnostic and therapeutic applications [6]. Examples of diagnostic needle insertion procedures are breast, liver and lung biopsies to sample lesions (Fig. 1.1(a)) [7, 8]. Therapeutic applications of needle insertion include brachytherapy, thermal ablation and localized drug delivery (Fig. 1.1(b)) [9]. If the needle fails to reach its goal, then it must be retracted and reinserted, and several attempts may be required before precise placement is achieved. Inaccurate placement may result in misdiagnosis and unsuccessful treatment. In order to achieve accurate needle tip placement, imaging modalities such as ultrasound, magnetic resonance (MR), and computed tomography (CT) are often used pre-operatively to localize the target. Image-guidance is also used during the clinical procedure to determine the positions of the needle and target during insertion [10]. Various types of needles and imaging modalities are used during clinical procedures. Understanding these procedures is essential for developing an accurate needle steering system.

## 1. INTRODUCTION

---

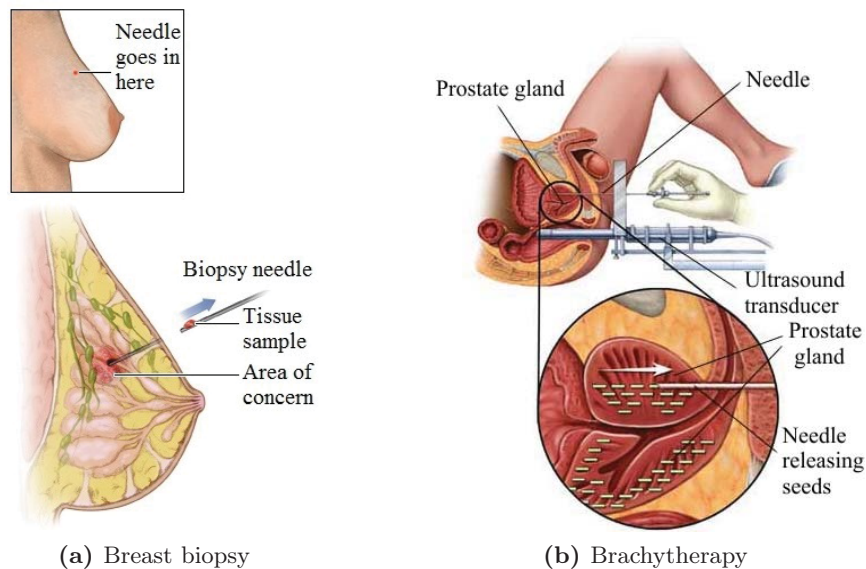


**Fig. 1.1:** Examples of procedures in which needles are used to reach a certain location in the human body. (a) Breast biopsy: the needle is used to take a tissue sample for diagnosis (©Healthwise, Incorporated). (b) Brachytherapy: a needle is used to place radioactive seeds near a tumor for treatment (©Mayo Foundation for Medical Education and Research)<sup>1</sup>.

### 1.1 Clinical procedures and imaging

Image-guidance during clinical procedures is used for accurate needle placement in different types of tissues such as breast, kidney and lung. Breast and prostate cancers are the most common types of cancers affecting women and men, respectively [11]. Therefore, in this thesis, we focus on needle insertion techniques that can improve the diagnostic and therapeutic outcomes of breast and prostate procedures. Further, these techniques can be extended to be used for other clinical applications with appropriate modifications. A brief description of breast and prostate clinical procedures is presented in this section.

#### 1.1.1 Needle-based interventions in the breast

Needle insertion in breast is mainly used for diagnostic procedures such as biopsy. During breast biopsy, the needle is used to extract a tissue sample. Further investigations are applied on the extracted sample for diagnosis. The common types of breast biopsies are described in the following sub-sections.

---

<sup>1</sup>Used with permission from Mayo Foundation for Medical Education and Research, and Healthwise, Incorporated. All rights reserved.

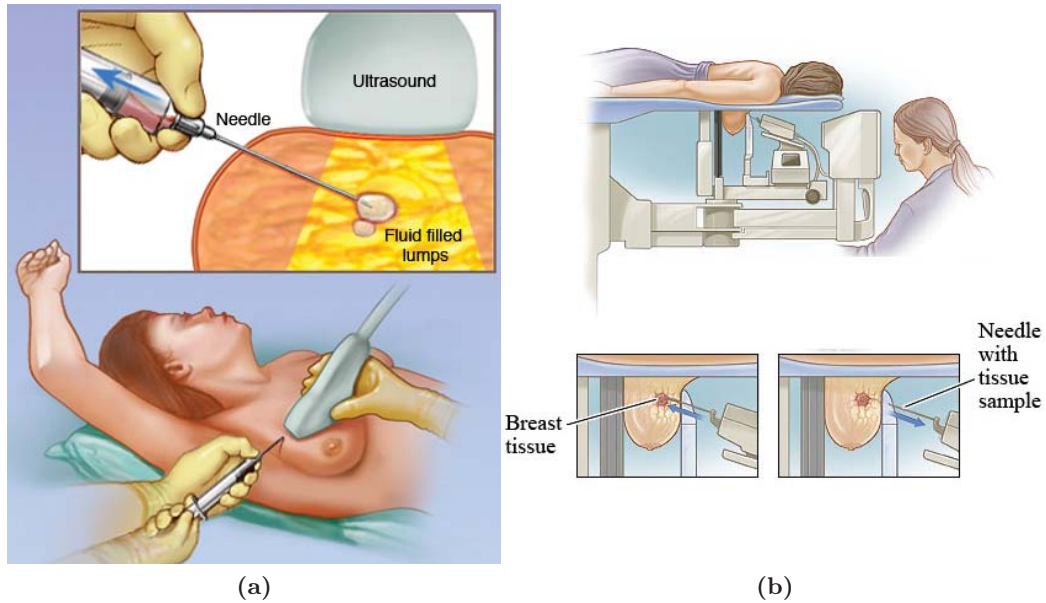


**Fig. 1.2:** Types of breast biopsy. (a) Fine needle aspiration biopsy: the needle is used to absorb fluid from the lesion (©Mayo Foundation for Medical Education and Research). (b) Stereotactic biopsy: mammography is used for needle-guidance (©Healthwise, Incorporated)<sup>2</sup>.

#### 1.1.1.1 Fine needle aspiration (FNA)

Ultrasound guidance is commonly used to determine the needle and target (lesion) positions [12]. In case the lesion is small and not localized using ultrasound, mammography is used for needle guidance. A fine hollow needle absorbs fluid or cells from a breast lesion (Fig. 1.2(a)). The clinician performs several insertions to ensure obtaining useful samples. The absorbed sample of fluid or cells is further examined in a laboratory. Fine needle aspiration biopsy is performed for diagnostic purposes and also for treatment planning [13].

#### 1.1.1.2 Core needle biopsy

In this type of biopsy a hollow needle is inserted into the breast to take cylindrical samples of the suspected breast tissue for further laboratory investigations. The needle size is larger than the needle using during the FNA procedure. In many cases, several insertions are performed for obtaining the samples. Ultrasound, MR and mammography (stereotactic biopsy) images are used to guide the needle to reach the suspect mass (Fig. 1.2(b)) [14, 15]. The choice of the imaging modality depends on the mass location. The success rate of the biopsy procedure is largely dependent on the type of lesion [13].

<sup>2</sup>Used with permission from Mayo Foundation for Medical Education and Research, and Healthwise, Incorporated. All rights reserved.

## 1. INTRODUCTION

---

### 1.1.1.3 Vacuum-assisted biopsy (VAB)

Vacuum-assisted biopsy was developed to address the limitations of core biopsy and FNA [13]. It addresses the need for larger volumes of tissue for histological examination. This type of biopsy is powered with suction and a rotating cutter, which obtains multiple samples from the lesion. The vacuum draws tissue into an aperture in the needle where it is separated from the surrounding breast tissue by the rotating cutter. The sample is collected without removing the needle from the biopsy site. This enables multiple samples to be taken by rotating the shaft of the needle after a single insertion. VAB is performed under ultrasound, x-ray or MR guidance. VAB provides relatively large specimens with respect to core needle biopsy. It is also less sensitive to targeting errors and thus, has lower re-biopsy rates. In practice, VAB is most commonly used for diagnostic sampling of microcalcification, but is also used for sampling soft-tissue abnormalities [13].

### 1.1.1.4 Surgical biopsy

Surgical biopsy is an MIS that is also called wide local excision. In this procedure, ultrasound is used to localize the lesion and in some cases it is used during the biopsy procedure. In this type of breast biopsy an incision is used to extract relatively large sizes of the suspected lesions. This type of biopsy is beyond the scope of this thesis since needles are not used during the procedure [12].

## 1.1.2 Needle-based interventions in the prostate

Prostate needle insertion is used for diagnostic and therapeutic applications. The needles are used for biopsy and also injection of radio-active seed for cancer treatment (brachytherapy). Transrectal ultrasound (TRUS) is the common clinical modality for imaging the prostate and the needle, for either diagnosis or therapy. In this section, we describe the prostate biopsy procedure as it is a needle-based intervention that is often used for diagnostic purposes.

### 1.1.2.1 Prostate biopsy

Prostate biopsy is performed after initial examinations such as prostate specific antigen blood test or digital rectal exam [16]. This procedure is performed by a urologist using a fine needle to determine the treatment options. There are three main techniques of prostate biopsy: (a) transrectal technique (Fig. 1.3), (b) transurethral technique and (c) transperineal technique. The transrectal technique is the most common type of prostate biopsy, and it is often performed under TRUS guidance. During the biopsy procedure hollow spring propelled needle is used to extract the samples. Several samples are obtained under ultrasound-guidance [16]. MR-imaging is also used in fusion with ultrasound for improved imaging outcome [17].

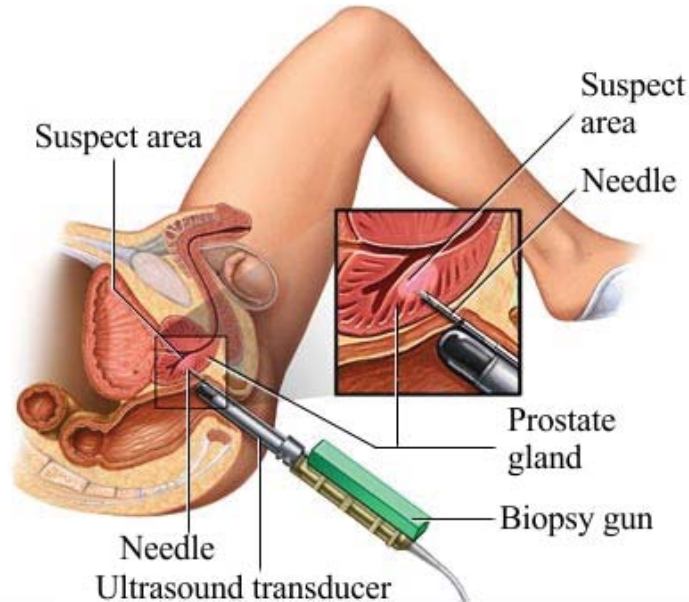


**Fig. 1.3:** In prostate biopsy, the needle is inserted to extract a sample from the suspect area of the prostate gland using a biopsy gun under ultrasound-guidance (©Mayo Foundation for Medical Education and Research<sup>3</sup>).

### 1.1.2.2 Prostate cancer therapy

There are several prostate cancer therapies such as hormone therapy, High intensity focused ultrasound (HIFU), laser ablation and surgical prostate gland removal [18]. In this section, we describe cryotherapy and brachytherapy as they are the main needle-based prostate therapeutic procedures.

#### Cryotherapy

Prostate cryotherapy is the ablation of the prostate gland using local induction of extremely cold temperatures. Liquid nitrogen or argon is used to freeze and thus, destroy prostate tumors [19]. The liquid is transported to the prostate via hollow needles. The diameter of argon-based needles is smaller than nitrogen-based needles [20]. Around 30 needles are inserted to have a uniform freezing pattern in the prostate. The needles are placed at least 8 mm from the urethra to avoid its freezing. A urethral warming device is used together with thermocouples to monitor the temperature of other structures in the area such as the bowel muscle and the rectum, and prevent freezing of the tissues surrounding the prostate [18]. The procedure is performed under TRUS guidance to monitor needle placement and the freezing of tissue.

<sup>3</sup>Used with permission from Mayo Foundation for Medical Education and Research. All rights reserved.

## 1. INTRODUCTION

---

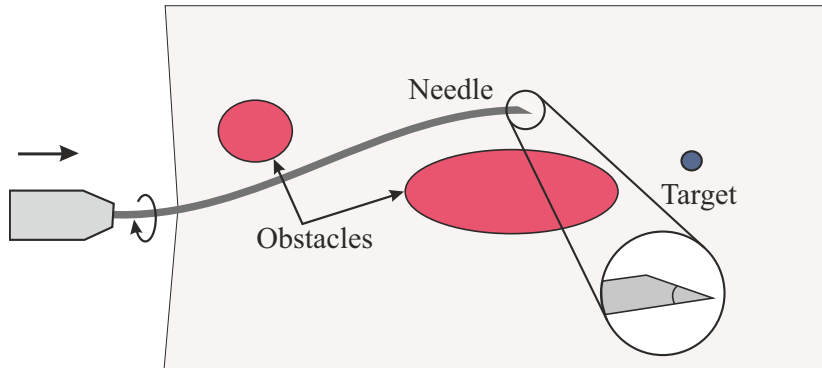


**Fig. 1.4:** A flexible needle with an asymmetric (bevel) tip is used to steer around obstacles. Steering is accomplished by a combination of insertion and rotation at the base of the needle.

### Brachytherapy

Prostate brachytherapy is a therapeutic procedure where radioactive seeds are implanted in the prostate using a hollow needle (Fig. 1.1(b)) [21]. The radiation generated from the seeds is used to destroy prostate cancer cells. Prior to the procedure, transrectal ultrasound images are used for mapping the prostate to determine its position and size. The radioactive seeds are made of iodine or palladium. Both materials have similar radioactive energy [22]. The main difference between iodine and palladium is their half-lives, 59.4 and 16.97 days, respectively. Palladium has higher dose rate than iodine, therefore its equivalent prescribed dose is lower than iodine (115 Gy vs 145 Gy) [22]. The seeds are 0.5 cm long and their thickness is 1 mm. The dose distribution is planned to deliver high dose to the prostate while minimizing the radiation delivered to adjacent structure such as bladder and urethra [22]. If the radioactive seeds are not placed accurately by the needle, the amount of dose reaching the cancer cells may not be sufficient for treatment and thus, the procedure can be repeated. This emphasizes the importance of accurate needle steering for effective and fast treatment.

### 1.2 Flexible needle steering

Rigid needles are usually used in the procedures described in Section 1.1. Such needles cause deformation of tissue, and this can result in target motion, which affects the targeting accuracy [23, 24]. Besides tissue deformation, other possible causes of targeting inaccuracy are patient motion during the procedure, and physiological processes such as fluid flow and respiration. Another disadvantage of using rigid needles is that they cause patient trauma. Thin needles were introduced to minimize patient discomfort [25]. Another advantage of using thin needles is that they are flexible, and therefore facilitate curved needle paths. This enables steering the needle around obstacles (such as sensitive tissues), and to reach locations which are unreachable by rigid needles. Manually steering thin, flexible needles towards a desired location is challenging [26]. Needle steering techniques and robotic systems were introduced to enable clinicians to

achieve accurate targeting. These techniques and systems include bevel-tip flexible needles (Fig. 1.4) [27], symmetric-tip needles that can be steered by applying forces at the base [26, 28], curved style tips [29], programmable bevel-tip needles [30], actuated-tip needles [31], and pre-bent concentric tubes [32, 33].

In this thesis, we focus on bevel-tipped flexible needles because the needle design is completely passive, and it is controlled solely at the base outside the tissue which make them safer than actuated-tip needles. In actuated needles, any failure can cause serious complications to the patient (such as tissue damage and break of parts in the tissue). Bevel-tipped needles have simpler designs and safer for the patient compared to actuated needles. These needles can be controlled robotically by axial rotations at the needle base outside the tissue. The deflection of a needle with a bevel tip can be controlled using duty-cycled axial rotations of the needle during insertion [34, 35]. This algorithm controls the needle curvature by varying the ratio between period of needle insertion with spinning to the total insertion period. The main disadvantage of the duty-cycling approach is that it requires excessive number of rotations of the needle inside the tissue that can increase tissue damage [36]. Several challenges need to be investigated to develop a robotic system to steer the needle accurately without excessive number of needle axial rotations. These challenges include developing a model for predicting the needle deflection, needle tracking for feedback control, path planning and a control techniques to steer the needle to reach a certain location while avoiding obstacles.

### 1.3 Challenges and proposed solutions

Robot-aided and ultrasound-guided needle insertion systems can assist in achieving high targeting accuracy for various clinical applications. Several challenges need to be addressed to develop such a steering system and make it suitable for clinical practice. The main challenges that are addressed in this thesis and their proposed solutions are presented in this section.

#### 1.3.1 Environment modeling

##### Challenge

Prior to developing a robotic needle steering system, the insertion environment needs to be investigated. In many needle insertion procedures, the needle first penetrates the skin tissue, fat tissue and then different tissues such as muscles. These tissues have various mechanical properties. This affects the bevel-tipped needle deflection during the insertion procedure, and consequently the targeting accuracy. The accuracy of needle placement is also affected by target motion that can take place during needle insertion. Target motion can occur due to tissue deformation during tissue penetration, and also physiological motion such as respiration and fluid flow. Accurate target localization is also a challenge that needs to be tackled to achieve improved targeting accuracy.

## 1. INTRODUCTION

---

### Proposed solutions

In Chapter 2, the environment is modeled by estimating the elastic properties of the soft-tissue phantom. This assists in predicting the effects of tissue properties on target motion. The elastic properties of the target, skin, and the surrounding tissue are estimated using a non-invasive ultrasound-based approach which uses Acoustic Radiation Force Impulse technique to determine the elastic moduli of tissue. The needle-tissue-interaction forces such as friction and insertion forces are affected by the tissue mechanical properties. A force sensor is used to measure these forces during needle penetration of tissue to estimate their effects on the target motion. Ultrasound images are used to track target motion during needle insertion into soft-tissue phantoms. In Chapter 6, we proceed further to investigate experimentally the effect of system parameters on target motion. These parameters include the needle diameter, bevel angle, insertion velocity and target size.

### 1.3.2 Needle tracking

#### Challenge

Real-time needle tracking is a requirement for closed-loop needle control. The challenge is to develop accurate and fast tracking algorithms that is suitable for real-time needle control. The tracking algorithm needs to detect the needle during insertion in various soft-tissue phantoms including biological tissues. The algorithm should track the needle in 2D and 3D space. Clinical 3D imaging modalities are not suitable for real-time tracking as the generation of 3D images requires considerable processing time.

#### Proposed solutions

Chapter 3 addresses real-time tracking of the needle tip in 2D using charge-coupled device (CCD) camera and ultrasound images. In Chapter 4, 3D real-time needle shape reconstruction is introduced using a non-imaging modality (Fiber Bragg Grating sensors). In Chapter 5, 3D needle tracking of the needle tip is achieved using 2D ultrasound transducer and a Cartesian robot to control the transducer that follows the needle tip during insertion. The 3D position of the needle is determined in real-time using a 2D ultrasound image and the 3D coordinates of the transducer control robot. The 2D ultrasound transducer and the control robot are then replaced by a novel clinical ultrasound-based scanning system for real-time 3D tracking (Chapter 9). The tracked needle tip position is used as feedback to the control algorithm for accurate needle steering.

### 1.3.3 Needle steering

#### Challenge

Since manual steering of bevel-tipped flexible needles is not intuitive, autonomous control is required for accurate steering. The control algorithms should be suitable for 3D

targeting and also for real-time control to compensate for needle deviation during insertion. During the insertion procedure, the sharp bevel edge of the needle cuts through the tissue. For this reason, the steering algorithm is recommended to be designed in a way to minimize the number of needle rotations in order to reduce the damage of the surrounding tissue.

### Proposed solutions

A closed loop control algorithm is developed to steer the needle in 2D (Chapter 3) and 3D (Chapter 4) space using imaging and non-imaging modalities as feedback. Unlike the duty-cycle steering algorithm, the control algorithm proposed in this thesis minimizes the number of axial needle rotations, thus reducing the chances of tissue damage. In the developed control algorithm, rotations are applied only when required to follow a certain trajectory as presented in Chapter 5. The control algorithm steers the needle to follow different paths during insertion to compensation for target motion or deviations in the insertion environment.

### 1.3.4 Obstacle avoidance

#### Challenge

Needles should be steered around obstacles including sensitive structures such as blood vessels and glands, and also impenetrable structures such as bones [25, 37, 38]. An example of sensitive tissue is the neurovascular bundles near the penile bulb in prostate needle interventions [39]. If the needle is able to maneuver around obstacles and reach locations that were not accessible using the present technology, new applications can be introduced to solve clinical problems. The 3D location of the obstacles and their geometry should be determined pre-operatively. The needle is inserted in a non-static environment where the target and obstacle can be displaced intra-operatively.

#### Proposed solutions

We propose using a 3D path planning algorithm to enable the needle to reach a target while avoiding obstacles in a 3D environment. Our system uses a sampling-based path planner to compute and periodically update a feasible path to the target that avoids obstacles (Chapter 5). The main advantage of the proposed implementation is that it is fast enough for real-time path planning during insertion. To enable fast performance, our path planner makes use of reachability-guided sampling for efficient expansion of the rapidly-exploring search tree [40]. The path planning algorithm can also account for the variation of the needle curvature in tissues with non-homogeneous properties.

## 1. INTRODUCTION

---

### 1.3.5 Practical issues

#### Challenge

The needle is inserted in various tissues with non-uniform surfaces, and these tissues have non-homogeneous properties. This makes difficulties while steering in tissues with different properties which implies different needle curvatures during insertion. We propose a robotic system to steer the needle in various soft-tissue phantoms. It is challenging to bring such a robotic system to clinical settings. The proposed algorithms should be adapted to maintain safety and acceptance by clinical community.

#### Proposed solutions

In clinical practice, the needle is inserted in biological soft-tissue with nonhomogeneous properties and also non-uniform surfaces. In Chapter 6, we introduce a robotic mechanism using a force/torque feedback that allows the ultrasound transducer to keep contact with soft-tissue phantoms with non-uniform surfaces. In Chapter 8, the proposed system is adapted to consider keeping the clinician in the control loop for safety concerns. This is achieved by establishing shared control between the robotic control system and the clinician. We involve subjects with clinical background to perform the steering experiments to investigate the system acceptance by clinical community. Chapter 9, we also attempt to apply the developed algorithms using clinically-approved devices. We replace the ultrasound transducer control robot by a novel Automated Breast Volume Scanner (ABVS), which is used in clinical practice for breast diagnosis. The ABVS transducer is used for pre-operative scanning of soft-tissue for target reconstruction and also intra-operatively for needle tip tracking during the steering process.

## 1.4 Outline of the thesis

The thesis divided into five parts. Each of the first four parts consists of two chapters. These chapters are adapted versions of the aforementioned research papers that are published (or under review) in archival journals and international peer-reviewed conferences. The last part of this thesis provides conclusions and future work. The thesis is outlined as follows:

In Part I, the effect of tissue properties on target motion is modeled, and 2D needle steering techniques are presented. Chapter 2 investigates the effect of skin thickness on target motion during needle insertion into soft-tissue phantoms. Chapter 3 describes a system that integrates deflection models and image feedback for real-time flexible needle steering in 2D. In Part II, the needle tracking and control algorithms are upgraded to detect and steer the needle in 3D-space. Image- and non-image-guided 3D needle control techniques are experimentally validated for accurate needle steering. Chapter 4 introduces Fiber Bragg Grating sensors for real-time needle shape reconstruction and as feedback for three-dimensional steering. Chapter 5 evaluates experimentally an ultrasound-guided 3D needle steering system during insertion in gelatin-based phantoms and in biological tissue. In the experiments that are presented in the previous

chapters, the soft-tissue phantoms are assumed to have uniform surfaces. In Part III, algorithms are presented to steer the needle in soft-tissue phantoms with non-uniform surfaces, and also in non-homogeneous tissue. Chapter 6 deals with developing algorithms for needle steering in gelatin-based and biological tissue phantoms with curved and/or inclined surfaces. Chapter 7 describes a clinical case of needle insertion into a prostate phantom where the needle is steered in a phantom with different layers of various elasticities, and a force/torque feedback is used for scanning the non-uniform surface of the prostate phantom. Besides the non-uniform soft-tissue surfaces and tissue inhomogeneity, additional practical issues need to be considered in order to bring the proposed algorithms to the clinical environments. In Part IV, the system is adapted to make developed algorithms compatible with the clinical settings. Chapter 8 presents an experimental evaluation of a teleoperated ultrasound-guided system for steering co-manipulation between the operator and the control algorithm. These experiments can help in evaluating the acceptance of the clinical community to such a robotic system. Chapter 9 presents the use of a clinically-approved ultrasound-based scanner (Automated Breast Volume Scanner) instead of the transducer control robot for needle tip tracking and target shape reconstruction. The developed system can facilitate the compatibility issue for moving the proposed algorithms from a research laboratory to the operating room. Finally, Part V concludes with the outlook on the thesis and gives recommendations for future work.

## 1.5 Contributions

The significant contributions of this thesis are:

- Developing an ultrasound-based 3D needle tracking combined with 3D real-time path planning for needle steering while avoiding real obstacles. The path planning algorithm is developed and tested in collaboration with the Computational Robotics Research Group in North Carolina University at Chapel Hill, USA.
- 3D steering and path planning during needle insertion in soft-tissue phantoms with inclined and curved surfaces and also biological tissue.
- Presenting a non-imaging approach (Fiber Bragg Grating sensors) for real-time needle shape reconstruction and tip tracking.
- Developing visual and vibratory feedback in a teleoperated system for needle steering. The teleoperation system is developed in collaboration with the Department of Information Engineering, University of Siena, Italy.
- Using a clinically approved ultrasound tracking system, Automated Breast Volume Scanner (ABVS), for 3D needle steering, and target localization and shape reconstruction.

Within the context of the thesis, the following articles were published (or are currently under review) in archival journals:

## 1. INTRODUCTION

---

1. **M. Abayazid**, R.J. Roesthuis, R. Reilink and S. Misra, “Integrating deflection models and image feedback for real-time flexible needle steering”, *IEEE Transactions on Robotics*, vol. 29, issue 2, pp. 542-553, 2013.
2. **M. Abayazid**, G.J. Vrooijink, S. Patil, R. Alterovitz and S. Misra, “Experimental evaluation of ultrasound-guided 3D needle steering in biological tissue”, *International Journal of Computer Assisted Radiology and Surgery (IJCARS)*, vol. 9, issue 6, pp. 931-939, 2014.
3. G.J. Vrooijink, **M. Abayazid**, S. Patil, R. Alterovitz and S. Misra, “Needle path planning and steering in a three-dimensional non-static environment using two-dimensional ultrasound images”, *International Journal of Robotics Research*, vol. 33, issue 10, pp. 1361-1374, 2014.
4. C. Pacchierotti, **M. Abayazid**, S. Misra and D. Prattichizzo, “Teleoperation of steerable flexible needles by combining kinesthetic and vibratory feedback”, *IEEE Transactions on Haptics*, vol. 7, issue 1, pp. 551-556, 2014.
5. **M. Abayazid**, P. Morriera, N. Shahriari, S. Patil, R. Alterovitz and S. Misra, “Ultrasound-guided three-dimensional needle steering in biological tissue with curved surfaces”, *Medical Engineering & Physics*, vol. 37, issue 1, pp. 145-150, 2015.
6. **M. Abayazid**, C. Pacchierotti, P. Moreira, S. Patil, R. Alterovitz, D. Prattichizzo and S. Misra, “Experimental evaluation of co-manipulated ultrasound-guided flexible needle steering”, *International Journal of Medical Robotics and Computer Assisted Surgery*, 2015 (Accepted).
7. **M. Abayazid**, P. Moreira, N. Shahriari, A. Zompas and S. Misra, “Reconstruction of 3D shapes and needle steering using automated breast volume scanner (ABVS)”, *Journal of Medical Robotics Research*, 2015 (Under Review).
8. T. Araújo, **M. Abayazid**, M.J.C.M. Rutten and S. Misra, “Segmentation and three-dimensional reconstruction of lesions using the automated breast volume scanner (ABVS)”, *International Journal of Computer Assisted Radiology and Surgery (IJCARS)*, 2015 (Under Review).

The following papers were published in leading international peer-reviewed conferences:

1. J. op den Buijs, **M. Abayazid**, C.L. de Korte and S. Misra, “Target motion predictions for pre-operative planning during needle-based interventions”, in *Proceedings of the IEEE International Conference of the IEEE Engineering in Medicine and Biology Society (EMBC)*, pp. 5380-5385, Boston, MA, USA, August-September 2011.
2. **M. Abayazid**, C.L. de Korte and S. Misra, “Effect of skin thickness on target motion during needle insertion into soft-tissue phantoms”, in *Proceedings of the IEEE RAS & EMBS International Conference on Biomedical Robotics and Biomechatronics (BioRob)*, pp. 755-760, Rome, Italy, June 2012.

3. R.J. Roesthuis, **M. Abayazid** and S. Misra, “Mechanics-based model for predicting in-plane needle deflection with multiple bends”, in *Proceedings of the IEEE RAS & EMBS International Conference on Biomedical Robotics and Biomechatronics (BioRob)*, pp. 69-74, Rome, Italy, June 2012.
4. **M. Abayazid**, M. Kemp and S. Misra, “3D flexible needle steering in soft-tissue phantoms using fiber bragg grating sensors”, in *Proceedings of the IEEE International Conference on Robotics and Automation (ICRA)*, pp. 5843-5849, Karlsruhe, Germany, May 2013.
5. G.J. Vrooijink, **M. Abayazid** and S. Misra, “Real-time three-dimensional flexible needle tracking using two-dimensional ultrasound”, in *Proceedings of the IEEE International Conference on Robotics and Automation (ICRA)*, pp. 1688-1693, Karlsruhe, Germany, May 2013.
6. **M. Abayazid**, N. Shahriari and S. Misra, “Three-dimensional needle steering towards a localized target in a prostate phantom”, in *Proceedings of the IEEE RAS & EMBS International Conference on Biomedical Robotics and Biomechatronics (BioRob)*, pp. 7 - 12, Sao Paulo, Brazil, August 2014.
7. C. Pacchierotti, **M. Abayazid**, S. Misra and D. Prattichizzo, “Steering of flexible needles combining kinesthetic and vibratory force feedback”, in *Proceedings of the IEEE/RSJ International Conference on Intelligent Robots and Systems (IROS)*, pp. 1202-1207, Chicago, Illinois, USA, September 2014.
8. P. Moreira, **M. Abayazid**, and S. Misra, “Towards physiological motion compensation for flexible needle interventions”, in *Proceedings of the IEEE/RSJ International Conference on Intelligent Robots and Systems (IROS)*, Hamburg, Germany, September-October 2015.

The following abstract submissions were published at conferences and workshops:

1. **M. Abayazid**, R. Reilink and S. Misra, “Image-guided flexible bevel-tip needle control”, in *Proceedings of the annual symposium of the Benelux Chapter of the IEEE Engineering in Medicine and Biology Society (EMBS)*, Leuven, Belgium, December 2011.
2. G.J. Vrooijink, **M. Abayazid**, S. Patil, R. Alterovitz, and S. Misra, “Three-dimensional flexible needle steering using two-dimensional ultrasound images”, in *Proceedings of the fourth Dutch Biomedical Engineering Conference*, Egmond aan Zee, The Netherlands, January 2013.
3. **M. Abayazid**, A. Zompas, and S. Misra, “Three-dimensional flexible needle steering using an automated breast volume ultrasound scanner”, in *Proceedings of the fifth Dutch Biomedical Engineering Conference*, Egmond aan Zee, The Netherlands, January 2015.

## 1. INTRODUCTION

---

## Part I

# Two-Dimensional Needle Steering



# *Preface*

## Two-Dimensional Needle Steering

Accurate needle placement is important for the success of many clinical procedures. The placement accuracy is affected by target displacement that can occur during insertion. One of the common applications of needle interventions is breast biopsy. During the insertion process, breast tissue is subjected to displacement upon needle indentation, puncture, and penetration. This results in target displacement and consequently inaccurate needle placement. The target displacement is affected by the elastic properties of the different tissues in the breast such as adipose tissue, skin and lesion. Skin is generally stiffer than adipose tissue, and thus skin penetration by the needle requires a relatively high insertion force. This motivated us to study the influence of skin thickness on target motion as it is important for enhancing targeting accuracy of needle steering (Chapter 2). An image-guided control system is presented in Chapter 3 to robotically steer flexible needles with a bevel tip. Knowledge about the bevel-tipped needle deflection is required for accurate steering. Kinematics-based and mechanics-based models are developed to predict the needle deflection during insertion into soft-tissue. The kinematics-based model is used in the proposed image-guided control system. The control system accounts for target motion during the insertion procedure by detecting the target position in each image frame. Camera and ultrasound images are used during the experiments as feedback to the closed-loop control system. The aim of conducting these experiments is to achieve a targeting accuracy that can accurately reach the smallest lesions that can be detected using state-of-art ultrasound imaging systems.

This part is based on the previously published versions of the following manuscripts:

**Chapter 2:** M. Abayazid, C.L. de Korte and S. Misra, “Effect of skin thickness on target motion during needle insertion into soft-tissue phantoms”, in *Proceedings of the IEEE RAS & EMBS International Conference on Biomedical Robotics and Biomechatronics (BioRob)*, pp. 755-760, Rome, Italy, June 2012.

**Chapter 3:** M. Abayazid, R.J. Roesthuis, R. Reilink and S. Misra, “Integrating deflection models and image feedback for real-time flexible needle steering”, *IEEE Transactions on Robotics*, vol. 29, no. 2, pp. 542-553, 2013.

---

# Effect of Skin Thickness on Target Motion during Needle Insertion into Soft-Tissue Phantoms

## Abstract

Small breast lesions are increasingly detected by medical imaging modalities. However, a biopsy of the lesion is required to make a definitive diagnosis. During the biopsy, displacement of the target (lesion) occurs as the needle indents and punctures the skin layer, and penetrates further into the breast soft tissue. Target displacement during the needle insertion process makes it difficult to reach the lesion. In this study, the elastic properties of a soft-tissue phantom were estimated, and the effects of skin thickness on target motion and insertion force during needle insertion were investigated. The elastic properties of the target, skin, and the surrounding tissue were estimated *in vivo* using an ultrasound-based approach which uses Acoustic Radiation Force Impulse technique to determine the elastic moduli of tissue. Ultrasound images were used to track target motion during needle insertion into soft-tissue phantoms. Target displacement was computed using digital image correlation. The experimental results show that the insertion force rate increases by 90.2% and the rate of target displacement increases by 275.9%, when the skin thickness is increased from 0 mm to 2.5 mm. Studying the effect of skin thickness on the target motion during needle insertion will help in pre-operative planning and thus, improve the clinical outcomes of the biopsy procedure.

## 2. EFFECT OF SKIN THICKNESS ON TARGET MOTION DURING NEEDLE INSERTION INTO SOFT-TISSUE PHANTOMS

---

### 2.1 Introduction

In 2008, 458,000 women died from breast cancer worldwide [41]. Early detection and diagnosis is of key importance for effective treatment of breast cancer. After lesion detection, insertion of a biopsy needle into the breast is a frequently used procedure for diagnosis. Subsequently, samples are extracted to be screened for malignancy [42]. During needle insertion, the clinician may use ultrasound, computed tomography or magnetic resonance images to target the suspected lesion [43, 44, 45]. With advances in medical imaging, smaller breast lesions can be detected, such that accurate needle placement during biopsy becomes difficult. As the needle indents, punctures and penetrates the breast tissue, motion of the target (lesion) may occur (Fig. 2.1). Target displacements of over 2.0 mm have been measured during breast biopsy [46].

Currently, breast biopsies are performed manually, where the clinician relies on a ‘mental picture’ of the needle path and target location. In some cases, target and needle locations are determined using imaging systems e.g., two-dimensional (2D) ultrasound imaging. Targeting accuracy during needle insertion could be improved by pre-operative planning of the needle insertion procedure [6]. An important part of the pre-operative plan is a patient-specific model of needle-tissue interactions [28, 47, 48], which can predict target motions. In previous studies, target displacement was expected to be due to needle-tissue interactions and the organ motion, such as in the case of respiration and fluid flow [49]. Other studies investigated the effect of the surrounding tissue elasticity, the insertion force and velocity on target motion [50, 51]. There are many factors that affect the target motion during needle insertion into soft tissue such as the organ geometry, the boundary constraints imposed by surrounding organs and connective tissue, and the mechanical properties of the surrounding tissue [47, 52]. Op den Buijs *et al.* studied the effect of different factors on the target motion during tissue indentation [23, 53]. It was observed using finite element (FE) calculations that the target displacement increases 54% when the skin thickness increases from 1.0 mm to 2.0 mm during tissue indentation. This large increase of the target displacement is expected to have a drastic effect on the targeting accuracy during the needle insertion procedure. The skin thickness of the human breast ranges from 0.8 mm to 3.0 mm [54]. Thus, studying the influence of skin thickness on target motion is important for enhancing targeting accuracy of needle insertion.

Skin tissue is generally stiffer than adipose tissue, and thus skin penetration by the needle requires a relatively high insertion force [50]. This results in increased displacement of the adipose tissue and lesion below the skin surface. Previous work by Ophir *et al.* and Galloti *et al.* showed that it is possible to estimate soft tissue properties *in vivo* and non-invasively using ultrasound-based elasticity tools such as elastography [55, 56, 57] and acoustic radiation force impulse (ARFI) imaging [58, 59]. In this study, we use the ultrasound-based ARFI technique to estimate the elastic moduli of the adipose tissue and lesion. ARFI technique is chosen to be applied in the current study because unlike elastography it does not require inverse FE calculations [53]. The aim of non-invasively estimating the mechanical properties of different tissue layers is to predict tissue deformation during needle insertion.

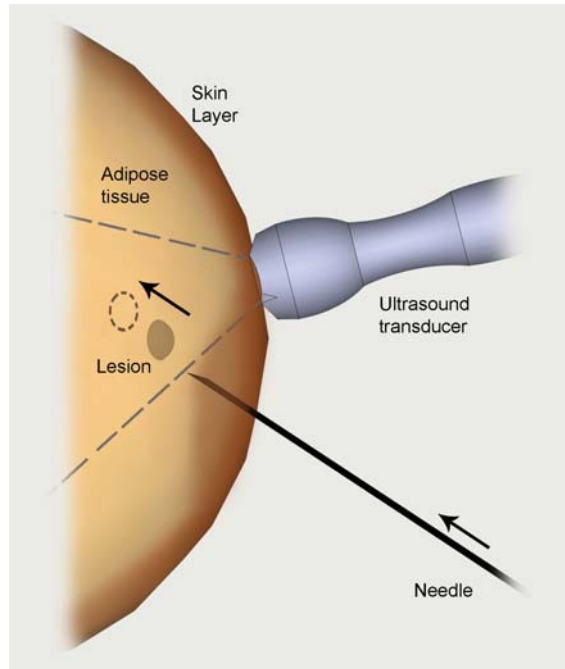


**Fig. 2.1:** Schematic of an ultrasound-guided needle insertion: Interactions between needle and breast soft tissue cause target (lesion) motion.

In this chapter, we investigate the influence of the skin thickness on the target motion during needle insertion into soft-tissue phantoms. Soft-tissue phantoms used in the experiments were made of layers representing skin and adipose tissue which contains the lesion. The phantom was made of gelatin and silicone rubber to model the mechanical properties of breast tissue [60]. The influence of the skin layer was investigated by testing phantoms without skin layer and with skin layer of different thicknesses. The needle insertion force rate was measured during the experiments, and the target displacement was detected. Several techniques were integrated to investigate the effect of the skin thickness on the target motion during needle insertion. An ultrasound-based ARFI technique is used to estimate the elastic modulus of the target and the surrounding tissue. Digital image correlation (DIC) algorithm was applied on B-mode ultrasound images to estimate the target motion. Insertion force rate and velocity were measured during the experiments to determine the relation between the skin thickness and the target motion.

This chapter is organized as follows: Section 2.2 describes the technique used to estimate the elastic modulus of a soft-tissue phantom from ultrasound measurements. Section 2.3 explains the preparation of tissue phantoms, the experimental setup used for needle insertion experiments, and the algorithm used to track the target motion. Section 2.4 discusses the experimental results, followed by conclusions and future work.

## 2. EFFECT OF SKIN THICKNESS ON TARGET MOTION DURING NEEDLE INSERTION INTO SOFT-TISSUE PHANTOMS

---

### 2.2 Elasticity of soft-tissue phantom

Ultrasound-based ARFI technique was used to determine the elastic moduli of the silicone rubber (target and skin) and gel (adipose tissue). The soft-tissue phantom preparation is described in the next section (Section 2.3.1). The Young's modulus is estimated using a commercially available implementation of ARFI technology, or known as Virtual Touch™ Quantification, installed on a Siemens Acuson S2000 ultrasound machine (Siemens AG, Erlangen, Germany). ARFI is a quantitative technique to estimate the tissue elasticity by measuring the velocity of the shear wave. Shear waves are generated by displacement of tissue. These waves are detected by the ultrasound transducer and the shear velocity is measured. Virtual Touch™ Quantification provides the shear wave velocity for the defined region of interest using the linear array transducer 9L4. The target and gel are assumed to be isotropic and incompressible. Young's modulus ( $E$ ) in different regions is calculated as [59]

$$G = \rho v_s^2, \quad (2.1)$$

where  $G$  and  $v_s$  are the shear modulus and the shear wave propagation velocity, respectively. The density ( $\rho$ ) of the material is calculated from the mass and volume of the soft-tissue phantom and the target. Young's modulus ( $E$ ) is calculated by

$$E = 2G(1 + \gamma), \quad (2.2)$$

where  $\gamma$  is Poisson's ratio which is assumed to be 0.495.

### 2.3 Experimental setup

In this section, the phantom preparation method is described. The experimental setup and the components used in the needle insertion measurements are presented. The algorithm used for tracking the target motion is also illustrated in this section.

#### 2.3.1 Soft-tissue phantom preparation

The adipose tissue, lesion and skin layer were needed to be represented in the soft-tissue phantom. Gelatin mixture was used to simulate the adipose tissue. Silicone rubber was used to mimic the properties of the lesion and the skin layer [23]. Gelatin (8.0%-by-weight) (Dr. Oetker, Ede, The Netherlands), and silica gel (1.0%-by-weight) (particle size  $< 63 \mu\text{m}$  SiC, E. Merck, Darmstadt, Germany) were mixed with boiling water. The silica gel served to mimic tissue acoustic scattering. The mixture was then put in a plastic container ( $46 \times 28 \times 71 \text{ mm}^3$ ). Small beads of silicone rubber (8.0 mm diameter) were used to model the stiff targets. Silicone rubber beads were positioned in the gelatin solution by hanging them using thin wires. The gel solidifies after one hour at temperature of  $7^\circ\text{C}$ . The wires that suspend the rubber beads are removed, and the phantoms are taken out of the container. The last step is to add the silicone layer (skin) on the phantom, and allow the layer to solidify at room temperature. We

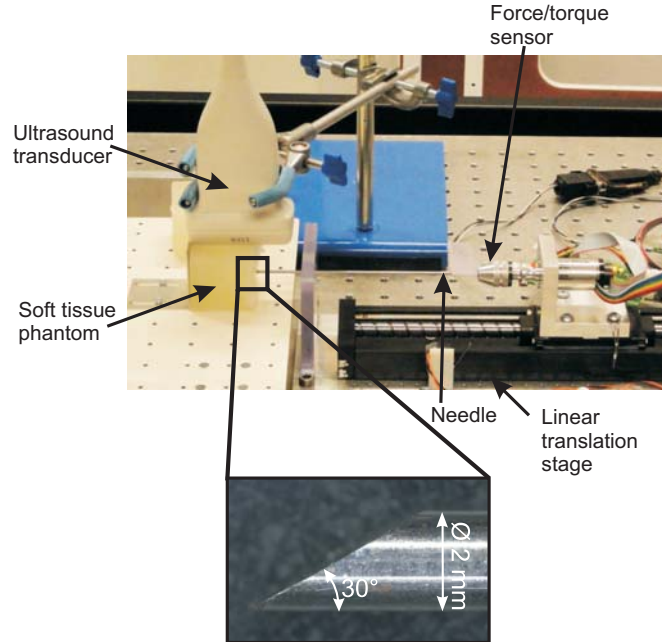


**Fig. 2.2:** Photograph of the needle insertion setup with the soft-tissue phantom. A linear array ultrasound transducer is mounted on top of a phantom. A needle, mounted on a linear translation stage, was inserted into a phantom at a speed of 30 mm/s. The inset contains a microscopic photograph of a 2.0 mm diameter stainless steel needle with bevel-edged tip ( $30^\circ$ ).

prepared three sets of phantoms. The first set consists of phantoms without skin layer. The second and third sets consist of phantoms with skin layers of 1.5 mm and 2.5 mm thickness, respectively. To measure skin thickness, B-mode ultrasound images of the phantom were recorded by a Philips HD 11XE ultrasound system (Philips Medical Systems, Best, The Netherlands), equipped with a linear array ultrasound transducer (L12-5). The phantoms used in elasticity measurements (Section 2.2) and in the needle insertion experiments (Section 2.3.2) were made of the same materials.

### 2.3.2 Needle insertion experiments

The experimental setup used for needle insertion into the tissue phantom is shown in Fig. 2.2. A stainless steel needle (2.0 mm diameter) with bevel tip ( $30^\circ$ ) is used in the experiments. The insertion process was performed by placing the needle into a sub-assembly mounted on a linear translation stage (Misumi Group Inc., Tokyo, Japan). The linear stage was actuated by a DC motor with planetary gear-head with transmission ratio of 4.4:1 and optical encoder (Maxon Motor AG, Sachseln, Switzerland), which was operated by a controller (Elmo Motion Control Ltd., Petach-Tikva, Israel). The needle insertion axis was positioned perpendicular to the skin layer plane of the tissue phantom. The needle was then inserted into the phantom at a speed of 30 mm/s [61]. The insertion distance was 30.0 mm. A six degrees of freedom (DOF) ATI nano17 force/torque sensor (ATI Industrial Automation, Apex, USA) was fixed at the base of

## 2. EFFECT OF SKIN THICKNESS ON TARGET MOTION DURING NEEDLE INSERTION INTO SOFT-TISSUE PHANTOMS

---

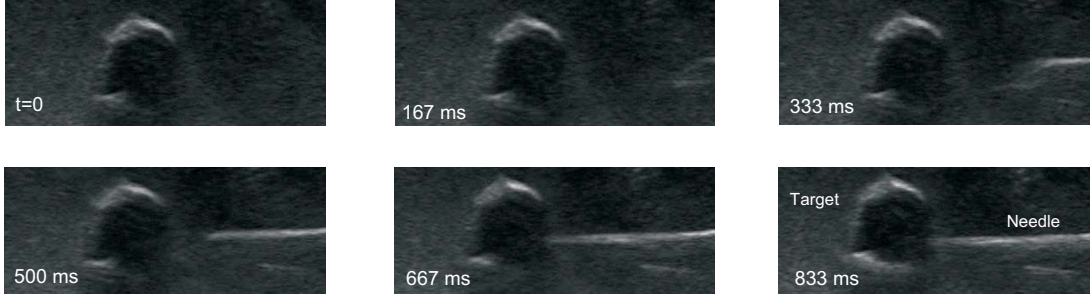


**Fig. 2.3:** Frames of ultrasound images during needle insertion into phantom with no skin layer.

the needle to record the forces acting on the needle during insertion. B-mode ultrasound images of the target were recorded at 15 frames per second to track the needle insertion and target motion. The ultrasound transducer was fixed by a clamp and positioned on top of the phantom touching its upper surface, such that the stiff target was in the field of view.

### 2.3.3 Target motion tracking

Ultrasound images with  $0.09 \times 0.09 \text{ mm}^2$  pixels were exported to Matlab (v7.11, Mathworks Inc., Natick, USA) for processing. Ultrasound image frames of needle insertion into soft-tissue phantom are shown in Fig. 2.3 to depict the geometry of the needle and the target in the ultrasound images. The target displacement was tracked using DIC algorithm. The DIC algorithm used 2D cross-correlation of a square of  $15 \times 15$  pixels around pixel coordinates  $(x_k, y_k)$  in frame  $k$  with a square of  $30 \times 30$  pixels in frame  $k + \Delta k$ . The peak location of the correlation values was detected by parabolic interpolation, resulting in determination of  $(x_{k+\Delta k}, y_{k+\Delta k})$  with sub-pixel resolution. Steps of  $\Delta k = 2$  frames were used. The target motion  $(u_k, v_k)$  was calculated as  $(x_k - x_0, y_k - y_0)$  where  $(x_0, y_0)$  is the initial pixel coordinates selected at the first frame. The total displacement  $(U_k)$  was calculated as  $U_k = \sqrt{u_k^2 + v_k^2}$ .

## 2.4 Results

In this section, the results of the elasticity measurements are discussed, and the elastic moduli of the soft-tissue phantom and the target are presented. The experimental results of target displacement and insertion forces during needle insertion into soft-tissue phantoms with different skin thicknesses are also presented.

### 2.4.1 Elastic modulus

The elastic moduli ( $E$ ) of the target and the gel are measured using the ultrasound-based ARFI technique as mentioned in Section 2.2. The shape of the target in the ultrasound image is shown in Fig 2.4. The shear velocity ( $v_s$ ) is measured five times

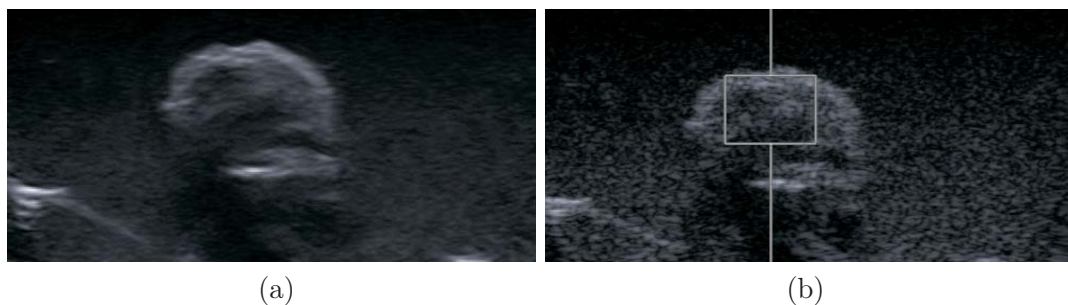


**Fig. 2.4:** Elastic moduli calculation: (a) The ultrasound image shows the target shape. The rectangle in (b) represents the region of interest where ultrasound-based ARFI is applied.

**Table 2.1:** The shear velocity ( $v_s$ ) was measured at different locations in the gel and the target (five trials each) to measure the elastic moduli ( $E$ ). The *Mean* is the average value of three experiments performed for each case, and *SD* is the standard deviation.

$v_s$ (m/s)				$\rho$ (kg/m <sup>3</sup> )		$G$ (kPa)		$E$ (kPa)	
Target		Gel		Target	Gel	Target	Gel	Target	Gel
<i>Mean</i>	<i>SD</i>	<i>Mean</i>	<i>SD</i>	2619.86	925.63	79.25	11.11	237	33.21
5.5	0.42	3.46	0.16						

for repeatability. The parameters used for calculating the elastic moduli are tabulated in Table 2.1.

### 2.4.2 Insertion force and target displacement

Using the needle insertion setup described in Section 2.3.2, needle insertion experiments were performed. Ultrasound was used to image the needle insertion process and to detect the target motion during the insertion procedure. Ultrasound measurements were recorded for three experimental cases:

- Case 1: The needle was inserted into phantoms with no skin layer.
- Case 2: The needle was inserted into phantoms with 1.5 mm skin layer.
- Case 3: The needle was inserted into phantoms with 2.5 mm skin layer.

For each case,  $n = 3$  experiments were performed on the same phantom to determine the repeatability of the insertion experiments. In order to eliminate the error that may arise due to inaccuracy in the placement of the target into the phantom during gel preparation, the rate of force and displacement increase were used in the measurements instead of the peak force and velocity to determine the effect of the skin thickness on the target motion during needle insertion.

## 2. EFFECT OF SKIN THICKNESS ON TARGET MOTION DURING NEEDLE INSERTION INTO SOFT-TISSUE PHANTOMS

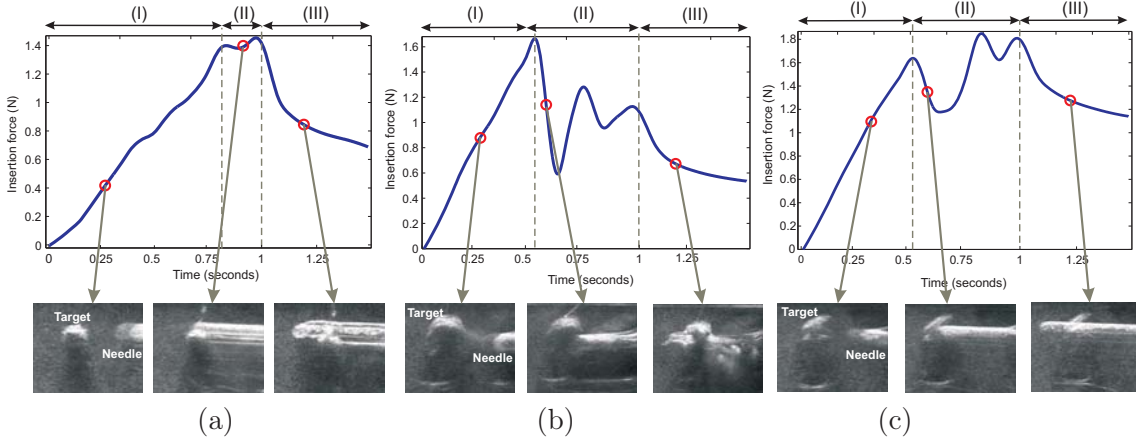


**Fig. 2.5:** Insertion force measured during insertion of the needle into phantoms with: (a) no skin layer (Case 1), (b) 1.5 mm skin layer (Case 2) and (c) 2.5 mm skin layer (Case 3). The insertion stages are represented by: (I) before reaching the target, (II) needle-target interaction and (III) stopping the insertion and phantom relaxation.

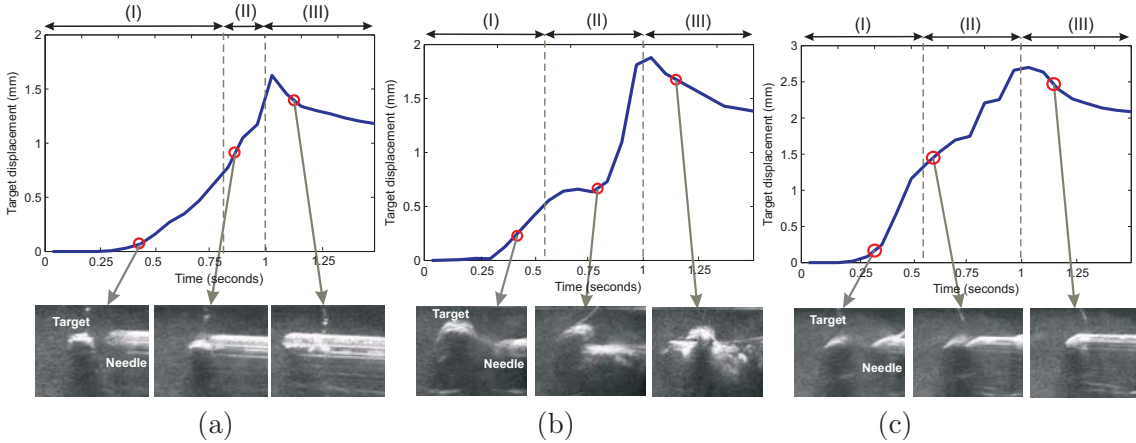


**Fig. 2.6:** Target displacement measured during insertion of the needle into phantoms with: (a) no skin layer, (b) 1.5 mm skin layer and (c) 2.5 mm skin layer. The insertion stages are represented by: (I) before reaching the target, (II) needle-target interaction and (III) stopping the insertion and phantom relaxation.

During the needle insertion process, the needle passes through three stages, as shown in Fig. 2.5 and Fig. 2.6. The first stage (I) starts when the needle penetrates the skin layer and ends just before reaching the target. In the second stage (II), the needle interacts with the target by penetrating it, and then proceeding to the soft-tissue phantom again. In the last stage (III), the needle motion stops, and the phantom relaxes and moves opposite to the direction of needle penetration. As shown in Fig. 2.5, in the first stage (I), the insertion force increases as the needle tip penetrates the soft-tissue phantom for the three cases. The slope of the insertion force curve in the first stage (I) shows the rate of force increase during needle penetration (Table 2.2). The slope is

**Table 2.2:** Experimental results for the insertion force and the target displacement rates in stage (I).

		Insertion force		Target displacement	
		per unit time (N/s)		per unit time (mm/s)	
		<i>Mean</i>	<i>SD</i>	<i>Mean</i>	<i>SD</i>
<b>No skin</b>	Case 1	1.95	0.23	0.54	0.11
<b>1.5 mm skin</b>	Case 2	3.50	0.29	1.31	0.20
<b>2.5 mm skin</b>	Case 3	3.71	0.36	2.03	0.57

calculated after fitting all the data points to a linear polynomial using Matlab (v7.11, Mathworks Inc., Natick, USA) curve fitting tool box. The insertion force increases at a higher rate when the needle is inserted into phantoms with thicker skin layers. In the second stage (II), the needle tip penetrates the target, and then it penetrates the soft-tissue phantom again. The needle interaction with the target, and the motion of the needle tip from one medium to another results in fluctuations of the force curves. In the last stage (III), when the motion stops, the force decreases smoothly because the phantom relaxes and applies force on the needle opposite to the direction of penetration.

The experimental results of the target displacement during needle insertion are shown in Fig. 2.6. In the first stage (I), the target displacement increases in the direction of penetration as the needle tip moves closer to the target. The slopes of the target displacement curves show that the rate of increase of target displacement in the first stage is dependent on the skin thickness (Table 2.2). In the second stage (II), the needle tip pushes the target, and then penetrates it, and that causes target displacement in the direction of needle penetration. In the last stage (III), the needle stops, and the displaced volume of the phantom moves back opposite to the direction of needle penetration. The measurements show that the target displacement is maximum for Case 3 and minimum for Case 1. The needle insertion stages are illustrated in Fig. 2.5 and Fig. 2.6, and an ultrasound image frame is attached to each stage for clarification.

### 2.4.3 Discussion

The results presented in Fig. 2.5 and Fig. 2.6 show that thicker skin results in higher rates of insertion force and target displacement. The experimental results show that thick skin layer (2.5 mm) causes 90.3% increase in the insertion force rate compared to a phantom with no skin layer (Table 2.2). The rate of target displacement increases 275.9% when the needle is inserted into a phantom with thick skin layer (2.5 mm) compared to a phantom with no skin layer. These results indicate the significance of modeling skin, since breast skin thickness ranges from 0.8 mm to 3.0 mm [54]. This range is large enough to affect the target motion during needle insertion. Consequently, it is recommended to measure the elasticity and thickness of the soft tissue layers before biopsy for accurate prediction of the target motion during needle insertion.

## 2. EFFECT OF SKIN THICKNESS ON TARGET MOTION DURING NEEDLE INSERTION INTO SOFT-TISSUE PHANTOMS

---

### 2.5 Conclusions and future work

In this study, we focused on studying the effects of the skin thickness on the insertion force rate and the target motion during needle insertion into soft-tissue phantom. The elasticity of the target and the surrounding gel were estimated non-invasively using ultrasound-based ARFI technique. DIC algorithm was used to calculate the target motion during needle insertion. It is concluded from the experiments that increasing the skin thickness leads to higher insertion force rates and larger target displacement rates during needle insertion.

Target motion can be also affected by other factors such as needle insertion speed, needle diameter and shape of needle tip. These factors are investigated in Chapter 6 using needle insertion setup. Ultrasound-based ARFI technology provides an estimation of the elastic moduli of the adipose tissue and target non-invasively. The elastic moduli can be used as inputs to FE models that compute the target motion and tissue deformation during needle insertion into soft tissue. Prediction of the target motion will improve the accuracy of needle steering.

# Integrating Deflection Models and Image Feedback for Real-Time Flexible Needle Steering

## Abstract

Needle insertion procedures are commonly used for diagnostic and therapeutic purposes. In this chapter, an image-guided control system is developed to robotically steer flexible needles with an asymmetric tip. Knowledge about needle deflection is required for accurate steering. Two different models for predicting needle deflection are presented. The first is a kinematics-based model, and the second model predicts needle deflection based on the mechanics of needle-tissue interaction. Both models predict deflection of needles undergoing multiple bends. The maximum targeting errors of the kinematics-based and the mechanics-based models for 110 mm insertion distance using a  $\phi$  0.5 mm needle are 0.8 mm and 1.7 mm, respectively. The kinematics-based model is used in the proposed image-guided control system. The control system accounts for target motion during the insertion procedure by detecting the target position in each image frame. Five experimental cases are presented to validate the real-time control system using both camera and ultrasound images as feedback. The experimental results show that the targeting errors of camera and ultrasound image-guided steering towards a moving target are 0.35 mm and 0.42 mm, respectively. The targeting accuracy of the algorithm is sufficient to reach the smallest lesions ( $\phi$  2 mm) that can be detected using state-of-art ultrasound imaging systems.

### 3. INTEGRATING DEFLECTION MODELS AND IMAGE FEEDBACK FOR REAL-TIME FLEXIBLE NEEDLE STEERING

---

#### 3.1 Introduction

Percutaneous needle insertion is one of the most common minimally invasive surgical procedure. Needles are often used for diagnostic and therapeutic applications such as biopsy and brachytherapy, respectively. Clinical imaging techniques such as ultrasound and magnetic resonance images, and computed tomography scans are commonly used during needle insertion procedures to obtain the needle and target positions. Needles used in clinical procedures often have a bevel tip to easily cut and penetrate soft tissue. Such needles naturally deflect from a straight path during insertion, which make them difficult to steer intuitively [62]. Moreover, the needles used in surgical procedures are often thick and rigid. Such thick needles cause deformation of tissue and this can result in target motion, which affects the targeting accuracy [23, 24]. Another disadvantage of using thick needles is that they cause patient trauma. Besides needle deflection and tissue deformation, other possible causes of targeting inaccuracy are patient motion during the procedure, and physiological processes such as fluid flow and respiration. Inaccurate needle placement may result in misdiagnosis or unsuccessful treatment.

Thin needles were introduced to minimize patient discomfort [25]. Another advantage of using thin needles is that they are flexible, and therefore facilitate curved needle paths. This enables steering the needle around obstacles (such as sensitive tissues), and to reach locations which are unreachable by rigid needles (Fig. 3.1). Manually steering thin, flexible needles towards a desired location is challenging [26]. Using a robotic system which automatically steers the needle can assist the clinician. Such a system requires a model for predicting the needle deflection to steer the needle to reach a certain location.

This work presents two different models for predicting needle deflection. The first is a kinematics-based model which assumes that the needle tip follows a circular path. This model is based on the unicycle model presented by Webster *et al.* [27], but modifications are made to account for cutting tissue at an angle by bevel-tipped needles. The second model is a mechanics-based model which predicts deflection using needle-tissue interaction forces [63]. The mechanics-based model for predicting deflection of needles undergoing multiple bends is presented in this study. Both models are validated using *double bend* experiments (Fig. 3.1).

In this study, image feedback is combined with the kinematics-based deflection model to steer the needle towards a target. Charge-coupled device (CCD) camera images are used for image feedback in the first set of experiments to evaluate the tracking and steering algorithms. Experiments are then performed using ultrasound images to demonstrate that the presented framework is applicable to a clinical imaging modality. To the best of our knowledge, the use of ultrasound images for steering a bevel-tipped flexible needle ( $\phi$  0.5 mm diameter) towards a moving target (less than 2 mm diameter) has not been investigated. The study also provides a method that allows the needle to move along a certain path using set-points during the insertion into a soft-tissue phantom. The elasticity of the phantom affects the needle deflection [64, 65]. Acoustic Radiation Force Impulse (ARFI) technique is an ultrasound-based noninvasive method used to measure the elasticity of the soft-tissue phantom.

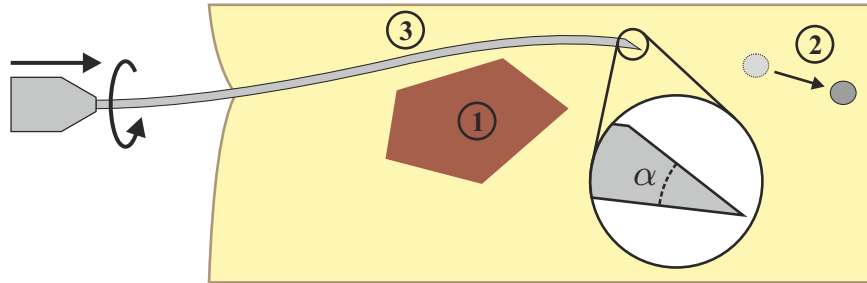


**Fig. 3.1:** A flexible needle with an asymmetric (bevel) tip can be used to steer around obstacles ①. Steering is accomplished by a combination of insertion and rotation at the base of the needle. Target motion ② may occur during needle insertion and this affects targeting accuracy. ③ Single needle rotation results in the needle having a *double bend* shape. The bevel angle is denoted by  $\alpha$ .

This Chapter is organized as follows: Section 3.2 presents the related work in the area of flexible needle steering. Section 3.3 describes the needle deflection models and the experimental setup used for model validation. Section 3.4 presents the control system used for steering the needle during insertion and the image processing techniques used for feedback. In Section 3.5, the experimental results are presented, followed by Section 3.6, which concludes and provides directions for future work.

## 3.2 Related work

In the recent years, several research groups have developed algorithms for image-guided needle steering. Some of these algorithms encompass needle deflection models (Section 3.2.1), and techniques to track the needle tip and target in real time (Section 3.2.2). In this section, algorithms used in previous studies are discussed. The section also concludes by briefly presenting our proposed method for needle steering.

DiMaio and Salcudean [66] were among the first to investigate steering needles through soft tissue. They developed a needle Jacobian which relates needle base motion outside the tissue to needle tip motion inside the tissue. Maneuvering the needle base causes the soft tissue around the needle to deform, and this enabled them to place the needle tip at a desired location. Glozman and Shoham [26] also used base maneuvering to steer the needle. A model was used to simulate the interaction between needle and soft tissue. Needle steering was accomplished by solving the forward and inverse kinematics of this model. Neither DiMaio and Salcudean [66], nor Glozman and Shoham [26] used needles with an asymmetric tip. The advantage of using needles with asymmetric tips is that the needle deflection can be used for steering. The direction of deflection (in the planar case) is changed by rotating the needle 180 degrees during insertion (Fig. 3.1). Several research groups have focused on the steering of flexible needles with a bevel tip, e.g., [27, 38, 62, 67, 68, 69, 70], [30, 71, 72]. The deflection of a needle with a bevel tip can also be controlled using duty cycle rotation [34].

### 3. INTEGRATING DEFLECTION MODELS AND IMAGE FEEDBACK FOR REAL-TIME FLEXIBLE NEEDLE STEERING

---

#### 3.2.1 Needle deflection models

Webster *et al.* [27] presented an approach in which they used the kinematics of unicycle and bicycle models to predict the needle deflection. In their work, they assumed that the needle tip moves along a circular path. The unicycle model assumed that the paths followed by the needle before and after rotation are tangent to each other. In the bicycle model, the paths before and after rotation are not assumed to be tangent to each other. They assumed relatively stiff tissue, and showed that their model agrees with experiments. The kinematics-based model by Webster *et al.* is limited since it did not account for needle-tissue interaction along the length of the needle.

Several groups focused on a mechanics-based approach for modeling needle deflection. They used the interaction between the needle and surrounding tissue to predict the needle curvature. Alterovitz *et al.* [68] presented a planning algorithm for a needle with a bevel tip to determine the insertion point in order to reach a desired target. Finite element (FE) modeling was used to model the needle-tissue interaction and this was employed in their planner to account for soft tissue deformation. FE modeling requires computing power that is not convenient to implement in real-time control. Therefore, analytical needle deflection models were proposed to predict the deflection of needles with a bevel tip during insertion in a soft-tissue [65, 69, 73, 74].

Kataoka *et al.* [73] presented a force-deflection model where they assumed a constant force per unit needle length. This assumption resulted in discrepancies with the experimental deflection. Abolhassani *et al.* [69] described a model that related force/torque data at the needle base to deflection. They did not account for tissue deformation along the needle shaft. This led to errors between measured and predicted deflections. Misra *et al.* [74] presented a mechanics-based model that predicted needle deflection using the Rayleigh-Ritz formulation. Roesthuis *et al.* [65] extended this model by adding spring supports along the needle shaft. However, none of these models could predict the needle deflection for the case when the needle is rotated during insertion (i.e., multiple bends). The authors presented a mechanics-based model for predicting deflection of a needle undergoing multiple bends [63]. In addition to the mechanics-based model, a modification of the unicycle model is presented in the current study. This model requires fewer parameters than the bicycle model to describe needle deflection accurately. This kinematics-based model is compared to the mechanics-based model. The deflection model and real-time needle tracking are used to develop a feedback control system for steering flexible needles.

#### 3.2.2 Needle and target tracking

In previous studies, needle (without a bevel tip) and target positions were tracked in fluoroscopic and ultrasound images using image processing algorithms [26, 75]. In ultrasound images, the needle visibility is affected by the operator's skill in aligning the needle in the ultrasound imaging plane [75, 76]. Okazawa *et al.* [77] developed two algorithms based on the Hough transform to detect the needle shape in ultrasound images during insertion. There are other segmentation techniques that can be used for needle tracking based on corner detection and subtraction [75, 78]. The main advantage of the subtraction and corner detection techniques is that the required processing time

is short, which makes these techniques suitable for real-time applications. The disadvantage of using the subtraction method is that it is sensitive to motion of soft tissue. Corner detection is immune to such artifacts that may appear in the image outside the processed region. Magnetic tracking sensors [6, 79] and fiber optic strain sensors [80] were also used for real-time needle tracking. Tracking the needle tip slope and the target position are also required for steering the needle. The tip slope changes during insertion due to needle deflection. Target displacements over 2.0 mm have been measured during placement of a biopsy needle in the breast [23, 46]. Target displacement introduces targeting errors [24]. The target position needs to be measured in each frame in order to increase the targeting accuracy of the steering algorithm.

#### 3.2.3 Proposed algorithm for steering

In the current study, two different (kinematics-based and mechanics-based) needle deflection models are presented. A revised set of experiments are performed to compare the results of the models. The kinematics-based model is used in the proposed control system. The system uses processed images for feedback control. A real-time needle tracking algorithm is developed based on processing camera and ultrasound images. The Harris corner detection technique is used for tracking the needle ( $\phi$  0.5 mm) tip position. The algorithm used for measuring the tip slope is based on image moments [81, 82]. The displacement of the target is detected to reduce the targeting error. Target motion is measured by calculating the centroid of the target shape using image moments [83]. The tracked moving target is of  $\phi$  2.0 mm. The proposed algorithms for needle and target motion tracking are applicable for both CCD camera and ultrasound images. The tracking algorithms are suitable for real-time applications. The steering algorithm uses set-points to specify a certain path for the needle to follow during insertion. In the control system, it is assumed that the needle follows a circular path during insertion. This assumption was used in previous studies [27, 68]. Deviation of the needle from its planned path due to disturbances or inaccurate assumptions is corrected in real-time by the developed algorithm.

### 3.3 Needle deflection models

In this section two models for predicting needle deflection are presented. Both models assume that the needle bends in-plane (two-dimensional). The first model uses a kinematics-based approach, while the second model is based on the mechanics of needle-tissue interaction. Both models assume that the needle shaft follows the path described by the needle tip. The experimental setup and the soft-tissue phantom used are described. Experiments are presented to fit the parameters of both models. Experiments are performed to validate both models in the case of steering towards a target with a single rotation. The tissue is considered to be stiff, and tissue deformation due to the needle moving through the tissue is minimal, and therefore neglected. This implies that the needle shaft follows the path described by the needle tip.

### 3. INTEGRATING DEFLECTION MODELS AND IMAGE FEEDBACK FOR REAL-TIME FLEXIBLE NEEDLE STEERING

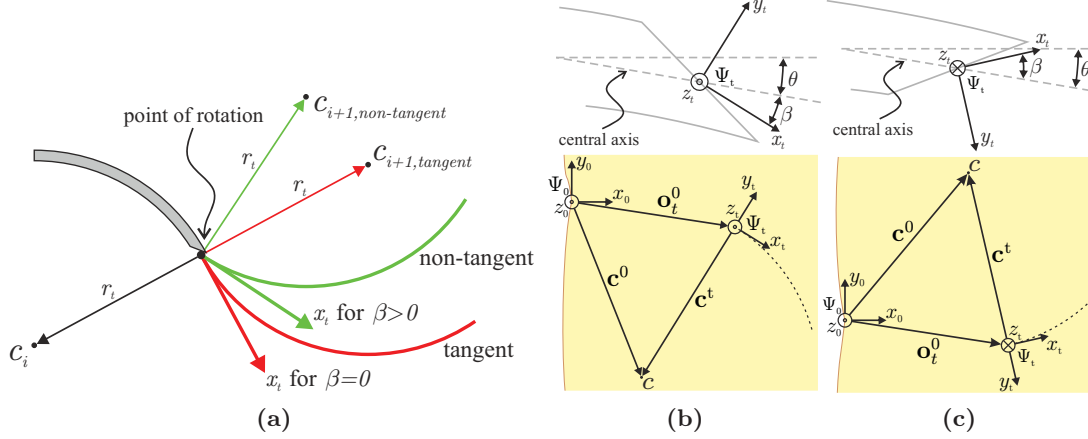


**Fig. 3.2:** Kinematics-based approach to describe the needle path: The needle travels in the direction of  $x_t$  along a circular path with centre ( $c$ ) and radius ( $r_t$ ). (a) The effect of the cut angle ( $\beta$ ) is shown: The resulting needle path after needle rotation for a tangent needle path ( $\beta = 0$ ) and a non-tangent needle path ( $\beta > 0$ ). (b) Frame ( $\Psi_t$ ) is rigidly attached to the needle tip and the cut angle is modeled by rotating the frame by the cut angle with respect to the central axis of the needle. Needle bevel tip is facing up, which causes the needle to deflect downwards. (c) Needle rotation is performed, indicated by a rotation of the tip frame around the central axis of the needle. This results in the needle to deflect upwards.

#### 3.3.1 Kinematics-based model

The idea of using nonholonomic kinematics to describe the needle path of a flexible, bevel-tipped needle has been demonstrated in [27]. The approach assumes that the needle tip follows a circular path. They proposed using a unicycle model with a steering constraint to describe the circular needle path. The unicycle model could not describe the needle path when needle rotation is performed during insertion. This is due to the fact that the circles describing the needle path before and after needle rotation are not tangent to each other (Fig. 3.2(a)). To describe the non-tangent needle path, the bicycle method is used.

In this study, a modification of the kinematics-based unicycle model is presented which accounts for the non-tangent needle path (Fig. 3.2). It has been observed that a bevel-tipped needle cuts the tissue at an angle from the central axis of the needle [68, 74]. We denote this angle as the cut angle ( $\beta$ ). The cut angle is modeled by placing a frame at the needle tip ( $\Psi_t$ ) which is rotated by the cut angle with respect to the central axis of the needle (Fig. 3.2(b)). The needle tip travels through soft tissue in the direction indicated by  $x_t$ . Rotation of the needle around its central axis results in a change of direction of  $x_t$  (Fig. 3.2(c)). This causes the needle tip to follow a path which is not tangent to its path before rotation (Fig. 3.2(a)).

The needle tip follows the circumference of a circle (centre ( $c$ ) and radius ( $r_t$ )) as shown in Fig. 3.2(a). The needle tip lies at the origin of frame  $\Psi_t$ ; expressed in the global coordinate frame this becomes:  $\mathbf{o}_t^0 = [x_{tip} \ y_{tip} \ z_{tip}]^T$ . Since planar needle deflection in the  $x_0y_0$ -plane is assumed,  $z_{tip}$  equals zero. The needle deflection ( $y_{tip}$ ) can be expressed

as a function of the needle tip  $x$ -coordinate ( $x_t$ )

$$y_{tip} = c_y^0 \pm \sqrt{r_t^2 - (x_{tip} - c_x^0)^2}, \quad (3.1)$$

where  $c_x^0$  and  $c_y^0$  are the  $x$ - and  $y$ -coordinates of the circle centre expressed in the global coordinate frame ( $\Psi_0$ ), respectively. The circle centre coordinates ( $\mathbf{c}^0$ ) expressed in the global coordinate frame are calculated by performing a homogeneous transformation

$$\mathbf{c}^0 = \mathbf{H}_t^0 \mathbf{c}^t, \quad (3.2)$$

where  $\mathbf{c}^t$  are the homogeneous coordinates of the circle centre expressed in the tip frame

$$\mathbf{c}^t = \begin{bmatrix} c_x^t & c_y^t & c_z^t & 1 \end{bmatrix}^T = \begin{bmatrix} 0 & -r_t & 0 & 1 \end{bmatrix}^T. \quad (3.3)$$

In (3.2),  $\mathbf{H}_t^0$  represents the homogeneous transformation from the tip coordinate frame to the global coordinate frame

$$\mathbf{H}_t^0 = \begin{bmatrix} \mathbf{R}_t^0 & \mathbf{o}_t^0 \\ \mathbf{0}_3^T & 1 \end{bmatrix}. \quad (3.4)$$

The rotation matrix ( $\mathbf{R}_t^0$ ) depends on the orientation of the bevel tip (Fig. 3.3). In the case of the bevel face pointing up, the tip frame ( $\Psi_{tu}$ ) needs to be rotated by the cut angle about the  $z_{tu}$ -axis to align it with the central axis of the needle

$$\mathbf{R}_{tu}^1 = \mathbf{R}_{z_{tu}}(\beta). \quad (3.5)$$

If the bevel face is pointed down, the frame  $\Psi_{td}$  first needs to be rotated about the  $z_{td}$ -axis by the cut angle, then a rotation of  $\varphi$  about the  $x_{td}'$ -axis is required to align it with the central axis of the needle

$$\mathbf{R}_{td}^1 = \mathbf{R}_{z_{td}}(\beta) \mathbf{R}_{x_{td}'}(\varphi). \quad (3.6)$$

Finally, a rotation equal to the needle tip slope ( $\theta$ ) around the  $z_1$ -axis has to be performed to align the  $x_1$ -axis with the  $x_0$ -axis

$$\mathbf{R}_1^0 = \mathbf{R}_{z_1}(\theta). \quad (3.7)$$

Thus, for the bevel face pointing up,  $\mathbf{R}_t^0$  in (3.4) is calculated by

$$\mathbf{R}_t^0 = \mathbf{R}_{tu}^0 = \mathbf{R}_1^0 \mathbf{R}_{tu}^1, \quad (3.8)$$

### 3. INTEGRATING DEFLECTION MODELS AND IMAGE FEEDBACK FOR REAL-TIME FLEXIBLE NEEDLE STEERING

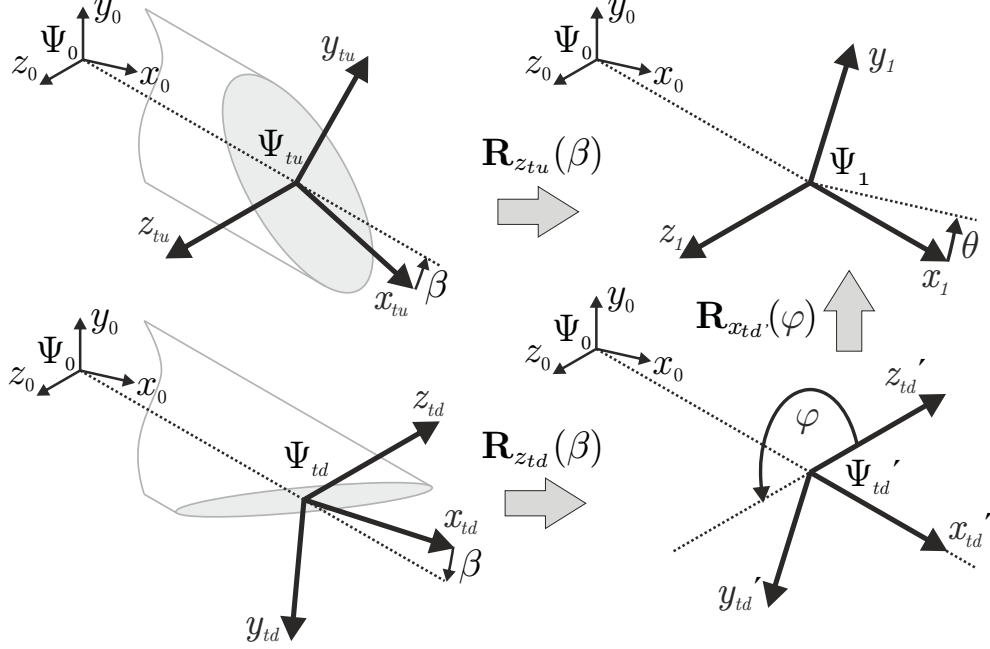


**Fig. 3.3:** Top left figure shows the needle tip when bevel face is pointed up ( $\Psi_{tu}$ ), while the bottom left figure shows the needle tip when bevel face is pointing down ( $\Psi_{td}$ ). The rotations are shown to align tip frames ( $\Psi_{tu}$  and  $\Psi_{td}$ ) with the global coordinate frame ( $\Psi_0$ ). The final rotation ( $\mathbf{R}_1^0$ ) is not shown.

and for the bevel face pointing down this is

$$\mathbf{R}_t^0 = \mathbf{R}_{td}^0 = \mathbf{R}_1^0 \mathbf{R}_{td}^1. \quad (3.9)$$

Using (3.2)-(3.9), needle tip position ( $x_{tip}, y_{tip}$ ) and needle tip slope ( $\theta$ ), the centre of the circle ( $c_{i+1}$ ) describing the next needle path can be determined at each instant during insertion. This allows predicting the future needle path if a rotation is to be made. This is essential for steering the needle which will be discussed in later sections.

#### 3.3.2 Mechanics-based model

A needle is subjected to needle-tissue interaction forces when it is inserted into soft tissue (Fig. 3.4(a)). When the needle travels through the tissue, force is required to cut the tissue and create a path through the tissue. This is modeled by a force at the tip of the needle ( $F_t$ ). If the needle has an asymmetric tip, the forces at the needle tip have an uneven distribution, causing the needle to deflect from a straight insertion path [74]. In the case of a bevel-tipped needle, the tip force is considered to act normal to the bevel face. When the needle travels through the tissue, friction acts on the needle shaft. This is modeled by a force ( $F_f$ ) acting tangent to the needle shaft. As the needle is inserted, it is supported by the surrounding tissue. The force exerted by the tissue surrounding

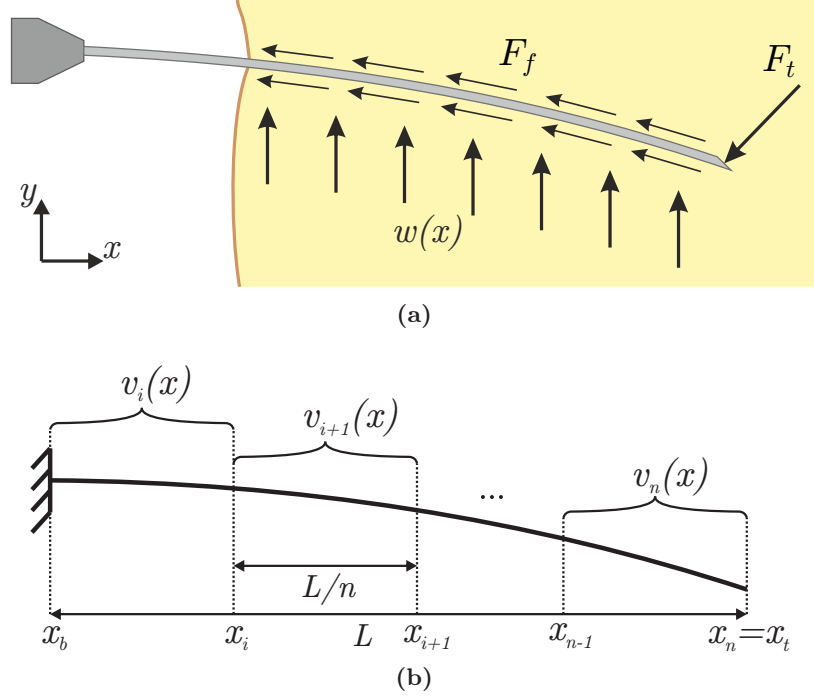


**Fig. 3.4:** (a) As a flexible needle with a bevel tip is inserted into soft tissue, it is subject to needle-tissue interaction forces. (b) The needle is modeled as a cantilever beam. The needle is divided into  $n$  elements each described by its own shape function ( $v_i(x)$ ).

the needle (i.e., an elastic support) is modeled as a distributed load ( $w(x)$ ) along the inserted part of the needle.

The needle is modeled as a cantilever beam (Fig. 3.4(b)). Assuming small needle deflections, only transversal needle deflection is considered. The needle is stiff in the axial direction and hence shortening of the needle is not considered. When the needle is inserted without being rotated, it has a *single bend* shape (Fig. 3.5(a)). The needle deflects due to a combination of the distributed load and the tip force. Needle rotation is performed when the insertion distance equals the rotation distance ( $x_t = x_r$ ). This results in a change of orientation of the bevel tip, and hence the tip force also changes direction (Fig. 3.5(b)). This causes the needle to deflect in the opposite direction. For a single rotation, this results in the needle having a *double bend* shape. To model this, the part of the needle before rotation is fixed by a series of springs. Given a sufficiently small spring spacing ( $\Delta l$ ), one can approximate an elastic foundation [84]. The stiffness of such an elastic foundation ( $K_0$ ) is described in terms of stiffness per unit length, and depends on needle and tissue properties. The length of the foundation in Fig. 3.5(b) equals  $x_r - x_0$ , resulting in a foundation stiffness ( $K_t$ ) of

$$K_t = K_0(x_r - x_0). \quad (3.10)$$

For a total number of  $m$  springs, this results in a spring stiffness ( $K_s$ ) of  $\frac{K_t}{m}$ . The

### 3. INTEGRATING DEFLECTION MODELS AND IMAGE FEEDBACK FOR REAL-TIME FLEXIBLE NEEDLE STEERING

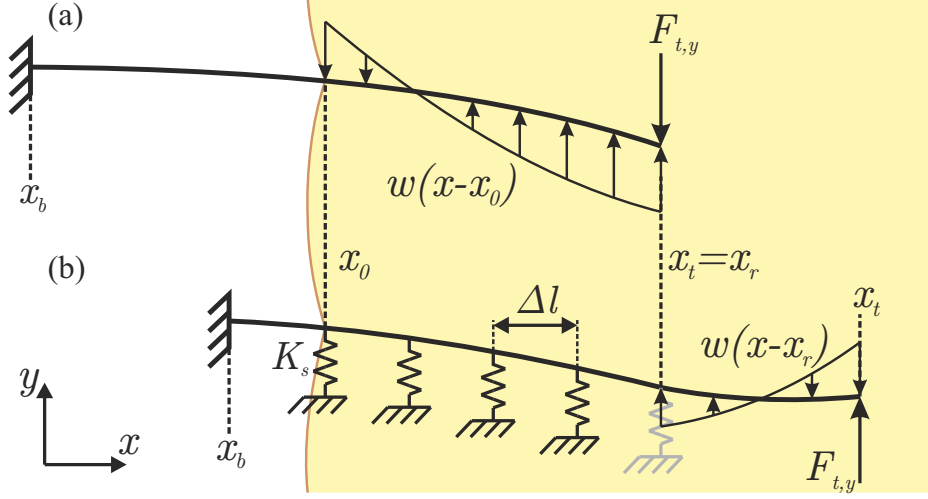


**Fig. 3.5:** (a) The needle deflects due to a combination of needle tip force ( $F_{t,y}$ ) and distributed load ( $w(x)$ ). (b) As the needle is rotated at  $x_r$ , the orientation of tip force and distributed load change. This causes the needle to deflect in the opposite direction. In order to model the *double bend* shape, the part of the needle prior to rotation ( $x_0 \leq x \leq x_r$ ) is fixed by a series of springs.

distributed load is applied to the part after rotation and this enables modeling of a needle undergoing multiple bends.

To evaluate the deflected needle shape ( $v(x)$ ) under the action of distributed load and tip force, the Rayleigh-Ritz method is used. Rayleigh-Ritz is a variational method in which equilibrium of the system is established using the principle of minimum potential energy [85]. For a mechanical system, the total potential energy is expressed as

$$\Pi = U - W, \quad (3.11)$$

where  $U$  represents the energy stored in the system, and  $W$  is the work done on the system by external forces. To find the deflected needle shape using the Rayleigh-Ritz method, an assumed displacement (shape) function has to be defined. Several shape functions were evaluated, and it is found that a cubic function is a suitable shape function

$$v(x) = a_0 + a_1x + a_2x^2 + a_3x^3. \quad (3.12)$$

For complex needle shapes, a single shape function as in (3.12) is not sufficient to approximate the deflected needle shape. Therefore, the needle is divided (Fig. 3.4(b)) into a number of elements ( $n$ ), each described by their own shape function ( $v_i(x)$ )

$$v(x) = \begin{cases} v_i(x), & x_{i-1} \leq x \leq x_i \\ v_{i+1}(x), & x_i \leq x \leq x_{i+1} \\ \vdots & \vdots \\ v_n(x), & x_{n-1} \leq x \leq x_n \end{cases} \quad (3.13)$$

where

$$v_i(x) = a_{0,i} + a_{1,i}x + a_{2,i}x^2 + a_{3,i}x^3. \quad (3.14)$$

The unknown coefficients  $a_{0,i} \dots a_{3,i}$  are determined using the Rayleigh-Ritz method.

For the first needle element ( $i = 1$ ),  $x_{i-1}$  equals  $x_b$ , and for the last element ( $i = n$ ),  $x_i$  equals  $x_t$ . Each of the shape functions has to satisfy the geometric boundary conditions of the system. Since the needle is fixed at the base, the needle slope ( $\theta(x)$ ) and deflection ( $v(x)$ ) are zero at the base

$$v_1(x_b) = 0 \text{ and } \theta_1(x_b) = \left. \frac{dv_1}{dx} \right|_{x=x_b} = 0. \quad (3.15)$$

Furthermore, the shape functions have to satisfy continuity conditions, meaning constant deflection and needle slope at the boundaries of the elements

$$v_i(x_i) = v_{i+1}(x_i) \text{ and } \theta_i(x_i) = \theta_{i+1}(x_i). \quad (3.16)$$

For the *single bend* case (Fig. 3.5(a)), the stored energy equals the strain energy due to transversal needle bending ( $U = U_b$ ). Using Euler-Bernoulli beam theory [86], the strain energy due to transversal bending ( $U_b$ ) is found to be

$$U_b = \frac{EI}{2} \int_{x_b}^{x_t} \frac{d^2v(x)}{dx^2} dx, \quad (3.17)$$

where  $E$  and  $I$  represent the Young's modulus and second moment of inertia of the needle, respectively. The needle is cylindrical and  $EI$  is constant along the length of the needle.

For a needle undergoing multiple bends, energy is also stored in the springs (Fig. 3.5(b)). The stored energy is the sum of the energy due to needle bending as defined in (3.17) and the spring energy for a total number of  $m$  springs

$$U_s = \sum_{k=0}^m \frac{1}{2} K_s v(x_k)^2, \quad (3.18)$$

where  $K_s$  represents the spring stiffness, and  $v(x_k)$  is the amount of deflection for the  $k$ th spring with respect to the bend configuration as shown in Fig. 3.5(b). The work done on the system by external forces is the sum of the work done by the distributed load ( $W_d$ ) and concentrated tip load ( $W_c$ )

$$W = W_d + W_c. \quad (3.19)$$

The work done by the distributed load is given by

$$W_d = \int_{x_0}^{x_t} w(x)v(x) dx, \quad (3.20)$$

### 3. INTEGRATING DEFLECTION MODELS AND IMAGE FEEDBACK FOR REAL-TIME FLEXIBLE NEEDLE STEERING

---

and the work done by concentrated tip load is given by

$$W_c = F_{t,y}v(x_t), \quad (3.21)$$

where  $v(x_t)$  is the deflection at the needle tip.

The shape functions defined in (3.14) are substituted in the equations for the stored energy ((3.17) and (3.18)) and work ((3.20) and (3.21)). This results in the total potential energy of the system, defined in (3.11), to be a function of the shape functions, and hence the unknown coefficients

$$\Pi = f(v_i(x)) = f(a_{0,i}, a_{1,i}, a_{2,i}, a_{3,i}). \quad (3.22)$$

The equilibrium of the system is found by taking the partial derivative of the total potential energy with respect to each of the shape functions' unknown coefficients

$$\frac{\partial \Pi}{\partial a_{k,i}} = 0, \quad (3.23)$$

for  $k = 0, 1, 2, 3$  and  $i = 1 \dots n$ . The unknown coefficients  $a_{k,i}$  are calculated by solving the system of equations obtained in (3.23). Substituting the coefficients back into (3.13) and (3.14) gives the deflected needle shape.

Experimental data are used to evaluate the parameters for both needle deflection models. These parameters are the radius of curvature and the cut angle for the kinematics-based model, and the distributed load for the mechanics-based model. In the next sections, the experimental setup is first introduced, and then experiments are presented which are used to evaluate the parameters. With the parameters known, both models are then validated in a series of (open-loop) steering experiments.

#### 3.3.3 Experimental setup

The experimental setup used to insert needles into soft-tissue phantoms is shown in Fig. 3.6 [65]. The setup has two degrees of freedom: translation along and rotation about the insertion axis for steering. A Sony XCDSX90 charge-coupled device (CCD) FireWire camera (Sony Corporation, Tokyo, Japan) is mounted 450 mm above the setup and is used for imaging. For ultrasound imaging, a Siemens ACUSON S2000 (Siemens Healthcare, Mountain View, CA, USA) is used.

The needle is made of Nitinol wire ( $\phi$  0.5 mm). Nitinol is a nickel-titanium alloy which, at a certain temperature range, has the property of being superelastic. This means the needle can undergo very large elastic deformations, without plastically deforming, allowing it to return to its initial (straight) shape. Nitinol ( $E = 75$  GPa) is also more flexible than steel ( $E = 200$  GPa); this increases the deflection, and hence improves the steering capabilities of the needle. The needle tip is polished to a bevel angle ( $\alpha$ ) of  $30^\circ$ . Gelatin is used as a soft-tissue phantom. Gelatin phantoms are made by mixing gelatin powder (Dr. Oetker, Bielefeld, Germany) with water at a temperature of  $40^\circ\text{C}$ . The mixture is then put in a plastic container ( $170 \times 30 \times 200$  mm<sup>3</sup>).

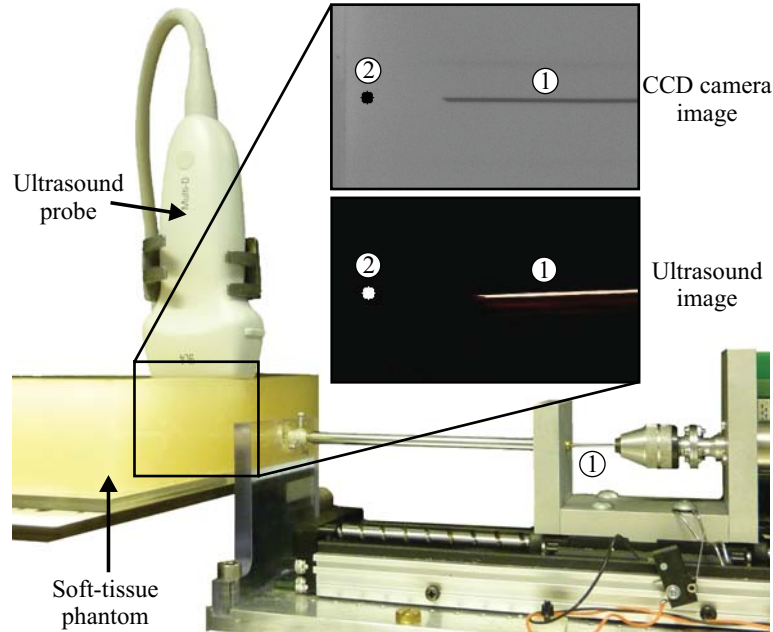


**Fig. 3.6:** Needle steering setup: A linear stage is used to insert the Nitinol needle ① into a soft-tissue phantom and steer it towards a target ②. Needle and target tracking is done using charge-coupled device (CCD) camera and ultrasound images. Steering can be performed either using CCD camera or ultrasound images.

The gel solidifies after five hours at a temperature of  $7^{\circ}\text{C}$ . For a gelatin-to-water mixture (by weight) of 14.9%, the elasticity is found to be 35.5 kPa. This elasticity is similar to what is found in breast tissue [87]. The elasticity is determined in a uni-axial compression test using the Anton Paar Physica MCR501 (Anton Paar GmbH, Graz, Austria). Van Veen *et al.* [64] investigated the effect of several system parameters on needle deflection including soft-tissue phantom elasticity. Each needle insertion is done at a new location in the soft-tissue phantom to avoid influence of previous insertions on the current experiment.

### 3.3.4 Model fitting

As mentioned in Section 3.3.2, experimental data are used to evaluate the parameters for both models. The kinematics-based model requires the cut angle and the radius of curvature, and the mechanics-based model requires the distributed load. To evaluate these parameters, both *single bend* and *double bend* experiments are performed. In all experiments, the Nitinol needle is inserted a total distance of 110 mm in the soft-tissue phantom at a speed of 5 mm/s. The insertion speed is chosen to be within the range of speeds used in clinical applications (0.4 mm/s–10 mm/s) [88]. In the *double bend* experiment, a  $180^{\circ}$  rotation is performed at an insertion distance ( $x_r$ ) of 30 mm. The needle tip is tracked during the experiment, and the resulting needle tip deflection is shown in Fig. 3.7.

### 3. INTEGRATING DEFLECTION MODELS AND IMAGE FEEDBACK FOR REAL-TIME FLEXIBLE NEEDLE STEERING

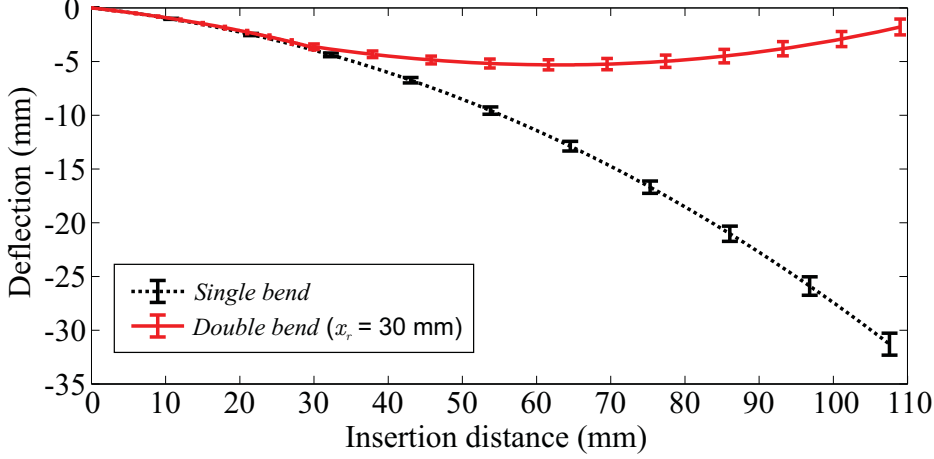


**Fig. 3.7:** Experimental needle tip deflection (mean) for the *single bend* and the *double bend* case ( $x_r$  is the distance at which rotation is performed). In both cases, five insertions are performed and the standard deviation ( $\sigma$ ) is shown by the error bars. The mean final tip deflection is -31.3 mm ( $\sigma = 1.0$  mm) and -1.8 mm ( $\sigma = 0.7$  mm) for the *single bend* and *double bend* case, respectively. The curves show the tracked needle tip positions during insertion.

In order to evaluate the radius of curvature ( $r_t$ ) for the kinematics-based model, a circle is fitted to the deflection of the *single bend* experiment. This fitting is done in a least-squares sense using a method described by Pratt *et al.* [89]. The result of this fitting, for a total of five insertions, is a circle with a radius of curvature of 270.5 mm (standard deviation ( $\sigma$ )= 5.7 mm). The cut angle ( $\beta$ ) is determined by fitting the path after needle rotation to the experimental deflection of the *double bend* case. This results in a cut angle of 2.0°.

The distributed load ( $w(x)$ ) for the mechanics-based model is evaluated by minimizing the difference between experimental deflection ( $v_{exp}(x)$ ) and simulated deflection ( $v_{sim}(x)$ ). The criterion used for fitting is a combination of error along the needle shaft ( $\varepsilon_1$ ) and error at the needle tip ( $\varepsilon_2$ )

$$\varepsilon = \varepsilon_1 + \varepsilon_2, \quad (3.24)$$

where

$$\varepsilon_1 = \int_{x_0}^{x_t} (v_{exp}(x) - v_{sim}(x))^2 dx, \quad (3.25)$$

and

$$\varepsilon_2 = (v_{exp}(x_t) - v_{sim}(x_t))^2. \quad (3.26)$$

Several load profiles were evaluated for the distributed load (e.g., constant, linear, triangular), but the best fit was found using a cubic load profile

$$w(x) = b_0 + b_1x + b_2x^2 + b_3x^3. \quad (3.27)$$

Further, using a cubic load profile for the distributed load agrees with the assumption

that the tissue acts as an elastic support for the needle as it bends. The assumed load profile is substituted in (3.20) and then the resulting needle deflection ( $v_{sim}(x)$ ) is evaluated using the Rayleigh-Ritz method. The coefficients ( $b_0, \dots, b_3$ ) are determined by minimizing (3.24).

Besides the distributed load, the mechanics-based model also requires the tip force ( $F_t$ ) and the stiffness of the elastic foundation per unit length ( $K_0$ ). The tip force depends on the geometric properties of the needle and tissue elasticity as already shown in other studies [62, 65, 74]. In Roesthuis *et al.* [65], the tip force was determined to be 0.4 N for a  $\phi$  1.0 mm needle with a 30° bevel angle. It was also observed that the tip force is almost constant during insertion. Misra *et al.* [74] showed that the magnitude of the tip force is proportional to the bevel surface area. Therefore, for the  $\phi$  0.5 mm needle used in this study, a constant tip force of 0.1 N is assumed ( $\frac{0.5^2}{1.0^2} \times 0.4 = 0.1$ ). The stiffness of the elastic foundation per unit length also depends on the geometric properties of the needle and tissue elasticity. The stiffness is calculated such that the difference between model-predicted deflection and experimental data is minimized. The best fit with experimental deflection is found for  $K_0 = 0.1$  N/mm<sup>2</sup>. When using different needle-tissue combinations, this value is expected to change.

With the parameters evaluated for both models, it is now possible to predict needle deflection. In the next section, both models will be validated by performing open-loop steering experiments.

#### 3.3.5 Open-loop needle steering

In order to validate both needle deflection models, experiments are performed in which the needle is steered towards two different target locations ( $y_T = -10$  mm and  $y_T = -20$  mm) by performing a single rotation. The insertion distance where rotation has to be performed ( $x_r$ ) is determined *a priori* using both models. These distances are presented in Table 3.1.

The resulting experimental deflection is compared to the predicted deflection using the models (Fig. 3.8). The errors between experimental deflection and predicted deflection are also presented in Table 3.1. For the first experiment ( $x_T = 110$  mm,  $y_T = -10$  mm)

**Table 3.1:** Results of steering the needle towards a target at two different locations ( $y_T$ ) using the kinematics-based and the mechanics-based models. (Note: rotation distance ( $x_r$ ), experimental tip deflection ( $y_{tip,exp}$ ), tip error ( $e_{x_T}$ ) and the standard deviation of final tip deflection ( $\sigma(x_T)$ ).

Model	$y_T$ (mm)	$x_r$ (mm)	$y_{tip,exp}$ (mm)	$e(x_T)$ (mm)	$\sigma(x_T)$ (mm)
Kinematics	-10.0	44.2	-10.8	0.8	0.4
	-20.0	64.2	-20.6	0.6	0.5
Mechanics	-10.0	42.8	-10.4	0.4	0.5
	-20.0	62.8	-18.3	1.7	0.2

### 3. INTEGRATING DEFLECTION MODELS AND IMAGE FEEDBACK FOR REAL-TIME FLEXIBLE NEEDLE STEERING

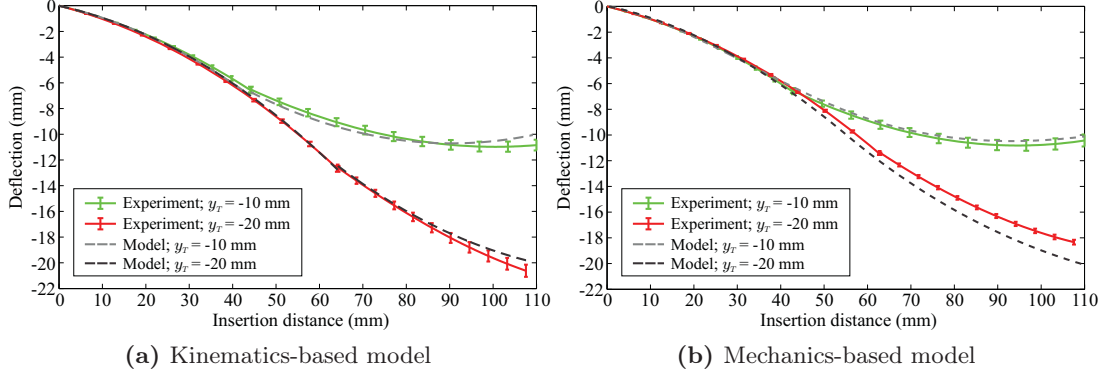


**Fig. 3.8:** Both needle deflection models are used to steer the needle towards two different target locations ( $y_T = -10$  mm and  $y_T = -20$  mm): (a) Kinematics-based model. (b) Mechanics-based model. For each experiment a total of five insertions are performed. The results of the experiments shown here are presented in Table 3.1.

the tip error is 0.8 mm and 0.4 mm for the kinematics-based model and the mechanics-based model, respectively. In the second experiment ( $x_T=110$  mm,  $y_T=-20$  mm) the difference in tip errors between both models is larger: 0.6 mm for the kinematics-based model and 1.7 mm for the mechanics-based model. It should be noted that the amount of needle deflection is sensitive to changes in experimental conditions. For example, it has been observed that the longevity and temperature of the soft-tissue phantom affects needle deflection. However, it is evident from these results that both models show good agreement with experimental deflection.

## 3.4 Control of flexible needles

The control system incorporates the kinematics-based deflection model as its accuracy is comparable to the mechanics-based model. Further, the kinematics-based model is computationally efficient and suitable for real-time applications. The images used for feedback are processed to obtain the needle tip position and slope and the target position. In this section, the algorithm used for steering a flexible needle towards a moving target, and the image processing algorithms used for needle and target tracking are discussed.

### 3.4.1 Closed-loop needle steering

In the feedback control system, the needle is assumed to follow a circular path with a constant radius ( $r_t$ ). By rotating the needle  $180^\circ$  around its central axis, the needle can bend either towards the positive (upwards) or negative (downwards)  $y$ -direction. In Fig. 3.9(a), the green circle (centre  $c_{i+1}$ ) represents the needle path if it rotates  $180^\circ$  about its axis. The distance between the target and  $c_{i+1}$  is  $L$ . If the green circle intersects the target ( $L = r_t$ ), the needle will rotate  $180^\circ$  about its axis. The location

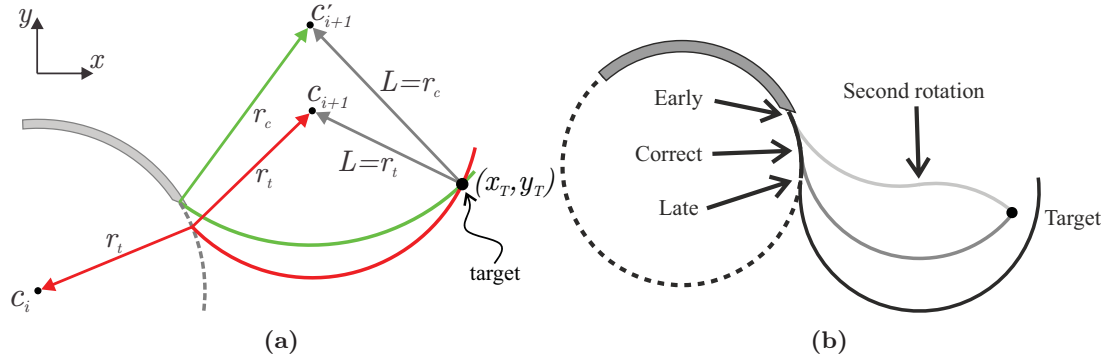


**Fig. 3.9:** (a) Variation in experimental conditions between insertions causes change in the radius of curvature of the needle ( $r_t$ ). Choosing the control radius ( $r_c$ ) larger than the expected needle radius of curvature ( $r_t$ ) results in an early rotation around the centre ( $c'_{i+1}$ ). (b) An early needle rotation is corrected by performing additional rotations (light gray). No additional rotation is required if the needle rotates at the correct instance (dark gray). If needle rotation is done late, then the target cannot be reached by performing additional rotations (black).

of  $c_{i+1}$  is calculated using (2)-(9). The needle tip position is determined using image processing (Section 3.4.2.1).

It is important to ensure that the needle rotation does not occur late, since the needle will overshoot the target, which cannot be corrected. The control radius ( $r_c$ ) used in the steering algorithm is chosen larger than the actual radius of curvature of the needle ( $r_t$ ) to maintain early rotation. If the rotation occurs early, a subsequent rotation can be made to ensure that the target is reached (Fig. 3.9(b)). The flow chart describing the steering algorithm is shown in Fig. 3.10. The targeting accuracy is also influenced by target motion [24]. The target moves due to tissue deformation caused during needle insertion and also physiological activities such as respiration or blood flow [23]. In the control system, target position is tracked in real-time using image processing. The target position is an input to the control system as explained in Section 3.4.2.

### 3.4.2 Needle and target tracking algorithms

Real-time needle and target tracking are required for closed-loop control of the needle (Fig. 3.11). The needle tip position and slope can be determined using either CCD camera or ultrasound images during insertion (Fig. 3.11(b)-(d)). The target motion is tracked in order to reduce the targeting error (Fig. 3.11(e)-(f)).

#### 3.4.2.1 Needle-tip tracking algorithm

Real-time needle tip tracking is used for steering the needle tip to reach a target location. A window of  $60 \times 60$  pixels is cropped from the gray-scale image of the captured frame around the needle tip position (Fig. 3.11(b)). The image is smoothed to remove image artifacts and then converted to a binary image by selecting an adaptive threshold value. Adaptive thresholding is used to separate the foreground from the background with nonuniform illumination (Fig. 3.11(c)). The resulting image is then inverted, if camera

### 3. INTEGRATING DEFLECTION MODELS AND IMAGE FEEDBACK FOR REAL-TIME FLEXIBLE NEEDLE STEERING

---

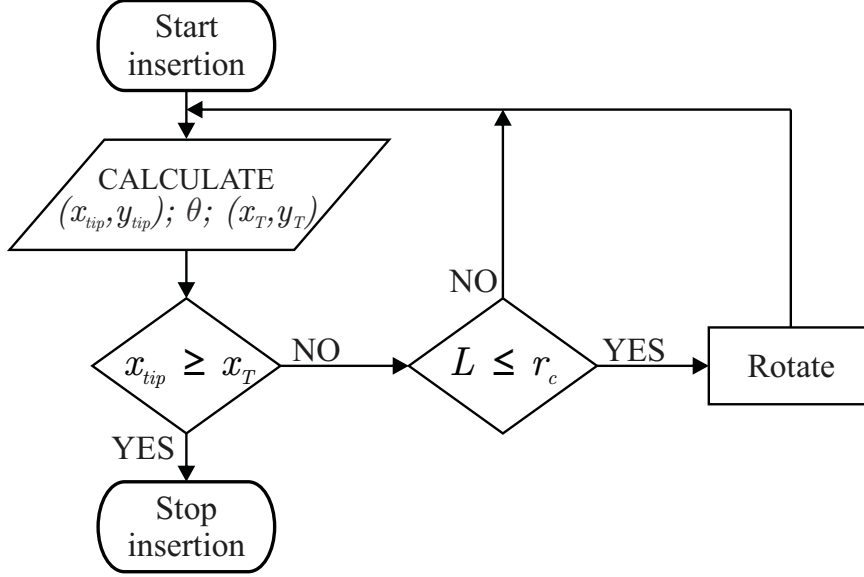


**Fig. 3.10:** The flow chart depicts the needle steering algorithm. Insertion is started and needle tip position  $(x_{tip}, y_{tip})$ , slope  $(\theta)$  and target position  $(x_T, y_T)$  are determined using image processing. The insertion continues until the needle tip reaches the centre of the target  $(x_{tip} \geq x_T)$ . Needle rotation is performed when the distance from the circle centre  $(c_{i+1})$  to the target is smaller or equal than the control radius  $(L \leq r_c)$ .

images are used as the needle is darker than the background in the camera images. The Harris corner detection algorithm is applied to the binary image to determine the tip position [78]. The output of the corner detection algorithm is a binary image with a bright region at the location of the corner (needle tip) (Fig. 3.11(d)). The centroid is then calculated in the image to obtain the coordinates of the needle tip. Image moments are used to determine the centroid of the image [81, 82]. The image moments  $M_{ij}$  are defined as

$$M_{ij} := \sum_x \sum_y x^i y^j I(x, y), \quad (3.28)$$

where  $I(x, y)$  is the pixel value at the position  $(x, y)$  in the image, and  $x$  and  $y$  range over the search window. In (3.28),  $i$  and  $j$  are the order of moment in the direction of  $x$  and  $y$ , respectively. The centroid of the image is calculated as

$$\begin{bmatrix} x_{cen} \\ y_{cen} \end{bmatrix} = \frac{1}{M_{00}} \begin{bmatrix} M_{10} \\ M_{01} \end{bmatrix}. \quad (3.29)$$

The  $x$ -coordinate and  $y$ -coordinate of the image centroid are  $x_{cen}$  and  $y_{cen}$ , respectively. The needle tip slope is also required for controlling the needle. The tip slope  $(\theta)$  is

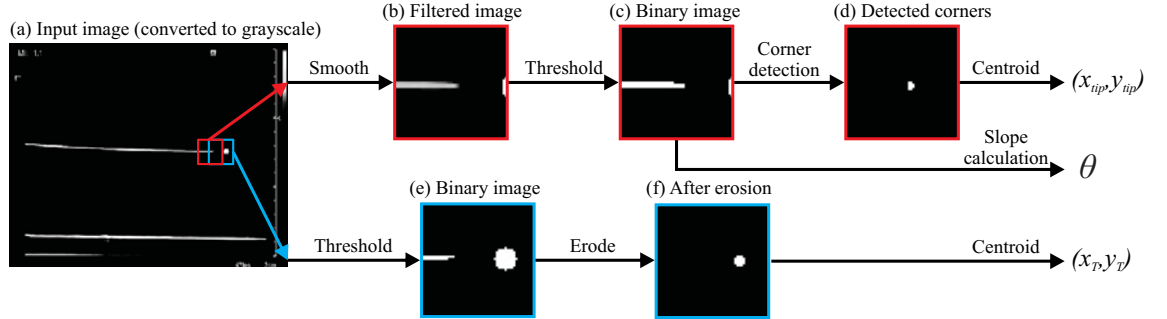


**Fig. 3.11:** The schematic shows the image processing algorithm applied to determine the needle tip position  $(x_{tip}, y_{tip})$  and tip slope  $\theta$  (red window), and target position  $(x_T, y_T)$  (blue window). (a) The input is an ultrasound image which is converted to gray-scale. (b) The gray-scale image is smoothed to filter out artifacts. (c) A threshold is then applied to produce a binary image. (d) Harris corner detection is applied, and then the centroid is calculated in the output image to detect the needle tip position. (e) Binary images are acquired after performing a threshold to detect the target position. (f) Erosion is used to filter out artifacts around the target, and then the centroid of the image is calculated to determine the target location. This algorithm is also used for CCD camera images but an additional processing step is applied. The image is inverted after applying the threshold.

computed as [83]

$$\theta = \frac{1}{2} \arctan \left( \frac{2 \left( \frac{M_{11}}{M_{00}} - x_{cen} y_{cen} \right)}{\left( \frac{M_{20}}{M_{00}} - x_{cen}^2 \right) - \left( \frac{M_{02}}{M_{00}} - y_{cen}^2 \right)} \right). \quad (3.30)$$

### 3.4.2.2 Target motion tracking

The target position used in the needle steering algorithm is the measured position in each captured image frame (Fig. 3.11(e)-(f)). A window is cropped around the target. A threshold value is then applied to the image to produce a binary image in the window (Fig. 3.11(e)). The binary image is inverted when CCD camera images are used (as the target is darker than the background). Erosion is then applied on the binary image to eliminate the shapes that may affect the accuracy of target tracking (Fig. 3.11(f)). The centroid of the shape is calculated using image moments (3.29). The center position of the target is determined for every image frame. The distances between the position of the target in the initial frame (before needle insertion) and the following frames represent the total target displacement during needle insertion.

## 3.5 Experimental results

In this section, the experiments which are performed for validation of the control system used for steering flexible needles are described. The results of the experiments are also presented in this section.

### 3. INTEGRATING DEFLECTION MODELS AND IMAGE FEEDBACK FOR REAL-TIME FLEXIBLE NEEDLE STEERING

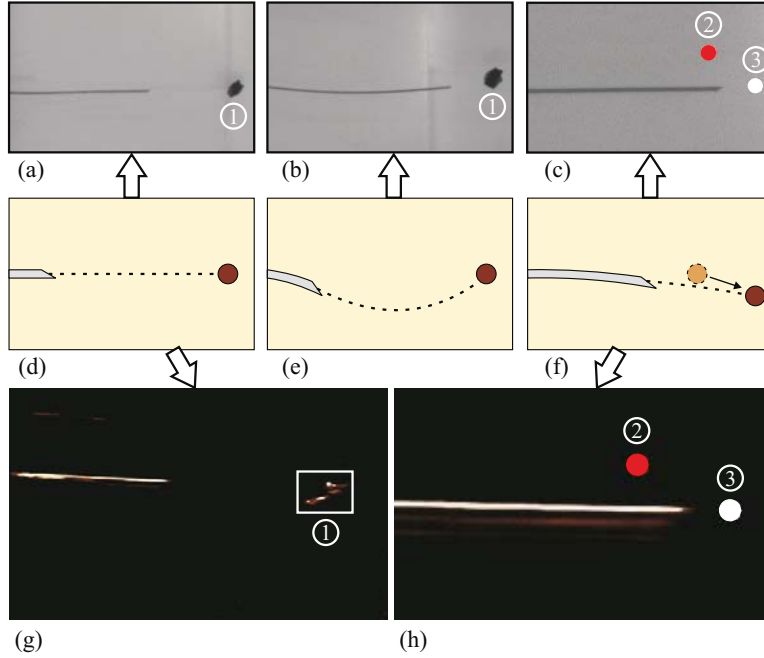


**Fig. 3.12:** Experimental cases: (a) Camera image-guidance is used to steer the needle along a straight path towards a real target ① using set-points (Case 1). (b) Camera image-guidance is used to steer the needle to follow a curved path using set-points (Case 2). (c) Camera image-guidance is used to steer the needle towards a moving virtual target where the red circle represents the initial position of the target ② and the white circle represents the final position of the target ③. (d) The needle is inserted to reach a real target (Case 1 and Case 4). (e) The needle moves along a curved path using set-points (Case 2). (f) The needle is steered towards a moving virtual target (Case 3 and Case 5). (g) Ultrasound image-guidance is used to steer the needle towards a real target (Case 4). (h) Ultrasound image-guidance is used to steer the needle towards a moving virtual target (Case 5).

#### 3.5.1 Experimental plan

The aim of the experiments is to validate the tracking and steering algorithms used for controlling the needle during insertion (Fig. 3.12). The kinematics-based model presented in Section 3.3 is used in the control system. The model shows accurate approximation to the actual needle deflection (Section 3.3.5). A Nitinol needle of  $\phi$  0.5 mm diameter is used during the experiments. The needle insertion velocity is 5 mm/s. The angular velocity during  $180^\circ$  needle rotation is 31.4 radians per second.

##### 3.5.1.1 Camera image-guided needle steering

The needle is steered towards a target using CCD camera images as feedback. The needle insertion distance is 81.4–116.1 mm. The soft-tissue phantom is the same as the one used in Section 3.3. Targets are embedded in the soft-tissue phantom.

Three experimental cases are conducted to validate the proposed control system. Each case is performed five times.

- In Case 1, the insertion point and the target are on the same horizontal line (Fig. 3.12(d)). Pre-defined set-points are used to guide the needle to follow a straight path. This experimental case is performed to test the ability of the control system to steer a bevel-tipped needle (that naturally deflects during insertion) in a straight path.
- In Case 2, the needle is again steered towards the same target position as in Case 1, but through a curved path using set-points as shown in Fig. 3.12(e). The curved path is required in clinical applications to avoid sensitive tissues (e.g., blood vessels).
- In Case 3, a moving virtual target is used to evaluate the performance of the steering algorithm (Fig. 3.12(f)). The total target displacement is chosen to be 23 mm, which is larger than the displacement measured during breast biopsy [46]. A virtual target is used to model target motion. The image processing algorithm is applied to track the virtual target position.

### 3.5.1.2 Ultrasound image-guided needle steering

Ultrasound is used for image feedback to validate the control system using a clinical imaging modality. The needle insertion distance is 29.2–30.1 mm. Two experimental cases are conducted. Each case is performed three times to estimate the targeting error as the needle visibility is affected by accuracy of aligning the needle in the ultrasound probe imaging plane [75, 76].

- In Case 4, the control system is used to steer the needle towards a real target which is embedded into the soft-tissue phantom (Fig. 3.12(g)).
- In Case 5, the control system steers the needle to a moving virtual target (to simulate target motion). The total target displacement is 5.0 mm (Fig. 3.12(h)). The image processing algorithm is used to detect the virtual target position.

In Case 4 and Case 5, silica powder is added to the ingredients of the soft-tissue phantom in order to mimic the acoustic scattering of biological tissue (14.9% gelatin powder (by weight), 1% silica gel and 83.9% water). The elasticity is affected by adding silica powder to the soft-tissue phantom. The elasticity of the soft-tissue phantom is measured using an ultrasound-based technique. The speed of the shear wave propagation in the soft-tissue phantom is measured by the ARFI technique (Virtual Touch™ Tissue Quantification, Siemens AG Healthcare, Erlangen, Germany). The Siemens ACUSON S2000 system is used to obtain ultrasound images and to apply the ARFI technique. The linear transducer 9L4 is used to obtain the ultrasound signals for the needle steering and the shear wave propagation speed measurements. The soft-tissue phantom is assumed to be isotropic, linear elastic and incompressible. Young's modulus ( $E$ ) is calculated as [59]

$$G = v_s^2 \rho, \tag{3.31}$$

### 3. INTEGRATING DEFLECTION MODELS AND IMAGE FEEDBACK FOR REAL-TIME FLEXIBLE NEEDLE STEERING

---

where  $G$ ,  $v_s$  and  $\rho$  are the shear modulus, shear wave propagation speed and density of the soft-tissue phantom, respectively. The density is calculated using the mass and volume of the soft-tissue phantom. Young's modulus ( $E$ ) calculated by

$$E = 2G(1 + \gamma), \quad (3.32)$$

where  $\gamma$  is Poisson's ratio which is assumed to be 0.495. The ARFI technique is not valid for transparent soft-tissue phantoms (without silica powder). The calculated elastic modulus of the soft-tissue phantom (after adding silica powder) is  $57.69 \pm 3.71$  kPa. The elasticity of the soft-tissue phantom sample was independently verified using the uni-axial compression test, and is found to be  $63.7 \pm 5.9$  kPa. Silica powder increases the elastic modulus of the soft-tissue phantom so the calculated radius of curvature ( $r_t$ ) is expected to decrease [64]. This will not affect the targeting accuracy of the control algorithm, as  $r_t$  remains less than  $r_c$ .

#### 3.5.2 Results

The pixel resolution of the CCD camera and ultrasound images are  $1024 \times 768$  pixels and  $720 \times 576$  pixels, respectively. The frame rate of the captured images is 25 frames per second. The experimental results in Section 3.3 are used to estimate the needle radius of curvature ( $r_t$ ). In all the experimental cases, the control radius ( $r_c$ ) is chosen to be equal to the maximum  $r_t$  measured in order to compensate for inaccuracies that might occur while performing the experiments. The five experimental cases are described in Fig. 3.12. The number of needle rotations and targeting errors during insertion are tabulated in Table 3.2.

In Case 1, Case 2 and Case 4, the diameter of the target is 4.0 mm (real target), and in Case 3 and Case 5, the target diameter is 1.7 mm (moving virtual target). The targeting error is measured by calculating the distance between the center of the target

**Table 3.2:** The needle insertion distance, number of rotations and targeting error for the various experimental cases during needle steering are presented. The mean needle insertion distance and number of rotations for each case are  $int$  and  $rot$ , respectively. The mean targeting error in  $x$  and  $y$  directions are  $e_x$  and  $e_y$ , respectively. The standard deviation in  $x$  and  $y$  directions are  $\sigma_x$  and  $\sigma_y$ , respectively. The mean and standard deviation of the absolute targeting error are  $e$  and  $\sigma$ , respectively.

Case	$int$ (mm)	$rot$	$e_x$ (mm)	$\sigma_x$ (mm)	$e_y$ (mm)	$\sigma_y$ (mm)	$e$ (mm)	$\sigma$ (mm)
1	86.7	19	0.38	0.16	0.30	0.25	0.55	0.04
2	105.0	6	0.45	0.10	0.34	0.17	0.59	0.04
3	81.7	2	0.13	0.08	0.23	0.17	0.35	0.15
4	29.2	3	0.36	0.30	0.11	0.05	0.39	0.28
5	30.1	2	0.29	0.24	0.25	0.12	0.42	0.18

and the needle tip position in the last frame. The maximum absolute targeting error is 0.59 mm (Case 2: Fig. 3.12(b) and (e)). In ultrasound image-guided experiments (Case 4 and Case 5), the absolute targeting errors are 0.39 mm and 0.42 mm, respectively. In Case 3 and Case 5, in which moving virtual targets are used, the targeting errors are 0.35 mm and 0.42 mm, respectively. The results show that the needle reaches the target for all cases. It is observed that the targeting error occurs mainly when the needle overshoots the target. Overshooting can occur due to time delay in the control system. This can be improved by reducing the loop time of the control system. *Please refer to the accompanying video<sup>4</sup> that demonstrates the experimental results.*

## 3.6 Discussion

This study combines needle deflection models and image-guided techniques to accurately steer bevel-tipped flexible needles to a moving target. Two different models have been presented to predict the deflection of a needle undergoing multiple bends. Image processing is used to determine the needle and target positions in camera and ultrasound images. Experiments are performed to evaluate the targeting accuracy of the proposed control system.

### 3.6.1 Conclusions

The needle deflection models presented include a modified kinematics-based unicycle model that accounts for needle cut angle, and a mechanics-based model that incorporates needle-tissue interactions. Both models predict deflections for multiple bends. The maximum needle deflection errors at the tip are 0.8 mm and 1.7 mm for the kinematics-based and mechanics-based models, respectively. This indicates that both models have good agreement with experimental results. The real-time image-guided control system uses the kinematics-based model to predict when needle rotation has to be performed for steering. Image processing is used to determine needle tip position and slope, and target position during needle insertion for feedback control. The steering algorithm accounts for target motion to improve targeting accuracy. The proposed real-time needle and target tracking algorithms are applicable to both camera and ultrasound images. The tracking algorithms can also be applied to other clinical imaging modalities. Experiments using ultrasound image-guided control demonstrate that the control system is able to steer the needle to a moving target with mean error of 0.42 mm. The smallest tumor that can be detected using ultrasound images has a diameter of around 2.0 mm [90]. This implies that with the achieved accuracy of the steering algorithm, we can target the smallest detected tumors using ultrasound images.

---

<sup>4</sup>Video link: <https://goo.gl/sqpYDA>

### 3. INTEGRATING DEFLECTION MODELS AND IMAGE FEEDBACK FOR REAL-TIME FLEXIBLE NEEDLE STEERING

---

#### 3.6.2 Future work

The control system will be used to steer flexible needles in biological tissue (Chapter 5). The effect of image artifacts that might appear while steering through biological tissue using ultrasound images needs to be investigated. Further, the effect of needle rotations on tissue damage should be quantified. Both (mechanics-based and kinematics-based) models need to be modified to predict needle deflection in three-dimensional space. In Part II, the tracking and the steering algorithm will be extended to three dimensions to enable the needle to reach out-of-plane targets. The control system will include path planning algorithms to select the optimal path that the needle can follow to reach a target while avoiding obstacles.

## Part II

# Three-Dimensional Needle Steering



# *Preface*

## **Three-Dimensional Needle Steering**

In this part, we upgrade the tracking and control algorithms presented in Chapter 3 to steer the needle in a 3D environment. Non-imaging and imaging modalities are developed for 3D needle tracking. Fiber Bragg Grating (FBG) sensor which is a non-imaging modality is introduced to 3D reconstruct the needle shape and track its tip during insertion (Chapter 4). Steering experiments are then performed to validate the control algorithm while using data from FBG sensors as feedback. The control algorithm is also validated using ultrasound images as feedback in Chapter 5. The developed control algorithm is implemented in a way to minimize the number of needle rotations to reduce the tissue damage while following a certain path. Pre-operative and intra-operative path planning allows the control algorithm to steer the needle towards a target while avoiding sensitive regions or organs such as blood vessels, glands and bone. We also evaluate the effect of target and obstacle motion can take place due to blood flow and patient respiration. Experiments are performed to evaluate steering the needle towards stationary and moving targets in gelatin phantoms and biological tissue while avoiding stationary and moving obstacles.

This part is based on the previously published versions of the following manuscripts: **Chapter 4:** M. Abayazid, M. Kemp and S. Misra, “3D flexible needle steering in soft-tissue phantoms using fiber bragg grating sensors”, in *Proceedings of the IEEE International Conference on Robotics and Automation (ICRA)*, pp. 5843-5849, Karlsruhe, Germany, May 2013.

**Chapter 5:** M. Abayazid, G.J. Vrooijink, S. Patil, R. Alterovitz and S. Misra, “Experimental evaluation of ultrasound-guided 3D needle steering in biological tissue”, *International Journal of Computer Assisted Radiology and Surgery (IJCARS)*, vol. 9, issue 6, pp. 931-939, 2014.

---

## 4

# 3D Flexible Needle Steering in Soft-Tissue Phantoms using Fiber Bragg Grating Sensors

### Abstract

Needle insertion procedures are commonly used for surgical interventions. In this chapter, we develop a three-dimensional (3D) closed-loop control algorithm to robotically steer flexible needles with an asymmetric tip towards a target in a soft-tissue phantom. Twelve Fiber Bragg Grating (FBG) sensors are embedded on the needle shaft. FBG sensors measure the strain applied on the needle during insertion. A method is developed to reconstruct the needle shape using the strain data obtained from the FBG sensors. Four experimental cases are conducted to validate the reconstruction method (single-bend, double-bend, 3D double-bend and drilling insertions). In the experiments, the needle is inserted 120 mm into a soft-tissue phantom. Camera images are used as a reference for the reconstruction experiments. The results show that the mean needle tip accuracy of the reconstruction method is 1.8 mm. The reconstructed needle shape is used as feedback for the steering algorithm. The steering algorithm estimates the region that the needle can reach during insertion, and controls the needle to keep the target in this region. Steering experiments are performed for 110 mm insertion, and the mean targeting accuracy is 1.3 mm. The results demonstrate the capability of using FBG sensors to robotically steer needles.

### 4.1 Introduction

Needle insertion into soft tissue is one of the most common minimally invasive surgical procedures. Needles are often used for diagnostic and therapeutic applications such as biopsy and brachytherapy, respectively. Imaging modalities such as ultrasound and

#### 4. 3D FLEXIBLE NEEDLE STEERING IN SOFT-TISSUE PHANTOMS USING FIBER BRAGG GRATING SENSORS

---

magnetic resonance (MR) images, and computed tomography (CT) scans are commonly used during needle insertion procedures to localize the needle and target for accurate tip placement. Inaccurate needle placement might cause misdiagnosis during biopsy, and unsuccessful treatment during brachytherapy. Rigid needles are used in such procedures, but they do not provide the clinician with sufficient steering capabilities to reach the target [6].

Flexible needles were introduced to facilitate curved paths to reach the target accurately. They can be used to avoid sensitive tissue that might be located along the path to the target [25, 37, 38]. Flexible needles with an asymmetric tip (e.g., bevel tip) naturally bend during insertion into soft tissue [27, 74]. Needle deflections due to tip-asymmetry can be used during insertion to steer the needle to reach a target [6, 37].

Recent studies have presented models for needle steering in two-dimensional (2D) space. DiMaio and Salcudean developed a control and path planning algorithm that relates the needle base (outside the soft-tissue phantom) motion to the tip motion inside the tissue [66]. Glozman and Shoham presented an image-guided closed-loop control for steering flexible needles [26]. Fluoroscopic images were used for real-time feedback of the needle position. They modeled the flexible needle as a beam supported by virtual springs. Forward and inverse kinematics of the needle were solved for path planning. Neubach and Shoham, and Abayazid *et al.* used ultrasound images for tracking the tip position as feedback for 2D steering [75, 91]. Duindam *et al.* developed a model that describes three-dimensional (3D) deflection of bevel-tipped flexible needles. They used the model for path planning to steer the needle towards the target [92]. Hauser *et al.* developed a 3D feedback controller that steers the needle along a helical path [93]. The results of Duindam *et al.* and Hauser *et al.* were based on simulations, and experiments were not conducted for validation of the algorithms.

A needle tracking algorithm is required to provide the system with feedback for closed-loop control. Needle tracking techniques were developed based on ultrasound and fluoroscopic image segmentation to determine the needle shape during the insertion procedure [26, 75, 91]. The spatial resolution of 3D ultrasound images is limited [94], and the use of x-ray-based imaging (CT or fluoroscopy) exposes the patient to high doses of radiation [95]. MR imaging suffers from low refresh rate and incompatibility with magnetic materials [96]. Electromagnetic position tracking sensors [6, 79] are also used for needle tracking, but its accuracy is sensitive to ferromagnetic materials in the range of measurement. Fiber Bragg Grating (FBG) sensors can be an alternative for real-time 3D shape reconstruction. FBG sensors are optical sensors that can measure strain [97, 98]. The use of FBG-based needle shape reconstruction for medical applications has been shown in [99, 100, 101, 102, 103, 104].

In the current study, an algorithm is developed to robotically steer flexible needles in 3D space (Fig. 4.1). The steering algorithm estimates the region that the needle tip can reach during insertion in real-time. The needle rotates about its axis to keep the target in this reachable region. The needle radius of curvature, tip position and orientation are the inputs to the steering algorithm during insertion. The steering algorithm is validated by conducting insertion experiments into a soft-tissue phantom. Real-time 3D needle shape reconstruction using FBG sensors provides feedback for the steering algorithm. To the best of our knowledge, the use of FBG sensors for

## 4.2 Three-dimensional needle shape reconstruction

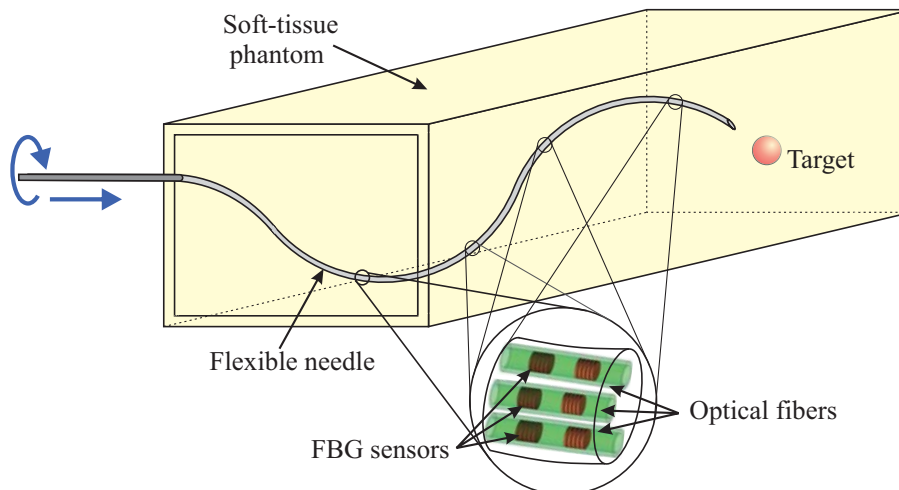


**Fig. 4.1:** Fiber Bragg Grating (FBG) sensors are used to reconstruct the needle shape during insertion into a soft-tissue phantom. Twelve FBG sensors are located on three optical fibers along the needle shaft. The reconstructed needle shape is used as feedback for the steering algorithm. Steering is accomplished by rotating the needle about its axis at the base.

real-time shape reconstruction, and using this data for 3D steering of a bevel-tipped flexible needle (undergoing multiple bends) inserted into soft-tissue phantoms have not been investigated. Further, we also demonstrate the feasibility of the reconstruction method in biological tissue by conducting experiments in chicken breast.

This chapter is organized as follows: Section 4.2 explains the methods used for needle shape reconstruction. Section 4.3 describes the technique used for 3D flexible needle steering. Section 4.4 discusses the experimental setup. The experimental results and validation are provided in Section 4.5, followed by discussion and recommendations for future work (Section 4.6).

## 4.2 Three-dimensional needle shape reconstruction

This section describes FBG sensors integrated on the flexible needle, and the method used for 3D needle shape reconstruction.

### 4.2.1 Fiber Bragg Grating sensors

An FBG sensor consists of gratings etched periodically on an optical fiber. The gratings reflect a certain wavelength ( $\lambda_B$ ) of light (Bragg wavelength), which is calculated as [97]

$$\lambda_B = 2n_{eff}\Lambda, \quad (4.1)$$

where  $n_{eff}$  and  $\Lambda$  are the effective refractive index and period of the grating, respectively. Mechanical strain and temperature affect the refractive index and the grating period of the sensor. In this study, we assume that FBG sensors are used at constant

## 4. 3D FLEXIBLE NEEDLE STEERING IN SOFT-TISSUE PHANTOMS USING FIBER BRAGG GRATING SENSORS

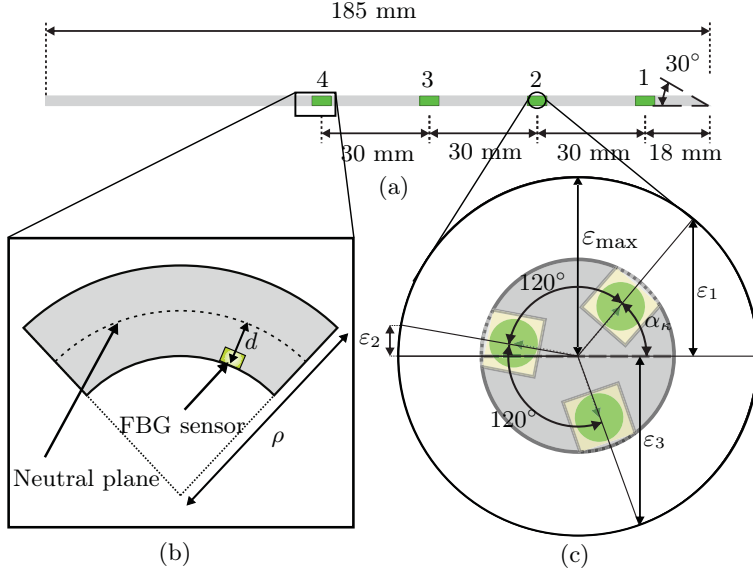


**Fig. 4.2:** Configuration of Fiber Bragg Grating (FBG) sensors on the needle. (a) The numbers 1, 2, 3 and 4 represent the sensor locations on the needle shaft. (b) The inset (left) depicts a curved needle with radius of curvature ( $\rho$ ), and the distance between the FBG sensor and the neutral plane is  $d$ . (c) The inset (right) shows the strains ( $\varepsilon_1$ ,  $\varepsilon_2$ ,  $\varepsilon_3$ ) measured by three FBG sensors. The measured strains are used to calculate the bending strain in the needle (magnitude ( $\varepsilon_{\max}$ ) and direction ( $\alpha_{\kappa}$ )) at a sensor location.

temperature. Applying strain on sensors causes shift in the wavelength of the reflected light ( $\Delta\lambda_B$ ). The relation between the strain ( $\varepsilon_i$ ) applied on each sensor ( $i$ ) and  $\Delta\lambda_B$  (at constant temperature) is given by [97, 105]

$$\varepsilon_i = \frac{1}{\lambda_B (1 - P_\varepsilon)} \Delta\lambda_B + \varepsilon_{T,B}, \quad (4.2)$$

where  $\varepsilon_{T,B}$  is the offset in the measured strain due to temperature and Bragg wavelength, and  $P_\varepsilon$  is the photo-elastic coefficient of the optical fiber. The strain measured at each sensor is used to calculate the magnitude and direction of the needle curvature.

### 4.2.2 Needle curvature calculation

In this study, we have three fibers embedded on the needle. Four FBG sensors are placed along each fiber. The configuration of the FBG sensors along the needle and at each sensor location is shown in Fig. 4.2(a). This configuration of sensors is used to measure the needle curvature. The relation between the needle curvature ( $\kappa$ ) at a sensor location and the magnitude of the bending strain ( $\varepsilon_{\max}$ ) is [86]

$$\varepsilon_{\max} = \frac{d}{\rho} = d \cdot \kappa, \quad (4.3)$$

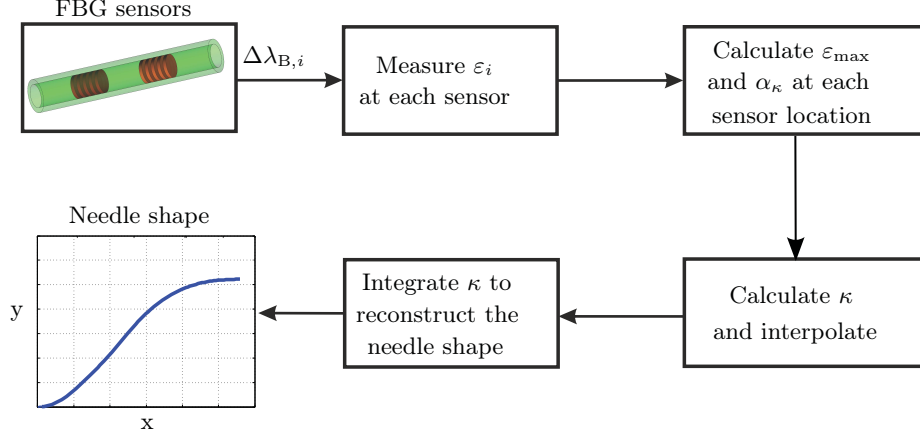


**Fig. 4.3:** The flowchart indicates the steps for needle shape reconstruction using Fiber Bragg Grating (FBG) sensors. Strains ( $\varepsilon_i$ ) are calculated according to the wavelength shifts ( $\Delta\lambda_{B,i}$ ) measured by the FBG sensors ( $i=1,\dots,12$ ). The bending strain ( $\varepsilon_{\max}$ ) and its direction ( $\alpha_\kappa$ ) at each sensor locations are interpolated to obtain the magnitude ( $\kappa$ ) and direction ( $\alpha_\kappa$ ) of the curvature function. The curvature function is integrated twice to determine the entire needle shape.

where  $d$  is the distance between the sensor and the neutral plane, and  $\rho$  is the radius of curvature of the needle at the sensor location (Fig. 4.2(b)).

The strain ( $\varepsilon_i$ ) measured by each sensor ( $i$ ) at a single location is calculated as [104]

$$\begin{aligned}
 \varepsilon_1 &= \varepsilon_{T,B} + \sin(\alpha_\kappa) \cdot \varepsilon_{\max}, \\
 \varepsilon_2 &= \varepsilon_{T,B} + \sin(\alpha_\kappa + 120^\circ) \cdot \varepsilon_{\max}, \\
 \varepsilon_3 &= \varepsilon_{T,B} + \sin(\alpha_\kappa + 240^\circ) \cdot \varepsilon_{\max},
 \end{aligned} \tag{4.4}$$

where  $\alpha_\kappa$  is the direction of the bending strain. By solving (4.3) and (4.4), we obtain the needle curvature and its direction at each sensor location (Fig. 4.2(c)).

### 4.2.3 Needle shape reconstruction

Needle shape reconstruction requires calculation of the curvature along the total inserted length. The magnitude and direction of the needle curvature at the four sensor locations (along the needle shaft) are used to reconstruct the needle shape. K-nearest neighbor interpolation algorithm is used to generate the continuous needle curvature function [106, 107]. It is assumed that the needle moves along a curved path with a constant radius. For small needle deflection, the curvature is calculated by integrating its function twice with respect to the insertion distance [108]. The needle is inserted perpendicular to the surface of the soft-tissue phantom (i.e., the slope and deflection of the needle at the insertion point are assumed to be zero). The flowchart in Fig. 4.3 de-

#### 4. 3D FLEXIBLE NEEDLE STEERING IN SOFT-TISSUE PHANTOMS USING FIBER BRAGG GRATING SENSORS

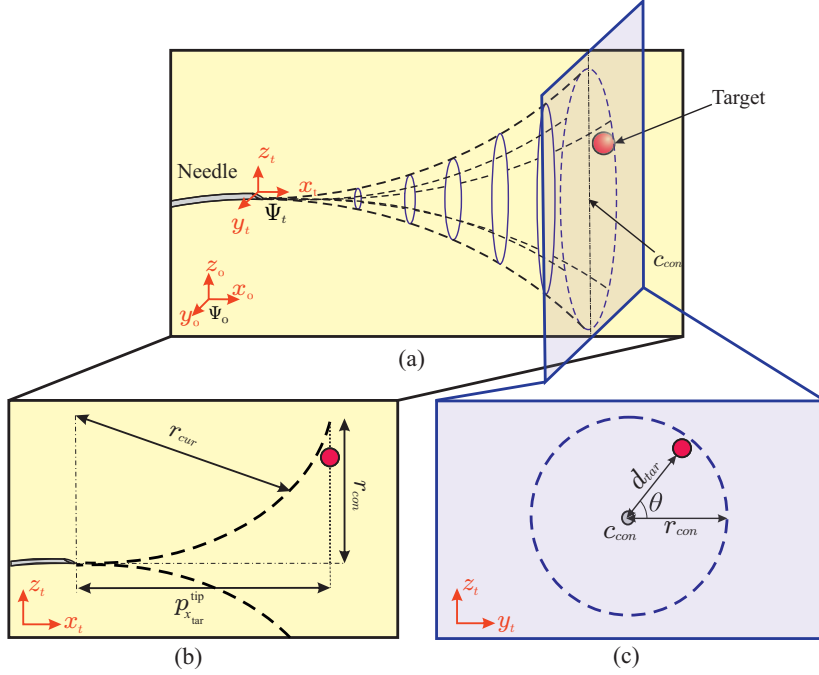


**Fig. 4.4:** The region the needle tip can reach is represented by a conical shape. (a) The frame ( $\Psi_t$ ) is attached to the needle tip, and the needle is inserted in the  $x_t$ -direction. The control circle with centre ( $c_{con}$ ) intersects the target and is perpendicular to the  $x_t$ -axis. (b) The radius ( $r_{con}$ ) is determined using the radius of curvature ( $r_{cur}$ ) of the needle and the distance ( $p_{x_{tar}}^{tip}$ ) between the tip and target along the  $x_t$ -axis. (c) The needle rotates about its axis by angle ( $\theta$ ) if the distance ( $d_{tar}$ ) between  $c_{con}$  and target is larger than or equal to  $r_{con}$ .

describes the needle shape reconstruction method. Real-time needle shape reconstruction using FBG sensors is used as feedback for steering.

### 4.3 Three-dimensional needle steering algorithm

In this section, we discuss the closed-loop control algorithm for steering a bevel-tipped flexible needle towards a target in 3D. The bevel-tipped needle is assumed to move along a circular path during insertion [27, 74]. Additionally, the soft-tissue phantom is assumed to be stiff enough to support the needle shaft to follow the path created by the needle. The direction of the circular path depends on the orientation of the bevel tip. The bevel tip orientation is controlled by needle rotation about its insertion axis at the base. This rotation enables the steering algorithm to direct the tip towards the target.

The steering algorithm assumes that frame ( $\Psi_t$ ) is attached to the needle tip (Fig. 4.4(a)). The algorithm obtains the needle tip position ( $\mathbf{p}_{tip}^0$ ) and orientation ( $\mathbf{R}_{tip}^0$ ) with respect to the global coordinate frame ( $\Psi_0$ ) using the reconstruction algorithm (Section 4.2.3). The target position is set to be a static point in 3D space. The target position ( $\mathbf{p}_{tar}^{tip}$ ) with respect to frame ( $\Psi_t$ ) is

$$\mathbf{p}_{tar}^{tip} = \begin{bmatrix} p_{x_{tar}}^{tip} & p_{y_{tar}}^{tip} & p_{z_{tar}}^{tip} \end{bmatrix}^T, \quad (4.5)$$

### 4.3 Three-dimensional needle steering algorithm

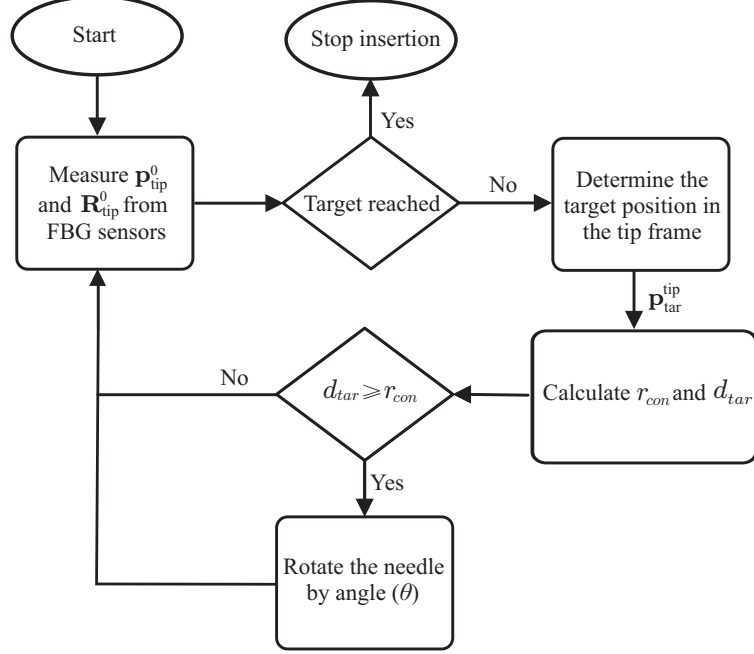


**Fig. 4.5:** The flowchart depicts the control algorithm used for needle steering. The needle tip position ( $\mathbf{p}_{tip}^0$ ) and orientation ( $\mathbf{R}_{tip}^0$ ) are obtained from the reconstruction algorithm (Section 4.2.3). The target position ( $\mathbf{p}_{tar}^{tip}$ ) with respect to the tip frame is determined. The distance between the centre ( $c_{con}$ ) of the control circle (with radius ( $r_{con}$ )) and target is  $d_{tar}$ . If  $d_{tar} \geq r_{con}$ , the needle will rotate about its axis by the angle ( $\theta$ ).

where  $p_{x_{tar}}^{tip}$ ,  $p_{y_{tar}}^{tip}$  and  $p_{z_{tar}}^{tip}$  are target positions along the  $x_t$ -,  $y_t$ - and  $z_t$ -axes, respectively. The region that the needle can reach in 3D is represented by a conical shape shown in Fig. 4.4(a). The plane of the control circle with centre ( $c_{con}$ ) intersects the target and lies on the plane perpendicular to the  $x_t$ -axis. The radius ( $r_{con}$ ) of the control circle is calculated using

$$r_{con} = r_{cur} - \sqrt{r_{cur}^2 - (p_{x_{tar}}^{tip})^2}, \quad (4.6)$$

where  $r_{cur}$  is the radius of curvature of the needle path (Fig. 4.4(b)), and it is obtained from experiments. The distance between  $c_{con}$  and the target position in  $y_t z_t$ -plane (Fig. 4.4(c)) is determined using

$$d_{tar} = \sqrt{(p_{z_{tar}}^{tip})^2 + (p_{y_{tar}}^{tip})^2}. \quad (4.7)$$

The radius ( $r_{con}$ ) decreases during insertion as the needle moves towards the target. If the control circle does not intersect the target ( $d_{tar} \geq r_{con}$ ), the needle will rotate about its axis to keep the needle in the reachable region. The needle rotates by the angle ( $\theta$ ) to direct the needle tip towards the target (Fig. 4.4(c)), and  $\theta$  is calculated as

## 4. 3D FLEXIBLE NEEDLE STEERING IN SOFT-TISSUE PHANTOMS USING FIBER BRAGG GRATING SENSORS

---

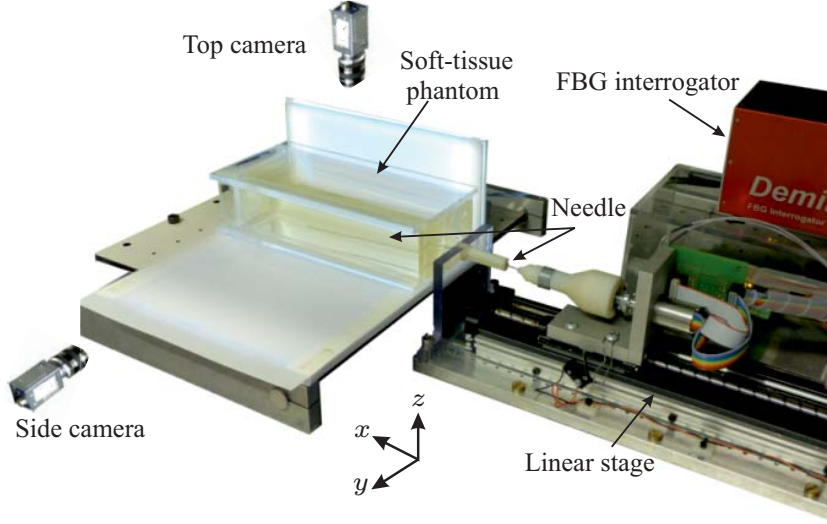


**Fig. 4.6:** Needle steering setup: A linear stage is used to insert the Nitinol needle (integrated with Fiber Bragg Grating (FBG) sensors) into a soft-tissue phantom. The needle shape is reconstructed using FBG sensors connected to an interrogator. Two charge-coupled device cameras (top and side) are used as reference for validation.

$$\theta = \tan^{-1} \left( \frac{p_{z_{tar}}^{\text{tip}}}{p_{y_{tar}}^{\text{tip}}} \right). \quad (4.8)$$

The flowchart in Fig. 4.5 describes the steering algorithm. The steering algorithm is implemented, and experiments are conducted for validation in the following section.

### 4.4 Experiments

This section presents the needle design and the location of the FBG sensors on the needle. The experimental setup used to insert the needle into the soft-tissue phantom is discussed, and the validation of the reconstruction method is also provided.

#### 4.4.1 Experimental setup

The needle is mounted in a two degrees-of-freedom (DOF) insertion device (Fig. 4.6). The two-DOF device allows the needle to be inserted and rotated about its axis. The details of the experimental setup are presented in [64, 65].

The needle is inserted into a soft-tissue phantom made up of a gelatin mixture [65]. The needle has a total length of 185 mm. The flexible needle is made of Nitinol alloy (nickel and titanium). The Nitinol needle has a diameter of 1.0 mm with a bevel angle (at the tip) of 30°. FBG sensors are placed at four locations along the needle shaft (Fig. 4.2(a)). At each sensor location, three FBG sensors are placed 120° apart (Fig. 4.2(c)). This enables us to measure the magnitude and direction of curvature (4.4).

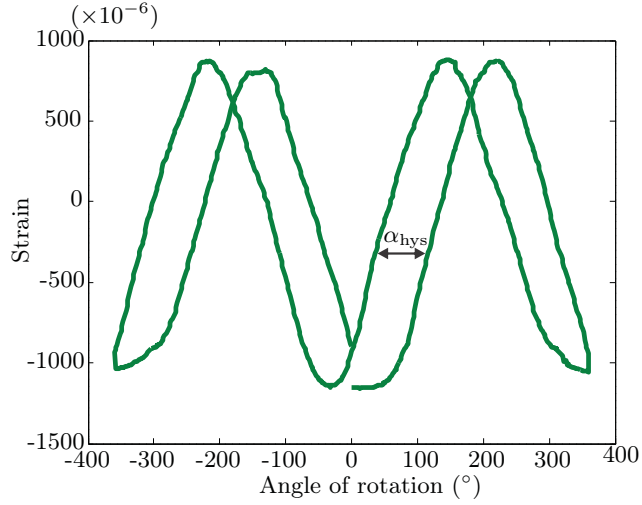


**Fig. 4.7:** The plot shows strain measurements obtained from the Fiber Bragg Grating sensor location 1 (Fig. 4.2). The hysteresis angle ( $\alpha_{\text{hys}}$ ) is illustrated when needle rotates about its axis  $360^\circ$  clockwise and counterclockwise, and then back to its original orientation at  $30^\circ/\text{s}$ . The measured  $\alpha_{\text{hys}}$  at this found to be  $74 \pm 6^\circ$ .

The sensors are connected to a Deminsys Pyton interrogator (Technobis, Uitgeest, The Netherlands). The interrogator measures the reflected wavelength for each FBG sensor at rate of 20 kHz. The data from the FBG sensors is transferred to a computer via an ethernet cable. The computer receives the sensor data as UDP-packets using C++.

#### 4.4.2 Hysteresis calibration of the Fiber Bragg Grating sensors

Calibration is applied for torsional compensation. Friction along the needle shaft during rotation around its axis results in a difference between the rotation angle applied at the needle base and the orientation angle at the tip. This difference in the rotation angle (hysteresis angle ( $\alpha_{\text{hys}}$ )) is measured experimentally. In the calibration experiments, the needle is inserted 120 mm in the soft-tissue phantom, and then the needle rotates  $360^\circ$  with an angular velocity of  $30^\circ/\text{s}$  in both directions (clockwise and counterclockwise) as shown in Fig. 4.7. The hysteresis is calibrated for the four sensor locations along the needle. The calibration experiments show that at sensor locations 1, 2, 3 and 4 (Fig. 4.2(a)), the angles ( $\alpha_{\text{hys}}$ ) are found to be  $74 \pm 6^\circ$ ,  $70 \pm 7^\circ$ ,  $62 \pm 9^\circ$  and  $51 \pm 7^\circ$ , respectively. The data from the calibrated FBG sensors are used for the needle shape reconstruction method (Section 4.2). By solving (4.4) to calculate  $\alpha_\kappa$  and measuring the hysteresis effect ( $\alpha_{\text{hys}}$ ), the calibrated direction of curvature of the needle ( $\alpha_{\kappa,\text{cal}}$ ) is calculated as [109]

$$\alpha_{\kappa,\text{cal}} = \alpha_\kappa + \alpha_{\text{rot}} \pm \frac{\alpha_{\text{hys}}}{2} , \quad (4.9)$$

where  $\varepsilon_1$ ,  $\varepsilon_2$  and  $\varepsilon_3$  are the strains measured by the three sensors at a single location, and  $\alpha_{\text{rot}}$  is the rotation applied at the base of the needle. The sign of  $\alpha_{\text{hys}}$  depends on the direction of needle rotation. The needle shape reconstruction method is validated using a 3D image-based technique.

## 4. 3D FLEXIBLE NEEDLE STEERING IN SOFT-TISSUE PHANTOMS USING FIBER BRAGG GRATING SENSORS

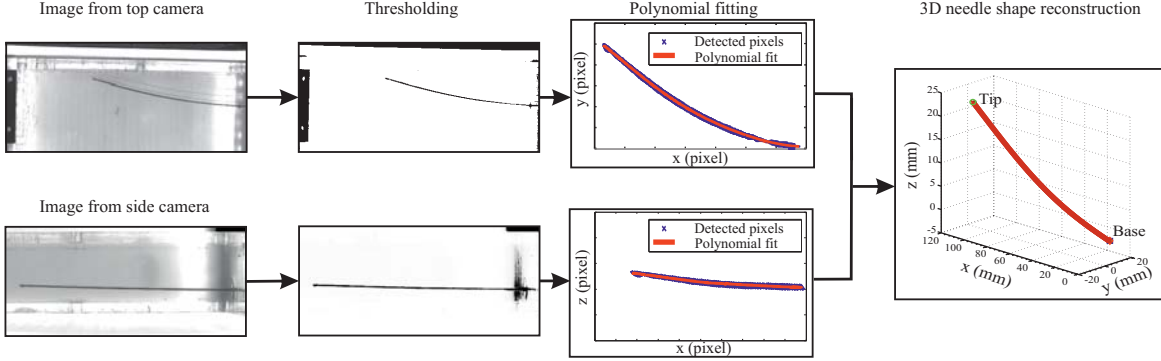


**Fig. 4.8:** Top and side camera images are used to validate the reconstruction method. Thresholding is applied on images obtained from both cameras. The pixels that represent the needle shape are localized. A polynomial is fit to the pixel positions. The resulting curves from both camera images are used to reconstruct the needle shape in three-dimensional space.

### 4.4.3 Validation of the needle shape reconstruction method

The needle shape reconstruction using FBG sensors in the soft-tissue phantom is verified using two charge-coupled device (CCD) cameras (positioned at the top and the side of the soft-tissue phantom) as a reference measurement (Fig. 4.6). A threshold is applied on the images captured from both cameras to produce binary images (Fig. 4.8). The resulting image after thresholding is inverted to make the background black, and the pixels that represent the needle white. The needle shape is obtained by localizing the white pixels in the images. Polynomial fitting of the localized pixels is used to produce the needle shape in each camera image. The 3D position of a pixel is calculated by selecting a matching pixel in the two camera images, as shown in Fig. 4.8. The algorithm used for 3D reconstruction is based on a 3D stereoscopic reconstruction method described by Jahya *et al.* [110]. The results of the validation experiments are presented in Section 4.5.1.

## 4.5 Results

In this section, we first present the experimental results of needle shape reconstruction using data from FBG sensors. We also conduct experiments to steer a flexible needle towards different target positions in 3D space.

### 4.5.1 Needle shape reconstruction

The needle shape reconstruction method (Section II) is verified for the following experimental cases, where the needle is inserted at 10 mm/s (within the range of insertion velocities used in clinical applications (0.4 - 10 mm/s) [88]) and it rotates about its axis at 30°/s:

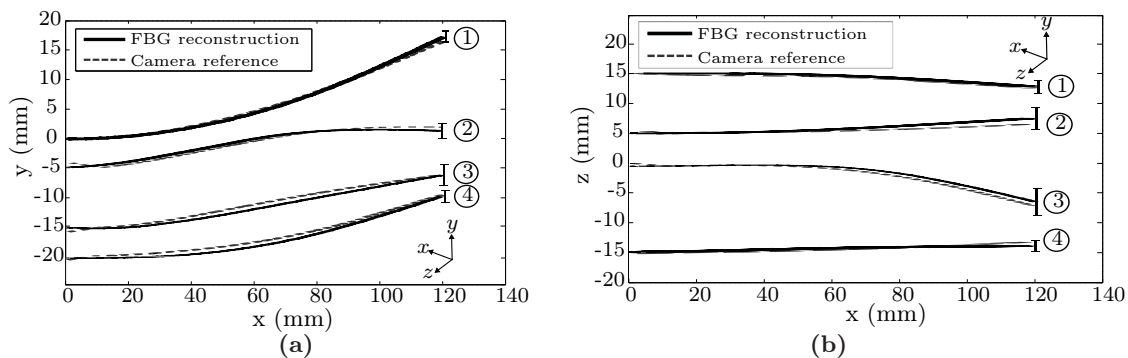


**Fig. 4.9:** Needle shape reconstruction ((a) top view and (b) side view) for insertion into a soft-tissue phantom: ① Single-bend (mean tip error ( $e_{tip}$ ) is  $1.5 \pm 0.8$  mm). ② Double-bend ( $e_{tip}$  is  $2.0 \pm 0.7$  mm). ③ Three-dimensional double-bend ( $e_{tip}$  is  $2.1 \pm 1.1$  mm). ④ Drilling ( $e_{tip}$  is  $1.7 \pm 1.2$  mm). Each experiment is repeated six times.

- (i) Single-bend: Needle is inserted 120 mm, with no rotation.
- (ii) Double-bend: Needle is inserted 120 mm, with  $180^\circ$  rotation at: (a) 40 mm, (b) 60 mm and (c) 80 mm insertion distance.
- (iii) 3D double-bend: Needle is inserted 120 mm, with  $90^\circ$  rotation at: (a) 40 mm, (b) 60 mm and (c) 80 mm insertion distance.
- (iv) Drilling: Needle rotates continuously (drilling motion) for the first: (a) 40 mm, (b) 60 mm and (c) full 120 mm insertion. This is followed by a single-bend insertion.

Each experimental case is repeated six times. The results of needle reconstruction experiments are shown in Fig. 4.9. The final needle shape is also determined using camera images to validate the reconstruction method. The difference ( $e_{tip}$ ) between the tip position ( $x$ -,  $y$ - and  $z$ -coordinates) obtained using FBG sensors and camera images is calculated as

$$e_{tip} = \|\mathbf{p}_{FBG} - \mathbf{p}_{cam}\|, \quad (4.10)$$

where  $\mathbf{p}_{FBG}$  and  $\mathbf{p}_{cam}$  are the tip positions measured using FBG sensors and camera images, respectively. The maximum mean tip error is  $2.1 \pm 1.1$  mm, and is observed for the 3D double-bend case.

#### 4.5.2 Needle steering

The data obtained from FBG sensors are used as feedback for closed-loop needle steering as described in Section 4.3. The radius of curvature ( $r_{cur}$ ) of the needle is determined experimentally from the single-bend experiments by fitting the needle shape to a circle and calculating the radius of the fitted circle. The value of  $r_{cur}$  used in the steering

## 4. 3D FLEXIBLE NEEDLE STEERING IN SOFT-TISSUE PHANTOMS USING FIBER BRAGG GRATING SENSORS

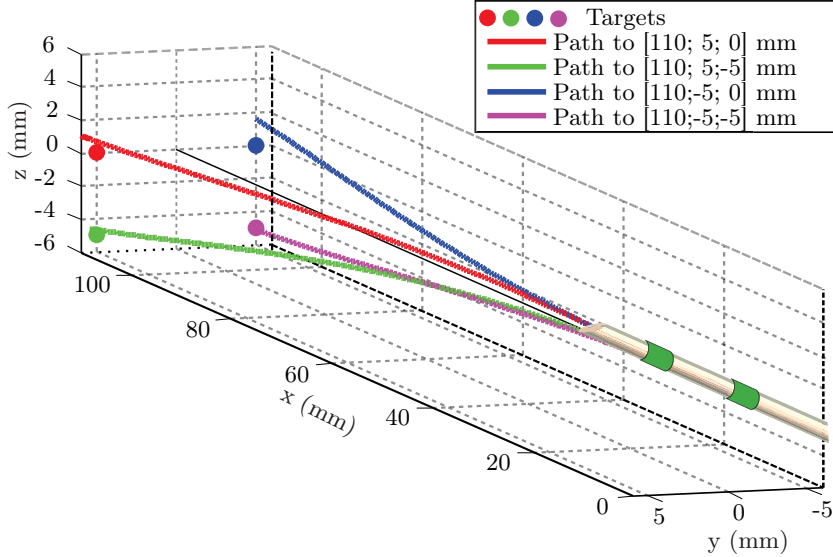


**Fig. 4.10:** Shape reconstruction results for the needle path during steering towards different target positions. The mean number of needle rotations to reach the target is 8. The mean targeting accuracy is  $1.3 \pm 0.9$  mm.

experiments is 375 mm. In the experiments, the target is positioned initially in the reachable region of the needle. The needle can rotate in both directions to reduce the effect of needle torsion in the soft-tissue phantom. Hysteresis calibration is performed online before every rotation during the steering experiments. Experiments are conducted to steer the needle towards four different target positions. The target positions and reconstructed needle shapes during steering experiments are shown in Fig. 4.10. Three steering experiments are performed for each target position. The mean targeting error is calculated as  $\|\mathbf{p}_{\text{tip}} - \mathbf{p}_{\text{tar}}\|$ , where  $\mathbf{p}_{\text{tip}}$  is the tip position and  $\mathbf{p}_{\text{tar}}$  is the target position. The needle shape is also reconstructed using camera images for validation. The results show that the mean targeting error ( $e_{\text{tip}}$ ) measured using the FBG sensors and camera images are  $1.2 \pm 0.5$  mm and  $1.3 \pm 0.9$  mm, respectively. *Please refer to the attached video<sup>5</sup> that demonstrates the results of needle steering experiments.*

### 4.6 Discussion

In this study, a 3D needle steering algorithm is developed to steer a flexible needle towards a target. The steering algorithm uses 3D needle shape as feedback from the FBG sensors. Twelve FBG sensors are embedded on a 1.0 mm diameter flexible Nitinol needle. The needle bending strain is measured at four locations along the needle shaft. 3D needle curvature is derived from the measured strains. K-nearest neighbor interpolation is used to estimate the curvature along the entire needle.

<sup>5</sup>Video link: <https://goo.gl/mVwMTC>

Hysteresis calibration is also applied to estimate difference between the needle orientation at the tip and base. This is caused by friction between the needle and the surrounding tissue during rotation about its axis. Hysteresis is compensated for by calculating the angle ( $\alpha_{\text{hys}}$ ) for accurate steering and shape reconstruction.

Needle shape is reconstructed in real-time for both in-plane and out-of-plane insertions in a soft-tissue phantom. The reconstructed needle shape using FBG sensors is validated using camera images as a reference. The errors between the 3D tip position obtained from FBG sensors and camera images are 1.5 mm, 2.0 mm, 2.1 mm and 1.7 mm for single-bend, double-bend, 3D double-bend and drilling insertions, respectively.

The steering algorithm estimates the region that the needle can reach during insertion in real-time. The needle is steered to keep the target in the reachable region. The volume of the reachable region decreases during insertion. Experiments are conducted to evaluate the steering algorithm. The needle is steered towards target positions in 3D space. The mean targeting error is 1.3 mm. These results show that FBG sensors can be combined with clinical imaging modalities or used independently for robotically steering needles. Furthermore, preliminary experiments show the feasibility of using the needle shape reconstruction method in biological tissue.

The accuracy of the 3D needle shape reconstruction method can be improved if we increase the number of sensors integrated on the needle. Needle steering will be extended to include path planning algorithms to select the optimal path that the needle can follow to reach a target. Target motion in 3D space will also be tracked in real-time to increase the targeting accuracy.

#### **4. 3D FLEXIBLE NEEDLE STEERING IN SOFT-TISSUE PHANTOMS USING FIBER BRAGG GRATING SENSORS**

---

# Experimental Evaluation of Ultrasound-Guided 3D Needle Steering in Biological Tissue

## Abstract

In this chapter, we present a system capable of automatically steering bevel-tip flexible needles under ultrasound guidance towards stationary and moving targets in gelatin phantoms and biological tissue while avoiding stationary and moving obstacles. We use three-dimensional (3D) ultrasound to track the needle tip during the procedure. Our system uses a fast sampling-based path planner to compute and periodically update a feasible path to the target that avoids obstacles. We then use a novel control algorithm to steer the needle along the path in a manner that reduces the number of needle rotations, thus reducing tissue damage. We present experimental results for needle insertion procedures for both stationary and moving targets and obstacles for up to 90 mm of needle insertion. We obtained a mean targeting error of  $0.32 \pm 0.10$  mm and  $0.38 \pm 0.19$  mm in gelatin-based phantom and biological tissue, respectively. The achieved submillimeter accuracy suggests that our approach is sufficient to target the smallest lesions ( $\phi 2$  mm) that can be detected using state-of-the-art ultrasound imaging systems.

## 5.1 Introduction

Needle insertion into soft-tissue is a minimally invasive procedure used for diagnostic and therapeutic purposes such as biopsy and brachytherapy, respectively. Examples of diagnostic needle insertion procedures are liver and lung biopsies to detect tumors [7, 8]. Therapeutic applications of needle insertion include brachytherapy of cervical, prostate

## 5. EXPERIMENTAL EVALUATION OF ULTRASOUND-GUIDED 3D NEEDLE STEERING IN BIOLOGICAL TISSUE

---

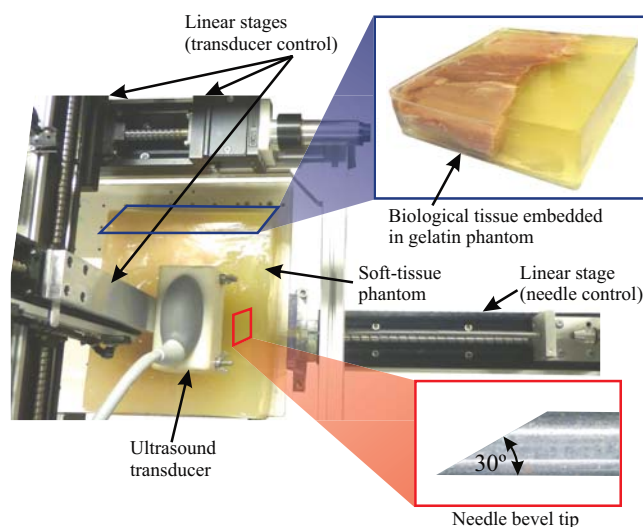


**Fig. 5.1:** The experimental setup shows the needle insertion device and the transducer control device. The upper inset depicts biological tissue (chicken breast) embedded in a gelatin phantom. The lower inset shows the needle bevel tip.

and breast cancers [9]. Imaging modalities such as ultrasound, magnetic resonance (MR), and computed tomography (CT) are often used during needle insertion procedures to determine the positions of the needle and target for accurate needle tip placement [10]. Inaccurate placement may result in misdiagnosis and unsuccessful treatment during biopsy and brachytherapy, respectively. The needles usually used in such procedures are rigid. Such needles do not provide the clinician with sufficient steering capabilities that allow the needle to avoid certain obstacles and reach the intended target [6].

The steerability of the needle is improved by introducing flexible needles. Such needles can be used to steer around sensitive and hard tissue such as blood vessels and bones, respectively [25, 37, 38]. The flexible needles fabricated with an asymmetric tip (bevel tip) naturally deflect during insertion into soft-tissue (Fig. 5.1) [27, 74]. The needle deflection due to its tip-asymmetry is used to steer the needle to reach a certain target position [6, 37]. The needle is assumed to deflect along a circular path during insertion. This assumption is used in various studies to model the needle deflection during insertion [27, 37, 74, 111].

The deflection of a needle with a bevel tip can be controlled using duty-cycling of the needle during insertion [34, 35]. This algorithm can vary the needle curvature by changing the ratio between period of needle insertion with spinning to the total period of insertion. The main disadvantage of the duty-cycling approach is that it requires excessive number of rotations of the needle inside the tissue that might increase tissue damage, and subsequently patient trauma [36]. In recent studies, control algorithms were developed for needle steering in two-dimensional (2D) space. These control algorithms enhanced the needle targeting accuracy compared to manual needle control but some improvements are required to bring these methods to clinical practice such as

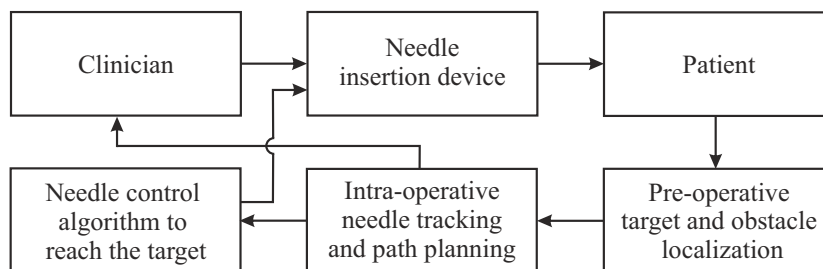


**Fig. 5.2:** The workflow presents a clinically viable robotic needle steering system. The needle insertion device controls the direction of insertion inside the patient’s soft tissue. Needle tip tracking and path planning are performed intra-operatively to provide control algorithm and the clinician with data required to control the insertion device.

considering the physiological motion, tissue inhomogeneity and fluid flow. DiMaio and Salcudean presented a path planning and control algorithm that related the needle motion at the base (outside the soft-tissue phantom) to the tip motion inside the tissue [66]. Glozman and Shoham, and Neubach and Shoham developed an image-guided closed-loop control algorithm for steering flexible needles using fluoroscopic and ultrasound images, respectively [26, 75]. They solved forward and inverse kinematics of the needle for 2D path planning. Abayazid *et al.* presented a 2D ultrasound image-guided steering algorithm, and a three-dimensional (3D) steering algorithm where they used Fiber Bragg Grating sensors for feedback [91, 112]. Chatelain *et al.* developed a real-time needle tracking method by servoing images obtained from a 3D ultrasound probe [113]. Reed *et al.* integrated a path planner and stabilizing controller for needle steering on a 2D plane [114]. Seiler *et al.* developed a planning method for correcting a path using Lie group symmetries [115]. Hauser *et al.* developed a 3D feedback controller that steers the needle along a helical path, although results were evaluated in simulation without physical experiments [93].

Several studies presented 2D path planning algorithms for steering flexible needles, but our focus in this chapter is on 3D steering [66, 116, 117, 118]. Duindam *et al.* presented fast 3D path planning algorithms based on inverse kinematics and optimization, although these methods do not offer any completeness guarantees, i.e., they may fail to return a solution for problems with obstacles [92, 119]. Park *et al.* developed a path-of-probability algorithm that considers uncertainty in needle motion using diffusion-based error propagation, but the presence of obstacles affects the completeness of the planner [102]. Several 3D path planning algorithms have been introduced that are based on Rapidly-exploring Random Trees (RRTs) [120, 121]. Our approach integrates ideas from Patil *et al.* to quickly compute feasible, collision-free paths in 3D that solves the problem of failure in providing the path during presence of obstacles [121].

The proposed system, depicted in Fig. 5.2, is a step forward to achieve a clinically viable robotic needle steering system. The anatomical regions of interest in the patient are acquired pre-operatively using ultrasound images. Based on the images, the clinician identifies the target location and sensitive structures such as glands or blood vessels and other obstacles such as bones. The path planning algorithm generates a needle trajectory to avoid obstacles and reach the target. The planner generates new

## 5. EXPERIMENTAL EVALUATION OF ULTRASOUND-GUIDED 3D NEEDLE STEERING IN BIOLOGICAL TISSUE

---

paths intra-operatively based on the updated needle tip position (obtained from ultrasound images) and target position during insertion. The needle insertion procedure is autonomous under supervision of the clinician.

In the current study, we integrate the presented 3D tracking, path planning and control algorithms to steer a bevel-tipped flexible needle to reach a target in 3D space while avoiding obstacles. The proposed control algorithm provides a reduced number of needle rotations to reach the target location to minimize tissue damage. The algorithms are validated by conducting insertion experiments into a soft-tissue phantom and biological tissue (chicken breast) while avoiding virtual and real obstacles. The contributions of this work include:

- The use of ultrasound-based 3D needle tracking combined with 3D real-time path planning for avoiding real obstacles.
- 3D steering and path planning for needle insertion into biological tissue.
- Experimental evaluation of needle steering towards a moving target while avoiding more than one moving obstacle.

In the following section, we describe the ultrasound-based needle tip tracking algorithm. We then describe the path planning method and the control algorithm, which reduces the number of needle rotations inside soft tissue to reduce patient trauma. Finally, we present our results in soft-tissue phantoms and biological tissue.

### 5.2 Three-dimensional needle tracking

We use a high resolution 2D ultrasound transducer to obtain the needle tip pose during insertion. The resolution of the ultrasound image is 0.12 mm per pixel. The ultrasound transducer is placed to visualize the tip, and orientated perpendicular to the needle insertion direction ( $X$ -axis of frame  $(\Psi_0)$ ) as shown in Fig 5.3. The resulting ultrasound image shows a radial cross-sectional view of the needle. The cross-section of the needle does not look circular in the ultrasound image due to reverberation artifacts [122]. These artifacts occur due to bouncing of the ultrasound waves between materials of different acoustic impedance such as the needle and the surrounding tissue. The resulting artifact visible in ultrasound images has a tail-shaped structure of equally spaced echoes along the sound wave. The length of the tail-shaped structure depends on the bouncing echoes that are received by the transducer. The reverberation artifact is often referred to as the comet tail artifact (CTA) [123]. An image processing algorithm is used to determine the centroid of the needle in the ultrasound images. The needle in ultrasound images is enhanced by a series of basic image processing techniques, including median filtering, thresholding, and erosion and dilation, as shown in Fig. 5.3. Some extra processing steps are performed to remove artifacts that appear in ultrasound images while scanning biological tissue (chicken breast). The ultrasound image is filtered to eliminate the speckles that look similar to the needle tip. This is achieved by applying an additional erosion step and by reducing the image intensity gain using the ultrasound device settings.

### 5.3 Three-dimensional needle path planning and control

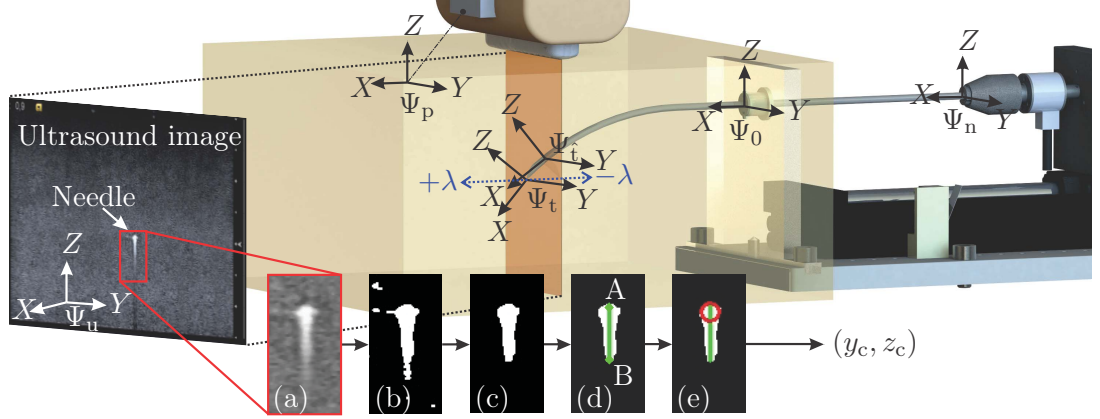


**Fig. 5.3:** Overview of the various coordinate systems and the image processing techniques used to evaluate the needle tip pose with respect to the fixed reference frame ( $\Psi_0$ ). The fixed reference frame ( $\Psi_0$ ) is located at the entry point of the needle in the soft-tissue phantom. Frame ( $\Psi_n$ ) is fixed at the needle insertion device end-effector. Frame ( $\Psi_p$ ) is fixed at the ultrasound transducer end-effector. Frame ( $\Psi_t$ ) is located at the needle tip, while frame ( $\Psi_t$ ) is located at the needle tip as determined by the tracking algorithm. The aberration in transducer position along the insertion axis ( $x$ -axis of frame ( $\Psi_0$ )) is given by  $\pm\lambda$ . The perpendicular placed 2D ultrasound transducer provides a radial cross-sectional view of the needle which is affected by the comet tail artifact (CTA). An image processing methodology is used to evaluate the needle centroid location in the ultrasound image frame ( $\Psi_u$ ). (a) A median filter is applied to suppress speckle in the ultrasound image. (b) Thresholding is performed to obtain a binary image. (c) Erosion and subsequently dilation is applied to remove the remaining speckle. (d) A feature extraction algorithm based on Hough transform is applied to determine a line segment denoted  $\overline{AB}$  to describe the needle with CTA. (e) The needle centroid  $(y_c, z_c)$  is evaluated as the circle, from  $A$  which represents a point on the surface of the needle in the direction of  $B$  at a distance equal to the radius of the needle.

The 2D ultrasound transducer needs to compensate for needle tip motion along the  $x$ -axis of frame ( $\Psi_0$ ). A positioning device is used to control the ultrasound transducer. The positioning device moves the transducer corresponding to the needle motion to provide ultrasound images of the needle tip during insertion. This allows the needle tip pose to be expressed in the fixed reference frame using a series of coordinate transformations between frames ( $\Psi_u$ ,  $\Psi_p$  and  $\Psi_0$ ). Further details regarding coordinate transformations and control of the transducer motion are presented in the work of Vrooijink *et al.* [124]. The tracking algorithm is evaluated in gelatin phantoms and the mean errors of the needle tip position along  $X$ -,  $Y$ - and  $Z$ -axes (frame ( $\Psi_0$ )) are 0.64 mm, 0.25 mm and 0.27 mm, respectively, using insertion velocities between 1 – 5 mm/s.

### 5.3 Three-dimensional needle path planning and control

The tracking algorithm determines the needle tip location for feedback to the control system. The control system incorporates a path planning algorithm to generate the optimal needle trajectory towards the target. In the current section, we describe the 3D path planning and control algorithms.

## 5. EXPERIMENTAL EVALUATION OF ULTRASOUND-GUIDED 3D NEEDLE STEERING IN BIOLOGICAL TISSUE

---

### 5.3.1 Path planning

We use a 3D path planning algorithm to enable the needle to reach a target while avoiding obstacles in a 3D environment [121]. Using feedback from ultrasound imaging, the system steers the needle to approximately track the planned path using the control algorithm described in Section 5.3.2.

For path planning, the system uses a customized RRT, a sampling-based method for path planning [125]. The main advantage of using an RRT is that our implementation is fast enough for real-time path planning during insertion if the needle is inserted with the insertion velocities used in clinical applications (0.4 – 10 mm/s) [88]. To enable fast performance, our path planner makes use of reachability-guided sampling for efficient expansion of the rapidly-exploring search tree [40]. We also relax the constraint of constant-curvature needle trajectories by assuming that the controller can realize bounded-curvature needle trajectories by alternating the bevel tip direction. These customizations help us to reduce the computational time compared to prior sampling-based planners and make the path planner suitable for closed-loop needle steering [120]. We refer the reader to Patil *et al.* for additional details on the planning algorithm [121].

Given pre-operative medical images, the clinician can specify the insertion location, the target location, and the geometry of obstacles, which can include sensitive structures such as glands or blood vessels as well as impenetrable structures such as bones. After specifying the entire environment, the path planner computes a path that (1) reaches the target, and (2) is feasible, i.e., avoids obstacles. The output of the path planning algorithm is a sequence of milestones along the path defined at 6 mm intervals. The control algorithm discussed in Section 5.3.2 begins by steering the needle toward the first milestone along the path. As soon as a milestone is reached, the control algorithm steers the needle toward the next milestone along the path.

Since the obstacles or target may move during the procedure, the system operates in a closed-loop fashion by replanning every second. At each replanning step, a path is computed from the needle pose that is estimated by the needle tip tracking algorithm. The path planner also uses the actual positions of the target and the obstacles at each replanning step. After a new plan is computed, the method updates the milestones used by the control algorithm.

### 5.3.2 Control algorithm

We assume that the needle moves along a circular path during insertion based on the bevel direction [27, 74]. Axially rotating the needle about its insertion axis adjusts the tip orientation to control the direction of insertion. This rotation enables the control algorithm to direct the tip towards a target.

The control algorithm guides the needle toward the planned path’s next milestone, which we refer to in this paragraph as the target of the control algorithm. The frame  $(\Psi_t)$  is attached to the needle tip (Fig. 5.4(a)). Unless otherwise stated all variables are expressed in frame  $(\Psi_t)$ . The needle tip position  $(\mathbf{p}_{\text{tip}}^0 \in \mathbb{R}^{3 \times 1})$  and orientation  $(\mathbf{R}_{\text{tip}}^0 \in \mathbb{R}^{3 \times 3})$  with respect to the global coordinate frame  $(\Psi_0)$  are obtained using the needle tip tracking algorithm (Section 5.2). The target position is set to be a static

### 5.3 Three-dimensional needle path planning and control

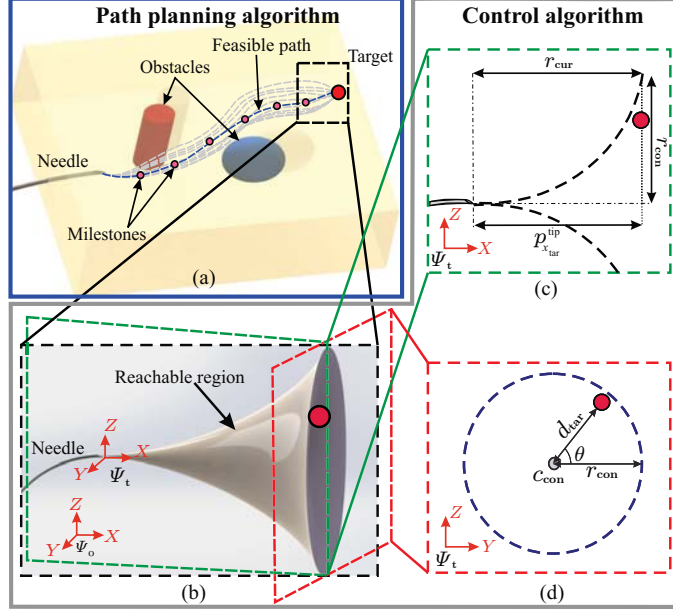


**Fig. 5.4:** (a) The path planning algorithm generates a feasible path by exploring the state space using a rapidly exploring random tree. The path planner generates milestones along the path, and the control algorithm steers the needle from milestone to milestone to reach the target. (b) In the control algorithm, the region the needle tip can reach is represented by a three-dimensional conical shape. The frame  $(\Psi_t)$  is attached to the needle tip, and the needle insertion starts in the  $X$ -direction. The area of the control circle (with center  $c_{con}$ ) intersects the target and is perpendicular to the  $X$ -axis (frame  $(\Psi_t)$ ). (c) The radius ( $r_{con}$ ) is determined using the radius of curvature ( $r_{cur}$ ) of the needle and the distance ( $p_{x_{tar}}^{tip}$ ) between the tip and target along the  $X$ -axis. (d) The needle rotates about its axis by angle ( $\theta$ ) if the distance ( $d_{tar}$ ) between  $c_{con}$  and target is larger than or equal to  $r_{con}$ .

or a moving point in 3D space. The target position ( $\mathbf{p}_{tar}^{tip} \in \mathbb{R}^{3 \times 1}$ ) with respect to frame  $(\Psi_t)$  is  $\mathbf{p}_{tar}^{tip} = \begin{bmatrix} p_{x_{tar}}^{tip} & p_{y_{tar}}^{tip} & p_{z_{tar}}^{tip} \end{bmatrix}^T$ , where  $p_{x_{tar}}^{tip}$ ,  $p_{y_{tar}}^{tip}$  and  $p_{z_{tar}}^{tip}$  represent the target positions along the  $X$ -,  $Y$ - and  $Z$ -axes, respectively. In Fig. 5.4(a), the conical shape represents the region that the needle can reach during insertion. The plane containing the control circle with center ( $c_{con}$ ) intersects the target and lies on the plane perpendicular to the  $X$ -axis. The radius ( $r_{con}$ ) of the control circle is calculated using  $r_{con} = r_{cur} - \sqrt{r_{cur}^2 - (p_{x_{tar}}^{tip})^2}$ , where  $r_{cur}$  is the radius of curvature of the needle path (Fig. 5.4(b)), and it is obtained experimentally. The distance between  $c_{con}$  and the target position ( $d_{tar}$ ) in  $YZ$ -plane (Fig. 5.4(c)) is determined from trigonometry. As the needle moves towards the target during insertion, the radius ( $r_{con}$ ) decreases. The needle will rotate about its axis if the target intersects the circumference of the control circle ( $d_{tar} \geq r_{con}$ ) to keep the needle in the reachable region. The needle rotates by the angle ( $\theta$ ) to direct the needle tip towards the target (Fig. 5.4(c)). The control algorithm updates the value of  $\theta$  every 40 ms.

Additional details concerning the control algorithm are presented in the work of

## 5. EXPERIMENTAL EVALUATION OF ULTRASOUND-GUIDED 3D NEEDLE STEERING IN BIOLOGICAL TISSUE

---

Abayazid *et al.* [112]. The control algorithm is validated experimentally, as demonstrated in the following section.

### 5.4 Experiments

In this section, we present the experimental setup used to insert the needle into the soft-tissue, the experimental plan, and the results.

#### 5.4.1 Setup

The experimental setup is divided into two parts. First, the insertion device allows the needle to be inserted and rotated about its axis. The details of the needle insertion device are presented in previous work [91]. Second, a transducer control device that permits the ultrasound transducer to move in three degrees of freedom, as shown in Fig. 5.1. The 18 MHz transducer (18L6 HD with a mean ultrasound beam width of 0.4 mm) is connected to a Siemens Acuson S2000 ultrasound machine (Siemens AG, Erlangen, Germany). Additional information about the transducer control device is presented by Vrooijink *et al.* [124].

The needle is inserted into a soft-tissue phantom made up of a gelatin mixture [112]. Silica powder is added to the mixture to mimic the acoustic scattering of human tissue. The flexible needle is made of Nitinol alloy (nickel and titanium). The Nitinol needle has a diameter of 0.5 mm with a bevel angle (at the tip) of 30°.

#### 5.4.2 Results

In the current section, different experimental scenarios are conducted to evaluate the performance of the proposed needle tracking, path planning and control algorithms. The needle radius of curvature in the phantom is determined empirically (270 mm) [112]. A safety margin is added to the needle curvature value to compensate for variations or disturbances that may take place during insertion. The needle is inserted with a velocity of 1 mm/s. Each experimental case is performed five times. The experimental cases are depicted in Fig. 5.5.

In Case 1 and Case 2, the steering algorithm controls the needle to reach a stationary and a moving virtual target, respectively (no path planning is applied) (Fig. 5.5(a) and (b)). In Case 3 and Case 4, path planning is applied pre-operatively to generate the optimal trajectory between the needle tip and the target. In Case 3, virtual obstacles used while in Case 4, real obstacles are embedded into the gelatin phantom. The real obstacles are 3D-printed plastic shapes (Fig. 5.5(d)). The phantom is scanned pre-operatively to localize the real obstacles in the soft-tissue phantom. The obstacles appear dark in the ultrasound image frames. The images are inverted and a threshold is set to obtain a binary image. The location of the obstacle is determined by calculating the centroid of the white region in each image frame (obstacle after inversion) and then along the frames that include the obstacle. The obtained obstacle location is exported to the path planning algorithm. Our system assumes that the shape of obstacles are recognized by the planner, which requires segmenting obstacles in pre-operative medical

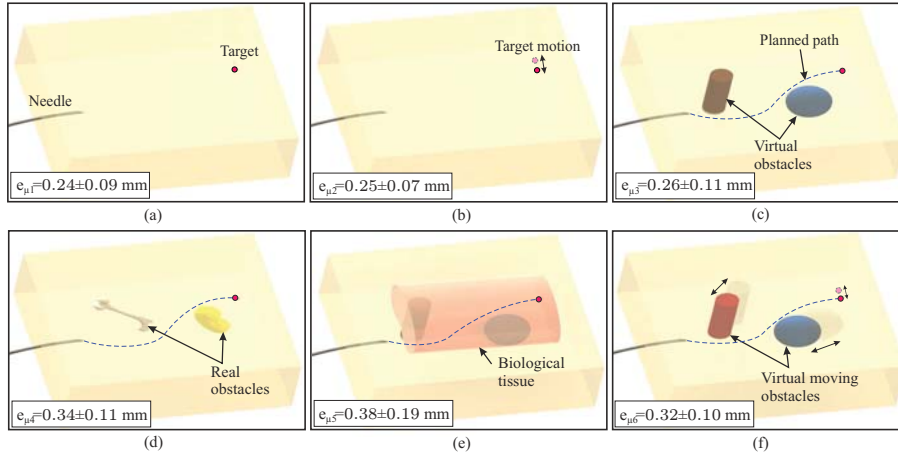


**Fig. 5.5:** The experimental cases. (a) Case 1: the needle is steered towards a stationary virtual target using a random path. (b) Case 2: the needle is steered towards a moving virtual target using a random path. (c) Case 3: the needle moves along a planned path to avoid virtual obstacles and reach a stationary virtual target in a gelatin phantom. (d) Case 4: the needle moves along a planned path to avoid real obstacles and reach a stationary virtual target. (e) Case 5: the needle moves along a planned path to avoid obstacles and reach a stationary virtual target in biological tissue (chicken breast). (f) Case 6: the needle moves along a planned path to avoid two moving obstacles and reach a moving virtual target. The mean targeting error (absolute distance between the needle tip and the target position at the end of insertion) of Case  $i$  is  $e_{\mu i}$ , where  $i = 1, 2, 3, 4, 5$  and 6. The planned path is updated every second.

imaging. The segmentations can be produced manually by a physician (for fixed obstacles) or automatically using segmentation software. (We note that automatic segmentation is a challenging problem that is actively being studied and is beyond the scope of this work.) The steering algorithm moves the needle along the generated path to avoid the obstacles and reach the target using milestones (Fig. 5.5(c) and (d)). In Case 5, the needle is steered towards a virtual target in biological tissue embedded in a gelatin phantom while avoiding virtual obstacles as shown in the lower inset in Fig. 5.1 and Fig. 5.5(e). In Case 6, the virtual target moves away from the needle tip in the direction of the needle orientation with a velocity of 0.125 mm/s. This results in a target motion of 10 mm. The target moves in the direction of needle insertion to simulate the effect of tissue deformation caused by the needle compression on the surrounding tissue. The path is updated every second to avoid the moving obstacles and reach the moving target. The obstacles move in the direction of the needle path with a velocity of 0.06 mm/s (Fig. 5.5(f)). The targeting error is the absolute distance between the target position that is pre-defined and needle tip position obtained from the needle tracking algorithm described in Section 5.2. The mean targeting errors for all experimental cases are provided in Fig. 5.5. *Please refer to the accompanying video<sup>6</sup> that demonstrates the experiments.*

<sup>6</sup>Video link: <https://goo.gl/MV4n1h>

## 5. EXPERIMENTAL EVALUATION OF ULTRASOUND-GUIDED 3D NEEDLE STEERING IN BIOLOGICAL TISSUE

---

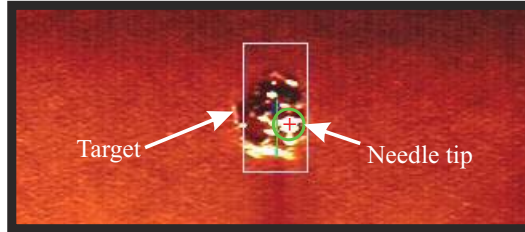


**Fig. 5.6:** The ultrasound image shows a cross-section of the target ( $\phi$  6 mm) embedded in a soft-tissue phantom at the end of the needle insertion, and the tip penetrating the target.

### 5.5 Discussion

This study combines a 3D real-time ultrasound-based needle tracking with path planning and control algorithms. These algorithms are used to accurately steer bevel-tipped flexible needles towards stationary and moving targets while avoiding virtual and real obstacles. The main advantage of the proposed control algorithm is that the needle rotates only when a change of the direction of insertion is required. This reduces the number of full rotations of the needle, and thus has the potential to reduce patient trauma [36]. In the implementation of the control algorithm, the needle can rotate in both directions to reduce the angle of rotation. The reduction of rotation angle suppresses the effect of torsion along the needle shaft which reduces the error between its orientation at the tip and base. Experiments were also performed using duty-cycling algorithm and compared to the proposed control algorithm to estimate its influence on the number of needle rotations (tissue damage). For the same insertion distance and path planner settings, the duty-cycling control algorithm required 51 complete rotations of the needle, while the proposed algorithm performed the procedure with just 11 complete rotations.

Experiments are performed to evaluate the targeting accuracy of the proposed system. Six experimental cases are performed to validate the tracking, path planning and control algorithms. The needle is steered in gelatin phantom and biological tissue. The needle visibility in ultrasound images is deteriorated due to shadows surrounding the solid obstacles during insertion, and this affects the targeting accuracy in Case 4. The targeting error increases while steering in biological tissue (Case 5) due to tissue inhomogeneity. This causes variation in the needle behavior during insertion. The experimental results show that the mean targeting error ranges between  $0.24 \pm 0.09$  mm and  $0.38 \pm 0.19$  mm. An extra experiment is conducted to validate the proposed system using a real  $\phi$  6 mm target made of an aqueous solution of 20 wt.% polyvinyl alcohol (PVA) (Sigma-Aldrich Chemie B.V., Zwijndrecht, The Netherlands). This experiment is performed five times, and the insertion distance ranges between 86 and 102 mm. The target and the obstacle are stationary, and their positions are determined using a pre-operative ultrasound scan. The needle tip reaches the target in each experimental trial. Fig. 5.6 shows a representative ultrasound image of the cross-section of the target penetrated by the needle tip.

The needle insertions performed in the current study are conducted in an experimental environment where the needle is inserted into a static phantom that contains

two types of materials (gelatin and chicken breast tissue). In a clinical environment, we expect more variables that may reduce the targeting accuracy such as physiological motion, fluid flow and tissue inhomogeneity. Further improvements are required to bring the system to the clinical practice. In future work, the ultrasound needle tracking device will be adapted to track the needle tip while scanning curved surfaces. A technique should also be developed for 3D reconstruction of the shape of targets and obstacles pre-operatively and then tracking of real targets and obstacles in real-time during insertion into biological tissue in order to improve the targeting accuracy. The steering system can be extended to detect the patient movements that occur during needle insertion such as respiration and fluid flow. A model should be developed to estimate the needle curvature in different heterogeneous tissue for accurate targeting. Real-time shared control between the steering algorithm and the operator will be established to achieve a practical system for clinical operations.

## **5. EXPERIMENTAL EVALUATION OF ULTRASOUND-GUIDED 3D NEEDLE STEERING IN BIOLOGICAL TISSUE**

---

## Part III

# Steering in Phantoms with Non-Uniform Surfaces



# *Preface*

## **Steering in Phantoms with Non-Uniform Surfaces**

The system presented in the previous part (Part II) can accurately steer the needle in flat and uniform soft-tissue phantoms. In clinical needle interventions, the needle can be inserted in curved and multi-layer soft-tissue phantoms such as breast and prostate, respectively. In this part, we introduce a robot that allows the ultrasound transducer to keep contact with soft-tissue phantoms with non-uniform surfaces (Chapter 6). This robot is used to apply pre-operative scans for target and obstacle localization and shape reconstruction, and consequently intra-operative scans for needle tracking during steering towards the localized target. In Chapter 7, we focus on a specific clinical application which is needle insertion in prostate. In this application, the needle is inserted into an environment with different geometry and tissue elasticity properties such as rectal wall, bladder and prostate. The geometry of the different tissues is determined using magnetic resonance images of human organs surrounding the prostate while their elasticities are obtained using a non-invasive ultrasound-based (acoustic radiation force impulse imaging) technique. We investigate the effect of different tissue layers on the needle behavior during insertion and consider that in the steering system. Steering experiments are then performed while varying the needle insertion angle, phantom inclination and skin thickness to evaluate the system.

This part is based on the previously published versions of the following manuscripts:  
**Chapter 6:** M. Abayazid, P. Morriera, N. Shahriari, S. Patil, R. Alterovitz and S. Misra, “Ultrasound-guided three-dimensional needle steering in biological tissue with curved surfaces”, *Medical Engineering & Physics*, vol. 37, issue 1, pp. 145-150, 2015.  
**Chapter 7:** M. Abayazid, N. Shahriari and S. Misra, “Three-dimensional needle steering towards a localized target in a prostate phantom”, in *Proceedings of the IEEE RAS & EMBS International Conference on Biomedical Robotics and Biomechatronics (BioRob)*, pp. 7-12, Sao Paulo, Brazil, August 2014.

---

## 6

# Ultrasound-Guided Three-Dimensional Needle Steering in Biological Tissue with Curved Surfaces

### Abstract

In this chapter, we present a system capable of automatically steering a bevel-tipped flexible needle under ultrasound guidance towards a physical target while avoiding a physical obstacle embedded in gelatin phantoms and biological tissue with curved surfaces. An ultrasound pre-operative scan is performed for three-dimensional (3D) target localization and shape reconstruction. A controller based on implicit force control is developed to align the transducer with curved surfaces to assure the maximum contact area, and thus obtain an image of sufficient quality. We experimentally investigate the effect of needle insertion system parameters such as insertion speed, needle diameter and bevel angle on target motion to adjust the parameters that minimize the target motion during insertion. A fast sampling-based path planner is used to compute and periodically update a feasible path to the target that avoids obstacles. We present experimental results for target reconstruction and needle insertion procedures in gelatin-based phantoms and biological tissue. Mean targeting errors of  $1.46 \pm 0.37$  mm,  $1.29 \pm 0.29$  mm and  $1.82 \pm 0.58$  mm are obtained for phantoms with inclined, curved and combined (inclined and curved) surfaces, respectively, for insertion distance of 86-103 mm. The achieved targeting errors suggest that our approach is sufficient for targeting lesions of 3 mm radius that can be detected using clinical ultrasound imaging systems.

## 6. ULTRASOUND-GUIDED THREE-DIMENSIONAL NEEDLE STEERING IN BIOLOGICAL TISSUE WITH CURVED SURFACES

---

### 6.1 Introduction

Needle insertion into soft-tissue is a minimally invasive procedure used for diagnostic and therapeutic purposes such as biopsy and brachytherapy, respectively. In the current study, we present an image-guided robotic system that scans the soft-tissue phantom with a curved surface to localize the target and reconstruct its shape, pre-operatively. The image-guided robotic system then steers the needle to reach the localized target position while avoiding obstacles (Fig. 6.1). Two-dimensional (2D) and three-dimensional (3D) ultrasound imaging were used to localize the target and the needle during needle insertion [126]. The ultrasound transducer used for visualization of the needle and target needs to be controlled in order to scan the curved surface of the soft-tissue phantom. An algorithm based on implicit force control is proposed to move a transducer over a curved surface to maximize contact surface area for improved needle and target visualization.

The effect of system parameters on needle deflect and target movement during biopsy were investigated in several studies [69, 127, 128, 129]. These parameters include needle diameter, insertion speed and bevel angle. Prior to needle insertion, these parameters can be set to minimize the target movement during insertion and consequently, improve the targeting accuracy.

#### 6.1.1 Related work

In previous studies, robotic systems have been used to control the ultrasound transducer for scanning [130, 131, 132, 133]. An example of an early study that explores the advantage of robotic ultrasound systems for scanning curved surfaces is the development of *Hippocrate*, a robot arm for medical applications with force feedback [134]. One of the applications of *Hippocrate* is the manipulation of an ultrasound transducer on a patient's skin in an automatic manner while maintaining a constant exerted force. The ultrasound images are used to reconstruct the 3D profile of arteries. The same robot has been used in studies of Krupa *et al.* that investigated an ultrasound-based visual servoing system [135, 136]. Abolmaesumi *et al.* developed a tele-operated ultrasound system that allows the radiologist to view and manipulate the ultrasound transducer at remote site, while being assisted by force and image servo controllers [137]. Javier *et al.* developed an ultrasound system to 3D reconstruct the shape of *in-vitro* stenoses using an industrial robotic arm with force feedback [138]. Nadeau *et al.* presented a hybrid visual/force control to automatically align the transducer and keep the ultrasound image static even in the presence of physiological motion disturbances [139]. Besides proper contact force, the alignment/orientation of the ultrasound transducer is important to maintain the image quality. This alignment can be achieved by visual servoing [135] and also by force/torque control. However, the presented scanning systems require a pre-determined transducer path. This means that any deformation or change in the path causes scanning inaccuracies and consequently, errors in needle steering.

Flexible needles are used to steer around sensitive and hard tissue such as blood vessels and bones, respectively [25, 37, 38]. Such needles are fabricated with an asymmetric tip (bevel tip) that naturally deflect during insertion into soft-tissue [27]. The needle deflection due to its tip-asymmetry is used to steer the needle towards a certain

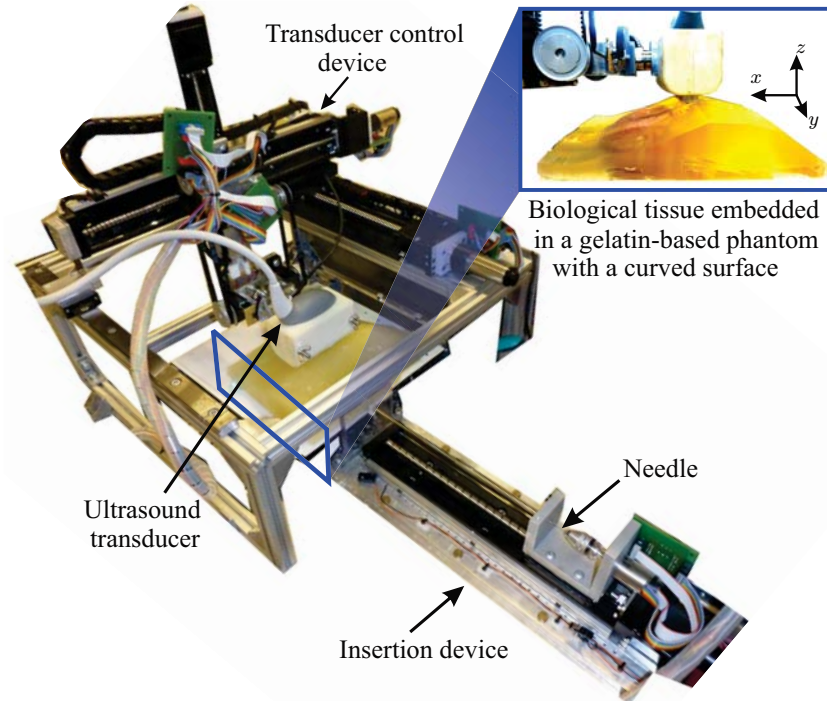


**Fig. 6.1:** The experimental setup used for needle insertion into a soft-tissue phantom that includes biological tissue (chicken breast tissue) with a curved surface. The inset shows an ultrasound transducer moving over a curved surface.

target position [6, 37]. In previous studies, control algorithms were developed for needle steering in 2D space. DiMaio and Salcudean presented a path planning and control algorithm that related the needle motion at the base (outside the soft-tissue phantom) to the tip motion inside the tissue [66]. Abayazid *et al.* presented a 2D ultrasound image-guided steering algorithm, and a 3D steering algorithm where they used Fiber Bragg Grating sensors for feedback [91, 112]. Several 3D path planning algorithms have been introduced that are based on Rapidly-exploring Random Trees (RRTs) [120, 121]. Our approach integrates the algorithm presented by Patil *et al.* to quickly compute feasible, collision-free paths in 3D-space [121].

### 6.1.2 Contributions

In the current study, we introduce a complete system where we scan a curved (breast-like) soft-tissue phantom to localize the target and obstacle positions, and also reconstruct the target shape. In previous studies, the ultrasound-guided steering experiments were performed on soft-tissue phantoms with flat surfaces but this is not the case in many needle insertion procedures such as breast biopsy [140, 141]. In the current study, a robot is used to control the ultrasound transducer to keep contact between the transducer and the curved surface of the soft-tissue phantom using force feedback. We then

## 6. ULTRASOUND-GUIDED THREE-DIMENSIONAL NEEDLE STEERING IN BIOLOGICAL TISSUE WITH CURVED SURFACES

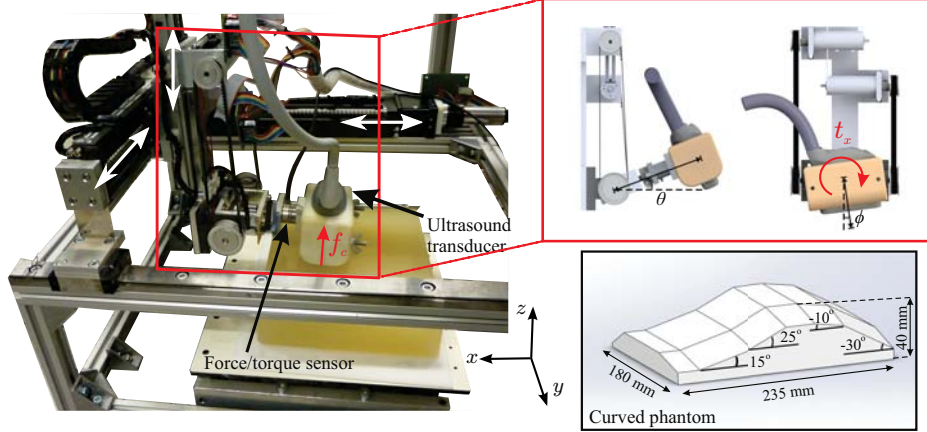


**Fig. 6.2:** Ultrasound transducer positioning device with a 2 degrees-of-freedom rotational mechanism. The positioning device provides movements in  $x$ -,  $y$ - and  $z$ -axis and the rotation mechanism allows for pitch ( $\theta$ ) and roll ( $\phi$ ) movements. The force/torque sensor is attached to the rotational mechanism to measure the contact force ( $f_c$ ) and the torque ( $t_x$ ) round the  $x$ -axis. The geometry of the curved phantom consists of different inclination angles. The dimensions of the cuboidal flat phantom are  $230 \times 148 \times 48 \text{ mm}^3$ .

integrate 3D tracking, path planning and control algorithms to steer a bevel-tipped flexible needle in a curved phantom to reach the localized target in 3D-space while avoiding a physical obstacle. Before conducting the insertion experiments, we investigate experimentally the effect of system parameters on target movement in biological tissue. The parameters include the needle insertion speed, bevel angle, needle diameter, skin thickness, target distance and target size. The results of this study is used to select the system parameters that reduce the target motion to minimize the targeting error while steering the needle. The algorithms are validated by conducting insertion experiments into a soft-tissue phantom and biological tissue (*ex vivo* chicken breast tissue) while avoiding a physical obstacle. To the best of our knowledge, the use of 3D ultrasound tracking combined with 3D path planning for needle steering towards a target and avoiding physical obstacles in a curved phantom has not been demonstrated.

### 6.2 Ultrasound scanning over curved surfaces

In this section, we present a method for ultrasound scanning of phantoms with curved surfaces. The scan is performed in steps using an ultrasound transducer. The target location is estimated using the ultrasound images that are captured at the end of each scanning step. Proper contact between the ultrasound transducer and the phantom surface is crucial for generating ultrasound images. A five degrees-of-freedom (DOF) device is designed in order to properly scan curved surfaces using a 2D ultrasound transducer. The system is an extension of the 3DOF Cartesian transducer positioning device presented by Vrooijink *et al.* [124]. In this study, a rotational mechanism is attached to the previous device in order to include two more DOF (Fig. 6.2).

### 6.2.1 Mechanical design

The ultrasound positioning device is augmented with a 2-DOF rotational mechanism. The mechanism design allows the transducer to roll and pitch using differential gears (Fig. 6.2). The midpoint of the transducer contact surface is assumed to be the end-effector of the system. The rotational mechanism is actuated by two ECTMax22 motors with GP22 gear head (Maxon Motor, Sachseln, Switzerland), which are controlled by Elmo Whistle 2.5/60 motor controller (Elmo Motion Control Ltd, Petach-Tikva, Israel). The system has a force/torque sensor (ATI Nano-17, Industrial Automation, USA) to measure the contact forces applied to the transducer. The force measurements are used to align the transducer contact surface with the curved phantom surface.

### 6.2.2 Alignment control algorithm

A controller based on implicit force control [142], is developed to align the transducer with the phantom surface. The alignment control is important to assure the maximum contact area between the transducer and the phantom. The alignment control is done in three steps as described in Algorithm 1, where  $f_{ref-c}$  is the reference contact force,  $f_c$  is the exerted contact force,  $\mathbf{f}_{ref}$  is the vector with reference forces (which is non-zero only in the contact normal direction),  $\mathbf{f}_s$  is the vector force measured by the force/torque sensor,  $a$  is a constant,  $\mathbf{K}_f$  is the controller gain,  $\mathbf{v}_e$  is the end-effector velocity,  $\mathbf{J}^\dagger$  is the pseudo-inverse of the Jacobian of the robot and  $\dot{\mathbf{q}}$  is the joint velocities. First, the transducer moves vertically downward until it gets in contact with the phantom with a reference contact force of 3 N. This reference force guarantees proper ultrasound images [143]. The alignment control loop keeps the exerted force constant using the implicit force control algorithm described in Algorithm 1. The Cartesian transducer velocities ( $\mathbf{v}_e$ ) are defined by the force error ( $\mathbf{f}_s - \mathbf{f}_{ref}$ ) multiplied by the controller gain ( $\mathbf{K}_f$ ). The joint velocities of the rotational mechanism ( $\dot{\mathbf{q}}$ ) are then calculated using the pseudo-inverse of the Jacobian ( $\mathbf{J}^\dagger$ ). After aligning the transducer, the ultrasound image and the transducer pose are saved in order to be used as an input to the target localization algorithm. Finally, the transducer is moved forward a step of 0.4 mm in the scan direction, and again the control loop is executed. This step length is set to be equal to the thickness of the ultrasound image plane in order to prevent overlap or loss of ultrasound image data. The outputs of the alignment control algorithm are sequence of ultrasound image frames and the corresponding transducer pose at each step. The mean error of the alignment angle of the ultrasound transducer is  $0.67 \pm 0.33^\circ$ . The detailed experimental evaluation and validation of the alignment control algorithm using force feedback are presented in [143].

### 6.2.3 Target localization and shape reconstruction

The set of ultrasound images and the corresponding transducer poses while capturing the images are processed offline to determine the target location and reconstruct its 3D shape (Fig. 6.3). First, each image is inverted and has its contrast enhanced by a contrast-limited adaptive histogram equalization. The images are then converted to a binary image based on a threshold value. The image is morphologically closed

## 6. ULTRASOUND-GUIDED THREE-DIMENSIONAL NEEDLE STEERING IN BIOLOGICAL TISSUE WITH CURVED SURFACES

---



---

**Algorithm 1** Transducer alignment control during the scan

---

```

while  $f_c \neq f_{ref-c}$  do
  if  $f_s > f_{ref}$  then
    moveup()
  else
    movedown()
  end if
end while
{Starting the scan with N steps}
for  $i = 0 : N$  do
  while  $f_c < f_{ref-c} - a$  or  $f_{ref-c} + a < f_c$  do
     $\mathbf{v}_e = \mathbf{K}_f(\mathbf{f}_s - \mathbf{f}_{ref})$  {End-effector velocity is defined by the force error}
     $\dot{\mathbf{q}} = \mathbf{J}^\dagger \mathbf{v}_e$  {Transform end-effector velocities to joint velocities}
    SendVelocityCommand( $\dot{\mathbf{q}}$ ) {send the velocity commands to the robot}
  end while
  GetUltrasoundImage() {Save the ultrasound image}
  GetTransducerPose() {Save the transducer pose}
  MoveTransducer(StepSize) {move the transducer in the scan direction}
end for

```

---

resulting in the segmented cross-sectional view of the target. The center of mass of this segmented target area is computed for each image and the average of all centers of mass is defined as the target center of mass. The target surface is reconstructed using the contour points of the segmented images. The volume that this surface comprises is used to calculate the corresponding diameter. The target reconstruction is evaluated using the Mean Absolute Distance (MAD) [144] and target shape is assumed to be an ideal sphere. The location of the reconstructed target is used as an input to the control algorithm to steer the needle towards the target.

### 6.3 Ultrasound-guided needle steering

The ultrasound-based needle tracking algorithm provides the needle control algorithm with the tip position during insertion. The needle tracker used for feedback is based on the method presented by Vrooijink *et al.* [124]. The tracker is modified to allow the ultrasound probe to scan curved surfaces. The ultrasound image should visualize the needle tip, and the image plane should be always perpendicular to the needle insertion axis. This is achieved by moving the transducer with variable velocities to keep the needle tip in the image. The transducer orientation is kept constant by controlling the position of pitch and roll angles (Fig. 6.2). An implicit force control is implemented to keep the transducer orthogonal to the needle insertion axis and to properly adjust the probe position over the curved surface during the insertion. The desired probe velocity

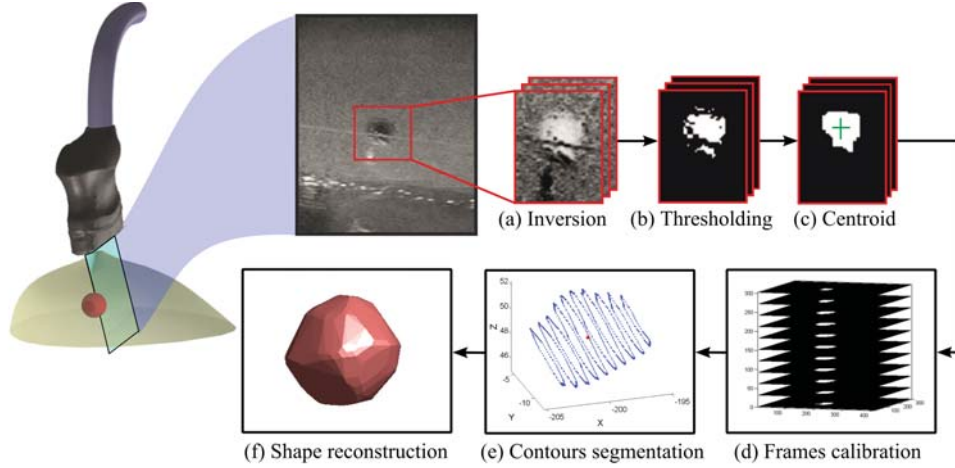


**Fig. 6.3:** Target localization and reconstruction. (a) The image is inverted and the contrast is enhanced by transforming the values using contrast-limited adaptive histogram equalization. (b) The image is converted to a binary image based on threshold. (c) Small pixel groups are removed and the image is morphologically closed resulting in the final segmented image. (d) The binary images are stacked together based on the position and orientation of the probe while acquiring each image frame. (e) The centroid of the target volume is calculated using all image frames that include the target. (f) The target surface is reconstructed using the contour points of the segmented images.

in  $z$ -axis ( $v_z$ ) is defined as

$$v_z = k(f_d - f_c), \quad (6.1)$$

where  $k$  is the feedback gain,  $f_d$  is the desired contact force and  $f_c$  is the exerted contact force. Constant contact force is essential to keep the needle tip visible in the ultrasound images while steering.

The bevel-tipped needle is assumed to move along a path composed of circular arcs during insertion [27, 74]. The needle path is computed by a path planner [121]. The planner is re-executed in a closed-loop manner using the tip pose estimated from the ultrasound imaging. The direction of the circular path depends on the orientation of the bevel tip. The bevel tip orientation is controlled by needle rotation about its insertion axis at the base. This rotation enables the needle to move along the planned path and reach the target position. Further details regarding the steering algorithm is presented in the work by Abayazid *et al.* [112].

## 6.4 Experimental results

This section presents the experimental setup used for target motion study, target reconstruction and needle steering. The aim of performing the target motion experiments is to determine the effect of needle parameters on target motion. The results are used to adjust the parameters to minimize the target motion during steering experiments. The

## 6. ULTRASOUND-GUIDED THREE-DIMENSIONAL NEEDLE STEERING IN BIOLOGICAL TISSUE WITH CURVED SURFACES

**Table 6.1:** Experimental plan for ultrasound measurements to investigate the effect of system parameters on target motion. Each experiment is repeated five times.

Experiment		Insertion speed (mm/s)					Bevel angle (°)			Needle diameter (mm)					Skin thickness (mm)			Target distance (mm)					Target diameter (mm)					
		1	4	10	20	30	30	45	60	0.5	0.75	1	1.25	1.5	0	0.8	1.6	10	20	30	40	50	3	4	6	8		
#1		✓	✓	✓	✓	✓	✓				✓				✓						✓			✓				
#2				✓			✓	✓			✓				✓						✓			✓				
#3				✓			✓			✓	✓				✓						✓			✓				
#4				✓			✓			✓	✓				✓						✓			✓				
#5				✓			✓			✓	✓				✓						✓			✓				
#6				✓			✓			✓	✓				✓						✓			✓				

System parameters

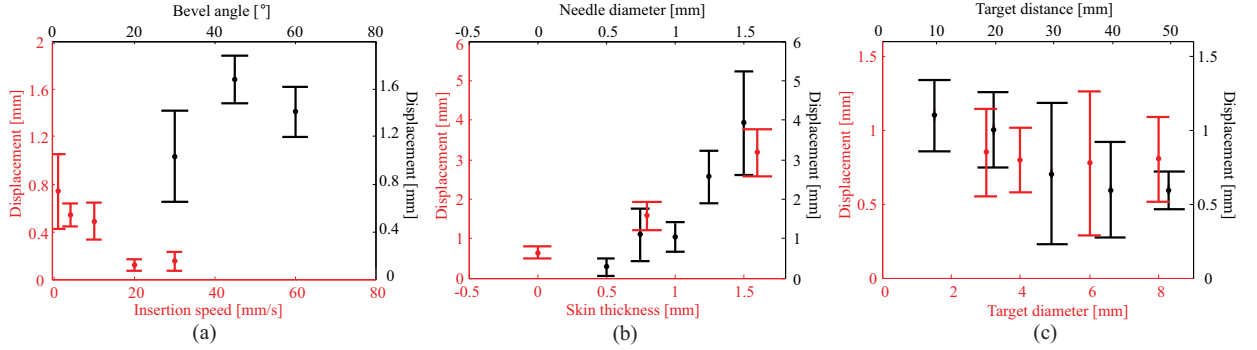


**Fig. 6.4:** Effect of system parameters (Table 6.1) on the absolute displacement of the target during needle insertion. (a) Needle insertion speed and bevel angle. (b) Skin thickness and needle diameter. (c) Target size and target distance.

results of the target reconstruction and steering experiments are also described in the current section.

#### 6.4.1 Experimental setup

The experimental setup consists of a needle insertion device and an ultrasound transducer positioning device (Fig. 6.1). The insertion device has two DOFs: Translation along and rotation about the needle insertion axis [91]. On the other hand, the positioning device has five DOFs and is designed to position an ultrasound transducer in 3D space [124]. The rotational mechanism with the force/torque sensor described in Section 6.2.1 to ensure having a sufficient ultrasound image quality.

#### 6.4.2 Effect of needle parameters on target motion

The experiments are performed in a biological tissue (*ex vivo* chicken breast tissue). The default parameters include a 1 mm diameter nitinol needle with a 30° bevel angle which is inserted 40 mm into the biological tissue with a velocity of 4 mm/s. A 4 mm diameter silicone target is embedded into the biological tissue phantom, which is the size of a clinically significant tumor [145]. The silicon target is made using two different gel components, Wacker SilGel 612A (Wacker Chemie AG, Germany) and Wacker SilGel 612B. The components are mixed in a 1.5:1 ratio and then cast into a mold. The needle is inserted until it hits the target but does not penetrate it. Every experiment is performed five times.

The experimental plan is presented in Table 6.1 and results are presented in Fig. 6.4. The results show that increasing the insertion speed (between 1 mm/s and 30 mm/s) and target distance (between 10 mm and 50 mm) cause decrease in the target motion by 0.73 mm and 0.51 mm, respectively, while increasing the needle diameter (between 0.5 mm and 1.5 mm) and the skin thickness (between 0 mm and 1.6 mm) lead to increased target motion by 3.47 mm and 2.63 mm, respectively. Varying the target size or bevel angle does not influence the target motion.

## 6. ULTRASOUND-GUIDED THREE-DIMENSIONAL NEEDLE STEERING IN BIOLOGICAL TISSUE WITH CURVED SURFACES

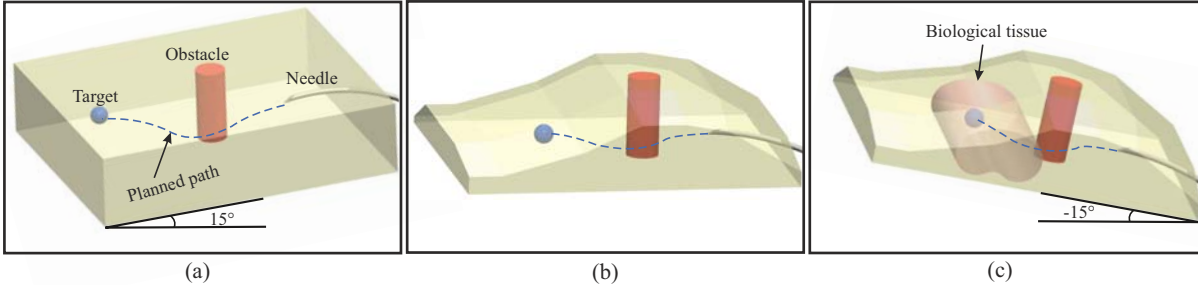


**Fig. 6.5:** Experimental cases. The steering algorithm controls the needle to avoid an obstacle reach a 3 mm radius target in a soft tissue phantom. (a) Case 1: The phantom is placed on an inclined surface. (b) Case 2: The phantom has a curved surface. (c) Case 3: The target is embedded in biological tissue. The biological tissue is embedded into a curved gelatin phantom placed on an inclined surface.

### 6.4.3 Needle steering results

The needle parameters are selected based on the results presented in Section 6.4.2. A 0.5 mm diameter nitinol needle is used during the experiments as it minimizes the target motion. The bevel angle does not affect the target motion. A  $30^\circ$  bevel angle is used to increase the needle curvature and the steering capabilities of the needle [64]. The effect of needle insertion velocity on target motion is not significant as varying the insertion speed from 1 mm/s to 30 mm/s increases the target motion by less than 0.70 mm. In order to reduce the effect of delay of the steering system, we use 1 mm/s insertion velocity during the steering experiments. The target localization and shape reconstruction are determined by ultrasound scanning of the soft-tissue phantom surface before steering the needle (as described in Section 6.2.3).

#### 6.4.3.1 Experimental plan

Different experimental scenarios are conducted to evaluate the performance of the proposed target reconstruction, needle tracking, path planning and control algorithms. The needle radius of curvature (270 mm in the gelatin phantom), used as an input to the control algorithm, is determined empirically [112]. Closed-loop control corrects possible curvature deviations. The insertion distance ranges between 86 mm and 103 mm. Each experimental case is performed five times. Before every experiment the phantom is scanned to localize the 3 mm radius target and reconstruct its shape.

In Case 1, the steering algorithm controls the needle to avoid a cylindrical obstacle of 7.5 mm radius and reach the target in a soft tissue phantom with a flat surface. The phantom is placed on an inclined surface (Fig. 6.5(a)). In Case 2, the needle is steered to avoid the obstacle and reach the target embedded in a phantom with a curved surface (Fig. 6.5(b)). In Case 3, the needle is steered to avoid the obstacle and reach the target in biological tissue. The biological tissue is embedded into a curved gelatin phantom placed on an inclined surface (Fig. 6.5(c)).

**Table 6.2:** The results of target reconstruction and steering experiments. The target reconstruction is evaluated using the Mean Absolute Distance (MAD) geometric comparison method [144] assuming that the actual target shape is spherical (3 mm radius). The targeting error is the absolute distance between the target and needle tip at the end of insertion. Each experiment is performed five times.

Cases	Target reconstruction		Needle steering
	Radius (mm)	MAD (mm)	Targeting error (mm)
Case 1	2.88±0.07	0.36±0.05	1.46±0.37
Case 2	2.90±0.18	0.38±0.03	1.29±0.29
Case 3	2.95±0.06	0.47±0.06	1.82±0.58

### 6.4.3.2 Results

The target reconstruction is evaluated using the MAD method and target shape is assumed to be an ideal sphere of 3 mm radius. The results of the MAD evaluation method and target radius obtained using the reconstruction algorithm are presented in Table 6.2.

In the steering experimental cases presented in Fig. 6.5, the error is defined as the absolute distance between the tip and the center of the target that is localized pre-operatively. The experimental results for the experimental cases are also presented in Table 6.2. The needle tip reaches the target in each experimental trial. The maximum targeting error is 1.82 mm, and it is noted in Case 3. On the other hand, the minimum targeting error is 1.29 mm, and it is observed in Case 2. The results show that the targeting error increases while steering in biological tissue due to its inhomogeneity. The inhomogeneity of the biological tissue causes deviation of the needle from its circular path. *Please refer to the accompanying video<sup>7</sup> as supplementary material that demonstrates the experimental procedure and results.*

## 6.5 Conclusions and recommendations

This study introduces a complete steering system that combines pre-operative 3D target localization and shape reconstruction algorithms with intra-operative path planning and ultrasound-guided control algorithms to steer a bevel tip needle towards a physical target while avoiding a physical obstacle in soft-tissue phantoms. The effect of system parameters such as insertion speed, needle diameter and bevel angle on target motion during needle insertion are investigated experimentally. The results of this study can be used to improve target motion models and hence improve steering and path planning.

---

<sup>7</sup>Video link: <http://goo.gl/LxhjuV>

## 6. ULTRASOUND-GUIDED THREE-DIMENSIONAL NEEDLE STEERING IN BIOLOGICAL TISSUE WITH CURVED SURFACES

---

An algorithm is developed using feedback from a force/torque sensor to keep the ultrasound transducer in contact with phantom surface to ensure sufficient images during the insertion procedure. Three experimental cases are performed to validate the steering system in soft-tissue phantoms and biological tissue (chicken breast) with inclined and curved surfaces. The phantom is scanned before every experimental trial to localize the target and reconstruct its shape. The reconstruction evaluation method (MAD) results for the three experimental cases are  $0.36\pm 0.05$  mm,  $0.38\pm 0.03$  mm and  $0.47\pm 0.06$  mm, respectively. The steering experimental results show that needle reaches the target in each experimental trial and the mean targeting errors range between  $1.29\pm 0.29$  mm and  $1.82\pm 0.58$  mm.

Further improvements are required to bring the system to the clinical practice. A technique should also be developed for 3D reconstruction of different irregular target and obstacle shapes, and a model should be developed to estimate their deformation intra-operatively. In future work, the ultrasound needle tracking device will be adapted to track target position during insertion. The steering system can be extended to detect the patient movements that occur during needle insertion such as respiration and fluid flow. Real-time shared control between the steering algorithm and the operator will be established to achieve a practical system for clinical operations.

# Needle Steering Towards a Localized Target in a Prostate Phantom

## Abstract

Prostate biopsy and brachytherapy are commonly used for surgical interventions. In this chapter, we present a three-dimensional (3D) pre-operative target localization algorithm and a real-time closed-loop control algorithm to robotically steer flexible needles with an asymmetric tip towards a real target in a prostate phantom. The phantom is composed of different tissues including rectal wall, bladder and prostate. The elasticities of these tissues are obtained using an ultrasound-based (acoustic radiation force impulse imaging) technique, and their geometry are obtained using magnetic resonance images. Six experimental cases are performed to evaluate the steering system while inserting the needle into a prostate phantom with different skin thicknesses, insertion angles and surface inclinations. The experimental results show that the target is reached by the needle in all trials. The mean targeting errors between the needle tip and the center of the target embedded in phantoms with 0 mm, 1.5 mm and 2.5 mm skin thicknesses are 1.12 mm, 0.93 mm and 0.49 mm, respectively. The variation of the insertion angle does not have an appreciable affect on the targeting accuracy. The mean targeting error during insertion into a phantom with an inclined surface is 0.85 mm. The results demonstrate the capability of proposed system to robotically steer needles towards a target for interventions in the prostate.

## 7. NEEDLE STEERING TOWARDS A LOCALIZED TARGET IN A PROSTATE PHANTOM

---

### 7.1 Introduction

Percutaneous needle insertion procedures such as biopsy and brachytherapy are frequently used to detect and treat prostate cancer, respectively [146]. In both procedures, an accurate tip placement is important for successful diagnosis and treatment. The prostate is small, located within the pelvic cavity, and surrounded by critical structures, e.g., nerve bundles and blood vessels. The volume of the prostate is approximately  $40 \text{ mm} \times 20 \text{ mm} \times 20 \text{ mm}$  [147]. Thus, physicians have to carefully maneuver the needle around the critical structures in order to obtain tissue samples or deliver radioactive seeds during biopsy or brachytherapy procedures, respectively. A robotic system can aid the physicians to accurately target a suspected lesion during the procedure. Such systems require target localization, and also a control algorithm to steer the needle towards the target (lesion).

In this study, we present an ultrasound-based system that scans a soft-tissue phantom to localize the target in three-dimensional (3D)-space, and then a control algorithm is used to accurately steer the needle towards the localized target. The needle is inserted into a prostate phantom and the target is located within the prostate. Subsequently, the control algorithm can be used for steering. A method for needle control is to use its tip asymmetry (bevel tip) such as biopsy and brachytherapy needles [148]. Such a needle deflects naturally as it is inserted into soft tissue due to asymmetric forces applied on its tip. The curvature of the needle is dependent on the stiffness of the surrounding tissue.

Several research groups have used the bevel tip to steer flexible needles around obstacles in order to reach a target [27, 38, 62]. Webster *et al.* showed that non-holonomic kinematics of the unicycle and bicycle models can be used to predict needle path during the insertion into soft tissue [27]. Further, Abayazid *et al.* presented a two-dimensional (2D) ultrasound image-guided steering algorithm, and a 3D steering algorithm where they used both Fiber Bragg Grating sensors and ultrasound for feedback [91, 112, 140, 141]. Hauser *et al.* developed a 3D feedback controller that steers the needle along a helical path, although results were evaluated in simulation without physical experiments [93].

The proposed system is a step forward to achieve a clinically-viable robotic needle steering system. The anatomical regions of interest in the patient are acquired pre-operatively using ultrasound images. A needle guide is designed to adjust the insertion angle into tissue to facilitate the procedure for the clinician. The stiffness of different tissues are determined using an ultrasound-based acoustic radiation force impulse imaging (ARFI) technique [59]. Based on the images, the clinician identifies the target location and the stiffness of the region to predict the needle curvature in each region. The needle insertion procedure is autonomous under supervision of the clinician.

In the current study, we integrate the presented 3D tracking and control algorithms to steer a bevel-tipped flexible needle to reach a target in 3D space in a phantom. The phantom consists of different elasticities to mimic the properties of the tissues surrounding the target such as spine, adipose tissue, rectal wall, urinary bladder, prostate and pubic bone. This assists us to determine the effect of the tissue properties on needle deflection and the targeting accuracy during the insertion procedure. The needle is also inserted at different skin thicknesses, insertion angles and phantom inclinations

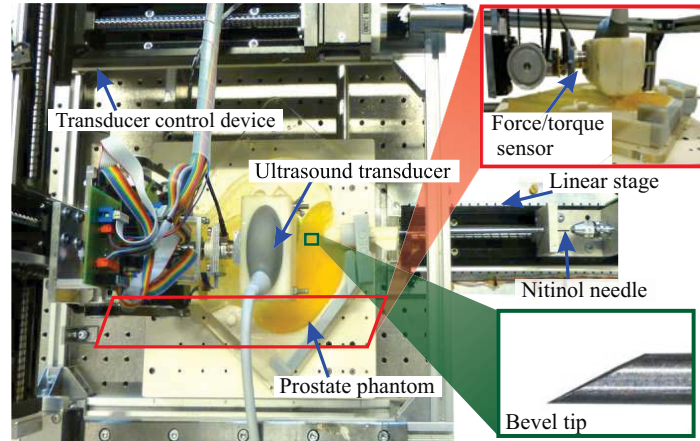


**Fig. 7.1:** The experimental setup: The setup consists of a needle insertion device to insert the bevel-tipped Nitinol needle into the soft-tissue phantom and an ultrasound control device for needle tracking. The top-right inset shows the force sensor used to keep the ultrasound probe in contact with the prostate phantom. The bottom-right inset shows the needle bevel tip.

to evaluate the accuracy of the steering system. The skin thickness in human ranges between 0.8 mm and 3 mm [54]. The needle guide is used to change the insertion angle. An alignment control algorithm is also developed in this study to maintain sufficient contact between the ultrasound transducer and the phantom at different surface inclinations. The alignment closed loop algorithm is based on force and torque feedback from a sensor attached to the transducer control robot (Fig. 7.1).

The novel aspect of our study is that we present a framework for 3D localization of the target pre-operatively. Consequently, the control algorithm steers the needle in a phantom with different skin thicknesses and elasticities, and thus different needle curvatures toward the localized target. The framework combines both target localization and control algorithms with an ultrasound-based tip tracking algorithm to steer the needle in a soft-tissue phantom with different elasticities towards a target. Such a framework can be used for intra-operative control of needle insertion during prostate interventions (biopsy and brachytherapy). In this study, magnetic resonance (MR) images are also used to develop the anatomically accurate phantom. To the best of our knowledge, the usage of known medical imaging modalities (MR and ultrasound images), and control algorithm to steer a bevel-tipped needle towards a real target in has not been investigated.

This chapter is organized as follows: The experimental setup is presented in Section 7.2. Descriptions of the control algorithm for 3D needle steering, target localization and transducer alignment are also presented in Section 7.2. Section 7.3 describes the experimental results. Section 7.4 concludes the results and shows directions for future work.

## 7. NEEDLE STEERING TOWARDS A LOCALIZED TARGET IN A PROSTATE PHANTOM

---

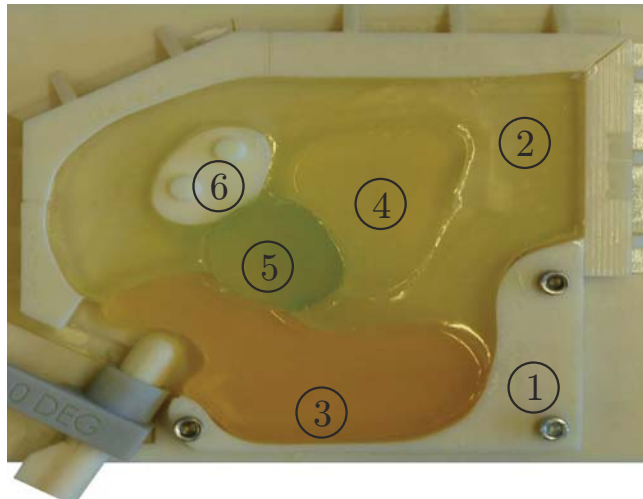


**Fig. 7.2:** The phantom that incorporates the anatomy of the male pelvic region. The anatomy is coloured for clarity. ①: Spine, ②: Adipose tissue (fat), ③: Rectal wall, ④: Urinary bladder, ⑤: Prostate and ⑥: Pubic bone.

### 7.2 Methods

First, in Section 7.2.1, details of the experimental setup are presented. Subsequently, in Section 7.2.2 presents the control algorithm that utilizes ultrasound images for tip tracking.

#### 7.2.1 Experimental setup

The experimental setup consists of a needle insertion device, an ultrasound transducer positioning device and a needle guide holder (Fig. 7.1). The insertion device has two degrees-of-freedom (DOFs): Translation along and rotation about the needle insertion axis [91]. On the other hand, the positioning device has three DOFs and is designed to position an ultrasound transducer in 3D space [124]. A force/torque sensor (ATI Nano-17, Industrial Automation, USA) is attached to the positioning device to measure the contact forces applied. The force measurements are used to align the transducer contact with the phantom surface to ensure having a sufficient ultrasound image quality. The guide holder is used to move the needle guide along the insertion axis. This movement of the needle guide results in the deformation of a phantom that incorporates the anatomy of the male pelvic region, i.e., prostate and surrounding structures that support it (Fig. 7.2). The needle is made of a Nitinol wire of 0.5 mm diameter and 30° bevel tip.

The 3D model of the phantom is developed from a series of anatomically accurate MR images and using commercial software ScanIP (Simpleware Ltd, Exeter, UK) and SolidWorks 3D Computer Aided Design (CAD) software (Dassault Systèmes SolidWorks Corp., Concord, USA) [151]. Further, the phantom is made using a gelatin mixture (Dr. Oetker, Bielefeld, Germany). The compositional percentage of gelatin in the mixture is varied in order to manufacture a phantom with different elasticities.

**Table 7.1:** Elasticities of the prostate and its surrounding tissue.  $E_L$  represents the elasticities of various soft tissue reported in literature [149, 150].  $E_{\text{exp}}$  is calculated using an ultrasound-based acoustic radiation force impulse imaging technique based on the shear wave velocity in the phantom [110]. For the spine and pubic bone,  $E_{\text{exp}}$  is the elasticity of Verowhite–Fullcure830.

Item # (Fig. 7.2)	Soft tissue	$E_L$ (kPa)	$E_{\text{exp}}$ (kPa)
2	Adipose tissue (fat)	10.24	10.63
3	Rectal wall	191.72	172.61
4	Urinary bladder	96.87	100.38
5	Prostate	60.50	65.89
1 and 6	Spine and pubic bone	$1.82 \times 10^6$	$2.50 \times 10^3$

The elasticities of the phantom are calculated using the shear wave velocity in the phantom, and also verified using dynamic mechanical analysis. Measurement of the shear wave velocity in the phantom is done using an ultrasound-based ARFI technique (Virtual Touch™ Tissue Quantification, Siemens AG Healthcare, Erlangen, Germany) [110]. The phantom is assumed to be isotropic and incompressible. Young’s modulus ( $E$ ) in different regions is calculated as,  $G = \rho v_s^2$ , where  $G$  and  $v_s$  are the shear modulus and the shear wave propagation velocity, respectively [59]. The density ( $\rho$ ) of the material is calculated from the mass and volume of the soft-tissue phantom and the target. Young’s modulus ( $E$ ) is calculated by,  $E = 2G(1 + \gamma)$ , where  $\gamma$  is Poisson’s ratio which is assumed to be 0.495. Siemens ACUSON S2000 system (Siemens AG, Erlangen, Germany) with a linear ultrasound transducer 18L6 is utilized to obtain ultrasound images and the transducer 9L4 is used to measure the shear wave velocity in the phantom. The spine and pubic bone (① and ⑥, Fig. 7.2, respectively) are made of VeroWhite - FullCure830 and printed with an Objet Eden250 3D printer (Objet Geometries Inc., Billerica, USA). Table 7.1 summarizes the elasticities calculated for the prostate and its surrounding structures (Fig. 7.2). The needle curvature varies during insertion into different tissue elasticities.

During needle insertion, the needle guide is pushed against the rectal wall (item ③, Fig. 7.2) using the needle guide holder. The control algorithm then steers the needle towards the predicted target location. The control algorithm uses ultrasound images for tip tracking. Both the control and tip tracking algorithms are described in Section 7.2.2.

## 7. NEEDLE STEERING TOWARDS A LOCALIZED TARGET IN A PROSTATE PHANTOM

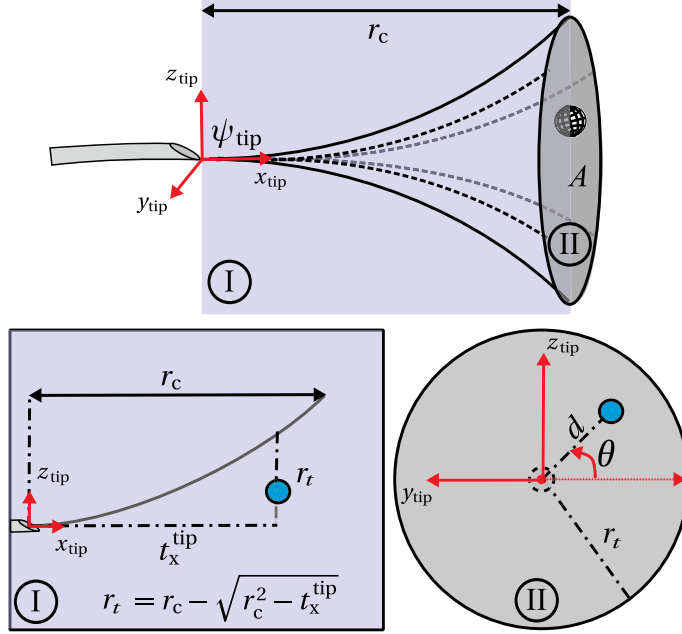


**Fig. 7.3:** Methods used for 3D needle steering. In the top figure,  $\psi_{\text{tip}}$  represents the frame attached at the tip while blue sphere represents the target. Further,  $r_c$  is defined as the radius of curvature of the circular path [27]. In inset (I),  $t_x^{\text{tip}}$  represents the distance between the plane of the control circle (plane A) and the origin of  $\psi_{\text{tip}}$ . On the other hand,  $r_t$  represents the radius of plane A. In inset (II),  $d$  and  $\theta$  represents the distance of target from the center of plane A and the angle of needle rotation, respectively. In both insets (I) and (II), blue circle represents the target. In inset (II), the gray circle at the center of the figure represents center of plane A.

### 7.2.2 Needle steering

The control algorithm for 3D needle steering estimates in real-time the region reachable by the needle. Assuming that the needle moves along a circular path during insertion [27], this region can be represented by a conical shape. Direction of the circular path depends on the bevel tip orientation, and this orientation is controlled by needle rotation about its insertion axis. This rotation enables 3D needle steering towards the target. The method used in the control algorithm is presented in Fig. 7.3.

The algorithm uses a frame of reference ( $\psi_{\text{tip}}$ ) attached at the tip. Further, the ultrasound-based tip tracking algorithm updates in real-time the changes in the pose (position and orientation) of  $\psi_{\text{tip}}$  with respect to a global frame. The target location with respect to the needle tip ( $\mathbf{p}_{\text{tar}}^{\text{tip}}$ ) is given by

$$\mathbf{p}_{\text{tar}}^{\text{tip}} = [t_x^{\text{tip}} \ t_y^{\text{tip}} \ t_z^{\text{tip}}]^T \quad (7.1)$$

where  $t_x^{\text{tip}}$ ,  $t_y^{\text{tip}}$ , and  $t_z^{\text{tip}}$  are the target location along the  $x_{\text{tip}}$ -,  $y_{\text{tip}}$ -, and  $z_{\text{tip}}$ -axis, respectively. Fig. 7.3 shows the conical region reachable by the needle, and the plane of the control circle (plane A). Plane A is parallel to the  $y_{\text{tip}}z_{\text{tip}}$ -plane of  $\psi_{\text{tip}}$ , and passes through the centroid of the target.

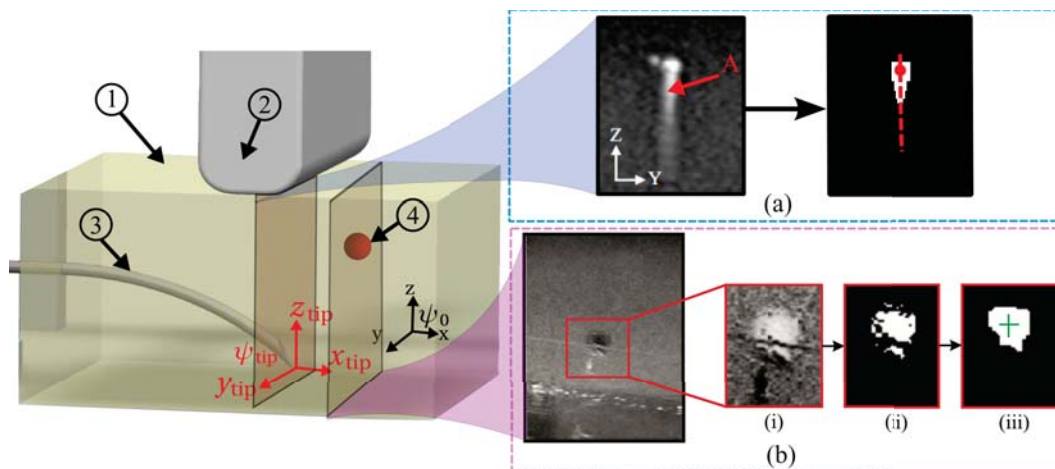


**Fig. 7.4:** A sketch of the setup for the tip tracking algorithm. ①: Phantom, ②: Transducer, ③: Needle, and ④: Target.  $\psi_{\text{tip}}$  and  $\psi_0$  are the tip and global frames, respectively. During needle insertion, the transducer is moved along needle insertion direction such that the tip is always in the field-of-view of the transducer. (a) Ultrasound image of the tip and the comet tail artifact (A). Image processing techniques (median blur, thresholding, erosion and dilation) are applied to increase the contrast between the needle and its surrounding. Hough transform is then used to extract features of the needle and artifact. Further, the artifact has a symmetry along the red dotted line. Finally, the centroid location of the needle is shown with a red dot [124]. (b) A cropped section of the target is used for further image processing. (i) The image is inverted and the contrast is enhanced by transforming the values using contrast-limited adaptive histogram equalization. (ii) The image is converted to a binary image based on threshold. (iii) Small pixel groups are removed and the image is morphologically closed resulting in the final segmented image.

The radius of plane  $A$  ( $r_t$ ) is calculated based on the radius of curvature of the needle path ( $r_c$ ) and  $t_x^{\text{tip}}$  (inset ①, Fig. 7.3). The radius ( $r_c$ ) is obtained empirically. Experiments are performed where the needle is inserted without rotation into a soft-tissue phantom that mimics the elastic properties of the rectal wall and the prostate. The needle path is then fitted to a circular curve and its radius is determined to obtain  $r_c$ . The distance between the target and the center of plane  $A$  is given by

$$d = \sqrt{(t_y^{\text{tip}})^2 + (t_z^{\text{tip}})^2} \quad (7.2)$$

During insertion,  $r_t$  decreases as the needle moves towards the target. This results in the target intersecting with the circumference of plane  $A$  ( $d \geq r_t$ ). At this instance, the needle is rotated in order to keep the needle in the reachable region. The angle of needle rotation ( $\theta$ ) directs the tip towards the target (inset ②, Fig. 7.3) and is given by

$$\theta = \tan^{-1} \left( \frac{t_z^{\text{tip}}}{t_y^{\text{tip}}} \right) \quad (7.3)$$

Using both the position and angle of needle rotation, the algorithm steers the needle towards the target. Additional details of the control algorithm for needle steering is presented in the work by Abayazid *et al.* [112].

## 7. NEEDLE STEERING TOWARDS A LOCALIZED TARGET IN A PROSTATE PHANTOM

---

The tip tracking algorithm utilizes ultrasound images obtained using the 2D transducer. Initially, the transducer is positioned perpendicular with respect to the needle insertion direction (Fig. 7.4). During needle insertion, this transducer is moved along the needle path using the positioning device (item ②, Fig. 7.4) such that the tip is always in the field-of-view of the transducer. The displacement velocity of the transducer is related to the tip velocity along the  $x$ -axis of the global frame. Tip orientation about the  $x$ -axis is obtained from the needle insertion device with an assumption that no torsion occurs along the needle shaft during insertion. Using both tip location and orientation, the pose of  $\psi_{\text{tip}}$  with respect to the global frame is deduced.

In order to improve the accuracy of the tip tracking algorithm, a closed-loop controller is used to position the transducer during needle insertion. The controller is based on the proportional-derivative algorithm and it minimizes the error between the ultrasound scanning velocity and the needle insertion velocity at its tip which is obtained from the controller. Further, Kalman observer is also added to minimize the noise influence on the states of both tip location and velocity, and to predict the subsequent states based on the needle tip velocity [152].

Ultrasound images are also processed in real-time using basic image processing techniques such as median blur, thresholding, erosion and dilation. These techniques increase the contrast between the tip and surrounding phantom, preventing false tip detection. One point to note is that the difference in the acoustic impedance between the needle and the phantom results in a reverberation effect known as a comet tail artifact (A, Fig. 7.4(a)) [123]. Further, the artifact has a symmetry along a vertical center line (red dotted line, Fig. 7.4(a)) and its size changes during needle insertion.

In this study, Hough Transform is used to extract features of the needle and comet tail artifact [153]. The result of the Hough transform is the series of vertical lines that describe the boundaries of the needle and comet tail artifact. By using both the symmetry property of the artifact and the set of vertical lines, the line segment that describe the symmetry line of the needle with artifact can be deduced. Subsequently, the needle centroid location along this symmetry line can be computed. Further details of the tracking algorithm is presented in the work by Vrooijink *et al.* [124]. The pose of the needle tip and hence,  $\psi_{\text{tip}}$  can be determined up to an accuracy of 0.64 mm and 2.68°.

### 7.2.3 Alignment control algorithm

To find the position of the target and the needle with respect to the ultrasound transducer, a pre-scan is taken and then the acquired images are processed using Matlab (v8.2, Mathworks Inc., Natick, USA). During the scan, it is essential that the ultrasound probe be kept perpendicular and in contact with the prostate phantom to acquire visible ultrasound images. As a matter of fact, we have developed a controller based on implicit force control [154], to align the transducer face with the phantom surface.

As described in Algorithm 2, where  $\mathbf{f}_{ref}$  is the reference forces, which are all zero except for the contact direction,  $\mathbf{f}_s$  is the force measured by the force/torque sensor,  $\mathbf{a}$  is a constant,  $\mathbf{K}_f$  is the controller gain,  $\mathbf{v}_e$  is the end-effector velocity,  $\mathbf{J}^\dagger$  is the pseudo-inverse of robot Jacobian and  $\dot{\mathbf{q}}$  is the joint velocities, the alignment control

is done in three steps. First, the transducer is vertically moved until it is in contact with the phantom and the contact force is equal to the reference contact force defined by the user. The force control loop is then used to minimize the force error. Finally, the transducer is moved forward in the scan direction, and again the control loop is executed. At the end of each step the ultrasound image and the transducer pose are saved as an input to the target localization algorithm.

---

**Algorithm 2** Transducer alignment control during the scan

---

```

while  $\mathbf{f}_s \neq \mathbf{f}_{ref}$  do
  if  $\mathbf{f}_s > \mathbf{f}_{ref}$  then
    moveup()
  else
    movedown()
  end if
end while
{Starting the scan with N steps}
for  $i = 0 : N$  do
  while  $\mathbf{f}_s < \mathbf{f}_{ref} - a$  or  $\mathbf{f}_{ref} + a < \mathbf{f}_s$  do
     $\mathbf{v}_e = \mathbf{K}_f(\mathbf{f}_s - \mathbf{f}_{ref})$  {End-effector velocity is defined by force error}
     $\dot{\mathbf{q}} = \mathbf{J}^\dagger \mathbf{v}_e$  {Transform end-effector velocities to joint velocities}
    SendVelocityCommand( $\dot{\mathbf{q}}$ ) {send the velocity commands to the robot}
  end while
  MoveTransducer(StepSize) {move the transducer in the scan direction}
  GetUltrasoundImage() {Save the ultrasound image}
  GetTransducerPose() {Save the transducer pose}
end for

```

---

#### 7.2.4 Target localization

The set of ultrasound images captured during the scan are processed in order to define the target location (Fig. 7.4(b)-(i)). First, each image is inverted and has its contrast enhanced by a contrast-limited adaptive histogram equalization. The images are then converted to a binary image based on a threshold value (Fig. 7.4(b)-(ii)). The image is morphologically closed resulting in the segmented cross-sectional view of the target (Fig. 7.4(b)-(iii)). The center of mass of this segmented target area is computed for each image using image moments and the average of all centers of mass is defined as the target center of mass. The location of the target is used as an input to the control algorithm to steer the needle towards the target.

## 7.3 Experiments

In this section, the experimental plan is described and the validation results for target localization and needle steering algorithms are presented.

## 7. NEEDLE STEERING TOWARDS A LOCALIZED TARGET IN A PROSTATE PHANTOM

**Table 7.2:** Experimental plan.  $t$ : skin thickness,  $\beta$ : insertion angle and  $\gamma$ : surface inclination angle of the phantom. Each case is performed three times.

	$t$ (mm)			$\beta$ ( $^\circ$ )			$\gamma$ ( $^\circ$ )	
	0	1.5	2.5	0	5	-5	0	15
Case I	✓			✓			✓	
Case II		✓		✓			✓	
Case III			✓	✓			✓	
Case IV	✓				✓		✓	
Case V	✓					✓	✓	
Case VI	✓			✓				✓

### 7.3.1 Experimental plan

A  $\phi$  0.5 mm nitinol needle with  $30^\circ$  bevel angle is used during all the experiments. Different experimental scenarios are conducted to evaluate the performance of the proposed needle tracking and control algorithms. The needle radius of curvature, used as an input to the control algorithm varies depending on the tissue elasticity. The radius of curvature of the needle in the different tissues are determined empirically. The needle is inserted with a velocity of 1 mm/s and its rotational speed is 31.4 rad/s [88]. Each experimental case is performed three times. The targets are located at various locations in the prostate phantom (48-66 mm from the needle tip initial position). The needle penetrates the rectal wall (23 mm) and the prostate phantom during insertion. Before each experiment, the phantom is scanned to localize the target. The experimental cases are provided in Table 7.2 and depicted in Fig. 7.5.

Case I, Case II and Case III are performed to estimate the effect of skin thickness on the targeting accuracy. Silicone is used to mimic the elasticity of the skin layer (237 kPa) [129]. Case IV, Case V and Case VI evaluate the steering system with different insertion angles using the needle guide to increase the reachable region by the needle tip, and scanning phantoms with inclined surfaces.

### 7.3.2 Results

The error is defined as the absolute distance between the tip and the center of the target that is localized pre-operatively. The results for the six experimental cases are presented in Table 7.3. The needle tip reaches the target in each experimental trial. Ultrasound and camera images of the needle reaching the target are shown in Fig. 7.6. The maximum targeting error is 1.12 mm, and it is noted in Case I. On the other hand, the minimum targeting error is 0.49 mm, and it is observed in Case III. The results show that the targeting accuracy increases as the skin thickness increases from 0 mm to 2.5 mm. The skin layer is stiffer than the other tissues in the phantom, and it supports the needle at the insertion point, and consequently, reduces needle deviation. Based on the experimental results, it is found that the effect of changing the insertion angle and tissue inclination does not have an appreciable effect on the targeting accuracy. (See the accompanying video<sup>8</sup> as supplementary material that demonstrates the experimental results.)

<sup>8</sup>Video link: <https://goo.gl/MDe0Cp>

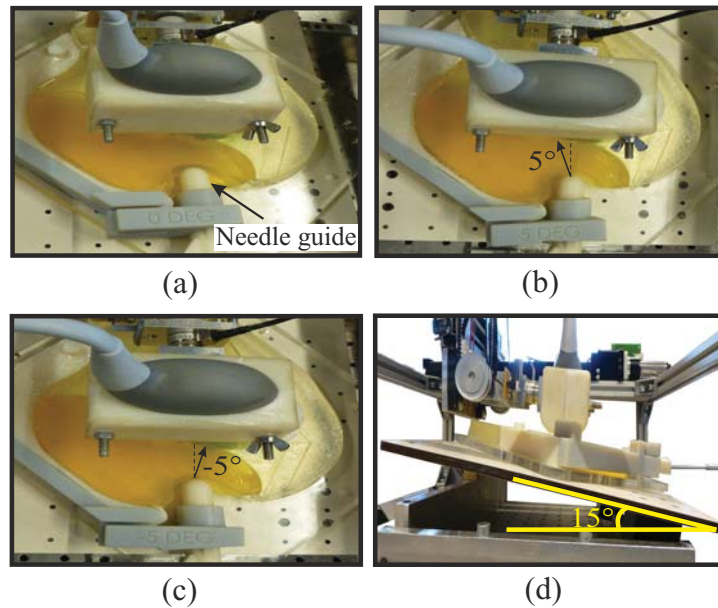


**Fig. 7.5:** In the experimental cases, the control algorithm steers the needle to reach a real target of  $\phi$  6 mm embedded in the prostate phantom. (a) In Case I, II and III, the needle is inserted with  $5^\circ$  angle into a prostate phantom with 0 mm, 1.5 mm and 2.5 mm skin thickness, respectively. (b) In Case IV, the needle is inserted with  $5^\circ$  angle into a prostate phantom with 0 mm skin thickness. (c) In Case V, the needle is inserted with  $-5^\circ$  angle into a prostate phantom with 0 mm skin thickness. (d) In Case VI (side-view), the needle is inserted with  $0^\circ$  angle into an inclined prostate phantom ( $15^\circ$ ) with 0 mm skin.

**Table 7.3:** The results of the experimental cases. The error is the absolute distance between the needle tip at the end of insertion and the center of the localized target, where the mean error ( $\mu$ ) and standard deviation ( $\sigma$ ) are presented in mm.

	Case I	Case II	Case III	Case IV	Case V	Case VI
$\mu$	1.12	0.93	0.49	0.64	0.75	0.85
$\sigma$	0.10	0.17	0.04	0.14	0.26	0.20

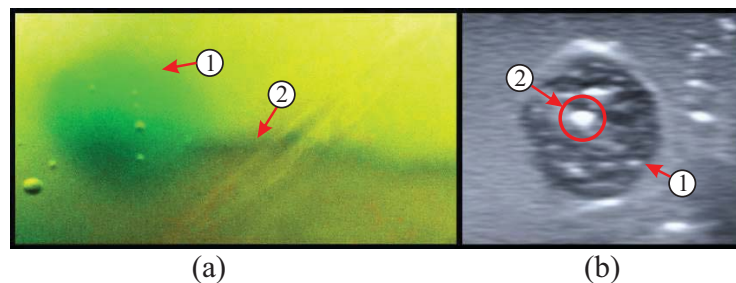


**Fig. 7.6:** The needle tip ① reaches the target ② (embedded in the prostate phantom) at the end of an insertion experiment as shown in (a) camera and (b) ultrasound images.

## 7. NEEDLE STEERING TOWARDS A LOCALIZED TARGET IN A PROSTATE PHANTOM

---

### 7.4 Conclusions and future work

This study combines pre-operative 3D target localization algorithm with a real-time ultrasound-based control algorithm to steer a bevel tip needle towards a real target embedded in a prostate phantom. The prostate phantom is made of different tissue elasticities (spine, adipose tissue, rectal wall, urinary bladder, prostate and pubic bone). The elasticities of these tissues are obtained using ARFI technique and their geometries are obtained using MR images. An algorithm is developed using feedback from a force/-torque sensor to keep the ultrasound transducer in contact with the prostate phantom to ensure sufficient images during the insertion procedure. Six experimental cases are performed to validate the steering system using different skin thicknesses, insertion angles and inclined surfaces. The experimental results show that the mean targeting errors range between 0.49 mm and 1.12 mm. The targeting accuracy of the steering system is not drastically affected by changing the skin thickness, insertion angle and surface inclination as the target was reached during each experimental trial.

Further improvements are required to bring the system to the clinical practice. During minimally invasive interventions in the prostate, the pelvic bone may restrict the needle visibility in ultrasound images. Hence, advanced tracking algorithms using existing clinical imaging modalities need to be developed to obtain the 3D needle tip position during insertion. In future work, the ultrasound needle tracking device will be adapted to track the needle tip while scanning curved surfaces. A technique should also be developed for 3D reconstruction of the shape of targets and obstacles pre-operatively and then tracking of targets and obstacles in real-time during insertion in order to improve the targeting accuracy. The steering system can be extended to detect the patient movements that occur during needle insertion such as respiration and fluid flow. Real-time shared control between the steering algorithm and the operator will be established to achieve a practical system for clinical operations.

## Part IV

# Towards Clinical Practice



# *Preface*

## **Towards Clinical Practice**

In previous chapters, we could achieve high steering accuracy using an automated robotic system. In order to bring the developed steering system to clinical practice, we need to consider some practical issues such as acceptance by the clinical community and using clinically-approved devices. Fully automated systems are not desirable by the clinical community. For this reason, we propose a system that enables clinicians to directly control the insertion procedure while receiving navigation feedback from the control algorithm (Chapter 8). The ultrasound-guided control algorithm computes the optimal needle orientation during the insertion, but it does not directly control the needle's motion. Navigation cues about the computed optimal orientation are provided through a combination of haptic (vibratory) and visual feedback to the operator who controls the needle for steering. In Chapter 9, we adapt the developed algorithms to be compatible with clinical environments by using clinically-approved devices. We replace the ultrasound transducer control device by a novel Automated Breast Volume Scanner (ABVS), which is used in clinical practice breast diagnosis. The ABVS transducer is used for pre-operative scanning of soft-tissue for target reconstruction and also intra-operatively for needle tip tracking during the steering process.

This part is based on accepted and under-review versions of the following manuscripts:

**Chapter 8:** M. Abayazid, C. Pacchierotti, P. Morriera, R. Alterovitz, D. Prattichizzo, and S. Misra, "Experimental evaluation of co-manipulated ultrasound-guided flexible needle steering", *International Journal of Medical Robotics and Computer Assisted Surgery*, 2015 (Accepted).

**Chapter 9:** M. Abayazid, P. Morriera, N. Shahriari, A. Zompas and S. Misra, "Reconstruction of 3d shapes and needle steering using automated breast volume scanner (ABVS)", *Journal of Medical Robotics Research*, 2015 (Under Review).

---

# Experimental Evaluation of Co-Manipulated Ultrasound-Guided Flexible Needle Steering

## Abstract

We present and evaluate a teleoperation system for bevel-tipped flexible needle steering. Robotic systems with autonomous control algorithms have been exploited as the main tool to achieve high accuracy and reliability. However for reasons of safety and acceptance by the surgical community, keeping the physician tightly in the loop is preferable. Our system uses a combination of ultrasound imaging, path planning, and control to compute the desired needle orientation during the insertion and intuitively passes this information to the operator, who teleoperates the motion of the needle's tip. Navigation cues about the computed orientation are provided through a combination of haptic (vibratory) and visual feedback to the operator who controls the slave robot to steer the needle. The targeting accuracy of several co-manipulation strategies were studied in four sets of experiments involving human subjects with clinical backgrounds. Experimental results show that receiving feedback regarding the desirable needle orientation improves the targeting accuracy with a factor of 9 with respect to manual insertions.

## 8.1 Introduction

Needle insertion into soft-tissue is a minimally invasive procedure used for diagnostic and therapeutic purposes. Examples of diagnostic needle insertion procedures are liver, kidney and lung biopsies to detect tumors [7]. Therapeutic applications of needle insertion include brachytherapy of cervical, prostate, breast cancers, and also thermal ablation

## 8. EXPERIMENTAL EVALUATION OF CO-MANIPULATED ULTRASOUND-GUIDED FLEXIBLE NEEDLE STEERING

---

therapies such as cryotherapy [9]. Imaging modalities such as ultrasound, magnetic resonance (MR), and computed tomography (CT) are often used during needle insertion procedures to accurately determine the needle and target positions [10]. Inaccurate placement of the needle may result in misdiagnosis or unsuccessful treatment.

Flexible needles were introduced to provide enhanced steering capabilities, allowing the needle to avoid obstacles and accurately reach the target position [38]. Flexible needles fabricated with an asymmetric tip (e.g., bevel tip) naturally deflect during insertion into soft-tissue [27]. This can be exploited to make the needles move in non-straight paths and reach certain target positions [38]. The path of a bevel-tip steerable needle's tip in soft tissue can be predicted using the nonholonomic kinematics of a bicycle or unicycle model [27, 155]. The needle deflection can be also controlled using duty-cycling of the needle during insertion [34]. This approach varies the needle curvature by changing the ratio between the period of needle insertion with spinning to the total period of insertion.

Due to the nonholonomic kinematics, accurately steering an asymmetric-tip needle to a target is challenging [38]. Control algorithms can facilitate accurate needle placement. Several research groups have developed flexible needle deflection models for needle steering [38]. Hauser *et al.* developed a 3D feedback controller that steers the needle along a helical path, although results were evaluated only in simulation [93]. Furthermore, Abayazid *et al.* presented an autonomous two-dimensional (2D) ultrasound image-guided steering system, and a 3D robotic system where they used both Fiber Bragg Grating sensors and ultrasound for feedback [91, 112, 140].

In the aforementioned studies, the needle steering is performed autonomously and the operator does not intervene during insertion. The main advantage of autonomous robotic systems is providing a significantly higher accuracy with respect to that of manual insertions. However, autonomous systems are not currently widely accepted by the clinical community due to concerns about safety [156, 157]. For this reason, Hungr *et al.* developed an autonomous robotic system that switches to manual mode in case of predefined emergency conditions [158]. Majewicz and Okamura presented a teleoperated system where the operator commands the desired position in Cartesian space and the system provides force feedback that represents kinematic constraints and the position error of the robot. The evaluation of the system was based on simulations performed by an operator [159]. Romano *et al.* presented a robotic system where clinicians directly control the insertion and orientation of the needle using a 6-DOF haptic device [157]. Finally, other researchers guarantee the insertion system safety using force feedback techniques [160, 161].

### 8.1.1 Haptic feedback for shared control

Robotic teleoperation systems for medical procedures can enable high accuracy and repeatability while providing physicians with a level of manual control. Robotic teleoperation systems are composed of a slave robot, which interacts with a remote environment, and a master system, operated by a human (Fig. 8.1). The slave robot is in charge of reproducing the movements of the operator, who in turn, needs to observe the operative environment with which the robot is interacting. This is possible through

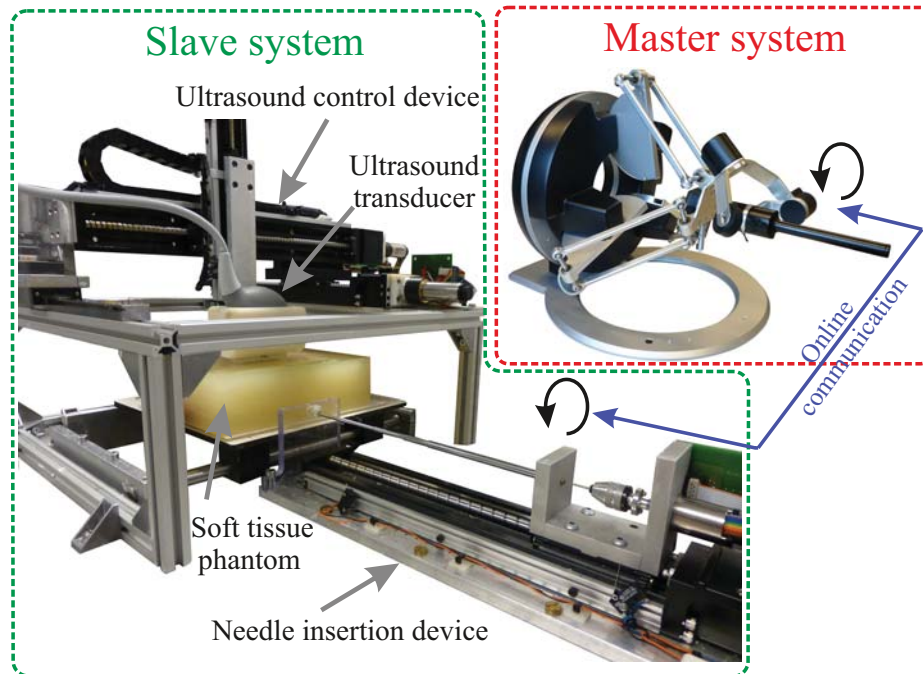


**Fig. 8.1:** The slave system includes the needle control device for needle insertion and rotation about its axis, and also the ultrasound control device used for three-dimensional needle tip tracking. The master system includes the haptic device that allows the operator to control the needle.

different types of information that flow from the remote scenario to the operator. They are usually a combination of visual and haptic stimuli. Visual feedback is already employed in commercial robotic surgery systems (e.g., the da Vinci Si Surgical System, Intuitive Surgical, Sunnyvale, CA, USA) while it is not common to find commercially-available devices implementing haptic force feedback. One of the few examples is the Sensei robotic catheter system (Hansen Medical, Mountain View, CA, USA).

However, haptic feedback is widely considered to be a valuable navigation tool during teleoperated surgical procedures [159, 162, 163]. It enhances clinicians' performance in terms of completion time of a given task [164], accuracy [165], peak and mean applied force [162, 164, 166]. In medicine, haptic feedback has been shown to improve performance in fine microneedle positioning [167], telerobotic catheter insertion [168], suturing simulation [169], cardiothoracic procedures [170], and cell injection systems [171]. Wagner *et al.* [166], for example, examined the effect of haptic force feedback on a blunt dissection task and showed that system performance improved up to 150% in comparison with providing no force feedback, while also decreasing the number of tissue damaging errors by over a factor of 3. Pacchierotti *et al.* presented preliminary results of a needle steering system that provides the operator with only vibratory feedback [172]. Experiments were performed using a limited number of subjects and no path planning was implemented for obstacle avoidance. Other studies have linked the lack of significant haptic feedback to increased intraoperative injury in minimally invasive surgery operations [173] and endoscopic surgical operations [174]. Moreover, haptic feedback can

## 8. EXPERIMENTAL EVALUATION OF CO-MANIPULATED ULTRASOUND-GUIDED FLEXIBLE NEEDLE STEERING

---

prevent undesirable trauma and incidental tissue damage, as it relays surgical tool-tissue interaction forces to the operator.

Haptic feedback can be also employed to *augment* the operating environment, providing additional valuable information to the operator, such as navigation cues. For example, Nakao *et al.* [175] presented a haptic navigation method that allows an operator to avoid collision with forbidden regions during surgery. It employs kinesthetic feedback through a 2D master manipulator. More recently, Ren *et al.* [176] implemented dynamic 3D virtual constraints with haptic and visual feedback during minimally invasive beating-heart procedures.

In addition to these approaches, which mostly involve kinesthetic force feedback, there is also a growing interest in *vibratory* feedback. Van Erp *et al.* [177], for instance, employed a vibrating waist belt to provide navigation information to the operator. Results indicated the usefulness of vibratory cues for navigation purposes as well as for situational awareness in multi-tasks environments. Lieberman *et al.* [178] presented a robotic suit for improved human motor learning. It provided vibratory feedback proportional to the error between the effective and learned motion. Schoonmaker and Cao [179] demonstrated that vibratory stimulation is a viable substitute for force feedback in minimally invasive surgery, enhancing operators' ability to control the forces applied to the tissue and differentiate its softness in a simulated tissue probing task. More recently, McMahan *et al.* [180] developed a sensing and actuating device for the da Vinci S Surgical System able to provide vibrotactile feedback of tool contact accelerations. Eleven surgeons tested the system and expressed a significant preference for the inclusion of vibratory feedback.

### 8.1.2 Contributions

In this study, we combine the advantages of manual steering with the high accuracy of autonomous (robotic) needle insertion. The proposed system enables operators to control the needle rotations while receiving navigation feedback from the path planning and control algorithms. In previous studies, haptic feedback was used mainly for avoiding collision, conveying kinematic constraints or sensing tissue stiffness [159, 162, 181]. To the best of our knowledge this is the first study to use vibratory and visual feedback to give the operator navigation cues using an ultrasound-guided system with an intra-operative path planner. Such types of feedback do not limit the operator's freedom of moving and controlling the haptic device as in the case of force feedback. We carry out several experiments that allow an operator to control the needle orientation using different combinations of visual and vibratory feedback as computed by the path planning and control algorithms. The subjects are provided with an online 3D view of the needle, target and obstacle positions to comprehend the system and its operating environment during the insertion procedure. The term "visual feedback" refers to the navigation cues, while the term "online 3D view" indicates displaying the overall operating environment.

We also attempt to employ subjects with a clinical background to be able to experimentally compare the case of manual control with the case of receiving navigation cues from the control algorithm under the same experimental conditions. This comparison will show the significance of using a co-manipulated needle steering system to

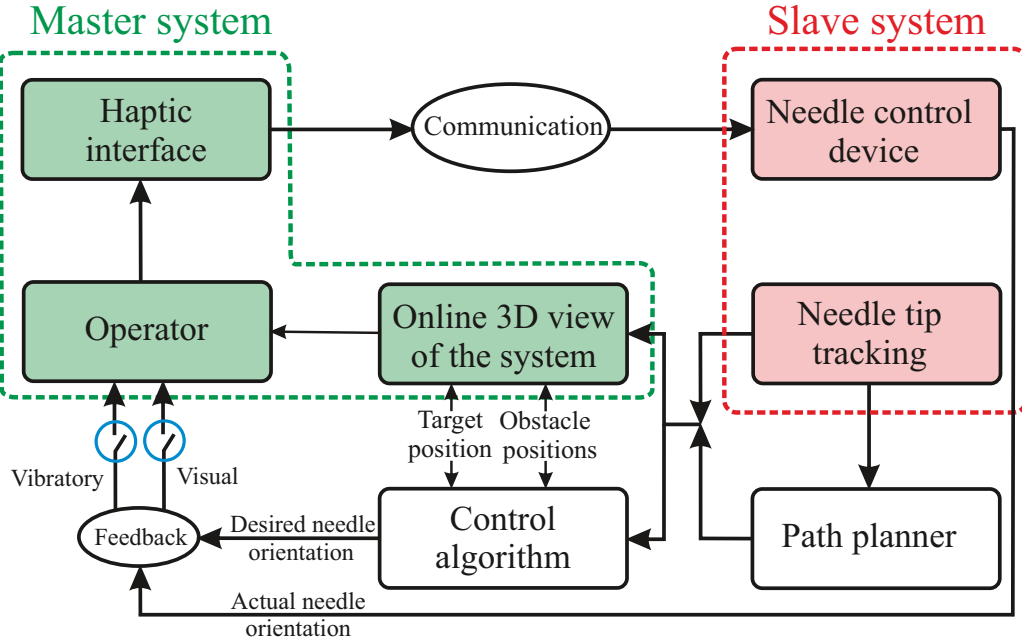


**Fig. 8.2:** Through the Omega 6 haptic device, the operator controls the motion of the slave robot and, thus, the needle. The needle tracking system provides the control algorithm and path planner with the needle tip pose. An online three-dimensional (3D) view of the needle path, position and orientation, together with the target and obstacles positions, is displayed to the operator on a computer screen. The control algorithm computes the desired needle orientation to allow the needle to move along the planned path. The difference between the actual and the desired needle orientations is provided to the operator with visual or vibratory feedback. The feedback system loops every 40 ms, and the planned path is updated every second.

improve the targeting accuracy. Different types of needle co-manipulation conditions, where the control algorithm assists the subject to steer the needle, are performed to assess which achieves the highest degree of accuracy and safety. The block diagram depicted in Fig. 8.2 shows the algorithms forming the steering system to highlight the main contributions of this study. In the current study, we combine teleoperated control with path planning to steer the needle towards a target while avoiding two obstacles.

## 8.2 Materials and methods

### 8.2.1 Slave system

The slave system includes the needle control device and the transducer control device. They are in charge of the needle tip tracking, control and path planning.

## 8. EXPERIMENTAL EVALUATION OF CO-MANIPULATED ULTRASOUND-GUIDED FLEXIBLE NEEDLE STEERING

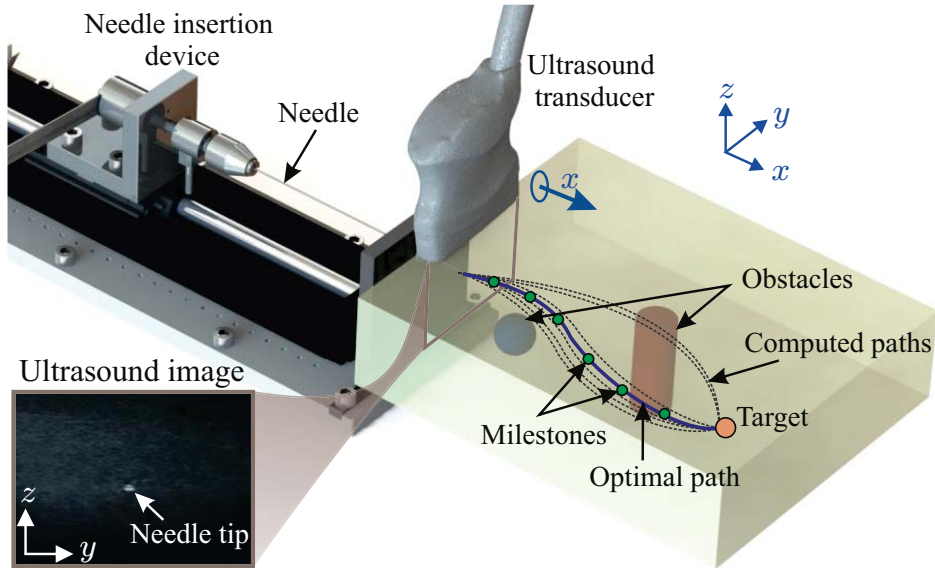


**Fig. 8.3:** The needle tip pose is determined in three-dimensional space using a two-dimensional ultrasound transducer positioned to visualize the needle tip where the ultrasound image plane is perpendicular to the needle insertion axis ( $x$ -axis). The path planning algorithm generates a feasible path by exploring the state space using a rapidly exploring random tree. The path planner generates milestones along the path, and the control algorithm steers the needle using the milestones to move along the planned trajectory.

### 8.2.1.1 Needle tip tracking

Ultrasound imaging is used to track the needle tip in 3D-space during insertion. The resolution of the obtained ultrasound image is 0.12 mm per pixel. A 2D ultrasound image plane is positioned perpendicular to the insertion direction at the needle tip (see Fig. 8.3). The transducer moves along the needle path during insertion to keep the tip in its field-of-view. It uses a closed loop control system based on a proportional-derivative algorithm that minimizes the error between the transducer scanning velocity and the needle insertion velocity, which is obtained from the slave robot's controller. Furthermore, a Kalman observer is implemented to minimize the influence of noise on the states of location and velocity of the needle tip and to predict subsequent states according to the needle tip velocity [152].

Finally, basic image processing techniques, such as median blur, thresholding, erosion and dilation are applied on ultrasound images intra-operatively. This increases the contrast between the tip and the surrounding phantom, preventing false tip detections. After that, the system computes the needle centroid location using image moments. The centroid represents the  $y - z$  coordinates of the needle tip as shown in Fig. 8.3 while the insertion ( $x$ ) coordinates are obtained from the motor encoders of the ultrasound transducer control device. The controller provides an accuracy in estimating the needle tip pose up to 0.64 mm and  $2.68^\circ$  for position and orientation, respectively. Further details on the tracking algorithm have been presented by Vrooijink *et al.* [141].

### 8.2.1.2 Path planning and control algorithms

We use a 3D path planning algorithm to generate a trajectory for the needle to reach a target while avoiding obstacles in a 3D environment [121, 182]. Using the information obtained from ultrasound images, the system provides the subjects with navigation cues to steer the needle along the planned path using the control algorithm. The needle path is planned using a customized version of the rapidly-exploring random tree (RRT) algorithm, which is a sampling-based method for path planning [125]. To enable fast performance, our path planner effectively utilizes the needle’s kinematics model and makes use of reachability-guided sampling for efficient expansion of the search tree. The planner is sufficiently fast that it can be executed in a closed-loop manner, updating the path every second. This closed-loop execution can enable the system to compensate for disturbances such as target and obstacle motions [140]. We refer the reader to Patil *et al.* for additional details on the planning algorithm [121].

Given pre-operative medical images, the operator can specify the insertion location, the target location, and the geometry of obstacles, which can include sensitive structures such as glands or blood vessels as well as impenetrable structures such as bones. After specifying the entire environment, the path planner computes a path that (1) reaches the target, and (2) is feasible, i.e., it avoids obstacles. The output of the path planning algorithm is a sequence of milestones along the path. The control algorithm computes the desired orientation that allows the subject to steer the needle towards the first milestone. As soon as a milestone is reached, the control algorithm computes the desired orientation to steer the needle towards the next milestone along the path.

The needle tip pose (position and orientation) obtained from the tracking algorithm is the main input of the control algorithm. First, the control algorithm estimates the region that the needle tip can reach during insertion. The controller then computes intra-operatively the needle tip desired orientation every 40 ms to follow the planned trajectory and reach the target. As mentioned before, the needle can be assumed to move along arcs during its insertion into a soft-tissue phantom [27]. The direction of each arc depends on the bevel tip orientation, which is controlled by rotating the needle about its insertion axis (Fig. 8.3). Additional details about the control algorithm can be found in the work of Abayazid *et al.* [91, 140].

## 8.2.2 Master system

The master system is responsible for both steering the slave robot and displaying navigation cues regarding the desired needle orientation. Navigation cues allow co-manipulation between the subject (operator) and robotic system for needle steering. In order to avoid confusion and consequent possible errors in the medical intervention, the meaning of such cues must be easy to understand.

In this study, we propose to provide the subject with (1) an online 3D view of the system that includes the needle path, needle tip location, obstacle locations and target location, and (2) visual and vibratory feedback about the desired orientation of the needle as evaluated by the control algorithm described in Section 8.2.1. Details on how visual and vibratory feedback are provided to the subject are reported in Section 8.2.2.2 and Section 8.2.2.3, respectively.

## 8. EXPERIMENTAL EVALUATION OF CO-MANIPULATED ULTRASOUND-GUIDED FLEXIBLE NEEDLE STEERING

---

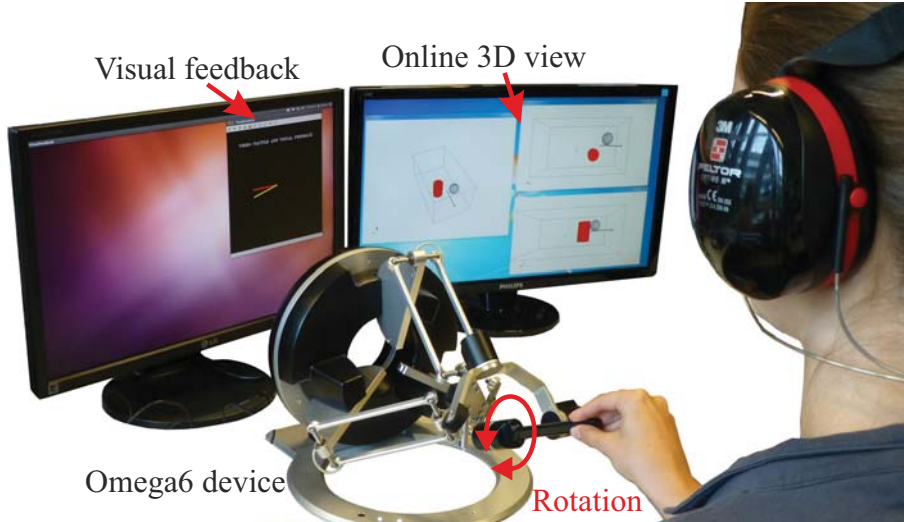


**Fig. 8.4:** Experimental evaluation. The subject performs an experimental trial while receiving both visual and vibratory feedback (VI+VB). The subject is asked to follow the online three-dimensional (3D) view of the system on the right screen and the visual feedback on the left screen.

### 8.2.2.1 Setup

The master system consists of two computer screens and a single-contact grounded haptic interface Omega 6 (Force Dimension, Nyon, Switzerland), as shown in Fig. 8.1 and Fig. 8.4. It provides the subject with navigation cues through visual and/or vibratory feedback, according to the feedback condition being considered (see Section 8.2.3). The needle is inserted automatically with a constant velocity while the haptic interface allows the subject to control the orientation of the needle during insertion. In fact, the needle orientation is actuated to match the orientation of the pen-shaped haptic probe controlled by the subject.

### 8.2.2.2 Visual feedback

Two straight line segments, one red and one yellow, are presented to the subject on a computer screen (see Fig. 8.4). The position of one of the end points of the lines is fixed, while the other one moves on a circumference whose center is the fixed end point and whose radius is the length of the segments. The coordinates of the moving end points with respect to the center of the circumference are  $(\cos \theta_i, \sin \theta_i)$  and  $(\cos \theta, \sin \theta)$  for the red and yellow line, respectively, where angles  $\theta_i(t)$  and  $\theta(t)$  are the desired and current orientation of the needle, respectively. The red and yellow lines thus represent the desired and current axial orientation of the needle tip, respectively. The subject is asked to align the yellow line with the red one, since a perfect alignment of the lines denotes the least deviation from the computed plan.

### 8.2.2.3 Vibratory feedback

Vibratory feedback is controlled by a penalty function based on the difference between the desired orientation  $\theta_i(t)$  and the current orientation  $\theta(t)$  of the needle:

$$\mathbf{f}_v = \mathbf{A}_1 |\theta_i(t) - \theta(t)| \operatorname{sgn}(\sin(2\pi ft)), \quad (8.1)$$

where  $\mathbf{A}_1 = \frac{3}{\pi} \mathbf{I}_{3 \times 1}$  N/rad and

$$f = \begin{cases} 100 \text{ Hz} & \text{if } \theta(t) - \theta_i(t) \geq 0, \\ 25 \text{ Hz} & \text{if } \theta(t) - \theta_i(t) < 0. \end{cases}$$

Vibrations thus provide information about the desired orientation  $\theta_i(t)$ , indicating in which direction and how much the subject should rotate the pen-shaped haptic probe. Frequency  $\omega$  indicates in which direction the subject should rotate the pen-shaped haptic probe: clockwise for  $f = 100$  Hz and counter-clockwise for  $f = 25$  Hz. Frequency values are chosen to maximally stimulate the Pacinian corpuscle receptors [183], be easy to distinguish [184] and fit the master device specifications. On the other hand, the amplitude of these vibrations indicates how much the subject should rotate the haptic probe: no vibrations indicated the best performance. Amplitude scaling matrix  $\mathbf{A}_1$  is chosen to maximize the just-noticeable difference [185] for the error  $|\theta_i(t) - \theta(t)|$  and fit the master device specifications.

## 8.2.3 Experiments

The aim of the experiments is to investigate the co-manipulation configurations that achieve sufficient targeting accuracy. We attempt to combine the advantages of a manual insertion with the high accuracy of autonomous (robotic) needle insertion.

### 8.2.3.1 Experimental protocol

The experimental setup is shown in Fig. 8.4. A 3D view of the planned path, target location, needle and obstacle positions using an isometric, top and side views is always displayed to the subject (right screen in Fig. 8.4). The task consists of rotating the pen-shape haptic probe about its axis to steer the needle towards the target point while avoiding two obstacles. The needle insertion velocity is fixed to 1 mm/s and the target point is placed at 85 mm from the insertion point. We used a Nitinol needle of 0.5 mm diameter and 30° bevel angle.

In the first three conditions, subjects receive visual and vibratory feedback from the control algorithm, in addition to the online 3D view of the system. In the last condition, subjects control the needle orientation relying only on the online 3D view. Each subject performs twelve randomized trials of the needle steering task, with three repetitions for each feedback condition proposed:

- visual feedback (VI) on the desired and current orientation of the needle, as described in Section 8.2.2.2,

## 8. EXPERIMENTAL EVALUATION OF CO-MANIPULATED ULTRASOUND-GUIDED FLEXIBLE NEEDLE STEERING

---

- vibratory feedback (VB) on the desired and current orientation of the needle, as described in Section 8.2.2.3,
- visual and vibratory feedback (VI+VB) on the desired and current orientation of the needle, as described in Sections 8.2.2.2 and 8.2.2.3,
- no feedback (N) from the control algorithm on the desired and current orientation of the needle except from the online 3D view.

### 8.2.3.2 Subjects

In order to determine the number of subjects needed for our research study, we run a power analysis using the the open source G\*Power software (University of Kiel, Germany). The completion times for each trial were compared using a repeated-measures analysis of variance (ANOVA). Power analysis revealed that, in order to have a 90% chance of detecting differences in our data, we need at least 14 participants (partial  $\eta^2 = 0.278$ , effect size 0.621, actual power 0.918).

Fourteen subjects with medical background participated in the experiment (3 males, 11 females, age 24 - 32). The subjects were mainly senior Technical Medicine<sup>9</sup> students who had completed a training in clinical insertions and endoscopy. Additionally, we enrolled one nurse with 5 years of clinical experience in a hospital, and 3 biomedical engineers to perform the experiments. The subjects participated on a voluntary basis and signed an informed consent form. Subjects were informed about the procedure before the beginning of the experiment and a 5-minute familiarization period was provided to make them acquainted with the experimental setup. Subjects were asked to wear a pair of noise canceling headphones, and they did not have direct visual access to the needle control device (slave system) in order to prevent visual cues that might alter their judgment. Before each trial, subjects were informed about which experimental condition was going to be considered.

## 8.3 Results

In order to evaluate the accuracy of the system we test the targeting accuracy (the deviation of the needle tip from the target position). Safety is evaluated by detecting the insertions where the obstacles are hit by the needle. Efficiency is evaluated by testing (a) the orientation error between the actual orientation and the needle orientation computed by the control algorithm, (b) the completion time of the insertion, and (c) comparing the first three experimental cases while visual or/and vibratory are provided to the subjects with the case where no visual nor vibratory feedback is provided to test the system efficiency. The completion time is also dependent on the path generated for a specific insertion. An optimized path is generated at the beginning of the insertion but as the user deviates the needle from initial path, the online generated paths correct for these deviations and the insertion completion time is expected to increased.

---

<sup>9</sup>Technical Medicine is a Master's level programme in which students learn to integrate advanced technologies within the medical sciences to improve patient care.

**Table 8.1:** The targeting error is calculated as the absolute distance between the needle tip at the end of insertion and the center of the localized target. Its mean error is  $\mu$  and its standard deviation is  $\sigma$ . The subject receives visual (VI), vibratory (VB), visual and vibratory (VI+VB), or no (N) feedback from the control algorithm.

	VI	VB	VI+VB	N
$\mu$ (mm)	1.07	1.39	1.03	9.23
$\sigma$ (mm)	0.59	0.70	0.64	6.68

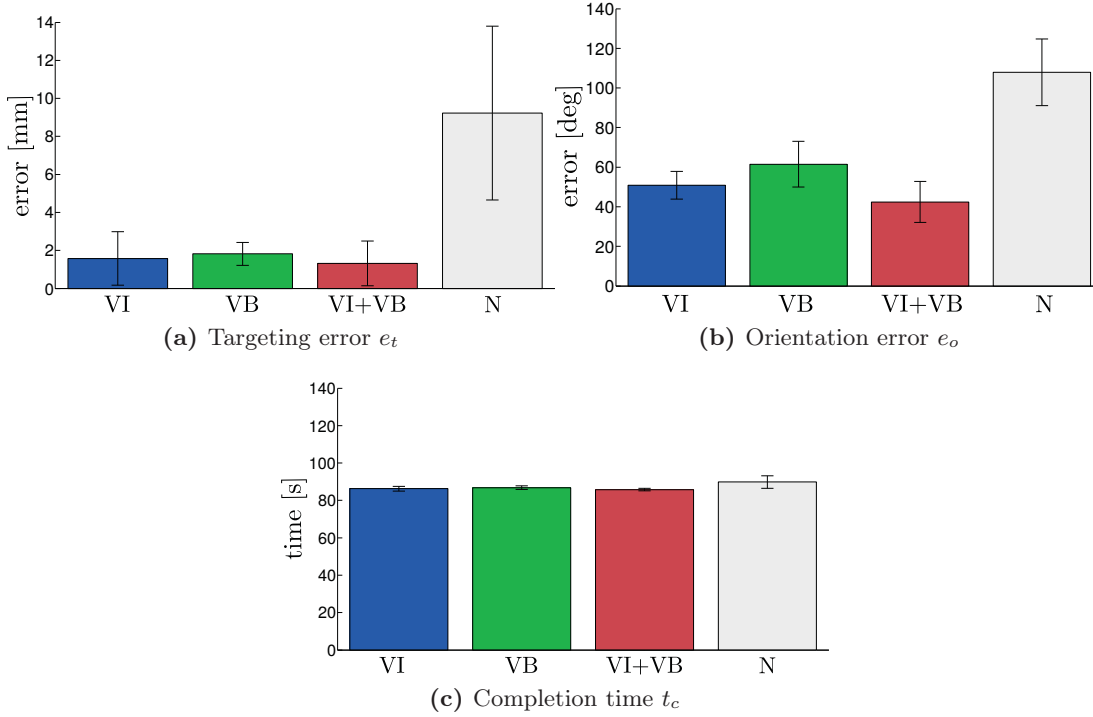
We evaluate the mean error in reaching the target point  $e_t$ , the mean error over time in following the desired orientation signals  $e_o$ , and the completion time  $t_c$ . Error  $e_t$  is calculated as  $\|\mathbf{n}_f - \mathbf{o}_t\|$ , where  $\mathbf{n}_f \in \mathbb{R}^{3 \times 1}$  represents needle tip position at the end of the task (see Table 8.1). Errors on the desired orientation signals  $e_o$  is computed as the mean over time of  $\|\theta(t) - \theta_i(t)\|$ . Data resulting from different repetitions of the same condition, performed by the same subject, were averaged before comparison with other conditions' data. Data have been transformed when necessary to meet the test's assumptions [186].

Fig. 8.5(a) shows targeting error  $e_t$  for the four experimental conditions. The collected data passed the Shapiro-Wilk normality test. Mauchly's Test of Sphericity indicated that the assumption of sphericity had been violated ( $\chi^2(2) = 105.054, p < 0.001$ ). A repeated-measure ANOVA with a Greenhouse-Geisser correction showed a statistically significant difference between the means of the feedback conditions ( $F_{1.017,13.226} = 69.734, p < 0.001, \alpha = 0.05$ ). Post-hoc analysis (Games-Howell post-hoc test) revealed statistically significant difference between all the groups ( $p < 0.001$ ). This means that conditions VI+VB and N performed, respectively, significantly better and worse than all the others. Condition VI outperformed condition VB.

Fig. 8.5(b) shows orientation error  $e_o$  for the four experimental conditions. The collected data passed the Shapiro-Wilk normality test. Mauchly's Test of Sphericity indicated that the assumption of sphericity had been violated ( $\chi^2(2) = 12.843, p = 0.025$ ). A repeated-measure ANOVA with a Greenhouse-Geisser correction showed a statistically significant difference between the means of the feedback conditions ( $F_{1.741,22.628} = 83.849, p < 0.001, \alpha = 0.05$ ). Post-hoc analysis (Games-Howell post-hoc test) revealed statistically significant difference between all the groups (VI vs VB,  $p = 0.016$ ; VI vs VI+VB,  $p = 0.035$ ; VI vs N,  $p < 0.001$ ; VB vs VI+VB,  $p < 0.001$ ; VB vs N,  $p < 0.001$ ; VI+VB vs N,  $p < 0.001$ ). As for Fig. 8.5(a), this also means that conditions VI+VB and N performed, respectively, significantly better and worse than all the others. Condition VI outperformed condition VB.

Fig. 8.5(c) shows the completion time  $t_c$  for the four experimental conditions. The collected data passed the Shapiro-Wilk normality test. Mauchly's Test of Sphericity indicated that the assumption of sphericity had been violated ( $\chi^2(2) = 24.629, p < 0.001$ ). A repeated-measure ANOVA with a Greenhouse-Geisser correction showed a statistically significant difference between the means of the feedback conditions ( $F_{1.380,17.942} = 16.440, p < 0.001, \alpha = 0.05$ ). Post-hoc analysis (Games-Howell post-hoc test) revealed statistically significant difference between conditions N and all the others (VI vs N,

## 8. EXPERIMENTAL EVALUATION OF CO-MANIPULATED ULTRASOUND-GUIDED FLEXIBLE NEEDLE STEERING



**Fig. 8.5:** Needle insertion experiment. Targeting error  $e_t$ , orientation error  $e_o$ , and completion time  $t_c$  (mean and SD) are plotted for the experimental conditions where the subjects receive visual (VI), vibratory (VB), visual and vibratory (VI+VB), and no (N) feedback from the control algorithm. Lower values of these metrics indicate better performance in completing the given task.

$p = 0.013$ ; VB vs N,  $p = 0.015$ ; VI+VB vs N,  $p = 0.001$ ), and between conditions VB and VI+VB ( $p = 0.009$ ). This means that subjects took significantly more time to complete the task while being provided with no feedback from the controller (condition N). On the other hand, subjects complete the task significantly faster in condition VI+VB than in condition VB.

In addition to the quantitative evaluation presented above, we also measured subjects' experience. Immediately after the experiment, participants were asked to fill in a 18-item questionnaire using bipolar Likert-type seven-point scales. It contained a set of assertions, where a score of 7 was described as "completely agree" and a score of 1 as "completely disagree" with the assertion. The evaluation of each question is reported in Table 8.2. Fig. 8.6 shows the mean ratings given by the subjects in eight questions of the post-experimental questionnaire. Fig. 8.6(a) shows the ratings given by the subjects to the question "In this feedback condition I performed the best" across the four different feedback conditions (Q11 vs. Q13 vs. Q15 vs. Q17, see Table 8.2). Since the data were registered at the ordinal level, we ran a Friedman test. Ratings were statistically significantly different for different feedback conditions,  $\chi^2(3) = 18.378$ ,  $p < 0.001$ . Pairwise comparisons were performed with a Bonferroni correction for multiple comparisons. Ratings were statistically significantly different between condition N and all

**Table 8.2:** Subjects' experience evaluation. Participants rated these statements, presented in random order, using a 7-point Likert scale (1 = completely disagree, 7 = completely agree). Means and standard deviations are reported for the visual (VI), vibratory (VB), visual-vibratory (VI+VB), and no feedback (N) conditions.

		Questions	Mean	$\sigma$
General	Q1	The system was intuitive.	3.36	1.08
	Q2	The system was easy to use.	3.79	0.70
	Q3	I needed support by the test administrator to be able to use the system.	2.50	1.16
	Q4	Most people would quickly learn how to use the system.	3.57	0.94
	Q5	I felt confident using the system.	3.00	1.11
	Q6	I needed more training to confidently use the system.	3.43	1.40
	Q7	Sound from the device caused disturbance while performing the experiments.	1.71	0.99
	Q8	I was well-isolated from external noises.	3.86	1.51
	Q9	At the end of the experiment I felt tired.	2.36	1.01
	Q10	I found useful to see the 3D representation of the needle insertion.	3.71	0.91
VI	Q11	In this feedback condition I performed the best.	3.76	1.12
	Q12	In this feedback condition I could pay attention to the 3D representation of the needle.	2.07	1.14
VB	Q13	In this feedback condition I performed the best.	3.29	0.99
	Q14	In this feedback condition I could pay attention to the 3D representation of the needle.	3.93	1.07
VI+VB	Q15	In this feedback condition I performed the best.	4.00	1.41
	Q16	In this feedback condition I could pay attention to the 3D representation of the needle.	2.21	1.19
N	Q17	In this feedback condition I performed the best.	1.71	1.14
	Q18	In this feedback condition I could pay attention to the 3D representation of the needle.	4.14	1.17

## 8. EXPERIMENTAL EVALUATION OF CO-MANIPULATED ULTRASOUND-GUIDED FLEXIBLE NEEDLE STEERING

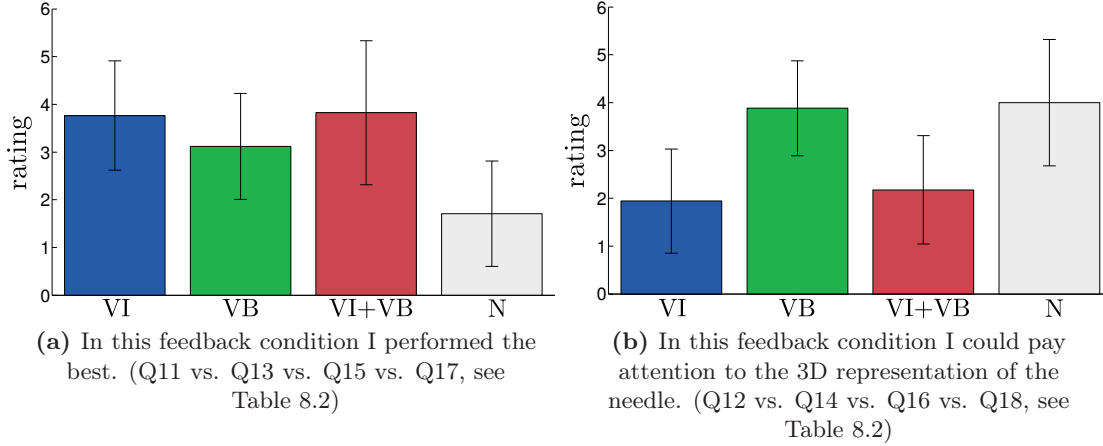


**Fig. 8.6:** Questionnaire. Answers (mean and SD) are plotted for the experimental conditions where the subjects receive visual (VI), vibratory (VB), visual and vibratory (VI+VB), and no (N) feedback from the control algorithm.

the others (VI vs N,  $p = 0.013$ ; VB vs N,  $p = 0.032$ ; VI+VB vs N,  $p = 0.001$ ). This means that subjects felt that they performed significantly worse in condition N with respect to all the others. Fig. 8.6(b) shows the ratings given to the question “In this feedback condition I could pay attention to the 3D representation of the needle” across the four feedback conditions (Q12 vs. Q14 vs. Q16 vs. Q18, see Table 8.2). This question has been asked to evaluate the ability of the subject to monitor the overall insertion procedure using the 3D system view while performing the experiments. We ran again a Friedman test. Ratings were statistically significantly different across the feedback conditions,  $\chi^2(3) = 21.095$ ,  $p < 0.001$ . Pairwise comparisons were performed with a Bonferroni correction for multiple comparisons. Ratings were statistically significantly different between conditions VI and VB ( $p = 0.008$ ), VI and N ( $p = 0.008$ ), VB and VI+VB ( $p = 0.020$ ), VI+VB and N ( $p = 0.020$ ). This shows that, as expected, providing the subjects with visual feedback about the desired orientation of the needle prevented them from focusing on the 3D view of the system (see Fig. 8.4). On the other hand, conditions VB and N enabled the subjects to look at the 3D view of the system. Moreover, the needle hit an obstacle in 9 trials (out of 42) while receiving no navigation feedback from the control algorithm (N), while the collision never occurred while receiving any type of control feedback (VI, VB, or VI+VB). *Please refer to the accompanying video<sup>10</sup> as supplementary material that demonstrates the experimental results.*

### 8.4 Discussion

Results show that all the subjects were able to steer the needle with an accuracy of  $\sim 1$  mm, while receiving feedback from the control algorithm. The mean targeting accuracy improved by a factor of 9 while receiving visual, vibratory or combined feedback

<sup>10</sup>Video link: <http://goo.gl/kFYsWt>

with respect to the condition where no navigation feedback from the control algorithm was provided to the subjects. This shows that steering a bevel-tipped flexible needle is not trivial, and receiving an online 3D view of the system may not be sufficient for accurate steering.

According to our post-experiment questionnaire, subjects preferred visual feedback (VI) over vibratory feedback (VB). The reason can be that humans are more used to dealing with visual cues with respect to vibratory ones, and, therefore, they feel more comfortable with them. However, employing visual feedback did not give the subject the chance to follow the 3D system view. It was difficult for the subject to follow the online 3D view (to monitor the overall insertion procedure) while receiving visual feedback from the control algorithm about the desired and current orientation of the needle (VI and VI+VB) (Fig. 8.4).

#### 8.4.1 Conclusions

In this study, we present a teleoperation system to steer bevel-tipped flexible needles. An ultrasound-guided system with an intraoperative path planner is used to assist the subject to steer the needle tip towards a target while avoiding two obstacles. The system enables subjects to directly maneuver the surgical tool while providing them with navigation cues through visual and vibratory feedback. Fully autonomous medical robotic systems are still not totally accepted by the medical community due to safety reasons. For this reason, in our work, a control algorithm computes the desired needle orientation during insertion but the needle motion is directly controlled by the subject. The desired orientation is provided to the master interface, which presents it to the subject, who commands the slave robot and steers the needle to follow the planned path. Four experimental conditions are taken into account. Subjects control the needle orientation using visual, vibratory, visual and vibratory (combined) or no feedback from the control algorithm. In all conditions subjects are provided with an online 3D view of the needle, target and obstacle positions. A questionnaire is also filled in by the subjects to obtain feedback about their experience with different co-manipulation configurations.

Experimental results show that navigation cues provided by the control algorithm (VI, VB and VI+VB) improve the targeting accuracy with respect to the experimental condition where only the online 3D view is displayed (N) for the subject. This result confirms the hypothesis that bevel-tipped needles are difficult to be manually steered without feedback. Although the targeting accuracy is similar for the three conditions with feedback from the control algorithm, the subjects felt more comfortable receiving visual feedback. However, they conclude that using vibratory feedback is convenient since it enables them to monitor the needle trajectory during the insertion.

The proposed system can be employed in prostate interventions using a transrectal transducer for ultrasound guidance where the needle should avoid the neurovascular bundles near the penile bulb [39]. Furthermore, in cases we cannot place the ultrasound probe for needle tracking we can use other modalities such as electromagnetic tracking.

## 8. EXPERIMENTAL EVALUATION OF CO-MANIPULATED ULTRASOUND-GUIDED FLEXIBLE NEEDLE STEERING

---

### 8.4.2 Future work

We will estimate the needle behavior during insertion in different inhomogeneous biological tissues. Since the proposed system received an initial acceptance by subjects with clinical background, advanced image processing algorithms will be implemented to track the needle tip in biological tissue to get the system closer to practice. Work is in progress to use kinesthetic force to provide subjects with force feedback regarding the mechanical properties of the tissue being penetrated. The visual feedback will be integrated in the same display of the online 3D view to make it easier for the subject to follow. Finally, the steering system can also be extended to detect the patient movements that occur during needle insertion such as respiration and fluid flow.

# Reconstruction of 3D Shapes and Needle Steering Using Automated Breast Volume Scanner (ABVS)

## Abstract

Robot-assisted and ultrasound-guided needle insertion systems assist in achieving high targeting accuracy for different applications. In this paper, we introduce the use of Automated Breast Volume Scanner (ABVS) for scanning different soft-tissue phantoms. The ABVS is a commercial ultrasound transducer used for clinical breast scanning. A pre-operative scan is performed for three-dimensional (3D) target localization and shape reconstruction. The ultrasound transducer is also adapted to be used for tracking the needle tip during steering towards the localized targets. The system uses the tracked needle tip position as a feedback to the needle control algorithm. The bevel-tipped flexible needle is steered under ABVS guidance towards a target while avoiding an obstacle embedded in soft-tissue phantom. We present experimental results for 3D reconstruction of different convex and non-convex objects with different sizes. Mean Absolute Distance (MAD) and Dice's coefficient methods are used to evaluate the 3D shape reconstruction algorithm. The results show that the mean MAD values are  $0.30\pm 0.13$  mm and  $0.34\pm 0.17$  mm for convex and non-convex shapes, respectively, while mean Dice values are  $0.87\pm 0.06$  (convex) and  $0.85\pm 0.06$  (non-convex). Three experimental cases are performed to validate the steering system. Mean targeting errors of  $0.54\pm 0.24$  mm,  $1.50\pm 0.82$  mm and  $1.82\pm 0.40$  mm are obtained for steering in gelatin phantom, biological tissue and a human breast phantom, respectively. The achieved targeting errors suggest that our approach is sufficient for targeting lesions of 3 mm radius that can be detected using clinical ultrasound imaging systems.

## 9. RECONSTRUCTION OF 3D SHAPES AND NEEDLE STEERING USING AUTOMATED BREAST VOLUME SCANNER (ABVS)

---

### 9.1 Introduction

Needle insertion into soft-tissue is a minimally invasive procedure used for diagnostic and therapeutic purposes such as biopsy and brachytherapy, respectively. Examples of diagnostic needle insertion procedures are liver and lung biopsies to detect tumors [7, 8]. Therapeutic applications of needle insertion include brachytherapy of cervical, prostate and breast cancers [9]. Inaccurate placement may result in misdiagnosis and unsuccessful treatment during biopsy and brachytherapy, respectively. Errors in needle placement can be caused by inaccurate target localization. Initial target localization is of utmost importance for accurate insertions. Imaging modalities such as ultrasound, magnetic resonance (MR), and computed tomography (CT) are often used during needle insertion procedures to determine the positions of the needle and the target [10]. X-ray based imaging modalities such as fluoroscopy, CT and mammography are used to localize lesions [26]. Such imaging techniques expose the patient to undesirable doses of ionizing radiation [95]. MR imaging suffers from low refresh rate and incompatibility with magnetic materials and tools [96]. The spatial resolution of three-dimensional (3D) ultrasound images is limited [94] with respect to CT and MR, therefore two-dimensional (2D) ultrasound is commonly used since it is real-time, inexpensive and does not expose the patient to harmful radiations. Needle-guides are usually attached to the ultrasound transducer to facilitate needle visualization, and hence control during insertion applications such as biopsy [133]. Robotic assistance for needle-guidance provides improved lesion localization and targeting accuracy [114].

#### 9.1.1 Robotic control of ultrasound transducers

Several researchers designed robotic ultrasound systems for lesion and needle detection insertion procedures [75, 141, 187]. An example of an early study that explores the advantage of robotic ultrasound systems is the development of *Hippocrate*, a robotic arm for medical applications with force feedback [134]. One of the applications of *Hippocrate* is the manipulation of an ultrasound transducer on a patient's skin to automatically reconstruct the 3D profile of arteries. Nadeau and Krupa developed a visual servoing method to control an industrial robotic system equipped with an ultrasound transducer [188]. Javier *et al.* presented an ultrasound system to 3D reconstruct the shape of *in-vitro* stenoses using an industrial robotic arm with force feedback [138]. Chate-lain *et al.* developed a real-time needle tracking method by servoing images obtained from a 3D ultrasound transducer [113]. Vrooijink *et al.* introduced a three-degrees-of-freedom Cartesian robot for controlling the ultrasound transducer for scanning flat surfaces and 3D needle tip tracking [141]. Abayazid *et al.* designed a rotational mechanism using force/torque feedback that controls a 2D transducer to scan curved surfaces and developed an algorithm to localize the target and reconstruct its 3D shape [189]. The reconstruction was done by computing the convex hull of the point cloud obtained with the contour points of each planar cross-section. However, the limitation of this algorithm is that it cannot reconstruct the shapes of non-convex tumors or anatomical obstacles. In the previously mentioned studies, robotic devices were used to control the ultrasound transducer during the scanning process. It is a challenging task to bring

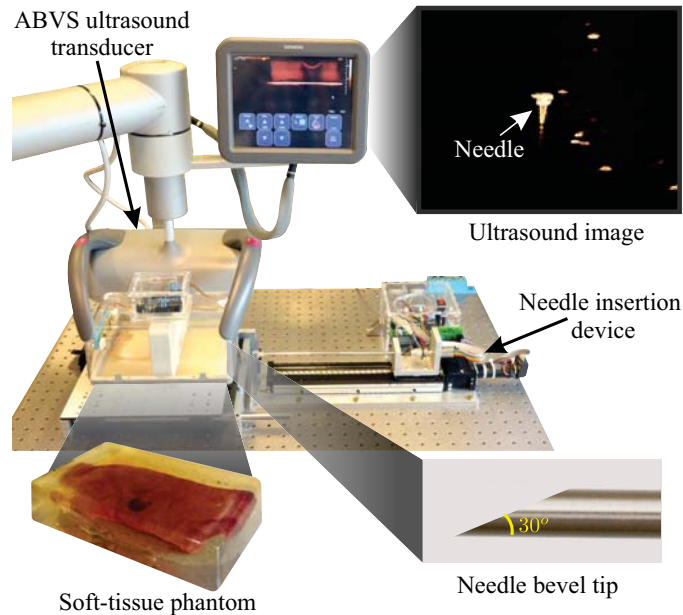


**Fig. 9.1:** The experimental setup shows the needle insertion device and the Automated Breast Volume Scanner (ABVS). The ultrasound image is used for three-dimensional needle tracking. The needle is inserted into a soft-tissue phantom including biological tissue. The ABVS is used for pre-operative scanning of the phantom and intra-operative bevel-tipped needle tip tracking. The associated custom-built electronics is used to synchronize the ABVS with the reconstruction and steering systems.

these mechanical and industrial robotic designs to the clinical environment due to safety restrictions. In the current study, we propose a system that can replace such robotic devices by a commercial ultrasound transducer which is the Automated Breast Volume Scan (ABVS) (Fig. 9.1). This transducer is currently used in clinical settings, and it performs an automated scan of the human breast to generate a 3D volume of the scanned region. Furthermore, the proposed system adapts the commercial ultrasound system for needle tracking during the insertion procedure. More importantly, our system can be used not only for breast biopsy but also adapted for other various types of needle-based procedures.

### 9.1.2 Flexible needle steering

Flexible needles are introduced as they improve the steerability and allow maneuvering around sensitive and hard tissue such as blood vessels and bones, respectively [25, 37, 38]. Such needles commonly have bevel tips that naturally deflect during insertion into soft-tissue due to the asymmetric forces acting on their tips [27]. The direction of needle deflection is controlled by rotating the needle about its insertion axis to steer it towards a certain target location. In previous studies, control algorithms were developed for needle steering in 2D and 3D space. DiMaio and Salcudean presented a path planning and control algorithm that related the needle motion at the base (outside the soft-tissue phantom) to the tip motion inside the tissue in 2D space [66]. Vrooijink *et al.* introduced

## 9. RECONSTRUCTION OF 3D SHAPES AND NEEDLE STEERING USING AUTOMATED BREAST VOLUME SCANNER (ABVS)

---

an ultrasound-guided needle steering system using duty-cycle technique where the needle is inserted with constant velocity [141]. The transducer scanning velocity was controlled to keep the needle tip visible in the ultrasound image. In the current study, since we are using a commercial ultrasound transducer which scans with a constant velocity, we apply a closed-loop control to adjust the insertion velocity to keep the needle tip always in the image-plane for steering and path planning. Several 3D path planning algorithms have been introduced based on Rapidly-exploring Random Trees (RRTs) for obstacle avoidance [120, 121]. The algorithm developed by Patil *et al.* is integrated to compute feasible collision-free paths in 3D-space [121].

### 9.1.3 Contributions

In the current study, we develop a system (Fig. 9.1) that performs ultrasound scanning of various soft-tissue phantoms to localize and reconstruct different target and obstacles shapes. The ABVS system then tracks a bevel-tipped flexible needle intra-operatively to steer it towards the localized target in 3D space while avoiding the obstacles. The algorithms are validated by conducting insertion experiments into a soft-tissue phantom and biological tissue (chicken breast and sheep liver) while avoiding virtual and real obstacles. We also steer the needle in a breast phantom used to train clinicians for ultrasound biopsy procedures. This breast phantom has similar mechanical and ultrasound visual properties of human breast tissue, and it also contains amorphous lesions. The major contributions of this work include:

- Replacing mechanical and industrial robotic devices used for ultrasound transducer control with patient-friendly commercial device for target localization and shape reconstruction.
- Developing algorithms for pre-operative target localization, and reconstruction of non-convex target geometries.
- Adapting a clinically-approved ultrasound imaging system (ABVS) to be used to 3D track the needle intra-operatively for various needle-based clinical procedures.
- Experimental evaluation of needle steering towards a physical target while avoiding an obstacle in different soft-tissue phantoms.

## 9.2 Target localization and shape reconstruction

In this section, we present the algorithms developed for 3D target localization and shape reconstruction. Evaluation methods are also described to validate the proposed reconstruction algorithm. The ABVS system is used to scan soft-tissue phantoms containing targets with various 3D geometries and sizes.

The soft-tissue phantom is pre-operatively scanned using a Siemens Acuson S2000 (Siemens AG, Erlangen, Germany) ultrasound device to localize the target and reconstruct its shape. Ultrasound images are obtained using the ABVS system (Siemens Medical Solutions, Mountain View, CA, USA). The ABVS scanner is composed of a

## 9.2 Target localization and shape reconstruction

---

cage that contains a transducer (14LBV). This transducer translates automatically using a linear stage with constant velocities of 1.55 mm/s or 2.55 mm/s. The transducer has 768 elements and a frequency bandwidth of 5-14 MHz. The width of the transducer is 154 mm and its maximum display depth is 60 mm. The frame rate of the system is 25 frames per second, and its voxel size is  $0.09 \times 0.16 \times 0.44$  mm<sup>3</sup> along the axial, lateral and elevation planes, respectively.

### 9.2.1 Registration and synchronization

The ultrasound transducer is initially located in the middle position of the ABVS cage then it moves to one ends of the cage. The scan starts as soon as the transducer hits the end of the cage, and the scan is completed as the transducer hits the other end. The ABVS system is adapted by fixing internally two buttons on each end of the cage. These buttons are connected to a microcontroller board (Arduino Uno, Arduino, Italy) to determine the start time of the scan. The ultrasound transducer presses the buttons when it reaches one end of the cage. As soon as the button is released, which means that the transducer started moving from one end to the other, the algorithm starts capturing the images and assigns them to their corresponding transducer positions. The images are captured every 40 ms. The transducer position of each captured image frame is determined using the starting time and the scanning velocity. The output data is then processed for target localization and shape reconstruction.

### 9.2.2 Localization

The images and their locations are analyzed to determine the frames that include the target. First, each image is inverted and its contrast is enhanced using contrast-limited adaptive histogram equalization [190]. The images are then converted to a binary image by thresholding. Small pixel groups are removed and each image is morphologically closed, resulting in the segmented cross-sectional views of the target. The centroid of the target cross-section of each image frame is calculated using image moments [81, 82]. The centroid of the target volume is computed using all the centroids of the image frames that contain the target. The contour points of each segmented image is extracted. The target reconstruction is accomplished using the point cloud representing the contour coordinates of the segmented ultrasound images. The point cloud is then used to reconstruct the 3D target shape.

### 9.2.3 Target reconstruction algorithm

The algorithms presented in our previous study could only reconstruct convex 3D target shapes [189]. In the current study, we developed an algorithm that can reconstruct different non-convex and convex volumes. First, the points of each image are sorted to draw the contour of the 2D section by linking each point to the next one. The outer points of the convex hull are determined [191]. Points that are not part of the convex hull are used for minimizing the length of the contour when it is possible. The step of minimizing the contour length allows the algorithm to reconstruct non-convex

## 9. RECONSTRUCTION OF 3D SHAPES AND NEEDLE STEERING USING AUTOMATED BREAST VOLUME SCANNER (ABVS)

---

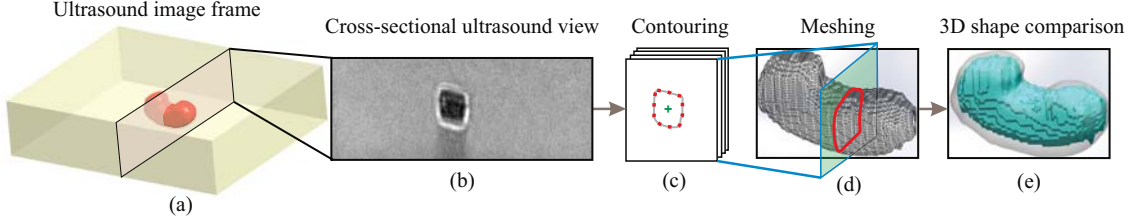


**Fig. 9.2:** Target localization and shape reconstruction. (a) The soft-tissue phantom is scanned and image frames that contain the target are segmented. (b) The target cross-section appears darker than the surrounding tissue in the raw ultrasound images. (c) The contour points of the target cross-section are obtained. The points are sorted and the centroid of each contour is computed (green “+”). The points of each frame are then connected to define the contour shape. The ultrasound images are stacked together for three-dimensional (3D) shape reconstruction. (d) The contours are connected together to form the mesh elements. (e) The 3D reconstruction algorithm is evaluated by comparing the reconstructed shape (green) with reference 3D shape (greyish) using Mean Absolute Distance and Dice’s coefficient methods.

shapes. This results in connected points in each image frame (cross-section of the target) (Fig. 9.2(c)). The consecutive contours are then connected to produce triangular meshing elements. Each triangular meshing element consists of one segment on one contour and two segments linking this contour to the next one. The sorting of points in the previous step facilitates the meshing process. The heuristic method presented by Ganapathy *et al.* is used to connect different contours and forming the meshing element [192]. The meshing elements are then added to the surface connecting the contours (Fig. 9.2(d)). In the last reconstruction step, the two planar cross-sections at both ends of the volume are meshed to close the 3D shape.

The target reconstruction algorithm is evaluated by quantifying the spatial agreement of different convex and non-convex 3D shapes with the 3D drawing of the molds designed for making the shapes. Dice’s coefficient and Mean Absolute Distance (MAD) methods are used for shape comparison (Fig. 9.2(e)) [144, 193]. The results of the evaluation methods are presented in Section 9.4. The location of the reconstructed target is used as an input to the control algorithm to steer the needle towards the target.

### 9.3 Three-dimensional needle steering

The ultrasound-based needle tracking algorithm provides the path planning and needle control algorithms with the tip position during insertion. In this section, the 3D needle tip tracking and control algorithms are described.

#### 9.3.1 Needle tip tracking

The ABVS ultrasound system scans the phantom with a constant velocity. The ultrasound images are used to visualize the cross-section of the needle tip during insertion. A proportional-integral-derivative (PID) controller is implemented to keep the needle tip in the ultrasound image frame by adjusting the needle insertion velocity. The needle

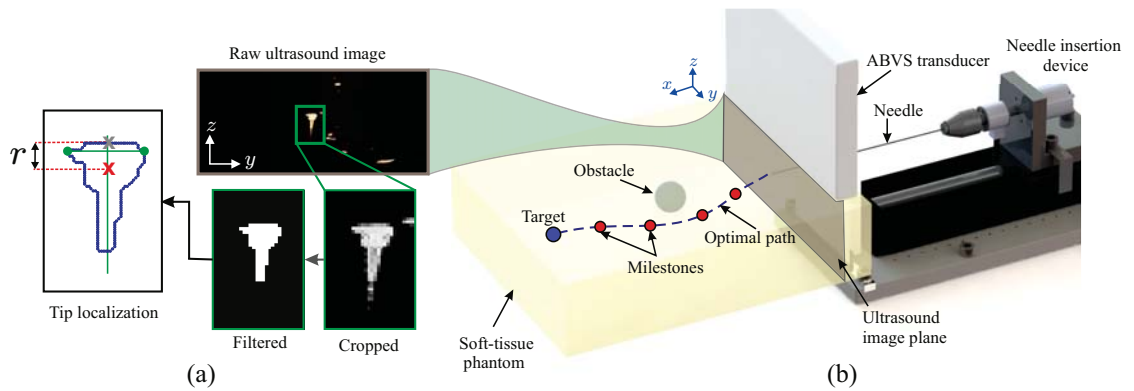


**Fig. 9.3:** The needle tip pose is determined in three-dimensional space using a two-dimensional Automated Breast Volume Scan (ABVS) transducer positioned to visualize the needle tip where the ultrasound image plane is perpendicular to the needle insertion axis ( $x$ -axis). (a) The region of interest the contains the needle tip is cropped and filtered and then contour of the needle cross-section is obtained. The  $y$ -coordinate of the needle center is the midpoint between the maximum and minimum  $y$ -coordinate values (green circles) of the points along the contour. Since the needle radius is known, we subtract the needle radius ( $r$ ) from the maximum  $z$ -coordinate (gray "x") along the contour to compute the center of the needle. The needle tip position (red "x") is an input of the path planning algorithm to generate the optimal needle path to avoid the obstacle and reach the target. (b) The path planner generates milestones along the path, and the control algorithm steers the needle using the milestones to move along the planned trajectory.

tracking algorithm is divided into two main parts. First, the image processing part that localizes the needle tip in ultrasound images. Second, the needle velocity control that synchronizes the needle and transducer velocities.

### 9.3.1.1 Image processing

The ultrasound transducer is placed perpendicular to the needle insertion direction (Fig. 9.3). The resulting ultrasound image shows a radial cross-sectional view of the needle. An image processing algorithm is used to localize the needle in the ultrasound images. The image processing is divided to pre-processing and post-processing phases. In the pre-processing phase, the ultrasound images are enhanced and filtered to eliminate speckles using a sequence of segmentation techniques, including Gaussian filtering, dilation and thresholding. In the post-processing phase, the contours of all objects in the image are determined. These objects include the needle cross-section and other artifacts that appear mainly in biological tissue. Fourier descriptors are used to extract the needle contour features in order to distinguish the needle from other artifacts [194]. The contour features are extracted from a sample image prior to the experiments. The needle cross-section contour is then used to localize its tip as shown in Fig. 9.3(a).

### 9.3.1.2 Velocity control

The ABVS transducer performs breast scans with a constant velocity of 1.55 mm/s. Therefore, the  $x$ -component of the needle tip velocity ( $v_{x_{tip}}$ ) has to be controlled to

## 9. RECONSTRUCTION OF 3D SHAPES AND NEEDLE STEERING USING AUTOMATED BREAST VOLUME SCANNER (ABVS)

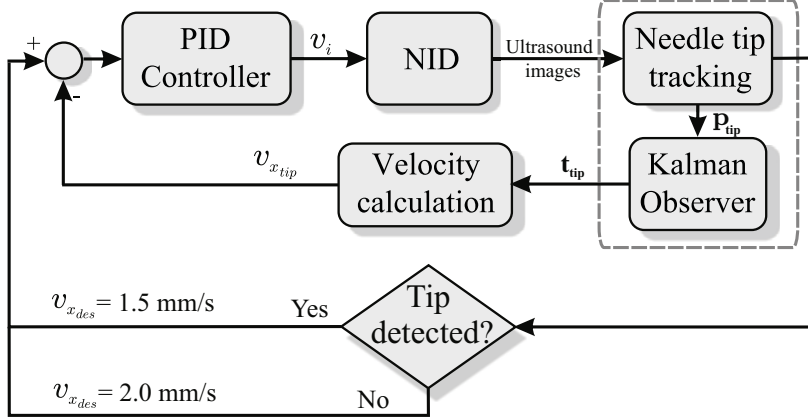


**Fig. 9.4:** A proportional integral derivative (PID) controller is implemented in order to keep the  $x$ -axis component of the needle tip velocity ( $v_{x_{tip}}$ ) equal to the desired velocity ( $v_{x_{des}}$ ). The needle tip position ( $\mathbf{p}_{tip}$ ) detected by the tracking algorithm is used as input for the Kalman observer to provide the output vector composed by both the needle tip positions ( $\mathbf{p}_{tip}$ ) and velocities ( $\mathbf{t}_{tip}$ ). The controller output is the insertion velocity ( $v_i$ ) performed by the needle insertion device (NID). The velocity ( $v_{x_{des}}$ ) is increased if the needle is not detected in the ultrasound image plane, and it is decreased if the needle is detected in the image plane.

keep the needle tip in the ultrasound image plane. Assuming that the needle is not compressed along its insertion axis, the  $x$ -component of the needle tip velocity ( $v_{x_{tip}}$ ) is calculated by  $v_{x_{tip}} = \sqrt{v_i^2 + v_{y_{tip}}^2 + v_{z_{tip}}^2}$ , where  $v_i$ ,  $v_{y_{tip}}$  and  $v_{z_{tip}}$  are the insertion velocity and the corresponding needle  $y$ - and  $z$ -components of the tip velocity, respectively. The tip velocities  $v_{y_{tip}}$  and  $v_{z_{tip}}$  are estimated by the image processing algorithm. A Kalman observer is used to filter the tip position information and to estimate the needle tip position and velocity when the tip is not visible in the ultrasound image frame. The system states in the Kalman observer are the Cartesian needle tip positions and velocities [141]. The gains of the observer are tuned as presented by Vrooijink *et al.* [124].

The needle insertion velocity ( $v_i$ ) is adjusted by a PID controller to maintain the  $x$ -component of the needle tip velocity ( $v_{x_{tip}}$ ) in order to keep it equal to a desired velocity ( $v_{x_{des}}$ ), as shown in Fig. 9.4. The desired velocity is increased if the needle is out-of-plane (i.e., the tip is not detected, and the needle is lagging) or decreased if the needle is in-plane (i.e., the tip is detected, and the needle is leading). This step is performed to ensure that the ultrasound detects the tip of the needle and not its shaft. The gains of the PID controller are experimentally tuned to assure a fast reaction, prevent overshoot and guarantee the accurate needle tip tracking required by the steering control and the path planner.

### 9.3.2 Three-dimensional needle path planning and control

The target and obstacle positions obtained from the ABVS pre-operative scan (presented in Section 9.2), and the needle tip pose computed intra-operatively from the

tracking algorithm (presented in Section 9.3) are used as input to the path planning and control algorithms.

The 3D path planning algorithm generates the optimal trajectory to steer the needle toward the target while avoiding an obstacle in 3D space [121]. The planning algorithm is based on the rapidly-exploring random tree (RRT) approach, which is a sampling-based method for path planning [125]. The optimal trajectory is replanned every second during needle insertion to compensate for uncertainties or disturbances in the system or environment. The path planner outputs a sequence of milestones along the optimal path. These milestones are used as an input to the needle control algorithm. The algorithm steers the needle tip toward the first milestone. As soon as a milestone is reached, the control algorithm steers the needle toward the next milestone until the target is reached (Fig. 9.3(b)).

The needle is assumed to move along arcs during its insertion into a soft-tissue phantom [27]. The direction of motion along the arc depends on the bevel tip orientation, which is adjusted by rotating the needle about its axis at the base. The needle tip pose obtained from the tracking algorithm, the milestone positions computed using the planner, and the final target position calculated from the preoperative scan are inputs of the control algorithm. We refer the reader to the work by Patil *et al.* and Abayazid *et al.* for additional details on the planning and control algorithms [121, 140].

## 9.4 Experiments

In this section, we present the experimental setup used for scanning the soft-tissue phantom and also for needle steering. Subsequently, the experiments performed for evaluation of the reconstruction and control algorithms are described.

### 9.4.1 Setup

The experimental setup is divided into two parts. First, the two-degrees-of-freedom insertion device which allows the needle to be inserted and rotated about its axis [91]. Second, the ABVS transducer that scans the soft-tissue phantom to localize the target and reconstruct its shape, as shown in Fig. 9.1. The ABVS is also used for needle tip tracking during the steering procedure. The needle is inserted into a soft-tissue phantom made up of a gelatin mixture, chicken breast and sheep liver. We also steer the needle in a commercial human breast phantom (CIRS, Norfolk, USA). This breast phantom contains lesions of different shapes and sizes and it is used for ultrasound biopsy training. The flexible needle is made of Nitinol alloy (nickel and titanium). The Nitinol needle has a diameter of 0.5 mm with a tip bevel angle of 30°.

### 9.4.2 Experimental plan

Various experimental scenarios are conducted to validate the proposed target reconstruction and control algorithms.

## 9. RECONSTRUCTION OF 3D SHAPES AND NEEDLE STEERING USING AUTOMATED BREAST VOLUME SCANNER (ABVS)

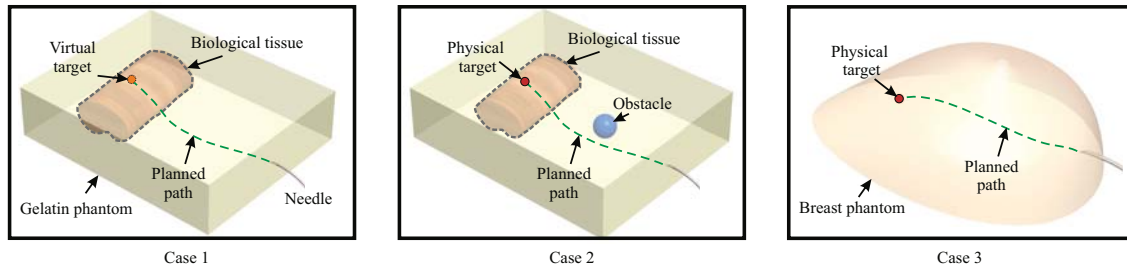


**Fig. 9.5:** Experimental cases. (a) The needle is steered towards a virtual target in a gelatin-based soft-tissue phantom (Case 1(a)), chicken breast (Case 1(b)) and sheep liver (Case 1(c)). (b) The needle is steered towards a physical target while avoiding a physical obstacle in gelatin-based soft-tissue phantom (Case 2(a)) and chicken breast (Case 2(a)). (c) The needle is steered towards a physical target while avoiding a physical obstacle in a human breast tissue phantom (Case 3).

### 9.4.2.1 Shape reconstruction

We assess the target reconstruction algorithm by scanning different 3D geometries. Targets are made of an aqueous solution of 20 wt.% polyvinyl alcohol (PVA) (Sigma-Aldrich Chemie B.V., The Netherlands) to mimic the ultrasound visual properties of breast lesions [195, 196]. The solution is cast in 3D printed mold with cavities of bean shapes and spherical shapes of 3 mm and 4 mm radius. The final material is prepared undergoing two freeze and thaw cycles. The output of the target reconstruction algorithm is compared to the 3D drawings used for designing the 3D printed molds. MAD and Dice's coefficient methods are used for shape comparison. The reconstruction algorithm is applied on five samples of each target shape.

### 9.4.2.2 Steering

The phantom is scanned pre-operatively to localize the obstacle and target in the soft-tissue phantom. The control algorithm moves the needle along the generated path to avoid the obstacle and reach the target. Three experimental cases are performed to evaluate the needle steering system.

- **Case 1:** The needle is steered towards a virtual target in (a) gelatin-based soft-tissue phantom, (b) chicken breast and (c) sheep liver (Fig. 9.5(a)). This experimental case is performed to test the ability of the ABVS-guided control algorithm to steer the needle towards a certain position in different types of tissues.
- **Case 2:** The needle is steered towards a physical target while avoiding a physical obstacle embedded in (a) gelatin-based soft-tissue phantom and (b) chicken breast (Fig. 9.5(b)). This experimental case is performed to validate the path planning and 3D localization algorithms.
- **Case 3:** The needle is steered towards a physical target in a breast tissue phantom that consists of several lesions. (Fig. 9.5(c)). This experimental case is performed to test ability of the system to steer the needle in an environment similar to human breast biopsy.

**Table 9.1:** The target reconstruction is evaluated using the Mean Absolute Distance (MAD) and Dice’s coefficient geometric comparison methods for shapes with various sizes. The dimensions of the bean shape are represented by the length, width and thickness, respectively. The target reconstruction algorithm is applied on five samples of each shape.

	Geometry	MAD (mm)	Dice
Sphere	3 mm radius	0.28±0.12	0.87±0.05
	4 mm radius	0.31±0.16	0.87±0.07
Bean shape	9.6×5.6×4 mm <sup>3</sup>	0.27±0.05	0.87±0.03
	12×7×5 mm <sup>3</sup>	0.26±0.06	0.88±0.03
	18×10.5×5.5 mm <sup>3</sup>	0.55±0.12	0.80±0.07

**Table 9.2:** The results of the needle path planning and steering experiments. The mean and standard deviation of the targeting error of each case are presented. Each experimental case is performed five times.

Case	Description	Targeting error (mm)
Case 1	(a) Gelatin-based phantom	0.42±0.14
	(b) Chicken breast	0.96±0.39
	(c) Sheep liver	2.53±0.40
Case 2	(a) Gelatin-based phantom	0.66±0.26
	(b) Chicken breast	1.01±0.27
Case 3	Human breast phantom	1.82±0.40

### 9.4.3 Results

The results of the MAD and Dice’s coefficient evaluation methods for reconstruction algorithm are presented in Table 9.1. The results show that the MAD values are less than 0.5 mm for all 3D geometrical shapes while Dice’s coefficient values are around 0.87 and 0.80 for convex and non-convex 3D shapes, respectively. These results show accurate shape reconstruction for such needle insertion applications (i.e., biopsy and brachytherapy).

In the steering experimental cases, the error is defined as the absolute distance between the tip and the center of the target that is localized pre-operatively. The results of the experimental cases are presented in Table 9.2. The needle tip reaches the target in each experimental trial (according to the images obtained during insertion). The maximum targeting error is 2.53 mm, and it is noted in Case 1(c). On the other hand, the minimum targeting error is 0.42 mm, and it is observed in Case 1(a). The results show that the targeting error increases while steering in biological tissue, especially

## 9. RECONSTRUCTION OF 3D SHAPES AND NEEDLE STEERING USING AUTOMATED BREAST VOLUME SCANNER (ABVS)

---

sheep liver, due to its inhomogeneity. The inhomogeneity of the biological tissue causes deviation of the needle from its predicted path and thus increased targeting error. The targeting error increases also while steering in the human breast phantom (Case 3) (with respect to the other Case 1 and Case 2) as the curvature of the bevel-tipped needle is limited in such soft tissue. *Please refer to the accompanying video<sup>11</sup> as supplementary material that demonstrates the experimental procedure and results.*

### 9.5 Conclusions and future work

This study introduces a needle steering system that uses ABVS for ultrasound scanning of different soft-tissue phantoms including biological tissue and human breast phantoms. The system combines pre-operative 3D target localization and shape reconstruction algorithms with intra-operative needle tip tracking, path planning and ultrasound-guided control algorithms to steer a bevel tip needle towards a physical target while avoiding a physical obstacle. The reconstruction algorithm is capable of estimating different convex and non-convex 3D shapes with different sizes. The reconstruction algorithm is evaluated using MAD and Dice's coefficient methods. The reconstruction evaluation methods are applied on spherical (convex) and bean-shaped (non-convex) geometries.

#### 9.5.1 Conclusions

The 3D shape reconstruction evaluation results show that the mean MAD values are  $0.30 \pm 0.13$  mm and  $0.34 \pm 0.17$  mm for convex and non-convex shapes, respectively, while mean Dice values are  $0.87 \pm 0.06$  and  $0.85 \pm 0.06$ . Three experimental cases are performed to validate the needle tracking, path planning and control algorithms. The needle is inserted in gelatin-based soft-tissue phantoms, biological tissue (i.e., chicken breast and sheep liver) and also human breast phantoms. The phantoms are scanned before every experimental trial to localize the targets and obstacles. The experimental results show that needle avoids the obstacle and reaches the target in each experimental trial and the mean targeting errors range between  $0.42 \pm 0.14$  mm and  $2.53 \pm 0.40$  mm. It is observed that the needle curvature in the human breast phantom is limited with respect to gelatin while the needle deflection in biological tissue varies due to its inhomogeneity. The results also show that the proposed system that uses ABVS ultrasound scanner which is compatible with clinical environments can achieve high targeting accuracy as the target is reached and the obstacle is avoided in all experimental trials.

#### 9.5.2 Future work

The needle behavior in different tissues should be investigated for improved planning of the insertion procedure. Models should also be developed to estimate the target motion and shape deformation intra-operatively. The steering system can be extended to detect the patient movements that occur during needle insertion such as respiration and fluid flow. Pre-operative planning can be introduced to optimize the insertion

---

<sup>11</sup>Video link: <https://goo.gl/uljwTQ>

## 9.5 Conclusions and future work

---

location and angle in order to minimize the insertion distance and facilitate the steering process. Clinical transducers can be designed and adapted to the ABVS for other needle insertion procedures. This opens the field for having automated scanners to assist in achieving improved targeting accuracy.

**9. RECONSTRUCTION OF 3D SHAPES AND NEEDLE STEERING  
USING AUTOMATED BREAST VOLUME SCANNER (ABVS)**

---

Part V

Outlook



## Conclusions and Future Work

Needle insertion procedures are commonly used for MIS. Flexible needles provide better steerability compared to rigid needles. However, manual control of flexible needles is not intuitive. Robotic needle insertion systems can assist in achieving improved steerability and thus, high targeting accuracy for various clinical applications. In this thesis, we started with modeling the effect of skin thickness on target motion during insertion. A closed-loop control algorithm was then developed for needle steering using camera images and 2D ultrasound for feedback (Part I). An ultrasound-based 3D needle tracking algorithm was then combined with real-time path planning for needle steering. The needle was steered during insertion in soft-tissue phantoms with different surface profiles (i.e., flat, inclined and curved surfaces) and also in biological tissue. We also used a non-imaging approach (FBG sensors) for real-time needle shape reconstruction and tip tracking (Part II). We then focused on target localization and 3D shape reconstruction for needle steering in curved phantoms. A clinical application was also investigated where the needle was steered in a multi-layer phantom with different tissue elasticities (Part III). In order to bring the proposed algorithms to clinical environments, we considered practical issues such as acceptance by the clinical community. Experiments were also conducted using a commercial device that is suitable for such environment (Part IV). The system was adapted to enable subjects with clinical background to directly control the insertion procedure while receiving navigation cues from the control algorithm. Navigation cues (the computed optimal orientation) were provided through a combination of haptic (vibratory) and visual feedback to the operator who controls the needle for steering. We replaced the ultrasound transducer control robot by a clinically-approved ultrasound-based imaging system (ABVS) which is used for breast diagnosis. The ABVS transducer was used for pre-operative scanning of soft-tissue for target localization, shape reconstruction, and also intra-operatively for needle tip tracking during the steering process.

### 10.1 Conclusions

In Part I (2D Needle Steering) of this thesis, we started by studying the effects of the skin thickness on the insertion force rate and the target motion during needle insertion into soft-tissue phantom (Chapter 2). The elasticity of the target and the surrounding gelatin were estimated non-invasively using the ultrasound-based ARFI technique. The experimental results show that thick skin layer (2.5 mm) caused 90.3% increase in the insertion force rate compared to a phantom with no skin layer. The rate of target displacement increased 275.9% when the needle was inserted into a phantom with thick skin layer (2.5 mm) compared to a phantom with no skin layer. In Chapter 3, we combined the needle deflection models and image-guided techniques to accurately steer bevel-tipped flexible needles to a moving target in 2D space. Two different models were presented to predict the deflection of a needle undergoing multiple bends. Image processing was used to determine the needle and target positions in camera and ultrasound images. Experiments were performed to evaluate the targeting accuracy of the proposed control system. The needle deflection models presented include a modified kinematics-based unicycle model that accounts for needle cut angle, and a mechanics-based model that incorporates needle-tissue interactions. Both models predict deflections for multiple bends. The maximum needle deflection errors at the tip were 0.8 mm and 1.7 mm for the kinematics-based and mechanics-based models, respectively. The control algorithm accounted for target motion to improve steering accuracy. Experiments using ultrasound image-guided control demonstrate that the control system was able to steer the needle to a moving target with mean error of 0.42 mm in 2D-space. The smallest tumor that can be detected using ultrasound images has a diameter of around 2.0 mm. This implies that with the achieved accuracy of the steering algorithm, we were able to target the smallest detected tumors using ultrasound images.

In Part II (3D Needle Steering), we used FBG sensors and ultrasound imaging for real-time needle shape reconstruction and tip tracking, respectively. In Chapter 4, FBG sensors were embedded in the needle and they provided online feedback to the control algorithm to compute the optimal needle orientation. Steering experiments were performed for 110 mm insertion, and the mean targeting accuracy was 1.3 mm. The results demonstrated the capability of using a non-imaging modality (FBG sensors) as feedback to robotically steer needles. In Chapter 5, we also developed an ultrasound-based system capable of automatically needle steering towards targets in gelatin phantoms and biological tissue while avoiding stationary and moving obstacles. Our system used a path planning algorithm to compute and periodically update a feasible path to the target that avoids obstacles. We presented experimental results of needle insertion procedures for both stationary and moving targets. Moving obstacles were also tested for insertion distances up to 90 mm. We obtained mean targeting errors of  $0.32 \pm 0.10$  mm and  $0.38 \pm 0.19$  mm in gelatin-based phantom and biological tissue, respectively.

In Part III (Steering in Phantoms with Non-Uniform Surfaces), the tracking, path planning and control algorithms were adapted to accurately steer bevel-tipped flexible needles towards targets while avoiding obstacles in phantoms with non-uniform surfaces and elasticities. Chapter 6 introduced a complete steering system that combines

pre-operative 3D target localization and shape reconstruction algorithms with intra-operative path planning and ultrasound-guided control algorithms to steer a bevel tip needle towards a physical target while avoiding a physical obstacle. The effect of system parameters such as insertion speed, needle diameter and bevel angle on target motion during needle insertion are investigated experimentally. These parameters were investigated to comprehend the environment for developing models and algorithms to achieve the highest targeting accuracy. An algorithm was developed using force/torque feedback to keep the ultrasound transducer in contact with the phantom surface. The contact was maintained to ensure obtaining the ultrasound images of the soft-tissue phantom being scanned during the insertion procedure. The phantom was scanned before every experimental trial to localize the target and reconstruct its shape. The reconstruction algorithm was evaluated using the MAD method. The MAD reconstruction results showed mean errors of less than 0.5 mm. The steering results show mean targeting errors of  $1.46 \pm 0.37$  mm,  $1.29 \pm 0.29$  mm and  $1.82 \pm 0.58$  mm which were obtained for phantoms with inclined, curved and combined (inclined and curved) surfaces, respectively, for insertion distance of 86-103 mm. In Chapter 7, we focused specifically on needle insertion in the prostate. The needle was inserted in an environment containing tissues with different elasticities (spine, adipose tissue, rectal wall, urinary bladder, prostate and pubic bone). The elasticities of these tissues were obtained using the ARFI technique and their geometries were obtained using MR images. Force/torque feedback was used to keep constant contact force between the ultrasound transducer and the prostate phantom. This assisted us to obtain reliable images, and also prevented excessive forces exerted on the soft-tissue phantom that may cause tissue damage. The experimental results show that the mean targeting errors range between 0.49 mm and 1.12 mm. The targeting accuracy of the steering system was not drastically affected by changing the skin thickness, insertion angle and surface inclination as the targets were reached during each experimental trial.

In Part IV (Towards Clinical Practice), we presented methods to bring the developed techniques and algorithms closer to clinical practice. Fully autonomous robotic systems are still not totally accepted by the clinical community due to safety reasons. For this reason, in Chapter 8, we demonstrated a teleoperation system to allow the clinician to be in the control loop. The developed control algorithm computes the optimal needle orientation during insertion but it does not apply the axial rotation directly. It provides the clinician with navigation cues through visual and vibratory feedback and the clinician controls the needle via master robotic device. The targeting accuracy of several co-manipulation strategies were studied in four sets of experiments involving human subjects with clinical backgrounds. Experimental results show that receiving feedback regarding the desirable needle orientation improved the targeting accuracy by a factor of 9 with respect to manual insertions. In Chapter 9, the transducer control robot was replaced by the clinically-approved ABVS system. The ABVS system was used pre-operatively to localize the target and reconstruct its 3D shape, and also intra-operatively to track the needle tip in 3D-space during insertion. The developed 3D reconstruction algorithm is capable of reconstructing convex and non-convex shapes. Three experimental cases were performed to validate the steering system. The steering results show mean targeting errors of  $1.30 \pm 0.98$  mm,  $0.83 \pm 0.31$  mm and  $1.82 \pm 0.40$  mm

## 10. CONCLUSIONS AND FUTURE WORK

---

while steering towards a virtual target, a physical target while avoiding an obstacle, and a physical target in human breast phantom, respectively. The achieved targeting errors suggest that our approach is convenient for targeting lesions of 3 mm radius that can be detected using clinical ultrasound imaging systems. These promising results allow us to proceed further in bringing our system towards clinical practice.

### 10.2 Future work

In Chapter 2 and Chapter 6, the effect of soft-tissue deformation on target motion was initially addressed for accurate needle targeting. Tissue deformation can be further investigated using finite element models to compute the target motion. Intra-operative modeling can be performed using Simulation Open Framework Architecture (SOFA) which provides an environment for real-time modeling and simulation of soft tissues based on finite element analysis [197]. The SOFA simulation can be used for online prediction of the target motion. Additionally, the target motion model should also include patient movements that occur during needle insertion. The steering system can be extended to detect the patient movements such as respiration and fluid flow. Prediction of the target motion can improve the accuracy of needle steering.

In the experiments presented in this thesis, optimization of the needle insertion point was not investigated, and the path planning algorithm presented in Chapter 5 was used mainly for obstacle avoidance. In future work, we recommend pre-operative planning to optimize the insertion point and angle in order to minimize the number of needle rotations, insertion distance, and facilitate the steering process. The deflection of the bevel-tipped needle is an essential input to the pre-operative planning model. The needle deflection is affected by the mechanical properties of the surrounding tissue. A model should be developed to estimate the needle deflection in different tissues for accurate targeting.

Needle tracking was evaluated during insertion into homogeneous tissue (gelatin) and non-homogeneous (biological) tissue such as chicken breast and sheep liver (Chapter 5, Chapter 6 and Chapter 9). Work is in progress to develop advanced image processing algorithms to track the needle tip accurately in various biological tissues. This will allow us to get closer to clinical experiments by steering the needle in human cadavers and animals. Prior to needle insertion in patients, the proposed steering system should be adapted to move from the research lab to the operation room. The system needs to be widely accepted by the clinical community and its design should be ergonomic for such users. In Chapter 8, we introduced the use of teleoperation and shared control for accurate needle steering. The study of shared control can be extended to provide clinicians with force feedback regarding the mechanical properties of the tissue being penetrated. This will provide the operator with an extra input to enhance his/her interaction with the steering environment and the patient. In order to get the proposed algorithms closer to clinical practice, we used the commercial ABVS system for 3D target shape reconstruction and needle tracking (Chapter 9). The ABVS system can be fused with FBG sensors to guarantee robust 3D needle tracking and real-time shape reconstruction. Similarly, ultrasound clinical scanners should be designed for specific procedures such as renal biopsy and brachytherapy, not only breast scanning as in

the case of the ABVS. This opens the field for having automated scanners to assist in achieving improved targeting accuracy. Higher resolution imaging modalities such as CT and MR can be used for enhanced tracking of the needle and also for target 3D shape reconstruction. This can be achieved by designing CT- and MR-compatible setups, and reducing the image acquisition time for real-time needle tracking.

## 10. CONCLUSIONS AND FUTURE WORK

---

# References

- [1] T. N. Robinson and G. V. Stiegmann, “Minimally invasive surgery,” *Endoscopy*, vol. 36, no. 1, pp. 48–51, 2004.
- [2] A. R. Lanfranco, A. E. Castellanos, J. P. Desai, and W. C. Meyers, “Robotic surgery: A current perspective,” *Annals of Surgery*, vol. 239, no. 1, pp. 14–21, 2004.
- [3] R. Cau, F. B. F. Schoenmakers, M. Steinbuch, T. J. M. van Mulken, and R. R. W. J. van der Hulst, “Design and preliminary test results of a novel microsurgical telemanipulator system,” in *Proceedings of the IEEE RAS EMBS International Conference on Biomedical Robotics and Biomechatronics (BIOROB)*, pp. 352–356, Sao Paulo, Brazil, August 2014.
- [4] M. J. H. Lum, D. C. W. Friedman, G. Sankaranarayanan, H. King, K. Fodero, R. Leuschke, B. Hannaford, J. Rosen, and M. N. Sinanan, “The raven: Design and validation of a telesurgery system,” *The International Journal of Robotics Research*, vol. 28, no. 9, pp. 1183–1197, 2009.
- [5] R. Konietschke, U. Hagn, M. Nickl, S. Jorg, A. Tobergte, G. Passig, U. Seibold, L. Le-Tien, B. Kubler, M. Groger, F. Frohlich, C. Rink, A. Albu-Schaffer, M. Grebenstein, T. Ortmaier, and G. Hirzinger, “The dlr mirosurge - a robotic system for surgery,” in *IEEE International Conference on Robotics and Automation (ICRA)*, pp. 1589–1590, Kobe, Japan, May 2009.
- [6] N. Abolhassani, R. Patel, and M. Moallem, “Needle insertion into soft tissue: a survey,” *Medical Engineering & Physics*, vol. 29, no. 4, pp. 413–431, 2007.
- [7] E. M. Boctor, M. A. Choti, E. C. Burdette, and R. J. Webster III, “Three-dimensional ultrasound-guided robotic needle placement: an experimental evaluation,” *The International Journal of Medical Robotics and Computer Assisted Surgery*, vol. 4, no. 2, pp. 180–191, 2008.
- [8] L. B. Kratchman, M. M. Rahman, J. R. Saunders, P. J. Swaney, and R. J. Webster III, “Toward robotic needle steering in lung biopsy: a tendon-actuated approach,” in *Proceedings of the Society of Photographic Instrumentation Engineers (SPIE), Medical Imaging: Visualization, Image-Guided Procedures, and Modeling* (K. H. Wong and D. R. Holmes III, eds.), vol. 7964, pp. 79641I–1–79641I–8, Florida, USA, February 2011.

## REFERENCES

---

- [9] P. Beddy, R. D. Rangarajan, and E. Sala, "Role of mri in intracavitary brachytherapy for cervical cancer: What the radiologist needs to know," *American Journal of Roentgenology*, vol. 196, no. 3, pp. W341–W347, 2011.
- [10] R. Seifabadi, S.-E. Song, A. Krieger, N. Cho, J. Tokuda, G. Fichtinger, and I. Iordachita, "Robotic system for mri-guided prostate biopsy: feasibility of tele-operated needle insertion and ex vivo phantom study," *International Journal of Computer Assisted Radiology and Surgery*, vol. 7, no. 2, pp. 181–190, 2012.
- [11] R. L. Siegel, K. D. Miller, and A. Jemal, "Cancer statistics, 2015," *CA: A Cancer Journal for Clinicians*, vol. 65, no. 1, pp. 5–29, 2015.
- [12] S. E. Singletary, G. L. Robb, and G. N. Hortobagyi, *Advanced Therapy of Breast Disease*. Pmph USA Ltd Series, B.C. Decker, 2004.
- [13] E. A. M. O'Flynn, A. R. M. Wilson, and M. J. Michell, "Image-guided breast biopsy: state-of-the-art," *Clinical Radiology*, vol. 65, no. 4, pp. 259–270, 2010.
- [14] J. A. Harvey and R. E. Moran, "Us-guided core needle biopsy of the breast: technique and pitfalls.," *RadioGraphics*, vol. 18, no. 4, pp. 867–877, 1998.
- [15] L. L. Fajardo, K. M. Willison, and R. J. Pizzutiello, *A Comprehensive Approach to Stereotactic Breast Biopsy*. Wiley, 1996.
- [16] J. H. Yacoub, S. Verma, J. S. Moulton, S. Eggener, and A. Oto, "Imaging-guided prostate biopsy: Conventional and emerging techniques," *RadioGraphics*, vol. 32, no. 3, pp. 819–837, 2012.
- [17] C. M. Moore, N. L. Robertson, N. Arsanious, T. Middleton, A. Villers, L. Klotz, S. S. Taneja, and M. Emberton, "Image-guided prostate biopsy using magnetic resonance imaging–derived targets: A systematic review," *European Urology*, vol. 63, no. 1, pp. 125–140, 2013.
- [18] G. Aus, "Current status of hifu and cryotherapy in prostate cancer – a review," *European Urology*, vol. 50, no. 5, pp. 927–934, 2006.
- [19] A. Wojtowicz, S. Selman, and J. Jankun, "Computer simulation of prostate cryoablation-fast and accurate approximation of the exact solution," *Computer Aided Surgery*, vol. 8, no. 2, pp. 91–97, 2003.
- [20] A. Zisman, A. J. Pantuck, J. K. Cohen, and A. S. Belldegrun, "Prostate cryoablation using direct transperineal placement of ultrathin probes through a 17-gauge brachytherapy template–technique and preliminary results," *Urology*, vol. 58, no. 6, pp. 988–993, 2001.
- [21] F. A. Vicini, V. R. Kini, G. Edmundson, G. S. Gustafson, J. Stromberg, and A. Martinez, "A comprehensive review of prostate cancer brachytherapy: defining an optimal technique," *International Journal of Radiation Oncology, Biology and Physics*, vol. 44, no. 3, pp. 483–491, 1999.

## REFERENCES

---

- [22] S. E. M. Langley and R. Laing, "Prostate brachytherapy has come of age: a review of the technique and results," *British Journal of Urology (BJU) International*, vol. 89, no. 3, pp. 241–249, 2002.
- [23] J. op den Buijs, M. Abayazid, C. L. de Korte, and S. Misra, "Target motion predictions for pre-operative planning during needle-based interventions," in *Proceedings of the Annual International Conference of the IEEE Engineering in Medicine and Biology Society (EMBS)*, pp. 5380–5385, Boston, USA, August-September 2011.
- [24] H. Tadayyon, A. Lasso, S. Gill, A. Kaushal, P. Guion, and G. Fichtinger, "Target motion compensation in mri-guided prostate biopsy with static images," in *Proceedings of the IEEE International Conference on Engineering in Medicine and Biology Society (EMBC)*, pp. 5416–5419, Buenos Aires, Argentina, September 2010.
- [25] A. Grant and J. Neuberger, "Guidelines on the use of liver biopsy in clinical practice," *Journal of Gastroenterology and Hepatology*, vol. 45, no. Supplement IV, pp. IV1–IV11, 1999.
- [26] D. Glozman and M. Shoham, "Image-guided robotic flexible needle steering," *IEEE Transactions on Robotics*, vol. 23, no. 3, pp. 459–467, 2007.
- [27] R. J. Webster, J. S. Kim, N. J. Cowan, G. S. Chirikjian, and A. M. Okamura, "Nonholonomic modeling of needle steering," *International Journal of Robotics Research*, vol. 25, no. 5-6, pp. 509–525, 2006.
- [28] S. P. DiMaio and S. E. Salcudean, "Interactive simulation of needle insertion models," *IEEE Transactions on Biomedical Engineering*, vol. 52, no. 7, pp. 1167–1179, 2005.
- [29] S. Okazawa, R. Ebrahimi, J. Chuang, S. Salcudean, and R. Rohling, "Hand-held steerable needle device," *IEEE/ASME Transactions on Mechatronics*, vol. 10, no. 3, pp. 285–296, 2005.
- [30] S.-Y. Ko, L. Frasson, and F. R. y Baena, "Closed-loop planar motion control of a steerable probe with a "programmable bevel" inspired by nature," *IEEE Transactions on Robotics*, vol. 27, no. 5, pp. 970–983, 2011.
- [31] R. J. Roesthuis, N. J. van de Berg, J. J. van den Dobbelsteen, and S. Misra, "Modeling and steering of a novel actuated-tip needle through a soft-tissue simulant using fiber bragg grating sensors," in *Proceedings of the IEEE International Conference on Robotics and Automation (ICRA)*, Seattle, USA, May-June 2015.
- [32] P. E. Dupont, J. Lock, B. Itkowitz, and E. Butler, "Design and control of concentric-tube robots," *IEEE Transactions on Robotics*, vol. 26, no. 2, pp. 209–225, 2010.

## REFERENCES

---

- [33] R. J. Webster III and B. A. Jones, “Design and kinematic modeling of constant curvature continuum robots: A review,” *The International Journal of Robotics Research*, vol. 29, no. 13, pp. 1661–1683, 2010.
- [34] J. A. Engh, G. Podnar, S. Y. Khoo, and C. N. Riviere, “Flexible needle steering system for percutaneous access to deep zones of the brain,” in *Proceedings of the IEEE Annual Northeast Bioengineering Conference (NEBEC)*, pp. 103–104, Easton, Pennsylvania, USA, April 2006.
- [35] D. S. Minhas, J. A. Engh, M. M. Fenske, and C. N. Riviere, “Modeling of needle steering via duty-cycled spinning,” in *Proceedings of the IEEE International Conference on Engineering in Medicine and Biology Society (EMBC)*, pp. 2756–2759, Lyon, France, August 2007.
- [36] P. J. Swaney, J. Burgner, H. B. Gilbert, and R. J. Webster, “A flexure-based steerable needle: High curvature with reduced tissue damage,” *IEEE Transactions on Biomedical Engineering*, vol. 60, no. 4, pp. 906–909, 2013.
- [37] V. Kallem and N. Cowan, “Image-guided control of flexible bevel-tip needles,” in *Proceedings of the IEEE International Conference on Robotics and Automation (ICRA)*, pp. 3015–3020, Rome, Italy, April 2007.
- [38] N. J. Cowan, K. Goldberg, G. S. Chirikjian, G. Fichtinger, K. B. Reed, V. Kallem, W. Park, S. Misra, and A. M. Okamura, *Surgical Robotics*, ch. Robotic Needle Steering: Design, Modeling, Planning, and Image Guidance, pp. 557–582. Springer US, 2011.
- [39] A. Garg, T. Siau, D. Berenson, J. A. M. Cunha, I.-C. Hsu, J. Pouliot, D. Stoianovici, and K. Goldberg, “Robot-guided open-loop insertion of skew-line needle arrangements for high dose rate brachytherapy,” *IEEE Transactions on Automation Science and Engineering*, vol. 10, no. 4, pp. 948–956, 2013.
- [40] A. Shkolnik, M. Walter, and R. Tedrake, “Reachability-guided sampling for planning under differential constraints,” in *Proceeding of the IEEE International Conference on Robotics and Automation (ICRA)*, pp. 2859–2865, Kobe, Japan, May 2009.
- [41] J. Ferlay, H. R. Shin, F. Bray, D. Forman, C. Mathers, and D. M. Parkin, “Cancer incidence and mortality worldwide.” International Agency for Research on Cancer, 2010.
- [42] M. Guray and A. A. Sahin, “Benign breast diseases: Classification, diagnosis, and management,” *Oncologist*, vol. 11, no. 5, pp. 435–449, 2006.
- [43] W. A. Kaiser, S. O. R. Pfleiderer, and P. A. T. Baltzer, “MRI-guided interventions of the breast,” *Journal of Magnetic Resonance Imaging*, vol. 27, no. 2, pp. 347–355, 2008.

- 
- [44] G. Schueller, C. Schueller-Weidekamm, and T. H. Helbich, "Accuracy of ultrasound-guided, large-core needle breast biopsy," *European Radiology*, vol. 18, no. 9, pp. 1761–1773, 2008.
- [45] R. G. Stock and N. N. Stone, "Current topics in the treatment of prostate cancer with low-dose-rate brachytherapy," *Urologic Clinics of North America*, vol. 37, no. 1, pp. 83–96, 2010.
- [46] E. E. Deurloo, K. G. Gilhuijs, L. J. Schultze Kool, and S. H. Muller, "Displacement of breast tissue and needle deviations during stereotactic procedures," *Investigative Radiology*, vol. 36, no. 6, pp. 347–353, 2001.
- [47] S. Misra, K. T. Ramesh, and A. M. Okamura, "Modeling of tool-tissue interactions for computer-based surgical simulation: a literature review," *Presence: Teleoperators and Virtual Environments*, vol. 17, no. 5, pp. 463–491, 2008.
- [48] E. Dehghan, X. Wen, R. Zahiri-Azar, M. Marchal, and S. E. Salcudean, "Modeling of needle-tissue interaction using ultrasound-based motion estimation," in *Medical Image Computing and Computer-Assisted Intervention, MICCAI* (N. Ayache, S. Ourselin, and A. Maeder, eds.), vol. 4791 of *Lecture Notes in Computer Science*, pp. 709–716, Springer Berlin / Heidelberg, 2007.
- [49] J.-S. Hong, T. Dohi, H. Makoto, K. Konishi, and N. Hata, "A motion adaptable needle placement instrument based on tumor specific ultrasonic image segmentation," in *Proceedings of the International Conference on Medical Image Computing and Computer-Assisted Intervention-Part I, MICCAI*, pp. 122–129, London, UK, Springer-Verlag, October 2002.
- [50] S. Badaan, D. Petrisor, C. Kim, P. Mozer, D. Mazilu, L. Gruionu, A. Patriciu, K. Cleary, and D. Stoianovici, "Does needle rotation improve lesion targeting?," *The International Journal of Medical Robotics and Computer Assisted Surgery*, vol. 7, no. 2, pp. 138–147, 2011.
- [51] H. Xu, A. Lasso, S. Vikal, P. Guion, A. Krieger, A. Kaushal, L. Whitcomb, and G. Fichtinger, "Mri-guided robotic prostate biopsy: A clinical accuracy validation," in *Medical Image Computing and Computer-Assisted Intervention (MICCAI)* (T. Jiang, N. Navab, J. Pluim, and M. Viergever, eds.), vol. 6363, pp. 383–391, Springer Berlin / Heidelberg, 2010.
- [52] S. Misra, K. B. Reed, K. T. Ramesh, and A. M. Okamura, "Observations of needle-tissue interactions," in *Proceedings of the IEEE International Conference on Engineering in Medicine and Biology Society (EMBS)*, pp. 262–265, Minneapolis, Minnesota, USA, 2009.
- [53] J. op den Buijs, H. H. G. Hansen, R. G. P. Lopata, C. L. de Korte, and S. Misra, "Predicting target displacements using ultrasound elastography and finite element modeling," *IEEE Transactions on Biomedical Engineering*, vol. 58, no. 11, pp. 3143–3155, 2011.

## REFERENCES

---

- [54] S. Willson, E. Adam, and A. Tucker, "Patterns of breast skin thickness in normal mammograms," *Clinical Radiology*, vol. 33, no. 6, pp. 691–693, 1982.
- [55] T. J. Hall, A. A. Oberait, P. E. Barbone, A. M. Sommer, N. H. Gokhale, S. Goenezent, and J. Jiang, "Elastic nonlinearity imaging," in *Proceedings of the Annual International Conference of the IEEE Engineering in Medicine and Biology Society (EMBS)*, pp. 1967–1970, Minneapolis, USA, September 2009.
- [56] T. R. Kumm and M. M. Szabunio, "Elastography for the characterization of breast lesions: initial clinical experience," *Cancer Control*, vol. 17, no. 3, pp. 156–161, 2010.
- [57] J. Ophir, I. Céspedes, H. Ponnekanti, Y. Yazdi, and X. Li, "Elastography: a quantitative method for imaging the elasticity of biological tissues," *Ultrasonic Imaging*, vol. 13, no. 2, pp. 111–134, 1991.
- [58] A. Gallotti, M. D'Onofrio, and R. Pozzi Mucelli, "Acoustic radiation force impulse (ARFI) technique in ultrasound with virtual touch tissue quantification of the upper abdomen," *La Radiologia Medica*, vol. 115, no. 6, pp. 889–897, 2010.
- [59] M. L. Palmeri, M. H. Wang, J. J. Dahl, K. D. Frinkley, and K. R. Nightingale, "Quantifying hepatic shear modulus in vivo using acoustic radiation force.," *Ultrasound in medicine biology*, vol. 34, no. 4, pp. 546–558, 2008.
- [60] M. O. Culjat, D. Goldenberg, P. Tewari, and R. S. Singh, "A review of tissue substitutes for ultrasound imaging," *Ultrasound in Medicine & Biology*, vol. 36, no. 6, pp. 861–873, 2010.
- [61] T. K. Podder, D. P. Clark, D. Fuller, J. Sherman, W. A. S. Ng, L. Liao, D. J. Rubens, J. G. Strang, E. M. Messing, Y. D. Zhang, and Y. Yu, "Effects of velocity modulation during surgical needle insertion," in *Proceedings of the Annual International Conference of the IEEE Engineering in Medicine and Biology Society (EMBS)*, pp. 5766–5770, Shanghai, China, September 2005.
- [62] A. M. Okamura, C. Simone, and M. D. O'Leary, "Force modeling for needle insertion into soft tissue," *IEEE Transactions on Biomedical Engineering*, vol. 51, no. 10, pp. 1707–1716, 2004.
- [63] R. J. Roesthuis, M. Abayazid, and S. Misra, "Mechanics-based model for predicting in-plane needle deflection with multiple bends," in *Proceedings of the IEEE International Conference on Biomedical Robotics and Biomechatronics (BioRob)*, pp. 69–74, Rome, Italy, June 2012.
- [64] Y. R. J. van Veen, A. Jahya, and S. Misra, "Macroscopic and microscopic observations of needle insertion into gels," *Proceedings of the Institution of Mechanical Engineers, Part H: Journal of Engineering in Medicine*, vol. 226, no. 6, pp. 441–449, 2012.

- 
- [65] R. J. Roesthuis, Y. R. J. van Veen, A. Jayha, and S. Misra, “Mechanics of needle-tissue interaction,” in *Proceedings of the IEEE International Conference on Intelligent Robots and Systems (IROS)*, pp. 2557–2563, San Francisco, California, USA, September 2011.
- [66] S. P. DiMaio and S. E. Salcudean, “Needle steering and model-based trajectory planning,” in *Proceedings of the International Conference on Medical Image Computing and Computer-Assisted Intervention (MICCAI)*, vol. 2878, pp. 33–40, Montréal, Canada, November 2003.
- [67] H. Kataoka, T. Washio, K. Chinzei, K. Mizuhara, C. Simone, and A. M. Okamura, “Measurement of the tip and friction force acting on a needle during penetration,” in *Proceedings of the International Conference on Medical Image Computing and Computer-Assisted Intervention (MICCAI)*, pp. 216–223, Tokyo, Japan, September 2002.
- [68] R. Alterovitz, A. Lim, K. Goldberg, G. S. Chirikjian, and A. M. Okamura, “Steering flexible needles under markov motion uncertainty,” in *Proceedings of the IEEE International Conference on Intelligent Robots and Systems (IROS)*, pp. 1570 – 1575, Alberta, Canada, August 2005.
- [69] N. Abolhassani and R. V. Patel, “Deflection of a flexible needle during insertion into soft tissue,” in *Proceedings of the IEEE International Conference on Engineering in Medicine and Biology Society (EMBC)*, pp. 3858–3861, New York City, USA, September 2006.
- [70] N. A. Wood, K. Shahrour, M. C. Ost, and C. N. Riviere, “Needle steering system using duty-cycled rotation for percutaneous kidney access,” in *Proceedings of the IEEE International Conference on Engineering in Medicine and Biology Society (EMBC)*, pp. 5432–5435, Buenos Aires, Argentina, September 2010.
- [71] A. Haddadi and K. Hashtrudi-Zaad, “Development of a dynamic model for bevel-tip flexible needle insertion into soft tissues,” in *Proceedings of the IEEE International Conference on Engineering in Medicine and Biology Society (EMBC)*, pp. 7478–7482, Boston, Massachusetts, USA, September 2011.
- [72] C. Chui, S. Teoh, C. Ong, J. Anderson, and I. Sakuma, “Integrative modeling of liver organ for simulation of flexible needle insertion,” in *Proceedings of the 9th International Conference on Control, Automation, Robotics and Vision (ICARCV)*, pp. 1–6, Singapore, December 2006.
- [73] H. Kataoka, T. Washio, M. Audette, and K. Mizuhara, “A model for relations between needle deflection, force, and thickness on needle penetration,” in *Proceedings of the International Conference on Medical Image Computing and Computer-Assisted Intervention (MICCAI)*, vol. 2208, pp. 966–974, Utrecht, The Netherlands, October 2001.

## REFERENCES

---

- [74] S. Misra, K. B. Reed, B. W. Schafer, K. T. Ramesh, and A. M. Okamura, “Mechanics of flexible needles robotically steered through soft tissue,” *International Journal of Robotic Research*, vol. 29, no. 13, pp. 1640–1660, 2010.
- [75] Z. Neubach and M. Shoham, “Ultrasound-guided robot for flexible needle steering,” *IEEE Transactions on Biomedical Engineering*, vol. 57, no. 4, pp. 799–805, 2010.
- [76] I. Schafhalter-Zoppoth, C. E. McCulloch, and A. T. Gray, “Ultrasound visibility of needles used for regional nerve block: An in vitro study,” *Regional Anesthesia and Pain Medicine*, vol. 29, no. 5, pp. 480–488, 2004.
- [77] S. H. Okazawa, R. Ebrahimi, J. Chuang, R. N. Rohling, and S. E. Salcudean, “Methods for segmenting curved needles in ultrasound images,” *Medical Image Analysis*, vol. 10, no. 3, pp. 330–342, 2006.
- [78] C. Harris and M. Stephens, “A combined corner and edge detector,” in *Proceedings of The Fourth Alvey Vision Conference*, vol. 15, pp. 147–151, Manchester, UK, August–September 1988.
- [79] N. D. Glossop, K. Cleary, L. Kull, and F. Banovac, “Needle tracking using the aurora magnetic position sensor,” in *Proceedings Computer Assisted Orthopaedic Surgery*, pp. 90–92, Santa Fe, USA, June 2002.
- [80] H. Su, M. Zervas, G. A. Cole, C. Furlong, and G. S. Fischer, “Real-time mri-guided needle placement robot with integrated fiber optic force sensing,” in *Proceedings of the IEEE International Conference on Robotics and Automation (ICRA)*, pp. 1583–1588, Shanghai, China, May 2011.
- [81] M.-K. Hu, “Visual pattern recognition by moment invariants,” *IRE Transactions on Information Theory*, vol. 8, no. 2, pp. 179–187, 1962.
- [82] M. R. Teague, “Image analysis via the general theory of moments\*,” *Journal of the Optical Society of America*, vol. 70, no. 8, pp. 920–930, 1980.
- [83] Intel Corporation, *Open Source Computer Vision Library, Reference Manual*, 1 ed., 2000.
- [84] E. S. Melerski, *Design Analysis Beams Circular Plates and Cylindrical Tanks on Elastic Foundations*. Taylor & Francis, 2000.
- [85] O. Bauchau and J. Craig, *Structural Analysis*. Springer, 2009.
- [86] J. Gere and S. Timoshenko, *Mechanics of Materials*. Stanley Thornes, 1999.
- [87] A. Gefen and B. Dilmoney, “Mechanics of the normal woman’s breast,” *Technology and Health Care*, vol. 15, no. 4, pp. 259–271, 2007.

- 
- [88] S. P. DiMaio and S. E. Salcudean, “Needle insertion modelling and simulation,” in *Proceedings of the IEEE International Conference on Robotics and Automation (ICRA)*, pp. 2098–2105, Washington, D.C., USA, May 2002.
- [89] V. Pratt, “Direct least-squares fitting of algebraic surfaces,” *Computer Graphics (ACM)*, vol. 21, no. 4, pp. 145–152, 1987.
- [90] Stjoeshealth.org, “The importance of mammography.” <http://www.stjoeshealth.org/>, 2011.
- [91] M. Abayazid, R. J. Roesthuis, R. Reilink, and S. Misra, “Integrating deflection models and image feedback for real-time flexible needle steering,” *IEEE Transactions on Robotics*, 2013. *In Press*.
- [92] V. Duindam, R. Alterovitz, S. Sastry, and K. Goldberg, “Screw-based motion planning for bevel-tip flexible needles in 3d environments with obstacles,” in *Proceedings of the IEEE International Conference on Robotics and Automation (ICRA)*, pp. 2483–2488, Pasadena, CA, USA, May 2008.
- [93] K. Hauser, R. Alterovitz, N. Chentanez, A. Okamura, and K. Goldberg, “Feedback control for steering needles through 3d deformable tissue using helical paths,” in *proceedings of Robotics: Science and Systems (RSS)*, vol. 37, Seattle, USA, June 2009.
- [94] P. M. Novotny, J. A. Stoll, N. V. Vasilyev, P. J. del Nido, P. E. Dupont, T. E. Zickler, and R. D. Howe, “Gpu based real-time instrument tracking with three-dimensional ultrasound,” *Medical Image Analysis*, vol. 11, no. 5, pp. 458 – 464, 2007.
- [95] H. L. Fred, “Drawbacks and limitations of computed tomography,” *Texas Heart Institute Journal*, vol. 31, no. 2, pp. 345–348, 2004.
- [96] S. P. DiMaio, E. Samset, G. Fischer, I. Iordachita, G. Fichtinger, F. Jolesz, and C. M. Tempany, “Dynamic mri scan plane control for passive tracking of instruments and devices,” in *Medical Image Computing and Computer-Assisted Intervention* (N. Ayache, S. Ourselin, and A. Maeder, eds.), pp. 50–58, Springer Berlin / Heidelberg, 2007.
- [97] A. Othonos, K. Kalli, D. Pureur, and A. Mugnier, “Fibre bragg gratings,” in *Wavelength Filters in Fibre Optics*, pp. 189–269, Springer Berlin / Heidelberg, 2006.
- [98] I. Payo, V. Feliu, and O. D. Cortázar, “Fibre bragg grating (fbg) sensor system for highly flexible single-link robots,” *Sensors and Actuators A: Physical*, vol. 150, no. 1, pp. 24–39, 2009.
- [99] Z. Lunwei, Q. Jinwu, S. Linyong, and Z. Yanan, “Fbg sensor devices for spatial shape detection of intelligent colonoscope,” in *Proceedings of the IEEE International Conference on Robotics and Automation (ICRA)*, vol. 1, pp. 834–840, April-May 2004.

## REFERENCES

---

- [100] L. Zhang, J. Qian, Y. Zhang, and L. Shen, "On sdm/wdm fbg sensor net for shape detection of endoscope," in *Proceeding of the IEEE International Conference on Mechatronics and Automation*, vol. 4, pp. 1986–1991, July-August 2005.
- [101] X. Yi, J. Qian, L. Shen, Y. Zhang, and Z. Zhang, "An innovative 3d colonoscope shape sensing sensor based on fbg sensor array," in *Proceedings of the International Conference on Information Acquisition (ICIA)*, pp. 227–232, July 2007.
- [102] Y.-L. Park, S. Elayaperumal, B. Daniel, C. R. Seok, S. Mihye, J. Savall, R. Black, B. Moslehi, and M. Cutkosky, "Real-time estimation of 3-d needle shape and deflection for mri-guided interventions," *IEEE/ASME Transactions on Mechatronics*, vol. 15, no. 6, pp. 906–915, 2010.
- [103] V. Mishra, N. Singh, U. Tiwari, and P. Kapur, "Fiber grating sensors in medicine: Current and emerging applications," *Sensors and Actuators A: Physical*, vol. 167, no. 2, pp. 279–290, 2011.
- [104] K. Henken, D. J. van Gerwen, J. Dankelman, and J. J. van den Dobbelsteen, "Accuracy of needle position measurements using fiber bragg gratings," *Minimally Invasive Therapy & Allied Technologies*, vol. 21, no. 6, pp. 408–414, 2012.
- [105] K. O. Hill and G. Meltz, "Fiber bragg grating technology fundamentals and overview," *Journal of Lightwave Technology*, vol. 15, no. 8, pp. 1263–1276, 1997.
- [106] J. H. Friedman, J. L. Bentley, and R. A. Finkel, "An algorithm for finding best matches in logarithmic expected time," *ACM Transactions on Mathematical Software*, vol. 3, no. 3, pp. 209–226, 1977.
- [107] T. Lehmann, C. Gonner, and K. Spitzer, "Survey: interpolation methods in medical image processing," *IEEE Transactions on Medical Imaging*, vol. 18, no. 11, pp. 1049–1075, 1999.
- [108] T. Megson, *Structural and Stress Analysis*. Elsevier Butterworth-Heinemann, second edition ed., 2005.
- [109] M. Kemp, "Flexible needle steering using fiber bragg grating sensors," Master's thesis, Faculty of Electrical Engineering, Mathematics and Computer Science, University of Twente, The Netherlands, August 2012.
- [110] A. Jahya, F. van der Heijden, and S. Misra, "Observations of three-dimensional needle deflection during insertion into soft tissue," in *Proceedings of the IEEE RAS/EMBS International Conference on Biomedical Robotics and Biomechanics (BioRob)*, pp. 1205–1210, Rome, Italy, June 2012.
- [111] K. G. Yan, T. Podder, D. Xiao, Y. Yu, T. Liu, C. W. S. Cheng, and W. S. Ng, "An improved needle steering model with online parameter estimator," *The International Journal for Computer Assisted Radiology and Surgery*, vol. 1, no. 4, pp. 205–212, 2006.

- 
- [112] M. Abayazid, M. Kemp, and S. Misra, “3d flexible needle steering in soft-tissue phantoms using fiber bragg grating sensors,” in *Proceedings of the IEEE International Conference on Robotics and Automation (ICRA)*, pp. 5823–5829, Karlsruhe, Germany, May 2013.
- [113] P. Chatelain, A. Krupa, and M. Marchal, “Real-time needle detection and tracking using a visually servoed 3d ultrasound probe,” in *Proceedings of the IEEE international conference on Robotics and Automation*, pp. 1668–1673, Karlsruhe, Germany, May 2013.
- [114] K. B. Reed, A. Majewicz, V. Kallem, R. Alterovitz, K. Goldberg, N. J. Cowan, and A. M. Okamura, “Robot-assisted needle steering,” *IEEE Robotics Automation Magazine*, vol. 18, no. 4, pp. 35–46, 2011.
- [115] K. Seiler, S. P. N. Singh, S. Sukkarieh, and H. F. Durrant-Whyte, “Using lie group symmetries for fast corrective motion planning,” *International Journal of Robotics Research*, vol. 31, no. 2, pp. 151–166, 2012.
- [116] R. Alterovitz, M. Branicky, and K. Goldberg, “Motion planning under uncertainty for image-guided medical needle steering,” *International Journal of Robotic Research*, vol. 27, no. 11-12, pp. 1361–1374, 2008.
- [117] A. Asadian, M. Kermani, and R. Patel, “Robot-assisted needle steering using a control theoretic approach,” *Journal of Intelligent and Robotic Systems*, vol. 62, no. 3–4, pp. 397–418, 2011.
- [118] M. C. Bernardes, B. V. Adorno, P. Poignet, and G. A. Borges, “Semi-automatic needle steering system with robotic manipulator,” in *Proceedings of the IEEE International Conference on Robotics and Automation (ICRA)*, pp. 1595–1600, St. Paul, USA, May 2012.
- [119] V. Duindam, J. Xu, R. Alterovitz, S. Sastry, and K. Goldberg, “Three-dimensional motion planning algorithms for steerable needles using inverse kinematics,” *International Journal of Robotics Research*, vol. 29, no. 7, pp. 789–800, 2010.
- [120] J. Xu, V. Duindam, R. Alterovitz, and K. Goldberg, “Motion planning for steerable needles in 3d environments with obstacles using rapidly-exploring random trees and backchaining,” in *Proceedings of the IEEE International Conference on Automation Science and Engineering (CASE)*, pp. 41–46, Washington, D.C., USA, August 2008.
- [121] S. Patil and R. Alterovitz, “Interactive motion planning for steerable needles in 3d environments with obstacles,” in *Proceedings of IEEE RAS and EMBS International Conference on Biomedical Robotics and Biomechatronics (BioRob)*, pp. 893–899, Tokyo, Japan, September 2010.
- [122] J. E. Aldrich, “Basic physics of ultrasound imaging,” *Critical Care Medicine*, vol. 35, no. 5, pp. S131–S137, 2007.

## REFERENCES

---

- [123] J. Huang, J. K. Triedman, N. V. Vasilyev, Y. Suematsu, R. O. Cleveland, and P. E. Dupont, “Imaging artifacts of medical instruments in ultrasound-guided interventions.,” *Journal of Ultrasound in Medicine*, vol. 26, no. 10, pp. 1303–1322, 2007.
- [124] G. J. Vrooijink, M. Abayazid, and S. Misra, “Real-time three-dimensional flexible needle tracking using two-dimensional ultrasound,” in *Proceedings of the IEEE International Conference on Robotics and Automation (ICRA)*, pp. 1680–1685, Karlsruhe, Germany, May 2013.
- [125] S. M. LaValle, *Planning Algorithms*. Cambridge University Press, 2006. Available at <http://planning.cs.uiuc.edu>.
- [126] R. W. Prager, U. Z. Ijaz, A. H. Gee, and G. M. Treece, “Three-dimensional ultrasound imaging,” *Proceedings of the Institution of Mechanical Engineers, Part H: Journal of Engineering in Medicine*, vol. 224, no. 2, pp. 193–223, 2010.
- [127] C. N. Riviere, A. Thakral, I. I. Iordachita, G. Mitroi, and D. Stoianovici, “Predicting respiratory motion for active canceling during percutaneous needle insertion,” in *Proceedings of the IEEE International Conference in Medicine and Biology Society (EMBS)*, vol. 4, pp. 3477–3480, Istanbul, Turkey, October 2001.
- [128] A. Majewicz, S. P. Marra, M. G. van Vledder, M. Lin, M. Choti, D. Y. Song, and A. M. Okamura, “Behavior of tip-steerable needles in ex vivo and in vivo tissue,” *IEEE Transactions on Biomedical Engineering*, vol. 59, no. 10, pp. 2705–2715, 2012.
- [129] M. Abayazid, J. op den Buijs, C. L. de Korte, and S. Misra, “Effect of skin thickness on target motion during needle insertion into soft-tissue phantoms,” in *Proceedings of the IEEE RAS & EMBS International Conference on Biomedical Robotics and Biomechatronics (BioRob)*, pp. 755–760, Rome, Italy, June 2012.
- [130] J. Hong, T. Dohi, M. Hashizume, K. Konishi, and N. Hata, “An ultrasound-driven needle-insertion robot for percutaneous cholecystostomy,” *Journal of Physics in Medicine and Biology*, vol. 49, no. 3, pp. 441–455, 2004.
- [131] C. Delgorge, F. Courreges, L. A. Bassit, C. Novales, C. Rosenberger, N. Smith-Guerin, C. Bru, R. Gilabert, M. Vannoni, G. Poisson, and P. Vieyres, “A tele-operated mobile ultrasound scanner using a light-weight robot,” *IEEE Transactions on Information Technology in Biomedicine*, vol. 9, no. 1, pp. 50–58, 2005.
- [132] S. Onogi, T. Yoshida, Y. Sugano, T. Mochizuki, and K. Masuda, “Robotic ultrasound guidance by b-scan plane positioning control,” *Procedia {CIRP}*, vol. 5, pp. 100–103, 2013.
- [133] C. Kim, D. Chang, D. Petrisor, G. Chirikjian, M. Han, and D. Stoianovici, “Ultrasound probe and needle-guide calibration for robotic ultrasound scanning and needle targeting,” *IEEE Transactions on Biomedical Engineering*, vol. 60, no. 6, pp. 1728–1734, 2013.

- 
- [134] F. Pierrot, E. Dombre, E. Dégoulange, L. Urbain, P. Caron, S. Boudet, J. Gariépy, and J. L. Mégnien, “Hippocrate: a safe robot arm for medical applications with force feedback,” *Medical Image Analysis*, vol. 3, no. 3, pp. 285–300, 1999.
- [135] A. Krupa and F. Chaumette, “Control of an ultrasound probe by adaptive visual servoing,” in *Proceeding of the IEEE/RSJ International Conference on Intelligent Robots and Systems (IROS)*, pp. 2681–2686, Alberta, Canada, August 2005.
- [136] A. Krupa, “Automatic calibration of a robotized 3D ultrasound imaging system by visual servoing,” in *Proceedings of the IEEE International Conference on Robotics and Automation (ICRA)*, pp. 4136–4141, Orlando, USA, May 2006.
- [137] P. Abolmaesumi, S. E. Salcudean, M. R. Siroospour, and S. P. DiMaio, “Image-guided control of a robot for medical ultrasound,” *IEEE Transactions on Robotics and Automation*, vol. 18, no. 1, pp. 11–23, 2002.
- [138] M.-A. Janvier, L.-G. Durand, M.-H. R. Cardinal, I. Renaud, B. Chayer, P. Bigras, J. de Guise, G. Soulez, and G. Cloutier, “Performance evaluation of a medical robotic 3D-ultrasound imaging system,” *Medical image analysis*, vol. 12, no. 3, pp. 275–90, 2008.
- [139] C. Nadeau, A. Krupa, P. Moreira, N. Zemiti, and J. Pognet, P. ; Gangloff, “Active stabilization of ultrasound image for robotically-assisted medical procedures,” in *5th Hamlyn Symposium on Medical Robotics*, London, Great Britain, 2012.
- [140] M. Abayazid, G. J. Vrooijink, S. Patil, R. Alterovitz, and S. Misra, “Experimental evaluation of ultrasound-guided 3d needle steering in biological tissue,” *International Journal of Computer Assisted Radiology and Surgery (IJCARS)*, vol. 9, no. 6, pp. 931–939, 2014.
- [141] G. J. Vrooijink, M. Abayazid, S. Patil, R. Alterovitz, and S. Misra, “Needle path planning and steering in a three-dimensional non-static environment using two-dimensional ultrasound images,” *International Journal of Robotics Research*, vol. 33, no. 10, pp. 1361–1374, 2014.
- [142] J. Roy and L. L. Whitcomb, “Adaptive force control of position/velocity controlled robots: theory and experiment,” *Robotics and Automation, IEEE Transactions on*, vol. 18, no. 2, pp. 121–137, 2002.
- [143] K. Gijsbertse, “3d localization of targets in curved soft-tissue phantoms using 2d ultrasound images,” Master’s thesis, Faculty of Science and Technology, University of Twente, The Netherlands, 2013.
- [144] S. Ghose, A. Oliver, R. Mart, X. Llad, J. Freixenet, J. Mitra, J. C. Vilanova, and F. Meriaudeau, “A hybrid framework of multiple active appearance models and global registration for 3d prostate segmentation in mri,” in *Proceedings of the Society of Photographic Instrumentation Engineers (SPIE), Medical Imaging: Image Processing* (D. R. Haynor and S. Ourselin, eds.), vol. 8314, pp. 83140S (1–9), San Diego, CA, USA, February 2012.

## REFERENCES

---

- [145] E. I. Canto, H. Singh, S. F. Shariat, D. Kadmon, B. J. Miles, T. M. Wheeler, and K. M. Slawin, “Effects of systematic 12-core biopsy on the performance of percent free prostate specific antigen for prostate cancer detection,” *The Journal of Urology*, vol. 172, no. 3, pp. 900–904, 2004.
- [146] T. De Silva, J. Bax, A. Fenster, J. Samarabandu, and A. D. Ward, “Quantification of prostate deformation due to needle insertion during TRUS-guided biopsy: comparison of hand-held and mechanically stabilized systems,” *Medical Physics*, vol. 38, no. 3, pp. 1718–1731, 2011.
- [147] Benninghoff, *Makroskopische Anatomie, Embryologie und Histologie des Menschen*. Urban und Schwarzenberg, 1 ed., 1993.
- [148] J. Ding, D. Stoianovici, D. Petrisor, P. Mozer, R. Avila, L. Ibanez, W. Turner, D. Yankelwitz, E. Wilson, F. Banovac, and K. Cleary, “Medical needle steering for lung biopsy: Experimental results in tissue phantoms using a robotic needle driver,” in *Proceedings of the 8th IEEE International Conference on Bioinformatics and BioEngineering (BIBE)*, pp. 1–5, Athens, Greece, October 2008.
- [149] S. Misra, K. J. Macura, K. T. Ramesh, and A. M. Okamura, “The importance of organ geometry and boundary constraints for planning of medical interventions,” *Medical Engineering & Physics*, vol. 31, no. 2, pp. 195–206, 2009.
- [150] Y. Hiroshi, *Strength of biological materials*. The Williams and Wilkins Company, 1 ed., 1970.
- [151] A. Jahya, M. Herink, and S. Misra, “A framework for predicting 3D prostate deformation in real time,” *International Journal of Medical Robotics and Computer Assisted Surgery*, vol. 9, no. 4, pp. e52–e60, 2013.
- [152] Y. Bar-Shalom, X. R. Li, and T. Kirubarajan, *Estimation with Applications to Tracking and Navigation: Theory Algorithms and Software*. John Wiley and Sons, Inc., 1 ed., July 2001.
- [153] S. Tsantis, G. C. Kagadis, K. Katsanos, D. Karnabatidis, G. Bourantas, and G. C. Nikiforidis, “Automatic vessel lumen segmentation and stent strut detection in intravascular optical coherence tomography,” *Medical physics*, vol. 39, no. 1, pp. 503–513, 2012.
- [154] A. Visioli, G. Ziliani, and G. Legnani, “Friction compensation in hybrid force/velocity control for contour tracking tasks,” *Industrial Robotics: Theory, Modeling and Control*, pp. 875–894, 2006.
- [155] W. Park, J. S. Kim, Y. Zhou, N. J. Cowan, A. M. Okamura, and G. S. Chirikjian, “Diffusion-based motion planning for a nonholonomic flexible needle model,” in *Proceedings of the IEEE International Conference on Robotics and Automation (ICRA)*, pp. 4600–4605, Barcelona, Spain, April 2005.

- 
- [156] J. Troccaz, M. Peshkin, and B. Davies, “Guiding systems for computer-assisted surgery: introducing synergistic devices and discussing the different approaches,” *Medical Image Analysis*, vol. 2, no. 2, pp. 101–119, 1998.
- [157] J. M. Romano, R. J. Webster III, and A. M. Okamura, “Teleoperation of steerable needles,” in *Proceedings of the IEEE International Conference on Robotics and Automation (ICRA)*, pp. 934–939, Roma, Italy, April 2007.
- [158] N. Hungr, J. Troccaz, N. Zemit, and N. Tripodi, “Design of an ultrasound-guided robotic brachytherapy needle-insertion system,” in *Proceedings of the IEEE international conference on Engineering in Medicine and Biology Society (EMBC)*, pp. 250–253, Minneapolis, MN, USA, September 2009.
- [159] A. Majewicz and A. M. Okamura, “Cartesian and joint space teleoperation for nonholonomic steerable needles,” in *World Haptics Conference (WHC)*, pp. 395–400, Daejeon, Korea, April 2013.
- [160] M. G. Schouten, J. Ansems, W. K. J. Renema, D. Bosboom, T. W. J. Scheenen, and J. J. Fütterer, “The accuracy and safety aspects of a novel robotic needle guide manipulator to perform transrectal prostate biopsies,” *Medical Physics*, vol. 37, no. 9, pp. 4744–4750, 2010.
- [161] D. Yakar, M. G. Schouten, D. G. H. Bosboom, J. O. Barentsz, T. W. J. Scheenen, and J. J. Fütterer, “Feasibility of a pneumatically actuated MR-compatible robot for transrectal prostate biopsy guidance,” *Radiology*, vol. 260, no. 1, pp. 241–247, 2011.
- [162] D. Prattichizzo, C. Pacchierotti, and G. Rosati, “Cutaneous force feedback as a sensory subtraction technique in haptics,” *IEEE Transactions on Haptics*, vol. 5, no. 4, pp. 289–300, 2012.
- [163] C. Pacchierotti, M. Abayazid, S. Misra, and D. Prattichizzo, “Teleoperation of steerable flexible needles by combining kinesthetic and vibratory feedback,” *IEEE Transactions on Haptics*, vol. 7, no. 4, pp. 551–556, 2014.
- [164] L. Meli, C. Pacchierotti, and D. Prattichizzo, “Sensory subtraction in robot-assisted surgery: fingertip skin deformation feedback to ensure safety and improve transparency in bimanual haptic interaction,” *IEEE Transactions on Biomedical Engineering*, vol. 61, no. 4, pp. 1318–1327, 2014.
- [165] C. Pacchierotti, A. Tirmizi, and D. Prattichizzo, “Improving transparency in teleoperation by means of cutaneous tactile force feedback,” *ACM Transactions on Applied Perception (TAP)*, vol. 11, no. 1, pp. 4:1–4:16, 2014.
- [166] C. R. Wagner, N. Stylopoulos, and R. D. Howe, “The role of force feedback in surgery: analysis of blunt dissection,” in *Proceedings of the Symposium of Haptic Interfaces for Virtual Environment and Teleoperator Systems*, pp. 68–74, Orlando, USA, March 2002.

## REFERENCES

---

- [167] S. E. Salcudean, S. Ku, and G. Bell, "Performance measurement in scaled teleoperation for microsurgery," in *Proceedings of the First Joint Conference on Computer Vision, Virtual Reality and Robotics in Medicine and Medial Robotics and Computer-Assisted Surgery*, pp. 789–798, Grenoble, France, November 1997.
- [168] A. Kazi, "Operator performance in surgical telemanipulation," *Presence: Teleoperators & Virtual Environments*, vol. 10, no. 5, pp. 495–510, 2001.
- [169] L. Moody, C. Baber, and T. N. Arvanitis, "Objective surgical performance evaluation based on haptic feedback," *Studies in health technology and informatics*, vol. 85, pp. 304–310, 2002.
- [170] C. W. Kennedy, T. Hu, J. P. Desai, A. S. Wechsler, and J. Y. Kresh, "A novel approach to robotic cardiac surgery using haptics and vision," *Cardiovascular Engineering*, vol. 2, no. 1, pp. 15–22, 2002.
- [171] A. Pillarisetti, M. Pekarev, A. D. Brooks, and J. P. Desai, "Evaluating the effect of force feedback in cell injection," *IEEE Transactions on Automation Science and Engineering*, vol. 4, no. 3, pp. 322–331, 2007.
- [172] C. Pacchierotti, M. Abayazid, S. Misra, and D. Prattichizzo, "Steering of flexible needles combining kinesthetic and vibratory force feedback," in *Proceeding of the IEEE Conference on Intelligent Robots and Systems (IROS)*, pp. 1202–1207, Chicago, USA, September 2014.
- [173] A. M. Okamura, "Haptic feedback in robot-assisted minimally invasive surgery," *Current opinion in urology*, vol. 19, no. 1, pp. 102–107, 2009.
- [174] M. Hashizume, M. Shimada, M. Tomikawa, Y. Ikeda, I. Takahashi, R. Abe, F. Koga, N. Gotoh, K. Konishi, S. Maehara, and K. Sugimachi, "Early experiences of endoscopic procedures in general surgery assisted by a computer-enhanced surgical system," *Surgical endoscopy*, vol. 16, no. 8, pp. 1187–1191, 2002.
- [175] M. Nakao, K. Imanishi, T. Kuroda, and H. Oyama, "Practical haptic navigation with clickable 3d region input interface for supporting master-slave type robotic surgery," *Studies in Health Technology and Informatics*, pp. 265–271, 2004.
- [176] J. Ren, R. V. Patel, K. A. McIsaac, G. Guiraudon, and T. M. Peters, "Dynamic 3-d virtual fixtures for minimally invasive beating heart procedures," *IEEE Transactions on Medical Imaging*, vol. 27, no. 8, pp. 1061–1070, 2008.
- [177] J. B. F. van Erp, H. A. H. C. van Veen, C. Jansen, and T. Dobbins, "Waypoint navigation with a vibrotactile waist belt," *ACM Transactions on Applied Perception*, vol. 2, no. 2, pp. 106–117, 2005.
- [178] J. Lieberman and C. Breazeal, "Tikl: Development of a wearable vibrotactile feedback suit for improved human motor learning," *IEEE Transactions on Robotics*, vol. 23, no. 5, pp. 919–926, 2007.

- 
- [179] R. E. Schoonmaker and C. G. L. Cao, "Vibrotactile feedback enhances force perception in minimally invasive surgery," in *Proceedings of Human Factors and Ergonomics Society Annual Meeting*, vol. 50, pp. 1029–1033, San Francisco, California, USA, October 2006.
- [180] W. McMahan, J. Gewirtz, D. Standish, P. Martin, J. A. Kunkel, M. Lilavois, A. Wedmid, D. I. Lee, and K. J. Kuchenbecker, "Tool contact acceleration feedback for telerobotic surgery," *IEEE Transactions on Haptics*, vol. 4, no. 3, pp. 210–220, 2011.
- [181] D. Ni, W.-Y. Chan, J. Qin, Y. Qu, Y.-P. Chui, S. S. Ho, and P.-A. Heng, "An ultrasound-guided organ biopsy simulation with 6dof haptic feedback," in *Proceedings of the International Conference on Medical Image Computing and Computer-Assisted Intervention (MICCAI)* (D. Metaxas, L. Axel, G. Fichtinger, and G. Székely, eds.), vol. 11, pp. 551–559, New York, USA, Springer Berlin / Heidelberg, September 2008.
- [182] S. Patil, J. Burgner, R. J. Webster III, and R. Alterovitz, "Needle steering in 3-D via rapid replanning," *IEEE Transactions on Robotics*, vol. 30, no. 4, pp. 853–864, 2014.
- [183] R. W. Cholewiak and A. A. Collins, "Sensory and physiological bases of touch," in *The Psychology of Touch* (M. A. Heller and W. Schiff, eds.), pp. 13–60, Laurence Erlbaum Associates, 1991.
- [184] K. A. Kaczmarek, J. G. Webster, P. Bach-y Rita, and W. J. Tompkins, "Electrotactile and vibrotactile displays for sensory substitution systems," *IEEE Transactions on Biomedical Engineering*, vol. 38, no. 1, pp. 1–16, 1991.
- [185] H. Pongrac, "Vibrotactile perception: examining the coding of vibrations and the just noticeable difference under various conditions," *Multimedia systems*, vol. 13, no. 4, pp. 297–307, 2008.
- [186] S. Wallenstein, C. L. Zucker, and J. L. Fleiss, "Some statistical methods useful in circulation research," *Circulation Research*, vol. 47, no. 1, pp. 1–9, 1980.
- [187] A. Krupa, "A new duty-cycling approach for 3d needle steering allowing the use of the classical visual servoing framework for targeting tasks," in *Proceedings of the IEEE RAS EMBS International Conference on Biomedical Robotics and Biomechatronics (BIOROB)*, pp. 301–307, August 2014.
- [188] C. Nadeau and A. Krupa, "Intensity-based ultrasound visual servoing: Modeling and validation with 2-D and 3-D probes," *IEEE Transactions on Robotics*, vol. 29, no. 4, pp. 1003–1015, 2013.
- [189] M. Abayazid, P. Moreira, N. Shahriari, S. Patil, R. Alterovitz, and S. Misra, "Ultrasound-guided three-dimensional needle steering in biological tissue with curved surfaces," *Medical Engineering & Physics*, vol. 37, no. 1, pp. 145–150, 2015.

## REFERENCES

---

- [190] E. D. Pisano, S. Zong, B. M. Hemminger, M. DeLuca, R. E. Johnston, K. Muller, M. P. Braeuning, and S. M. Pizer, “Contrast limited adaptive histogram equalization image processing to improve the detection of simulated spiculations in dense mammograms,” *Journal of Digital Imaging*, vol. 11, no. 4, pp. 193–200, 1998.
- [191] F. P. Preparata and S. J. Hong, “Convex hulls of finite sets of points in two and three dimensions,” *Communications of the Association Computing Machinery*, vol. 20, no. 2, pp. 87–93, 1977.
- [192] S. Ganapathy and T. G. Dennehy, “A new general triangulation method for planar contours,” *SIGGRAPH Computer Graphics*, vol. 16, no. 3, pp. 69–75, 1982.
- [193] L. R. Dice, “Measures of the amount of ecologic association between species,” *Ecology*, vol. 26, pp. 297–302, July 1945.
- [194] C. T. Zahn and R. Z. Roskies, “Fourier descriptors for plane closed curves,” *IEEE Transactions on Computers*, vol. C-21, no. 3, pp. 269–281, 1972.
- [195] K. J. M. Surry, H. J. B. Austin, A. Fenster, and T. M. Peters, “Poly(vinyl alcohol) cryogel phantoms for use in ultrasound and MR imaging,” *Physics in Medicine and Biology*, vol. 49, no. 24, pp. 5529–5546, 2004.
- [196] W. Xia, D. Piras, M. Heijblom, W. Steenbergen, T. G. van Leeuwen, and S. Manohar, “Poly(vinyl alcohol) gels as photoacoustic breast phantoms revisited,” *Journal of biomedical optics*, vol. 16, no. 7, pp. 075002 (1–9), 2011.
- [197] P. Moreira, I. Peterlik, M. Herink, C. Duriez, S. Cotin, and S. Misra, “Modelling prostate deformation: Sofa versus experiments,” *Mechanical Engineering Research*, vol. 3, no. 2, pp. 64–72, 2013.

# About the Author

Momen Abayazid was born in Gouda, the Netherlands on August 30, 1985. He received the B.Sc. degree in systems and biomedical engineering from Cairo University, Giza, Egypt, in 2007. During his B.Sc. study, he did internships in the VU University and AMC University in Amsterdam, the Netherlands. In June 2010, he received the M.Sc. degree in biomedical instrumentation from Delft University of Technology, Delft, The Netherlands. During his M.Sc. study, he did an internship in Philips Healthcare in Best, the Netherlands. He worked as software and administration engineer in Huisman Equipment before starting his PhD in the Robotics and Mechatronics group in the University of Twente, Enschede, the Netherlands, in 2011. He is currently working as a researcher in the Surgical Robotics Laboratory, Department of Biomechanical Engineering in the field of microrobotics in the University of Twente, Enschede, The Netherlands. His research interests include medical robotics, ultrasound-guided interventions and biomedical engineering.



## Publications

### International journals

- **M. Abayazid**, R.J. Roesthuis, R. Reilink and S. Misra, “Integrating deflection models and image feedback for real-time flexible needle steering”, *IEEE Transactions on Robotics*, vol. 29. issue 2, pp. 542-553, 2013.
- **M. Abayazid**, G.J. Vrooijink, S. Patil, R. Alterovitz and S. Misra, “Experimental evaluation of ultrasound-guided 3D needle steering in biological tissue”, *International Journal of Computer Assisted Radiology and Surgery (IJCARS)*, vol. 9, issue 6, pp. 931-939, 2014.

## REFERENCES

---

- G.J. Vrooijink, **M. Abayazid**, S. Patil, R. Alterovitz and S. Misra, “Needle path planning and steering in a three-dimensional non-static environment using two-dimensional ultrasound images”, *International Journal of Robotics Research*, vol. 33, issue 10, pp. 1361-1374, 2014.
- C. Pacchierotti, **M. Abayazid**, S. Misra and D. Prattichizzo, “Teleoperation of steerable flexible needles by combining kinesthetic and vibratory feedback”, *IEEE Transactions on Haptics*, vol. 7, issue 1, pp. 551-556, 2014.
- **M. Abayazid**, P. Morriera, N. Shahriari, S. Patil, R. Alterovitz and S. Misra, “Ultrasound-guided three-dimensional needle steering in biological tissue with curved surfaces”, *Medical Engineering & Physics*, vol. 37, issue 1, pp. 145-150, 2015.
- **M. Abayazid**, C. Pacchierotti, P. Moreira, S. Patil, R. Alterovitz, D. Prattichizzo and S. Misra, “Experimental evaluation of co-manipulated ultrasound-guided flexible needle steering”, *International Journal of Medical Robotics and Computer Assisted Surgery*, 2015 (Accepted).
- **M. Abayazid**, P. Moreira, N. Shahriari, A. Zompas and S. Misra, “Reconstruction of 3D shapes and needle steering using automated breast volume scanner (ABVS)”, *Journal of Medical Robotics Research*, 2015 (Under Review).
- T. Araújo, **M. Abayazid**, M.J.C.M. Rutten and S. Misra, “Segmentation and three-dimensional reconstruction of lesions using the automated breast volume scanner (ABVS)”, *International Journal of Computer Assisted Radiology and Surgery (IJCARS)*, 2015 (Under Review).

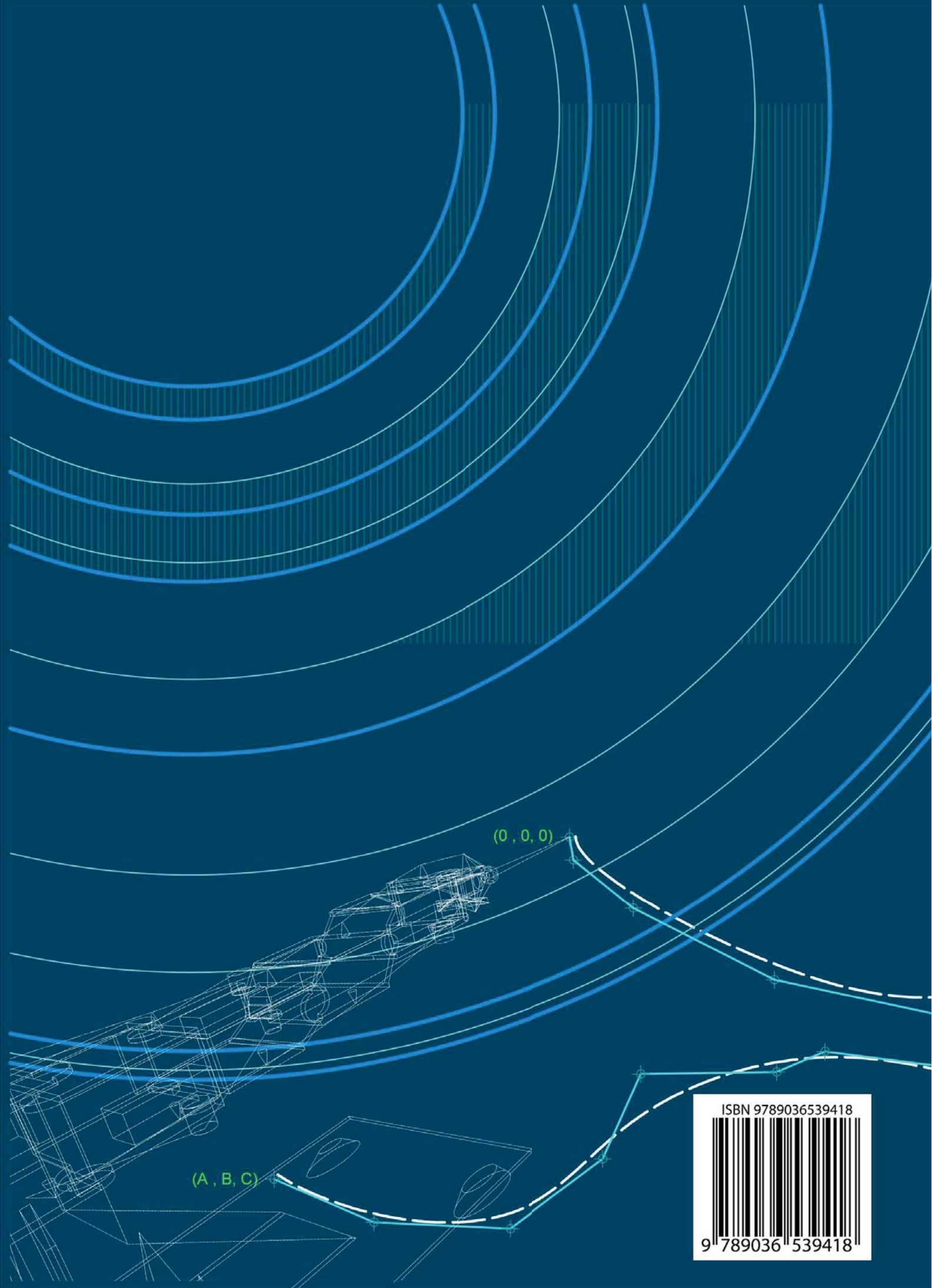
### International peer-reviewed conferences

- J. op den Buijs, **M. Abayazid**, C.L. de Korte and S. Misra, “Target motion predictions for pre-operative planning during needle-based interventions”, in *Proceedings of the IEEE International Conference of the IEEE Engineering in Medicine and Biology Society (EMBC)*, pp. 5380-5385, Boston, MA, USA, August-September 2011.
- **M. Abayazid**, C.L. de Korte and S. Misra, “Effect of skin thickness on target motion during needle insertion into soft-tissue phantoms”, in *Proceedings of the IEEE RAS & EMBS International Conference on Biomedical Robotics and Biomechanics (BioRob)*, pp. 755-760, Rome, Italy, June 2012.
- R.J. Roesthuis, **M. Abayazid** and S. Misra, “Mechanics-based model for predicting in-plane needle deflection with multiple bends”, in *Proceedings of the IEEE RAS & EMBS International Conference on Biomedical Robotics and Biomechanics (BioRob)*, pp. 69-74, Rome, Italy, June 2012.

- 
- **M. Abayazid**, M. Kemp and S. Misra, “3D flexible needle steering in soft-tissue phantoms using fiber bragg grating sensors”, in *Proceedings of the IEEE International Conference on Robotics and Automation (ICRA)*, pp. 5843-5849, Karlsruhe, Germany, May 2013.
  - G.J. Vrooijink, **M. Abayazid** and S. Misra, “Real-time three-dimensional flexible needle tracking using two-dimensional ultrasound”, in *Proceedings of the IEEE International Conference on Robotics and Automation (ICRA)*, pp. 1688-1693, Karlsruhe, Germany, May 2013.
  - **M. Abayazid**, N. Shahriari and S. Misra, “Three-dimensional needle steering towards a localized target in a prostate phantom”, in *Proceedings of the IEEE RAS & EMBS International Conference on Biomedical Robotics and Biomechatronics (BioRob)*, pp. 7 - 12, Sao Paulo, Brazil, August 2014.
  - C. Pacchierotti, **M. Abayazid**, S. Misra and D. Prattichizzo, “Steering of flexible needles combining kinesthetic and vibratory force feedback”, in *Proceedings of the IEEE/RSJ International Conference on Intelligent Robots and Systems (IROS)*, pp. 1202-1207, Chicago, Illinois, USA, September 2014.
  - P. Moreira, **M. Abayazid**, and S. Misra, “Towards physiological motion compensation for flexible needle interventions”, in *Proceedings of the IEEE/RSJ International Conference on Intelligent Robots and Systems (IROS)*, Hamburg, Germany, September-October 2015.

### Abstracts and workshops

- **M. Abayazid**, D.H.B. Wicaksono, P.J. French and J. Dankelman, “Modelling heat generation and temperature distribution for temperature sensing during dental surgical drilling”, in *Proceedings of Semiconductor Advances for Future Electronics and Sensors (SAFE) conference*, Veldhoven, the Netherlands, 2009.
- **M. Abayazid**, R. Reilink and S. Misra, “Image-guided flexible bevel-tip needle control”, in *Proceedings of the annual symposium of the Benelux Chapter of the IEEE Engineering in Medicine and Biology Society (EMBS)*, Leuven, Belgium, December 2011.
- G.J. Vrooijink, **M. Abayazid**, S. Patil, R. Alterovitz, and S. Misra, “Three-dimensional flexible needle steering using two-dimensional ultrasound images”, in *Proceedings of the fourth Dutch Biomedical Engineering Conference*, Egmond aan Zee, The Netherlands, January 2013.
- **M. Abayazid**, A. Zompas, and S. Misra, “Three-dimensional flexible needle steering using an automated breast volume ultrasound scanner”, in *Proceedings of the fifth Dutch Biomedical Engineering Conference*, Egmond aan Zee, The Netherlands, January 2015.



(0, 0, 0)

(A, B, C)

ISBN 9789036539418



9 789036 539418